ICRR ANNUAL REPORT 2020

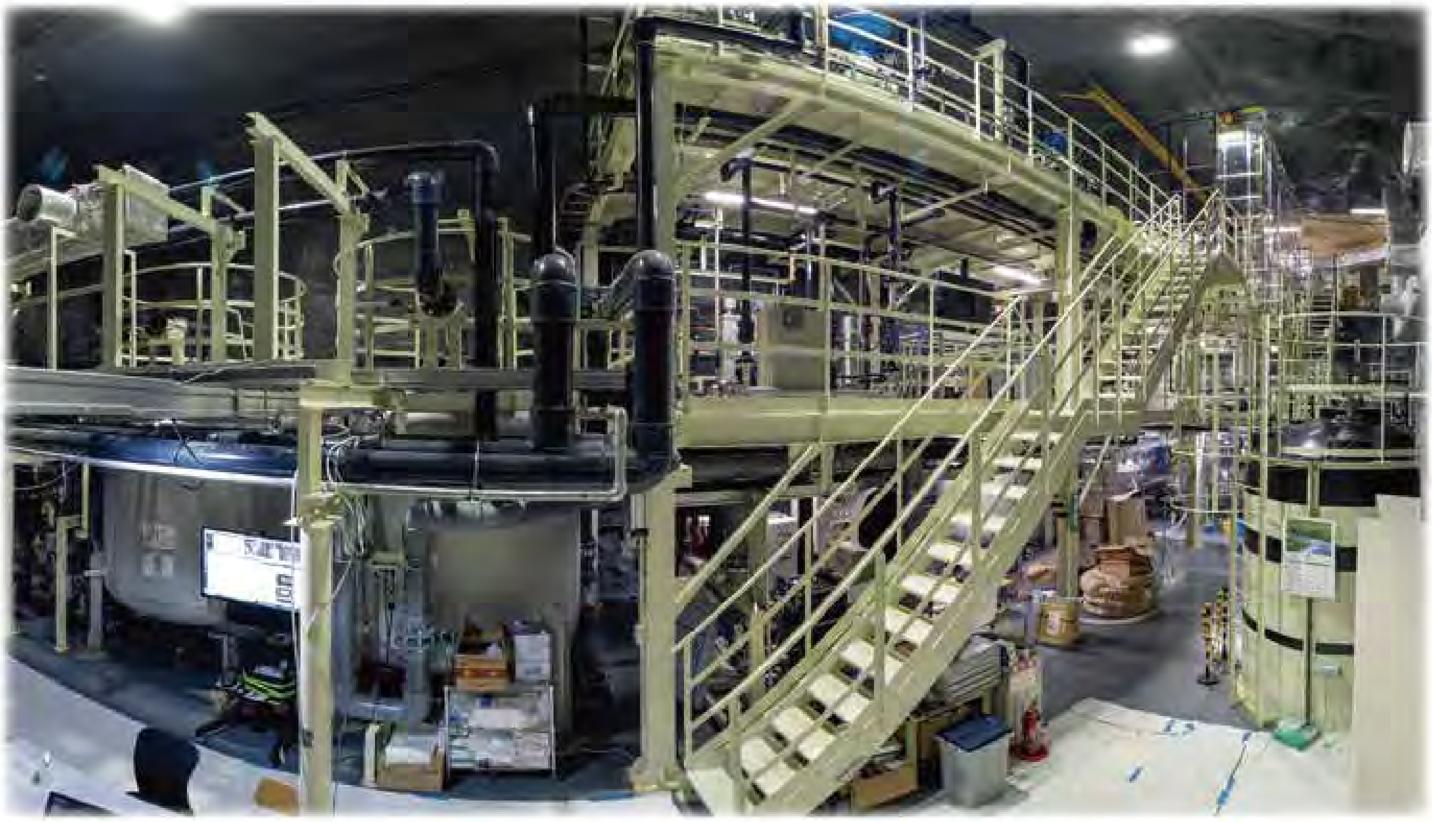

INSTITUTE

FOR

COSMIC RAY RESEARCH

THE UNIVERSITY OF TOKYO

ANNUAL REPORT
(APRIL 2020 – MARCH 2021)

ICRR
Institute for Cosmic Ray Research
University of Tokyo

5-1-5, Kashiwanoha, Kashiwa, Chiba 277-8582, Japan

Telephone: (81) 4-7136-3102
Facsimile: (81) 4-7136-3115
WWW URL: http://www.icrr.u-tokyo.ac.jp/

TABLE OF CONTENTS

PREFACE

This report summarizes the scientific activities of the Institute for Cosmic Ray Research (ICRR) of The University of Tokyo in the Japanese FY (JFY) 2020.

ICRR is an inter-university research institute for studies of cosmic rays. The headquarters of ICRR is located in Kashiwa, Chiba prefecture, Japan. In order to promote various cosmic-ray-related studies efficiently, ICRR has three research divisions; Neutrino and Astroparticle division, High Energy Cosmic Ray division, and Astrophysics and Gravity division. ICRR have four observatories in Japan; Kamioka Observatory and KAGRA Observatory (Kamioka underground, Gifu prefecture), Norikura Observatory (2770 meters above sea level, Mt. Norikura, Gifu prefecture), and Akeno Observatory (Yamanashi prefecture), together with 1 research center; Research Center for Cosmic Neutrinos (Kashiwa, Chiba prefecture). In addition, there are three major experimental facilities outside of Japan. They are located in Utah in USA, Yangbajing in Tibet, China and the La Palma island in Spain.

Many researchers from various Japanese institutions as well as those from overseas are involved in the research programs of ICRR. It should be noted that most of the scientific outputs from ICRR are the results of the collaborative efforts by many researchers from various institutions. In order to produce outstanding results, it is very important to carry out an experiment by an international collaboration composed of top-level researchers all over the world. Hence, all of the experimental collaborations that ICRR is involved are international ones. With these activities, ICRR has been selected as one of the institutions of the "International Joint Usage/Research Center" program by Ministry of Education, Culture, Sports, Science and Technology -Japan (MEXT) in November 2018.

In JFY 2020, our inter-university research activities have been largely affected by COVID-19. In many countries, overseas travels have been strictly restricted. Even the domestic travels within Japan have been limited. Therefore, we have had minimum amount of onsite works. On the other hand, many of us have been using online communication tools to carry out researches remotely. Now it is realized that our research works will continue to be affected by COVID-19 for some time. Therefore, we try to improve the research environment in our experiments and observatories so that the collaborators have easier access to the resources at each experiment or observatory remotely. We hope that, after the end of the pandemic, we will be able to carry out even closer collaborations with our international and domestic collaborators.

Even during the pandemic, ICRR has carried out various researches. Many exciting scientific activities of ICRR are described in this report. For example, the Super-Kamiokande and T2K (which uses Super-Kamiokande as the far detector) experiments have been continuously producing impressive results on neutrino oscillation physics. The KAGRA gravitational wave project has carried out an observation run in April 2020 with GEO, a German gravitational wave detector. TA (Telescope Array) has been producing impressive results on highest energy cosmic rays. The extension of TA (TAx4) at the Utah site has begun. In gamma-ray astronomy, the Tibet ASγ experiment observed a sub-PeV gamma ray signals. The MAGIC collaboration, in which ICRR is participating, has been significantly contributing to the TeV gamma-ray astronomy. ICRR is playing a major role in CTA, which is a global TeV gamma-ray astronomy project. ICRR is contributing substantially to the construction of Large-Sized Telescopes (LST) of the CTA-North observatory. The first LST has started the observations.

As an inter-university research institute, ICRR is reviewed by the top-level researchers in the field. In particular, future projects of ICRR are evaluated by a committee composed of top-level researchers from various nearby fields. The ICRR Future Project Evaluation Committee released its report in October 2017. Several projects have been recommended highly. Among them, Hyper-Kamiokande, which is the next generation neutrino detector, has been recommended as the top priority ICRR future project. The Hyper-Kamiokande project was approved by the Japanese government in early 2020. Following the approval, the construction has begun. The experiment is expected to start in 2027.

We hope that this report is useful for the understanding of the current research activities of ICRR. Finally, we appreciate the strong support of our colleagues in this research field, The University of Tokyo and MEXT. They are indispensable for the continuing, and exciting scientific outcome of ICRR.

Takaaki Kajita,

Director,

Institute for Cosmic Ray Research,

The University of Tokyo

The ICRR building at Kashiwa, Chiba, Japan.

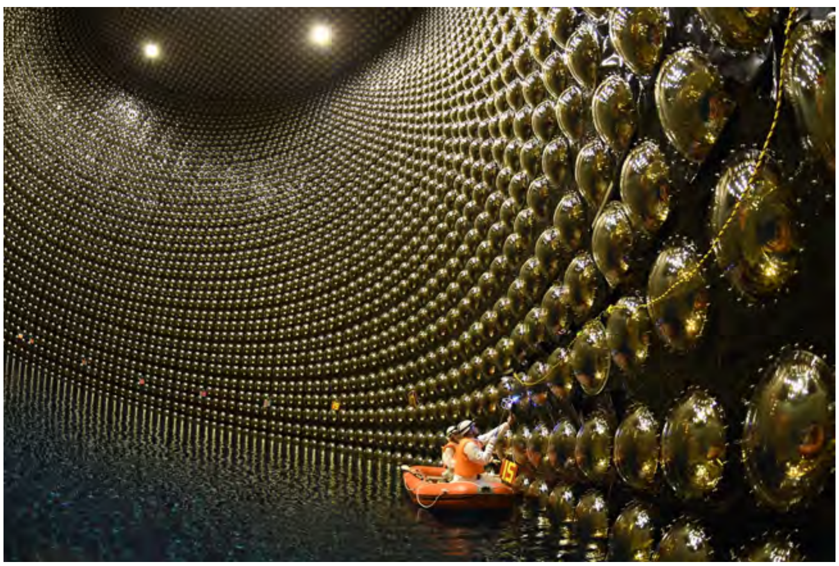

The Super-Kamiokande detector (the photo was taken during refurbishment work in 2018).

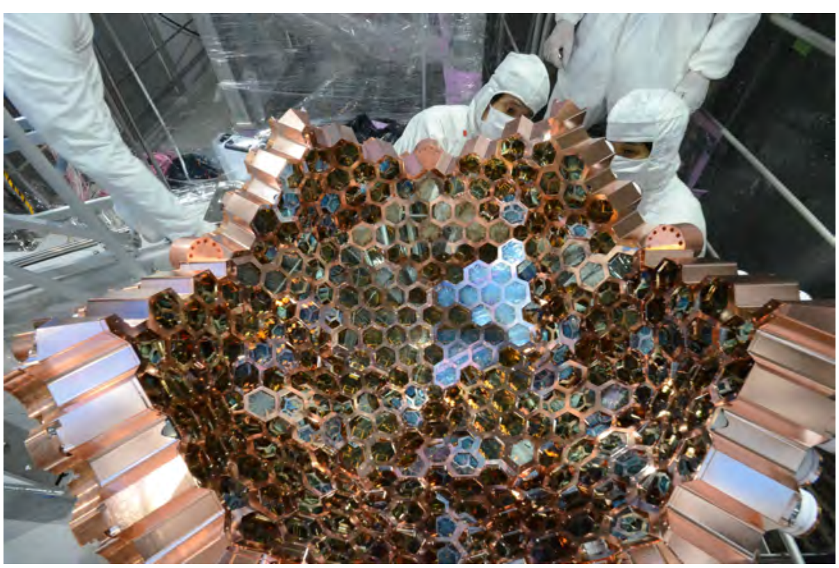

The XMASS detector (the photo was taken during the refurbishment work in 2013).

The first Large Size Telescope of CTA installed at Observatory Roque de los Muchachos inaugurated on October 10 2018.

Tibet-III air shower array (37000 m^2) at Yangbajing, Tibet (4300 m in altitude).

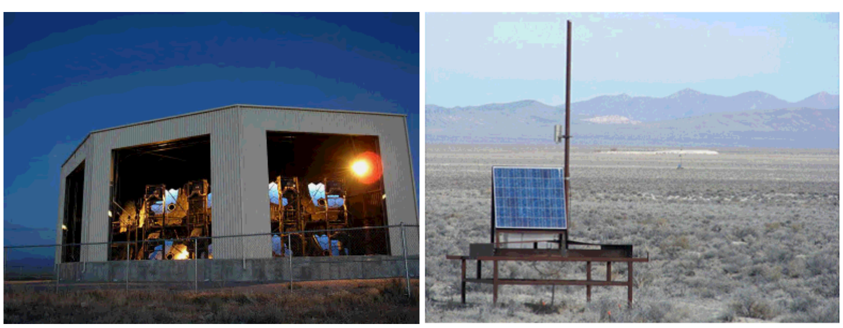

Air fluorescence telescopes (left) and a scintillator surface detector (right) of the Telescope Array experiment in Utah, USA to explore the origin of extremely high energy cosmic rays.

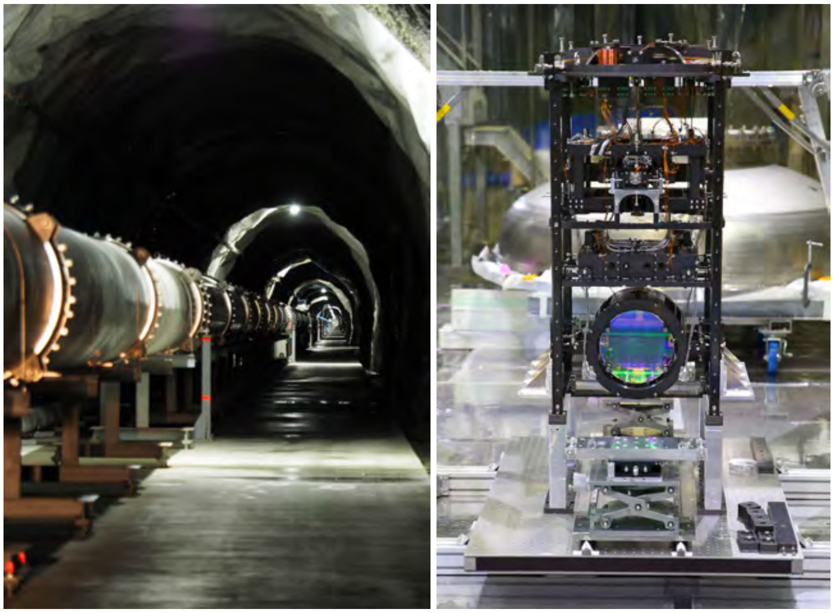

KAGRA's (left) 3km-long arm tunnel and (right) a sapphire mirror installed in a cryogenic suspension system.

Online public lecture co-organized with the Institute for the Physics and Mathematics of the Universe (Kavli IPMU).

Organization

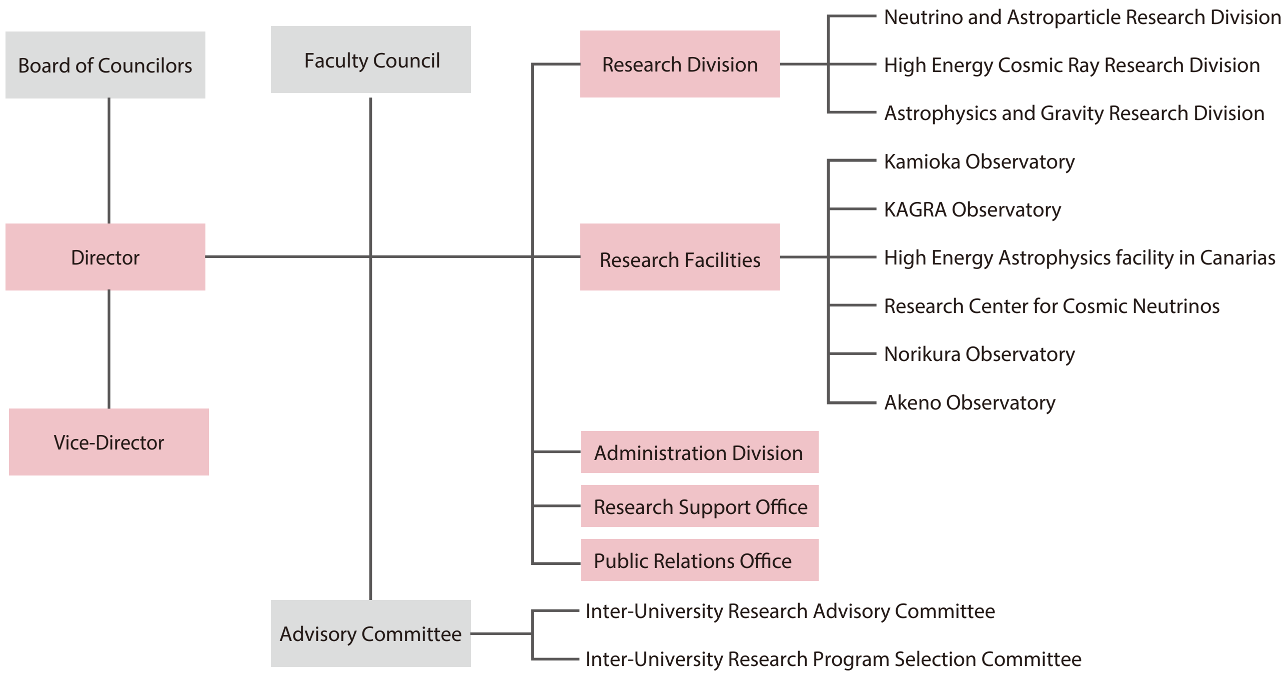

Number of Staff Members (As of May 1, 2020)

	Scientific Staff	Technical Staff	Research Fellows	Administrators and Secretaries	Total
Neutrino and Astroparticle Div.	24	4	2	18	48
High Energy Cosmic Ray Div.	20	10	8	2	40
Astrophysics and Gravity Div.	17	11	14	9	51
Administration	0	0	0	22	22
Total	61	25	24	51	161

FY 2013-2020 Budget

	2013	2014	2015	2016	2017	2018	2019	2020
Personnel expenses	687 000	706 000	684 000	683 000	779 000	823 000	872 000	898 000
Non-personnel expenses	1 095 000	1 282 000	1 595 000	1 288 000	1 514 000	1 729 000	1 611 000	1 173 000
Total	1 782 000	1 988 000	2 279 000	1 971 000	2 293 000	2 552 000	2 483 000	2 071 000

(in 1 000 yen)

RESEARCH DIVISIONS

NEUTRINO AND ASTROPARTICLE DIVISION

Overview

This division aims to study particle physics with prime interests in physics of neutrinos and proton decay, and astroparticle physics with the use of underground experimental facilities.

The Super-Kamiokande (SK) detector is a 50 kton water Cherenkov detector using 11,129 50 cm-diameter photomultipliers (PMTs) for its inner detector and 1,885 20 cm-diameter PMTs for its outer detector. The data taking of SK started in April 1996 and 20th anniversary was celebrated in 2016. The neutrino oscillations in atmospheric neutrinos were discovered in 1998 and thereby it was demonstrated that neutrinos have a finite mass. In 2001, the accurate measurements of the ^{8}B solar neutrino flux by SK and SNO discovered that neutrino oscillations are the solution of the solar neutrino problem beyond doubt. These findings became the research achievement for which the Nobel Prize in Physics was awarded in 2015. After the epoch-making discoveries, precise measurements of atmospheric neutrinos and solar neutrinos have been performed and they unraveled various phenomena of neutrino oscillations. The evidence of tau neutrino appearance in atmospheric neutrinos was confirmed in 2013 and atmospheric neutrino anomaly has been finally concluded. The indication of day-night asymmetry of the solar neutrino flux, which is expected from the matter effect of neutrino oscillations, was reported in 2014. At present, the most interesting subjects in those observations are the determination of neutrino mass hierarchy using atmospheric neutrinos and the consistency check of solar(ν_e) and reactor($\bar{\nu}_e$) oscillations.

A high intensity neutrino beam experiment using the J-PARC accelerator (T2K) was started in 2009. The T2K experiment uses the SK detector as the far detector. Search for leptonic *CP* violation and the high precision measurement of oscillation parameters are main physics subjects in T2K. An indication of electron neutrino appearance was found in June 2011, and later the electron appearance has been established with greatly improved significance. Since 2014, anti-neutrino beam data also have been taken in order to search for *CP* violation. T2K later reported the exclusion of the conservation of *CP* symmetry in neutrino oscillations at more than 95% CL.

The search for nucleon decay is another important subject at SK because it gives a direct evidence for the Grand Unified Theories (GUTs). SK gives the current best limit which strongly constrains various GUT models.

If a supernova happens in our galaxy, thousands of neutrino interactions are expected at SK and they will reveal detailed mechanism of the supernova explosion. SK is the only detector in the world which can identify the direction of the supernova neutrinos. So, SK has been operated almost all the time with small dead time and if a supernova is observed at SK, we will send burst information to astronomers as soon as it is detected. In addition, SK aims to observe supernova relic neutrinos, which is an accumulated supernova burst neutrinos from the beginning of the universe. For this purpose, it is planned to add 0.1% of gadolinium into the Super-K tank (called SK-Gd project) in order to tag neutrons for $\bar{\nu}_e$ detection. A feasibility study for the SK-Gd project is being performed using a 200 ton tank which mimics the Super-K detector. Refurbishment of the Super-K tank and upgrade of the water circulation system had been conducted in 2018 and 0.01% gadolinium has been dissolved in the detector water in the summer 2020.

Another activity of the Neutrino and Astroparticle division is a multi-purpose experiment using liquid xenon aiming at the detection of cold dark matter, neutrino absolute mass using neutrinoless double beta decay, and low energy solar neutrinos. A 800 kg liquid xenon detector was constructed in an experimental hall near the SK site. Data taking continued for more than five years and finished in February 2019. Searches for dark matter interactions and rare phenomena in liquid xenon are being conducted.

The Hyper-Kamiokande (Hyper-K or HK) experiment is proposed as a joint project of the University of Tokyo and KEK by combining a next generation underground water Cherenkov detector and upgraded J-PARC neutrino beam. The Hyper-K detector is an order of magnitude larger in detector fiducial mass than Super-K and has discovery potential of leptonic *CP* violation and proton decays. The project has officially started by receiving its first Japanese funding in the beginning of 2020. Its construction schedule includes 5 years of the cavern excavation, 2 years of instrumentation, and data taking commencement in 2027. In parallel, the J-PARC beam delivered to the detector will be upgraded from 0.5 to 1.3 MW over the same time period.

SUPER-KAMIOKANDE

[Spokesperson : Masayuki Nakahata
(Kamioka Observatory, ICRR, The University of Tokyo)]

Atmospheric neutrinos

Atmospheric neutrinos are produced from the decays of secondary particles produced in the collision of primary cosmic rays with nuclei in the atmosphere. Atmospheric neutrinos have several remarkable features:

- The flavor ratio, $(\nu_\mu+\bar{\nu}_\mu)/(\nu_e+\bar{\nu}_e)$ is 2 (>2 for above few GeV)
- Zenith angle distribution is up/down symmetry above a few GeV

These features are realized without neutrino oscillations, and provide a useful constraint in the study of these neutrinos.

Super-Kamiokande has been observing atmospheric neutrinos since 1996 and has accordingly made several important measurements, including the discovery of neutrino oscillations [1].

After refurbishment of the SK detector in preparation for Gd loading, atmospheric neutrino data was taken during the fifth run period from 2019 to 2020. These data have been demonstrated to be of similarly high quality as that in previous pure-water periods (c.f. Figure 1).

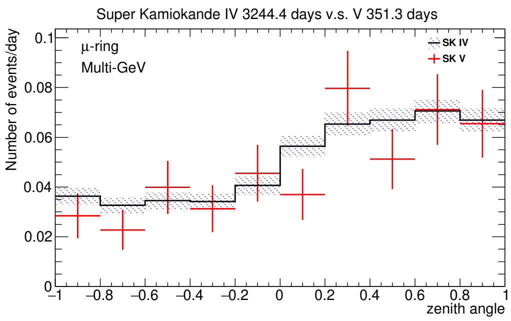

Fig. 1. Comparison of the atmospheric neutrino event rate in SK-IV and SK-V for the multi-GeV μ-like sample.

Three flavor oscillations and the neutrino mass hierarchy

The SK atmospheric neutrino data are described at leading order by two-flavor $\nu_\mu \to \nu_\tau$ oscillations with maximal mixing (θ_{23}=π/4). However, sub-leading contributions via $\nu_\mu \to \nu_e$ oscillations induced by the mixing angle θ_{13} as well as the "solar" mixing parameters ($\Delta m^2_{12}, \theta_{12}$) provide the ability to probe currently unknown aspects of the standard neutrino oscillation paradigm, such as the existence of leptonic *CP* violation and the neutrino mass ordering (hierarchy). Understanding these open questions may bring important insight into larger questions, such as the origin and evolution of today's matter-dominated universe.

Several sub-leading oscillation effects are expected to appear in atmospheric neutrinos:

- Resonant enhancement of $\nu_\mu \to \nu_e$ oscillations due to the effects of matter is expected to occur at energies between 2 and 10 GeV and will manifest as an excess of upward-going electron-like events (e-like) in the atmospheric sample.
- This enhancement exists for either ν_e or $\bar{\nu}_e$ depending on the mass hierarchy. Therefore the mass hierarchy can be probed by understanding the relative amount of neutrino and antineutrino interactions in the detector.
- The combination of the solar oscillation parameters and the octant of $\sin^2\theta_{23}$, may enhance or suppress the event rate, and to some extent alter the spectral shape, of Sub-GeV electron-like data the due to the $\nu_\mu \leftrightarrow \nu_e$ oscillations they induce.
- The standard oscillation paradigm includes a *CP*-violating factor, δ_{cp}, which is expected to induce several sub-dominant oscillation effects in many of the SK atmospheric neutrino samples, even if CP is conserved.

Super-Kamiokande has studied the effects of these oscillations on atmospheric neutrino data separated into fully-contained (FC) events, partially-contained (PC) events, and upward-going muon (UPMU) topologies. Fully-contained events are characterized by a primary interaction vertex that is located inside the fiducial volume of the detector and whose visible particles stop within the inner detector. On the other hand, though the primary vertex position of PC events is within the fiducial volume, they are characterized by having at least one charged particle escaping the inner detector and depositing light in the outer detector. In most cases the escaping particle is a muon. Upward-going muons originate from high energy muon-neutrino interactions in the rock surrounding the detector. Since all other particles are lost to interactions in the rock, only the muon is penetrating enough to reach the detector and be identified. The FC sample is separated into electron-like and muon-like (μ-like) subsamples by applying a particle identification algorithm to the most energetic Cherenkov ring of each event. Since PC and upward-going events are predominantly produced by muon neutrinos, no particle identification is applied. Though SK cannot distinguish on an event-by-event basis neutrino and antineutrino interactions, statistical separation of multi-GeV electron-like subsamples is performed to improve sensitivity to the mass hierarchy. A likelihood method designed to enhance the kinematic differences between neutrino and antineutrino interactions is applied to separate events into ν_e-like and $\bar{\nu}_e$-like subsamples.

Since the start of SK-IV the SK has had the ability to identify neutrons, albeit with a limited efficiency of 25%. In 2020 atmospheric neutrino events from this data set were separated into neutrino-like and antineutrino-like samples taking advantage of the fact that the former are expected to produce fewer neutrons on average than the latter. Further, a novel event selection based on a boosted decision tree was introduced to improve the classification of multi-ring events in all date periods. Using these new event selections all SK data until the end of the SK-IV period in 2018 were analyzed to update the analysis presented in [2, 3]. With an expected increase in hierarchy sensitivity of $\sim 15\%$ this new analysis found a preference for the normal mass ordering of of between 71.4% and 90.3% over the range of oscillation parameters allowed at 90% C.L.. This result is somewhat weaker than that of the publication, whose preference was 81.9% to 96.7%. Similarly the updated analysis prefers the first octant of $\sin^2\theta_{23}$ at roughly 1σ a weak preference for a non-zero CP-violating phase. These results are summarized in Table 1 and in Figure 2.

A search for flavor changing neutral current and lepton universality-violating interactions using atmospheric neutrino data has also been performed by incorporating their effects on the predicted oscillations. In particular, these exotic interactions can be represented as additional potentials arising from the presence of quarks in the matter these neutrinos observe as the pass through the Earth:

$$H_{matter} = V_{MSW} + \sqrt{2}G_F N_f(\vec{r}) \begin{pmatrix} \varepsilon_{ee} & \varepsilon^*_{e\mu} & \varepsilon^*_{e\tau} \\ \varepsilon_{\mu e} & \varepsilon_{\mu\mu} & \varepsilon^*_{\mu\tau} \\ \varepsilon_{\tau e} & \varepsilon_{\tau\mu} & \varepsilon_{\tau\tau} \end{pmatrix}. \quad (1)$$

Here the ε_{ij} represent additional non-standard interactions

Fit	Hierarchy	$\sin^2\theta_{23}$	$\lvert\Delta m^2_{32,31}\rvert$ [$\times 10^{-3}$ eV^2]	δ_{CP}
SK only	NH	$0.44^{+0.05}_{-0.02}$	$2.40^{+0.11}_{-0.12}$	$4.36^{+0.88}_{-1.39}$
	IH	$0.45^{+0.09}_{-0.03}$	$2.40^{+0.09}_{-0.32}$	$4.54^{+0.88}_{-1.32}$

Table 1. Best fit oscillation parameters obtained by the three flavor oscillation analysis. Fits are conducted for both the normal (NH) and inverted (IH) hierarchy assumptions The fit was performed assuming $\sin^2\theta_{13}$=0.0218, which is taken from PDG.

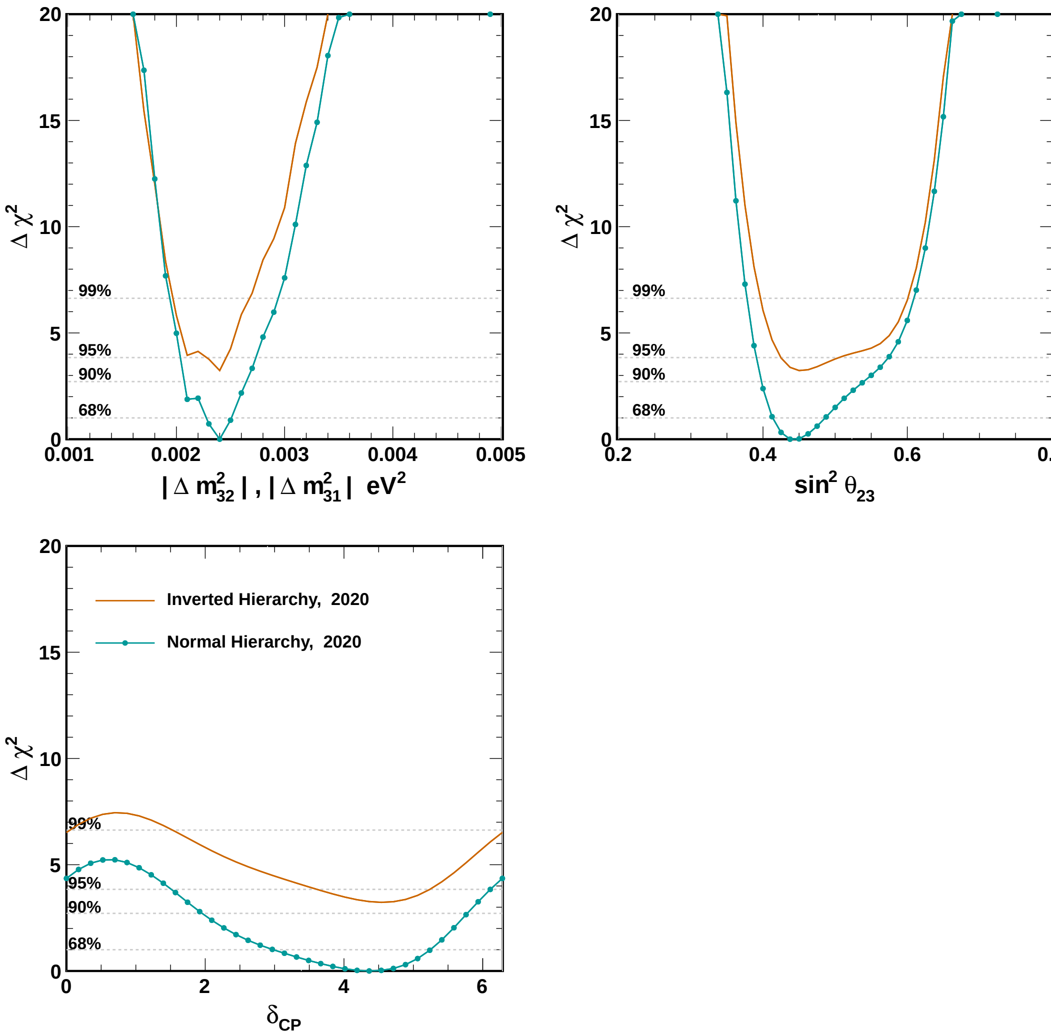

Fig. 2. The $\Delta\chi^2$ as a function of $\Delta m^2_{23,31}$, $\sin^2\theta_{23}$, and δ_{cp}. Fits to the normal (blue) and inverted (orange) hierarchy hypotheses are shown.

(NSI), N_f is the position-dependent fermion density, and V_{MSW} is the standard matter potential used to probe the mass hierarchy above. To avoid the computational complexity of fitting all of these parameters simultaneously, the analysis is broken into two parts. The first probes new interactions in the $\mu-\tau$ sector, allowing for NSI effects to appear atop of the normal atmospheric disappearance. In the second part the $e-\tau$ parameters, which modify the appearance of electron-type neutrinos, are studied. Note that this analysis is an update and upgrade of that in Ref. [4], that studied these phenomena using SK data up until 2005. The present analysis updates all aspects of the analysis, using the full data set up to 2016 and the event selection [3].

Neither of the NSI analysis parts found evidence of oscillations beyond the standard paradigm. At the 90% C.L. the parameters in the $\mu-\tau$ sector are constrained as

$$-4.5\times10^{-2} < \quad \varepsilon_{\mu\tau} \quad < 1.9\times10^{-2} \tag{2}$$

$$-5.1\times10^{-2} < \varepsilon_{\mu\mu}-\varepsilon_{\tau\tau} < 1.4\times10^{-1}. \tag{3}$$

Constraints on these parameters are shown in the left panel of Figure 3. The situation in the $e\tau$ sector is complicated by the inability of the SK data set to simultaneously determine the three relevant parameters. Instead the three are related as

$$\varepsilon_{\tau\tau} = \frac{\varepsilon_{e\tau}}{1+\varepsilon_{ee}}. \tag{4}$$

Here, constraints are extracted in the $\varepsilon_{\tau\tau}$ and $\varepsilon_{e\tau}$ plane for a series of fixed values of ε_{ee}. An example constraint is shown in the right panel of the figure. In both sectors the fit is slightly improved by allowing non-zero values of the NSI parameters.

Searches for Neutrinos Associated with Gravitational Waves

Since the direct observation of gravitational waves in the LIGO and subsequently LIGO and VIRGO detectors, there has been considerable effort to observe coincident signals with other forms of radiation. In addition to electromagnetic signals already observed in, for instance, neutron star-neutron star merger events, astrophysical objects creating gravitational waves may also emit MeV (or higher) neutrinos. At present, no such coincident observation of neutrinos and gravitational waves has been achieved.

Based on a preliminary version of the GWTC-2 [5] catalog of gravitational waves detected from the LIGO-Virgo Collaboration (LVC), Super-Kamiokande performed follow-up observations of the triggers listed therein. The search was performed in time intervals of 1000 s around each trigger and found 8 events, 6 FC and 2 UPMU events, in coincidence. For this search the expected background was 7.13 events, indicating no statistically significant excess. Given the large distances (Mpc) to the black hole or neutron star mergers that produce these triggers, the neutrino signal, if any, is expected to be weak. On the other hand, as the origin of the gravitational wave signal can be somewhat localized by LVC comparisons of the arriving neutrino direction with each trigger's skymap were used to calculate a p-value for coincident event. Even with this additional directional information, all neutrino events were found to be consistent with the background expectation. Table 2 summarizes the SK coincident observation and Figure 4 shows the skymap for the event with the smallest p-value, a FC event arriving just before trigger S190602aq.

Bibliography

[1] Y. Fukuda *et al.* [Super-Kamiokande Collaboration], Phys. Rev. Lett. **81**, 1562 (1998).

[2] R. Wendell *et al.* [Super-Kamiokande Collaboration], Phys. Rev. D **81**, 092004 (2010).

[3] K. Abe *et al.* [Super-Kamiokande Collaboration], Phys. Rev. D **97**, no. 7, 072001 (2018).

[4] G. Mitsuka *et al.* [Super-Kamiokande Collaboration], Phys.Rev.D **85**, 113008 (2011).

[5] R. Abbott *et al.* Phys.Rev.X **11**, 021053 (2021)

Solar Neutrinos

Introduction

Solar neutrinos constitute by far the largest component of neutrino flux on the Earth among those produced from natural sources. Most of solar neutrinos are produced by proton-proton fusion, $p+p \to d+e^{+}+\nu_e$, and its subsequent fusion reactions (pp-chain)[1]. They are categorized into the *pp*, *pep*, ^{7}Be, ^{8}B and *hep* neutrinos, whose predicted fluxes by the standard solar model [1] are shown in the left panel of Figure 5. Among these, Super-Kamiokande is sensitive to ^{8}B and *hep* neutrinos, which have relatively higher energy that extends up to $\sim$20 MeV.

Past observations of solar neutrino flux by Super-Kamiokande (SK) [2] and the Sudbury Neutrino Observatory (SNO) [3] led to the discovery of solar neutrino flavor conversion. Our current interest for solar neutrino measurements with the SK detector [4] is to make a precision test of the neutrino flavor conversion through the Mikheyev-Smirnov-Wolfenstein (MSW) effect [5, 6]. The MSW effect leads to a resonant conversion of the solar neutrinos within the Sun and results in an about 30% level of the survival probability above $\sim$5 MeV as shown in the left panel of Fig. 5. The survival probability of lower energy neutrinos are described by the vacuum oscillation probability of $\sim$ 50%, and the transition region between the two lies at a few MeV region. This transition from the matter dominant oscillation to the vacuum dominant oscillation is often called as the "up-turn" of the solar neutrino spectrum. This "up-turn" have not been directory demonstrated by the past experimental data.

SK aims to directly test the "Spectrum up-turn" by precisely measuring energy spectrum of ^{8}B solar neutrino in this transition region. This measurement is important not only to test the MSW effect but also to test several alternative theoretical models, such as sterile neutrinos [7, 8], mass-varying neutrinos [9], non-standard interactions [10, 11] and so on.

The matter effect can also be tested with the matter in the interior of the Earth. Electron flavor neutrinos are regenerated due to the matter effect of the Earth as shown in the right panel of Fig. 5, making the neutrino flux in night is larger than that in day by about a few % level depending on the neutrino oscillation parameters. In 2014, SK reported an indication of the terrestrial matter effects with a significance of about 2.7σ [12].

In this article, we report results of solar neutrino measurements using the data taken through the end the fourth SK data taking phase (SK-IV) in May 2018, with an analysis method improved from our previous publication [13]. The total livetime used for this analysis is 5,805 days, with 2970 days from the SK-IV phase.

Analysis improvements

In this analysis, we employed a number of improvements to the analysis methods.

The detector simulation was improved with more accurate modeling of the PMT timing response and the non-uniformity of the water quality. These improvements reduced the systematic uncertainties resulting from the event selection cuts and the reconstructed energy scale.

The energy reconstruction method was also improved with a correction for the PMT gain drift and also with a new correction of the energy scale non-uniformity. The correction for the gain drift was first introduced in 2017 and then refined in this analysis with an improved correction for the dark noise contribution. We successfully kept the reconstructed energy scale within $\pm 0.5\%$ for nearly 10 years of operation in the

*1 with a subdominant ($\sim$1%) contribution from the CNO cycle

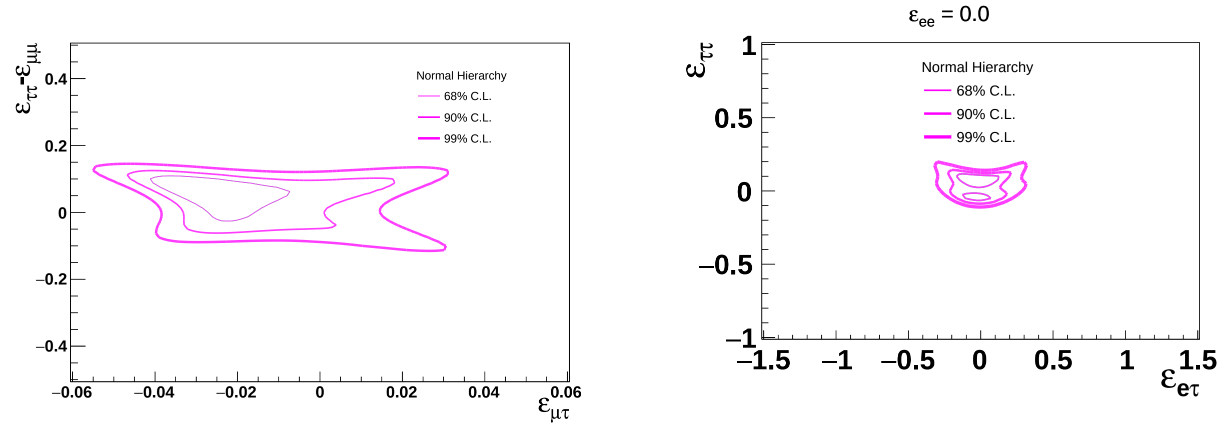

Fig. 3. Constraints on NSI parameters in the $\mu-\tau$ sector (left) and in the $e-\tau$ sector (right). These calculations assume standard PMNS oscillations at the best fit of the the 2018 SK analysis [3].

Name	Alert UTC	Obs.events (Δt)	p_{Λ} (%)	p_{χ^2} (%)
S190426c	2019-04-26 15:21:55	UPMU (+279s)	100.0	51.0
S190513bm	2019-05-13 20:54:28	FC (-183s)	5.7	15.5
S190602aq	2019-06-02 17:59:27	FC (-287s)	2.8	1.6
S190728q	2019-07-28 06:45:10	FC (+103s)	11.7	26.4
S190814bv	2019-08-14 21:10:39	FC (+249s)	48.1	57.9
S190924h	2019-09-24 02:18:46	FC (+412s)	48.1	76.5
S191213g	2019-12-13 04:34:08	FC (+289s)	15.4	11.7
S200316bj	2020-03-16 21:57:56	UPMU (-366s)	52.3	99.7

Table 2. Summary of atmospheric neutrino events found within 1000s of a gravitational wave trigger in the GWTC-2 catalog. Here Δt shows the time of the neutrino event to the trigger and the p-values describing the compatibility with the background hypothesis incorporating directional information p_{Λ} and additionally time information p_{χ^2}.

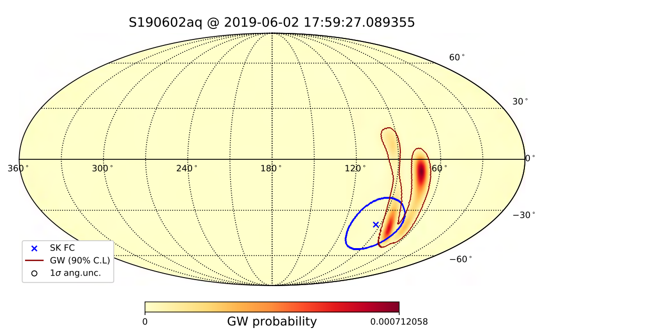

Fig. 4. Skymap showing the gravitational wave probability distribution from trigger S190602aq overlaid with the FC event found within 1000s of its trigger time. The cross denotes the arrival direction of the neutrino and the circle indicates the expected directional resolution.

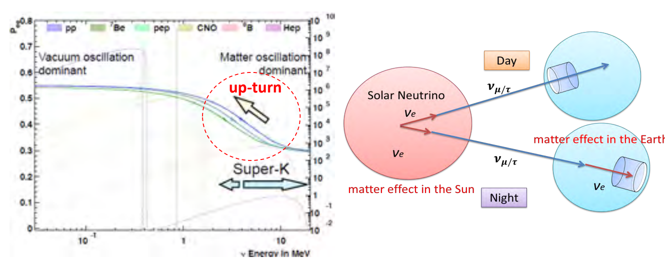

Fig. 5. Left: Several predictions of the survival probability of electron neutrinos emitted from the Sun as well as the fluxes of each solar neutrino; Right: The visual explanation of the day/night flux asymmetry.

SK-IV phase, as shown in Fig. 6. The correction for the energy scale non-uniformity was significantly improved in this analysis as follows. First,the correction for the PMT angular response was improved with more realistic simulation of the PMT response and arrangement. Then, a correction for position-dependent water transparency was newly developed and introduced in this analysis. Figure 7 shows relative difference of reconstructed energy scale for simulated mono-energetic electrons. The standard deviation of the energy scale variation across the detector volume was reduced from $\sim$1.7% to $\sim$0.5% for simulated data.

Finally, the method of removing backgrounds from cosmic muon induced spallation products was improved. The new method utilizes neutrons in the hadronic shower induced by cosmic muons. Spallation isotopes are often produced in a shower and they were efficiently removed by tagging associated neutrons. The signal of a neutron in pure water is a single 2.2 MeV γ and is difficult to trigger. Therefore, a special Wideband Intelligent Trigger (WIT) [14, 15], which operated for 388 days during the SK-IV phase, was used to detect those neutrons when it was available. The spalla-

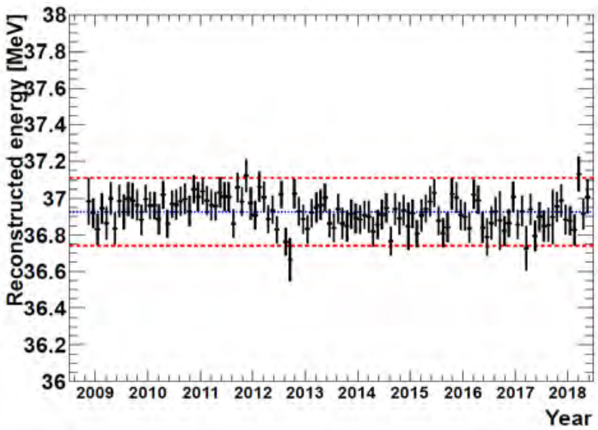

Fig. 6. Time variation of averaged reconstructed energy for decay–electrons from stopped cosmic muons. Black points show the data with statistical uncertainties. The horizontal blue line shows the average for the entire SK-IV period and the red lines show the $\pm 0.5\%$ range.

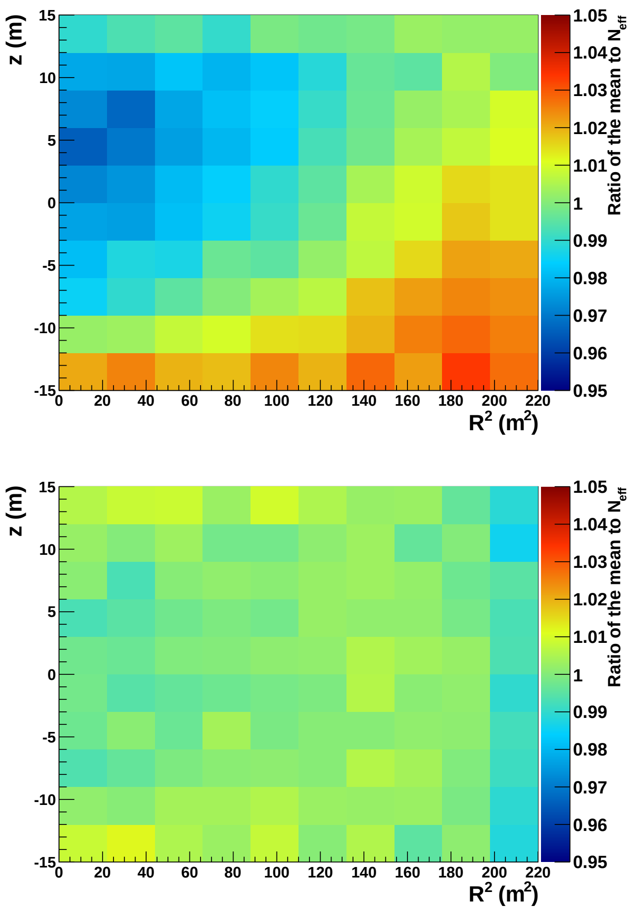

Fig. 7. Relative difference of reconstructed energy scale for simulated mono-energetic electrons at each $R^2 = X^2 + Y^2$ and Z position. The top (bottom) panel shows results for the reconstruction method used for the previous (this) analysis.

tion backgrounds were also reduced by vetoing consecutive spallation-like events and also by an improved muon reconstruction method. As a result, signal efficiency was improved by $\sim$12% while keeping spallation rejection efficiency at a similar level of $\sim$90%. Figure 8 shows the distribution of cosine of angle between the reconstructed direction of observed recoiled electrons and the direction of the Sun ($\cos\theta_{\rm Sun}$) for additional events gained by this new spallation cut.

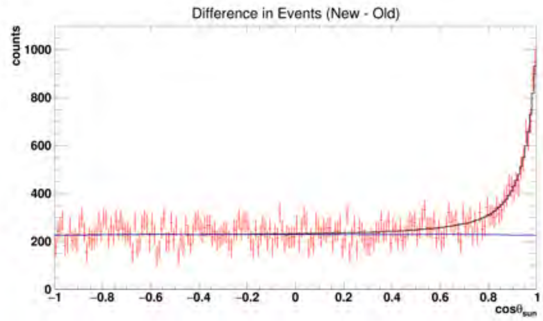

Fig. 8. Difference of number of accepted events between the spallation event rejection used for the old and new analyses, as a function of the cosine of the solar angle $\cos\theta_{\rm Sun}$. The red points shows the observed data, and black (blue) histogram shows the best-fit (background) shape.

^{8}B solar neutrino flux measurement

The SK detector observes solar neutrinos via elastic scatterings with electrons in pure water. The direction of a recoiled electron is highly correlated with the direction of the incident neutrino. Figure 9 shows the distribution of $\cos\theta_{\rm Sun}$ for solar neutrino candidates observed during the SK-IV phase. With the 2970 days of data in SK-IV, more than 60,000 events are observed over the background. Adding the solar neutrino events observed in other phases, the total number of the solar neutrino events is more than 100,000. Based on this data, the ^{8}B solar neutrino flux is determined to be $(2.35 \pm 0.04) \times 10^6$ /cm^2/sec assuming a pure electron neutrino flavor content. The ratio between the SK result and the SNO NC current flux (5.25×10^6 /cm^2/sec) [16] is found to be 0.447 ± 0.008.

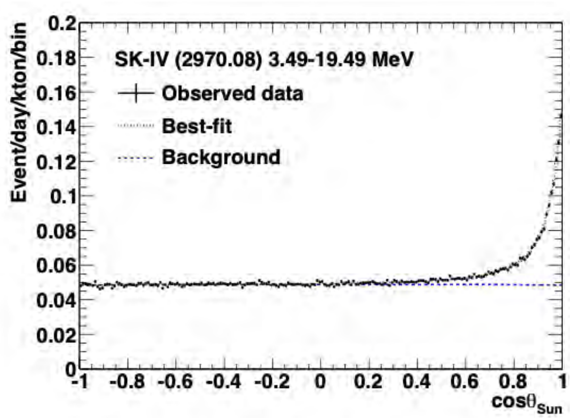

Fig. 9. The solar angle distribution in SK-IV. The horizontal axis shows the cosine of the solar angle $\cos\theta_{\rm Sun}$ and the vertical axis shows the number of the observed events. The black points shows the observed data, and the red (blue) histogram shows the best-fit (background) shape.

The solar activity cycle is the 11 years periodic change of sunspots releasing the magnetic flux at the surface of the Sun. The number of the sunspots strongly correlated with the solar activity cycle. The solar neutrino data set which is used for this analysis spans more than 21 years and covers about two solar activity cycles. Figure 10 shows the SK yearly flux measured throughout the different phases of SK together with the corresponding sunspot number (Source: WDC–SILSO, Royal Observatory of Belgium, Brussels [17]). The χ^2 between observed data and no time dependence hypothesis is calculated with the total experimental uncertainties as $\chi^2 = 23.25/22$ d.o.f., which corresponds to a probability of 38.8%. The SK solar rate measurements are fully consistent with a constant solar neutrino flux emitted by the Sun.

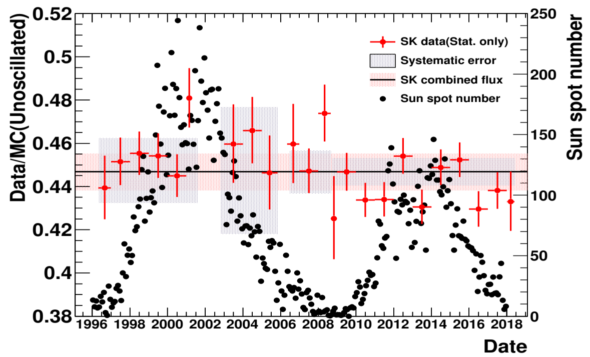

Fig. 10. The ratio of ^{8}B solar neutrino flux in SK over the SNO's NC current flux from 1996 to 2018. The red points show the yearly flux measured by SK (statistical uncertainty only), the gray bands show the systematic uncertainties for each SK phase, the black-horizontal line shows the combined measured flux with the uncertainty drawn as the red horizontal band. The back points show the sunspot number provided by [17].

Energy spectrum analysis

Analysis of solar neutrino energy spectrum was done using all the data from SK-I to SK-IV [2, 18, 19, 13]. The data quality for SK-IV was significantly improved thanks to the new front-end electronics for SK-IV [20], the improved water circulation system and the upgraded calibration methods [21]. Owing to these upgrades, SK has achieved the lowest background (induced by radioisotopes in pure water, especially ^{214}Bi) among all the SK phases [22]. The energy threshold in SK-IV have been lowered to 3.5 MeV in recoil electron kinetic energy (SK-I: 4.5 MeV, SK-III: 4.0 MeV) and this enabled SK to measure the solar neutrino energy spectrum with higher sensitivity. In addition, in May 2015, the trigger threshold was changed from 34 observed PMT signals within 200 nsec to 31 hits [23, 24]. Because of this lower threshold, the detection efficiency between 3.5 MeV and 4.0 MeV was improved from $\sim$86% to $\sim$100%. This improvement led to further reduction of the statistical uncertainty below 5 MeV in SK-IV.

In addition to these improvements of the data quality, the above-mentioned analysis method improvements were applied to the data corrected during SK-IV.

Figure 11 shows the energy spectra obtained from SK-I, II, III and IV, overlaid with the best-fits with generic polynomial and exponential functions, and the predictions assuming the current oscillation parameters described in the next section. Figure 12 shows the combined energy spectrum from SK-I to SK-IV with the predictions. Note that all SK the phases are combined without regard to energy resolution or systematic uncertainties in Figure 12, but those uncertainties are taken into account in the χ^2 calculation between the data and the prediction. Comparing χ^2 between the data (black) and the predictions (green or blue), the energy spectrum of SK is consistent within $\sim 1\sigma$ with the MSW up-turn with both the SK+SNO best fit parameters (green in Fig. 14) and the KamLAND best-fit parameters (blue in Fig. 14). The data also slightly disfavors the flat oscillation probability by $\sim 1\sigma$ significance.

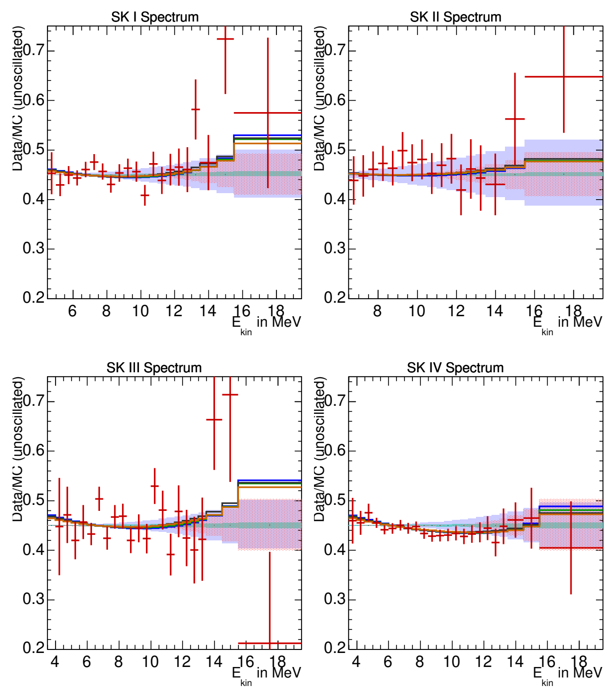

Fig. 11. SK-I, II, III and IV recoil electron spectra divided by the unoscillated expectation. The green (blue) line represents the best-fit to SK data using the oscillation parameters from the fit to SK and SNO (KamLAND) data. The orange (black) line is the best-fit to SK data of a general exponential or quadratic (cubic) P_{ee} survival probability. Error bars on the data points give the statistical plus systematic energy-uncorrelated uncertainties while the shaded purple, red, and green histograms give the energy-correlated systematic uncertainties arising from energy scale, energy resolution, and neutrino energy spectrum shift.

Day-night asymmetry

The day-night asymmetry of the solar neutrino flux for the full SK-IV data set was extracted with the same method described in Ref. [12]. Here, the day-night asymmetry is defined as,

$$A_{D/N} = \frac{\Phi_{\text{day}} - \Phi_{\text{night}}}{0.5(\Phi_{\text{day}} + \Phi_{\text{night}})},$$

where $\Phi_{\text{day(night)}}$ is the observed solar neutrino flux during day(night). Figure 13 shows the result of a day-night asymmetry amplitude fit as a function of Δm^2_{21} for the solar neutrino sample at $3.5 < E_{\text{kin}} < 19.5$(MeV). The fitted day-night

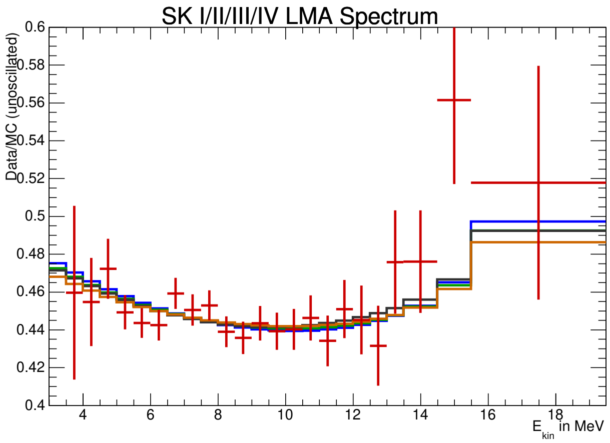

Fig. 12. The energy spectrum combining SK-I through SK-IV as a function of the recoil electron energy. The red points show the ratio of the data to the expected flux using a non-oscillated ^{8}B solar neutrino spectrum. The green (blue) curve shows the expected energy spectrum assuming the MSW effect inputting oscillation parameters of SK and SNO (KamLAND). The orange (black) line is the best-fit to SK data of a general exponential or quadratic (cubic) P_{ee} survival probability.

asymmetry, $A^{\mathrm{Fit}}_{D/N}$, assuming the SK+SNO best fit oscillation parameters (green in Fig. 14) was obtained as,

$$A^{\mathrm{Fit}}_{D/N} = (-2.1 \pm 1.1(stat))\% \quad (3.5 < E < 19.5(\mathrm{MeV})).$$

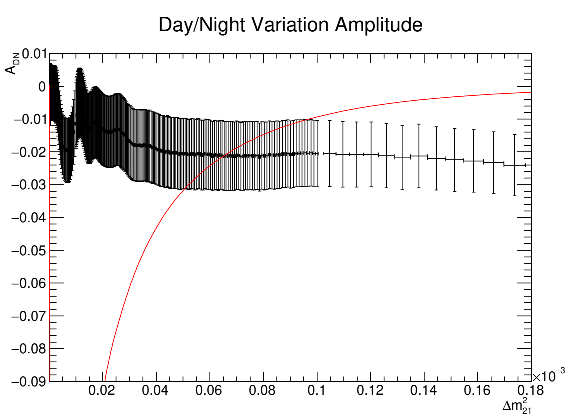

Fig. 13. Result of the day-night asymmetry amplitude fit as a function of the input Δm^2_{21} value. The black points show the data fit results with the statistical uncertainties, while the red curve show the expectation.

Oscillation parameter extraction

The oscillation parameters were extracted using the results from the solar neutrino measurements at SK and SNO [16], as well as the reactor antineutrino measurement by KamLAND [25, 26]. Figure 14 shows the allowed parameter region from the SK+SNO data as well as the KamLAND data. SK significantly contributes to the measurement of the solar angle θ_{12}. From the SK+SNO data, the mixing angle is determined to be $\sin^2\theta_{12} = 0.306 \pm 0.014$ and the mass difference is determined to be $\Delta m^2_{21} = 6.11^{+1.21}_{-0.68} \times 10^{-5}$ eV^{-2} as shown in Fig. 14. The SK+SNO fit results favors a lower Δm^2_{21} value compared to the KamLAND best fit value of $\Delta m^2_{21} = 7.54^{+0.19}_{-0.18} \times 10^{-5}$ eV^{-2}, although the tension is reduced compared to the previous results [27]. Currently, the SK+SNO data disfavors the KamLAND best fit value at $\sim$1.4σ, while it was $\sim$2σ in the previous analysis. Adding the KamLAND result, the oscillation parameters are determined to be $\sin^2\theta_{12} = 0.306^{+0.013}_{-0.012}$ and $\Delta m^2_{21} = 7.51^{+0.19}_{-0.18} \times 10^{-5}$ eV^2.

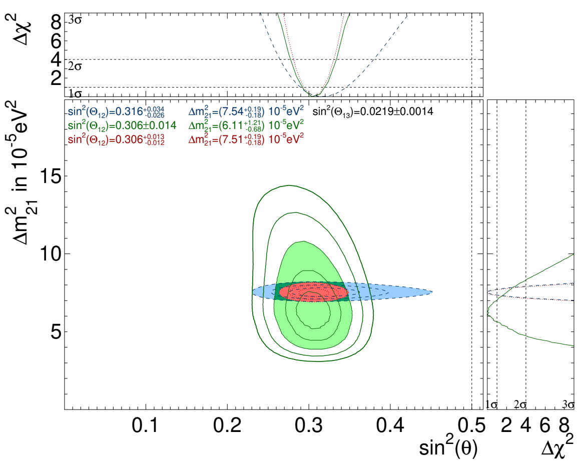

Fig. 14. The allowed contours for Δm^2_{21} vs. $\sin^2\theta_{12}$ from solar neutrino data at SK and SNO (green solid line). The allowed contour from KamLAND is also shown in blue. The combined allowed region is shown in red.

Summary and outlook

In summary, Super-Kamiokande has precisely measured the ^{8}B solar neutrino flux, its time variation and recoil electron spectrum. Using 5,805 days of data, more than 100,000 solar neutrino interactions were extracted over the background. No significant correlation between the observed solar neutrino flux and the sunspot number was found with more than 21 years of continuous observation of the solar neutrino flux. The measured energy spectrum of ^{8}B solar neutrino is consistent within $\sim$1σ with the MSW up-turn with both the solar best-fit parameters and the KamLAND best-fit parameters. The previously existed $\sim$2σ tension between the solar and KamLAND best fit Δm^2_{21} values was reduced to $\sim$1.4σ in this analysis. Combining the solar neutrino oscillation analyses by SK, SNO and KamLAND, the oscillation parameters are determined as $\Delta m^2_{21} = 7.51^{+0.19}_{-0.18} \times 10^{-5}$ eV^2 and $\sin^2\theta_{12} = 0.306^{+0.013}_{-0.012}$.

The Super-Kamiokande detector was recently upgraded by dissolving Gadolinium(Gd), and started a new phase of observation as SK-Gd. In order not to cause significant harm to the solar neutrino observation, ultra-pure $Gd_2(SO_4)_3$ powder with extremely low radio-impurity was newly developed and dissolved into the SK detector. Enhanced neutron detection capability with Gd can be used to further reduce the cosmic-ray spallation backgrounds. We aim to further improve our solar neutrino measurements with additional data and analysis improvements in the SK-Gd era.

Bibliography

[1] John N. Bahcall and Roger K. Ulrich, Rev. mod, Phys. **60**, 297 (1988).

[2] J. Hosaka *et al.*, Phys. Rev. D **73**, 112001 (2006).

[3] Q.R. Ahmad *et al.*, Phys. Rev. Lett. **87**, 071301 (2001).

[4] Y. Fukuda *et al.*, Nucl. Instrum. Meth. A **501**, 418 (2003).

[5] S.P. Mikheyev and A. Y. Smirnov, Sov. Jour. Nucl. Phys. **42**, 913 (1985).

[6] L. Wolfenstein, Phys. Rev. D **17**, 2369 (1978).

[7] P.C. de Holanda and Yu, Smirnov, Phys. Rev. D **69**, 113002 (2004).

[8] P.C. de Holanda and Yu, Smirnov, Phys. Rev. D **83**, 113011 (2011).

[9] V.Barger *et al.*, Phys. Rev. Lett. **95**, 211802 (2005).

[10] A. Friedland *et al.*, Phys. Rev. B **594**, 347 (2004).

[11] O.G. Miranda *et al.*, J. High Energy Phys. **10** 008 (2006)

[12] A. Renshaw *et al.*, Phys. Rev. Lett. **112**, 091805 (2014).

[13] K. Abe *et al.*, Phys. Rev. D **94**, 052010 (2016).

[14] G. Carminati, Phys. Procedia **61**, 666-672 (2015).

[15] M. Elnimr, J. Phys. Conf. Ser. **888**, no.1, 012189 (2017).

[16] B. Aharmin *et al.*, Phys. Rev. C **88**, 025501 (2013).

[17] WDC-SILSO, Royal Observatory of Belgium, Brussels. http://www.sidc.be/silso/datafiles

[18] J.P. Cravens *et al.*, Phys. Rev. D **78**, 032002 (2008).

[19] K. Abe *et al.*, Phys. Rev. D **83**, 052010 (2011).

[20] H. Nishino *et al.*, Nucl. Instrum. Meth. A **610**, 710 (2009).

[21] K. Abe *et al.*, Nucl. Instrum. Meth. A **737**, 253 (2014).

[22] Y. Nakano, J. Phys. Conf. Ser. **888**, 012191 (2017).

[23] S. Yamada *et al.*, IEEE Trans. Nucl. Sci. **57**, 428 (2010).

[24] Y. Nakano, PhD thesis, The Univ. of Tokyo (2016).

[25] S. Abe *et al.*, Phys. Rev. Lett **100**, 221803 (2008).

[26] A. Gando *et al.*, Phys. Rev. D **88**, 033001 (2013).

[27] M. Ikeda, Talk at XXVIII International Conference on Neutrino Physics and Astrophysics, 4-9 June 2018, Heidelberg, Germany, DOI: 10.5281/zenodo.1286858.

Search for nucleon decay

Proton decays and bound neutron decays (nucleon decays in general) are the most dramatic predictions of Grand Unified Theories (GUTs) in which three fundamental forces of elementary particles are unified into a single force. Super-Kamiokande (SK) is the world's largest detector to search for nucleon decays. Various nucleon decay modes have been looked for, but we have found no significant signal excess so far.

A proton decay into one charged lepton and one neutral pion ($p \to e^+\pi^0$, $p \to \mu^+\pi^0$) which baryon number is changed by 1, is one of the popular decay modes which most of GUT models predict and have relatively large detection efficiency. In the previous annual report, analysis of $p \to e^+\pi^0$ and $p \to \mu^+\pi^0$ with expanded fiducial volume, 27.5 kton, which is defined as 1 m inward from the inner detector wall, have been reported. We have not observed event excess in the signal region from expectation of atmospheric neutrino background from SK-I to SK-V data, 0.45 Megaton·year exposure in total, and we set lower limits of proton lifetime as $> 2.4 \times 10^{34}$ years and $> 1.6 \times 10^{34}$ years for $p \to e^+\pi^0$ and $p \to \mu^+\pi^0$, respectively. The results were published in 2020 [1].

As a baryon number violating process with $\Delta B = 2$, neutron-antineutron oscillation ($n - \bar{n}$) provides a unique test of baryon number conservation. Since the 1970's several models predicting $n - \bar{n}$ oscillations have been proposed, including those employing an $\mathrm{SU}(2)_L \times \mathrm{SU}(2)_R \times \mathrm{SU}(4)_c$ gauge group to generate a baryon asymmetry [2, 3] and others that propagate SM fields into extra space-time dimensions [4]. The predicted oscillation times vary from 10^9 s [4] to 5×10^{10} s [3] and correspond to energy scales of $10^2 \sim 10^3$ TeV, well above the scale that can currently be probed by accelerators. Experimental searches for $n - \bar{n}$ oscillation rely on observing particles (mostly pions) produced when a neutron oscillates into an antineutron and annihilates with a nearby nucleon. There have been a number of $n - \bar{n}$ searches using either free neutrons or bound neutrons, none of which have yielded a positive signal. Accordingly, constraints on the $n - \bar{n}$ oscillation time have been set at $\tau_{n-\bar{n}} > 0.86 \times 10^8$ s for free neutron oscillation [5] and at $\tau_{n-\bar{n}} > 2.7 \times 10^8$ s [6] for bound neutrons which was derived from only SK-I data. Here we are updating the results with data from SK-I to SK-V resulting 0.37 Megaton·years exposure with the conventional fiducial volume, with refined MC simulation for $n - \bar{n}$ oscillation, and with multivariate method to separate signal and background.

Following the oscillation of a neutron into an antineutron, the subsequent annihilation of the antineutron with a nucleon in the oxygen nucleus is expected to produce many visible particles, most of which are pions. The simulation of this signal is broken into stages: oscillation, hadronization, final state interactions of particles before exiting the nucleus, and finally propagation and subsequent reinteraction of those particles with detector media. During the first stage, the position of the oscillated neutron within the nucleus is determined using the standard Woods-Saxon distribution with a Fermi momentum simulation based on the spectral function, as the same as other nucleon decay simulations. Thereafter the oscillated antineutron is assumed to have an equal probability of annihi-

Table 3. Branching ratios (B_R), relative uncertainties, and corresponding efficiencies for $\bar{n}n$ annihilation products.

	B_R [%]	Relat. Uncer.	Efficiency [%]
$2\pi_0$	0.1	5%	3.2
$3\pi_0$	0.7	6%	3.6
$4\pi_0$	0.3	6%	4.4
$5\pi_0$	1.0	4%	3.8
$7\pi_0$	0.1	8%	2.1
$\pi^+\pi^-$	0.3	4%	4.8
$\pi^+\pi^-\pi_0$	1.6	15%	4.8
$\pi^+\pi^-2\pi_0$	13.1	15%	4.3
$\pi^+\pi^-3\pi_0$	11.2	15%	4.2
$\pi^+\pi^-4\pi_0$	3.3	14%	4.0
$\pi^+\pi^-5\pi_0$	1.4	15%	4.7
$2\pi^+2\pi^-$	6.0	16%	4.2
$2\pi^+2\pi^-\pi_0$	13.6	15%	4.5
$2\pi^+2\pi^-2\pi_0$	15.7	15%	4.5
$2\pi^+2\pi^-3\pi_0$	0.6	33%	4.9
$3\pi^+3\pi^-$	2.2	15%	3.7
$3\pi^+3\pi^-\pi_0$	2.0	15%	4.1
$\rho^0\pi^0$	1.8	15%	4.8
$\rho^{+/-}\pi^{-/+}$	3.7	15%	4.5
$\omega\omega$	3.5	15%	4.5
$\rho^0\omega$	2.4	15%	4.0
$\pi^0\pi^0\omega$	2.7	15%	3.8
$\pi^+\pi^-\omega$	7.1	15%	4.5
$\eta\omega$	1.6	15%	4.6
$\pi^+\pi^-\eta$	1.7	15%	3.8
Kaonic channels	2.3	15%	4.5

Table 4. Branching ratios (B_R), relative uncertainties, and corresponding efficiencies for $\bar{n}p$ annihilation products.

	B_R [%]	Relat. Uncer.	Efficiency [%]
$\pi^+\pi_0$	0.1	32%	3.4
$\pi^+2\pi_0$	0.7	32%	3.2
$\pi^+3\pi_0$	14.8	32%	3.5
$\pi^+4\pi_0$	1.4	32%	2.6
$2\pi^+\pi^-$	2.0	10%	3.6
$2\pi^+\pi^-\pi_0$	17.0	10%	3.5
$2\pi^+\pi^-2\pi_0$	10.8	10%	3.4
$2\pi^+\pi^-3\pi_0$	30.1	10%	3.8
$3\pi^+2\pi^-$	5.5	10%	3.2
$3\pi^+2\pi^-\pi_0$	3.2	10%	3.2
$\pi^+\pi^0\omega$	2.0	32%	3.4
$2\pi^+\pi^-\omega$	12.4	32%	3.6

lating with any remaining nucleons.

Modeling of the $\bar{n}n$ or $\bar{n}p$ annihilation products is done based on available accelerator data. Due to a lack of antineutron scattering data, the hadronization simulation uses results from antiproton scattering experiments instead. Assuming isospin symmetry, we used external data from the $\bar{p}p$ annihilation experiment [7, 8] to simulate the $\bar{n}n$ annihilation. For the $\bar{n}p$ channel, we used the $\bar{p}n$ annihilation branching ratio measurements [9] and bubble chamber data [10, 11, 12] and then flipped the signs of the charged pions to match $\bar{n}p$. Tables 3 and 4 show the branching ratios for $\bar{n}n$ and $\bar{n}p$ adopted in the simulation. The branching ratios of kaonic channels are artificially constructed due to lack of experimental data, and the kaonic production for $\bar{n}p$ is less than 1/2 from $\bar{n}n$, and thus is omitted.

Hadronization products are mostly pions. The pion interaction probability within the oxygen nucleus is expected to be large, and these so-called final state interactions (FSI) include quasi-elastic scattering, absorption, charge exchange, and pion production. FSI is simulated as the same as atmospheric neutrino and other nucleon decays.

Analysis is separated into two stage, precuts and multivariate analysis. Based on the distinct features of $n-\bar{n}$ and atmospheric neutrino events, several preliminary cuts are applied to reduce background rates while maintaining high signal efficiency. The $n-\bar{n}$ oscillation signal is expected to have multiple pions, while a large number of atmospheric neutrino interactions are elastic scatters with only one Cherenkov ring from the outgoing charged lepton. Therefore, the number of reconstructed rings is required to be >1. This cut removes $\sim$ 75% of the background while keeping 89% of the signal. Unlike the wide range of energies covered by atmospheric neutrinos, the $n-\bar{n}$ signal is more kinetically constrained, and thus a set of kinematic cuts are also applied. Here, the total reconstructed momentum is required to be within [35, 875] MeV/c, the visible energy in [30, 1830] MeV, and the total reconstructed invariant mass in [80, 1910] MeV/c^2. After the cut on the number of rings, these kinematic cuts further remove $\sim$ 50% of the background with a relative signal efficiency of 98%.

Due to the high ring multiplicity, the performance of ring reconstruction for $n \to \bar{n}$ signal events is not as satisfactory as typical sub-GeV neutrino events. To compensate for the limitation of ring reconstruction and to include more discriminant features, we applied a multivariate analysis (MVA) to events passing the pre-cuts. Compared to a conventional box-cut analysis [6], this analysis significantly enhance the separation between $n \to \bar{n}$ signal and background. An estimation using the same MC set shows that the sensitivity of the MVA method is twice that of the box-cut method.

Compared to atmospheric neutrino backgrounds, $\bar{n}n$ or $\bar{n}p$ annihilation within oxygen are generally expected to be more constrained kinematically and have more Cherenkov rings isotropically distributed in the detector. To exploit these features, we introduced 12 variables into the MVA, among which three are conventional kinematic quantities, including the visible energy, total momentum, and total invariant mass.

The remaining nine input variables are as follows. Since only a fraction of atmospheric neutrinos has sufficient energy to produce multiple charged particles, signal events are typically expected to have more visible Cherenkov rings. The number of such rings is used as a variable. However, the full reconstruction is limited to five rings. Therefore, an additional variable that counts ring fragments, or potential rings, is also introduced.

The total momentum of an $n-\bar{n}$ event is limited by the momenta of the interacting nucleons, while a background event can carry more momentum from the incident neutrino and is expected to be more forward-going at the energies needed to produce multiple particles. Therefore, this search employs four variables to quantify the isotropy of candidate events. The energy ring ratio is defined as $(E_{\rm tot}-E_{\rm max})/[E_{\rm tot}\cdot(n_{\rm ring}-1)]$, where $E_{\rm max}$ is the energy of the ring with highest energy in an event, $E_{\rm tot}$ is the total energy of the event, and $n_{\rm ring}$ is the number of rings. For the $n-\bar{n}$ signal, the annihilation energy is more uniformly distributed among the outgoing pions and therefore, the distribution of this variable is expected to have a sharper peak than than of backgrounds. Signal events are also expected to have higher sphericity than backgrounds, so this analysis adopts a sphericity variable. Fox-Wolfram moments, which are superpositions of spherical harmonics that measure correlations between particle momenta are also adopted to describe the correlation between rings. This analysis employs the first and second order Fox-Wolfram moments, since higher orders were found to provide little extra discrimination ability.

Finally, three variables related to particle identification are used: the number of e-like rings, the number of decay electrons, and the maximum distance to any decay electron from the primary vertex. Due to the large number of signal modes with one or more π^0s in the final state, signal events are expected to have more e-like rings from their decays into photons. Corresponding distributions for signal and background Monte Carlo (MC) after the pre-cuts are shown in Fig. 15.

These 12 variables are used in the construction of a multilayer perceptron (MLP), which is trained on $n-\bar{n}$ signal and atmospheric neutrino background MC. The MLP consists of a network of layers of nodes that are weighted and interconnected in order to optimize the discrimination between event types. Input variables form the input layer nodes and are combined in the MVA into a single node at the output layer, which is the estimator describing how signal- or background-like an event is. Between these layers there can be so-called hidden layers, whose structure and connectivity can be altered to optimize performance. In this analysis, a trial-and-error optimization for the hyper-parameters of the MLP structure was performed and the final structure was determined to be 1 hidden layer with 18 hidden nodes.

The signal efficiency and background efficiency as a function of the estimator value is shown in Fig. 16, where 0 corresponds to background-like and 1 is signal-like. A sensitivity analysis was performed assuming a 0.37 megaton·years exposure and realistic systematic errors (described below) using the Rolke method [13] to determine the optimal cut position in the output estimator. The optimized cut was found to be 0.789, where the signal (background) efficiency from the MVA alone is 5.0% (0.1%). Combined with the pre-selection efficiency, the total signal efficiency is 4.1% with an expected background of 0.56 events per year, or 9.3 events over the entire data period. Extimated systematic errors are 33 % and 28 % for efficiency and background, respectively.

This full SK-I-IV data set corresponds to an exposure of 0.37 megaton·years. After applying the cuts above, 11 events are found in data, which is consistent with the expected background of 9.3 ± 2.7 events. In the absence of a statistically significant excess in data, a lower limit is established. To account for both statistical and systematic uncertainties, we used Rolke method in confidence interval calculation. The observation limit on neutron lifetime is set at 3.6×10^{32} years (90% C.L.). The nuclear suppression factor, $R=0.517\times10^{23}$ s^{-1} [14] are used to derive the corresponding limit on the $n-\bar{n}$ oscillation time, $\tau_{n\to\bar{n}}>4.7\times10^{8}$ s.

Bibliography

[1] K. Abe *et al.* [Super-Kamiokande Collaboration], Phys. Rev. D **102**, 112022 (2020).

[2] K..S Babu, R.N Mohapatra, and S. Nasri, Phys. Rev. Lett, **97**, 131301 (2006).

[3] K..S Babu, P.S.B. Dev, E.C.F.S. Fortes, and R.N. Mohapatra, Phys. Rev. D **87**, 115019 (2013).

[4] S. Nussinov and R. Shrock, Phys. Rev. Lett, **88**, 171601 (2002).

[5] M. Baldo-Ceolin *et al.*, Z. Phys. C **63**, 409 (1994).

[6] K. Abe *et al.* [Super-Kamiokande Collaboration], Phys. Rev. D **91**, 072006 (2015).

[7] E. Klempt, C. Batty, and J.-M. Richard, Phys. Rep. **413**, 197 (2005).

[8] C. Amsler *et al.* [Crystal Barrel Collaboration], Nucl. Phys. A **720**, 357 (2003).

[9] T. Bressani and A. Filippi, Phys. Rep. **383**, 213 (2003).

[10] Nucleon-antinucleon annihilation at low energies, in *Physics at LEAR with Low-Energy Cooled Antiprotons*, edited by U. Gastaldi and R. Klapisch (Springer, New York, Boston, Massachusetts, 1984), pp. 193-200.

[11] P. Pavlopoulos *et al.*, AIP Conf. Proc. **41**, 340 (1978).

[12] G. Backenstoss *et al.*, Nucl. Phys. **B228**, 424 (1983).

[13] W.A. Rolke, A.M. Lopez, and J. Conrad, Nucl. Instrum. Methods Phys. Res. Sect. A **551**, 493 (2005).

[14] E. Friedman and A. Gal, Phys. Rev. D **78**, 016002 (2008).

EGADS: From R&D for the gadolinium project to standalone Supernova monitor

As mentioned above, although at SK a few SRN events a year are expected, SRNs have not been detected yet because of the large backgrounds that constrain our search. The observation of SRNs in general or neutrinos from distant supernovae in particular, would give us some information about the universe, for example the core collapse rate from SRNs, and about the neutrino itself too, for example its lifetime. The main signal from SRN is expected to be the inverse beta decay reaction ($\bar{\nu}_e+p\to e^{+}+n$), in which a positron and a neutron are produced, the delayed coincidence between the positron interaction and the neutron capture should allow to reduce the background affecting this analysis.

Before Gd loading in 2020, the SK detector had a poor neutron detection effficiency. It was then proposed to add

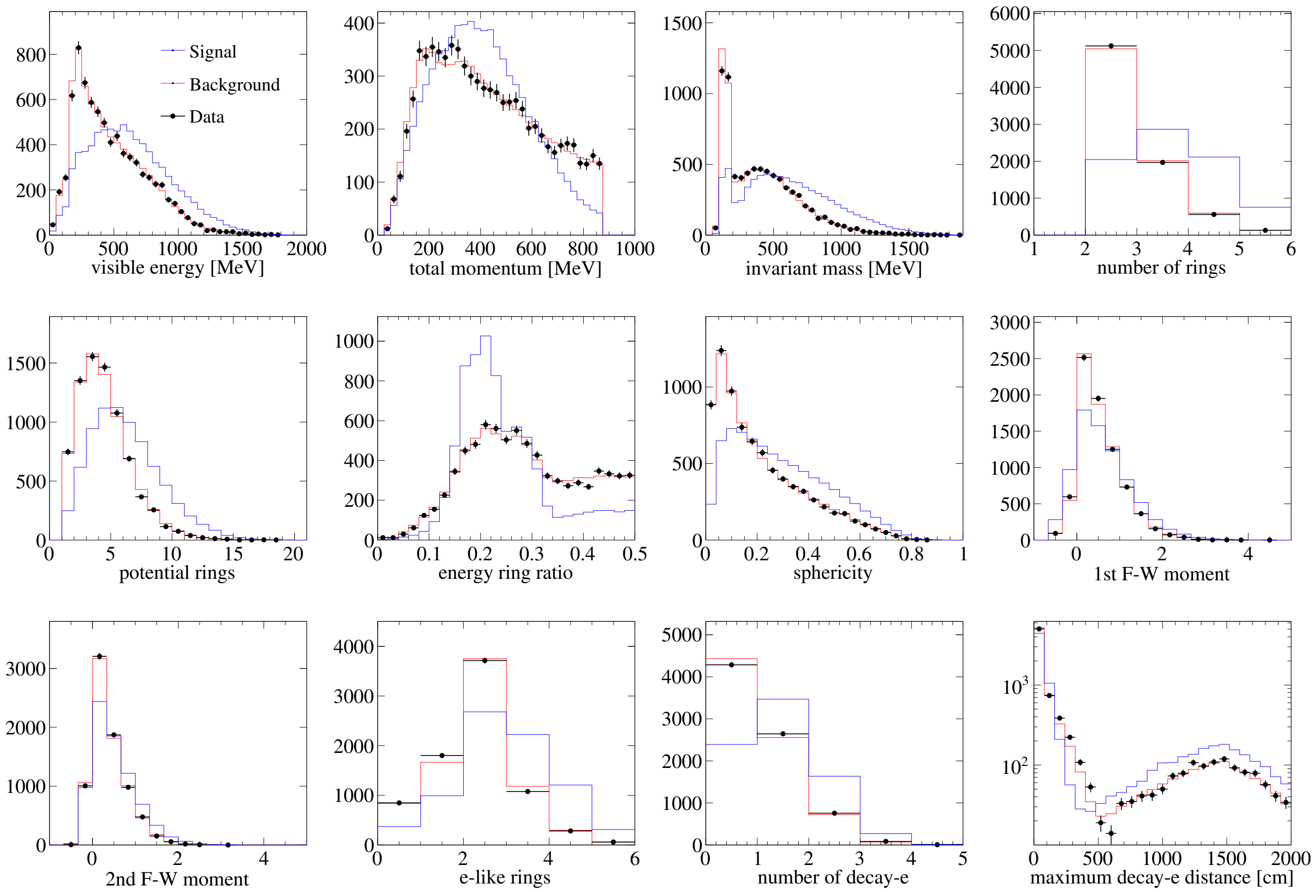

Fig. 15. The 12 input variables to the multivariate analysis for signal (blue), background (red), and data (black), after precuts. Signal and background simulations are normalized to data.

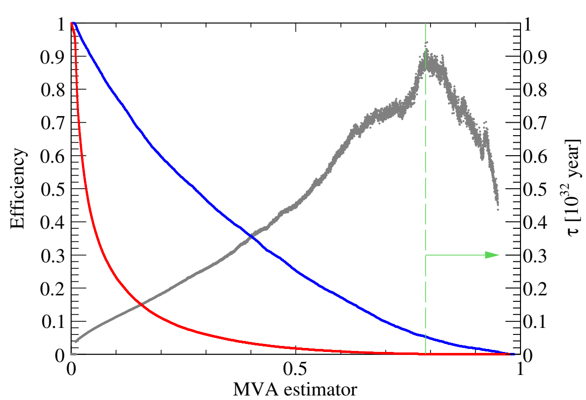

Fig. 16. Signal (blue) and background (red) efficiency as a function of the MVA output estimator threshold. The expected sensitivity at each value of the estimator threshold as estimated using the Rolke method is shown in the gray curve. The dashed line indicates the optimum cut point.

Fig. 17. In the new cavern, the 200-ton tank (a) with currently 240 photomultipliers installed, the Gd pre-mixing and pre-treatment 15-ton tank (b), the selective filtration system (d), Gd removal resins (c) for test and a device to measure the water transparency (e) have been installed.

0.2% of gadolinium (Gd) sulfate by mass into SK in order to achieve a high neutron detection efficiency. Since Gd has a neutron capture cross section of 49.000 barns (about 5 orders of magnitude larger than that of protons) and emits a gamma cascade of 8 MeV, neutrons could be easily detected at SK (in space, vertices within tens of cm and in time, with the neutron capture delayed about 30 μsec).

EGADS (Evaluating Gadolinium's Action on Detector Systems) project was funded in 2009. The main motivation of EGADS was to show that by adding Gd, SK will be able to detect anti-neutrinos using the delayed coincidence technique, while keeping all its capabilities in the other analyses like solar and atmospheric neutrinos. Since then, a new hall near the

SK detector has been excavated and a 200-ton tank with its ancillary equipment has been installed, see Fig.17, to mimic the conditions at SK. The selective water filtration system filters out water impurities while keeping the Gd in the water.

EGADS has been renamed as Employing Gadolinium to Autonomously Detect Supernovas after the installation of the new QBee electronics in 2017, following the Super-Kamiokande collaboration approvation of the SK Gd loading.

Water system operations

From January 2010 to July 2011 we circulated pure water through the 200-ton tank and proved that our water system is stable and achieves a high water quality. In 2013, from February 6th to April 20th, the 200-ton tank has been step wise loaded with Gd sulfate until the final 0.2% concentration was reached. Two values are monitored at three different depths: the Cherenkov light left after travelling 15 m (LL15) in water and the Gd concentration. Both values confirmed that we can achieve and maintain a good water quality and that Gd sulfate homogeneously and quickly dissolves in the 200-ton tank.

In summer 2013, we installed 240 photomultipliers and the data taking started from September without Gd and with a DAQ based on old SK ATM modules. In April 2015, the target concentration of 0.2% $Gd_2(SO_4)_3$ was achieved. Figure 18 shows the time variation of LL15. The blue band in the figure shows typical values for SK-III and SK-IV. As shown in the figure, the transparency of 0.2% $Gd_2(SO_4)_3$ water is within the SK range. In addition to the good water transparency, no Gd loss has been detected since the EGADS detector reached the final concentration until it was emptied again after about 2 years and 5 months, in October 2017.

Detailed studies have evaluated the impact on current analyses at SK. These studies show that current analyses will be basically unharmed after adding Gd in SK and all other tests and studies conducted have shown no showstoppers. As a consequence, the SK collaboration decided in spring 2015 to approve the SuperK-Gd project. The results of these analysis were published in [1].

In order to test the Gd-loading in SK, the detector was refilled with pure-water in November 2017, and loaded with 0.02% $Gd_2(SO_4)_3$ in the end of March 2018. This loading was performed using only the pre-treatment and the fast recirculation systems, with one pass, similar to what is expected for SK 0.02% loading.

Since then, different configurations of the water system have been tested in order to determine what is needed to ensure high water transparency in SK without band-pass system. Figure 19 shows the time variation of LL15 since this loading until May 2020. From March 2018 to June 2018 a slow but continuous decrease of the water transparency has been observed ith the fast recirculation system only. From June 2018 to August 2018 the use of the band-pass system allowed to recover high water transparency. There-after the fast-recirculation system only has been used.

In May 2019, the water system was stopped for about one week due to electrical damage following a power-cut. This led to a reduction of the water transparency. After restarting, the water transparency was recovered. On September 2019 the water flow was modified so that only half of the flow pass through the special cation exchange resin. The water transparency remained stable and high. Finally, in November 2020, in order to simulate the future additional Gd loading in Super-Kamiokande, EGADS was loaded from 0.01% to 0.03% Gd concentration.

Ion exchange resin tests

Impurities in water Cherenkov detector's water can be removed using anion and cation resins as a standard method.

In case of Gd-loaded water, standard cation exchange resins are expected to also remove Gd. Hence, a special cation exchange resin has been developed and installed in EGADS, in addition to the usual anion exchange resin. The installation was done in January-February 2019 (in January, the new cation exchange resin was used alone, leading a water transparency drop). As showed in Figure 19, we observed an improvement of the water transparency compared than with only anion exchange resin. This increase was enhanced following the replacement of the TOC and UV lamps in March 2019, which stresses the importance of the ionization lamps for the water transparency.

In 2020, we learned the AmberJet 4400 anion exchange resin will be discontinued soon by its manufacturer. In order to replace it we started to test several other resin substitute candidates. In May 2021, we started to test AmberJet 4002, which is expected to be similar to AmberJet 4400. Results will be reported in the next report.

DAQ operations

In June 2017, EGADS electronics have been upgraded from the ATM electronics to SK's QBee electronics, the DAQ system was also upgraded to use these new electronics. Thanks to this upgrade, the stability of the DAQ has been greatly improved, specially at high rate. Several SN tests were performed, and demonstrated that EGADS is able to detect and process a 10 second long burst of more than 100k Hz without trouble. This is much more than what is expected from a very close galactic SN burst: in case of Betelgeuse, about 25k events are expected according to Nakazato's model.

We developed an online fitter, HEIMDALL, based on SK WIT. It is able to reconstruct all the events online during a SN burst and then provides an alarm within few seconds. HEIMDALL is looking for IBD candidates, therefore taking advantage of the delayed coincidence to reduce the background. Thanks to this, EGADS is able to look for SN in the far end of our galaxy. This enable us to instantly and autonomously detect a galactic SN and report to local experts and neutrino and astronomy community.

Bibliography

[1] Marti, Ll. et al., NIM-A 959, 163549 (2020)

SK-Gd

SK-Gd is a project to improve Super-Kamiokande's neutron detection efficiency using Gadolinium (Gd). One of the main physic target is a discovery of the diffuse supernova neutrino background. In 2020 summer, 13 tons of

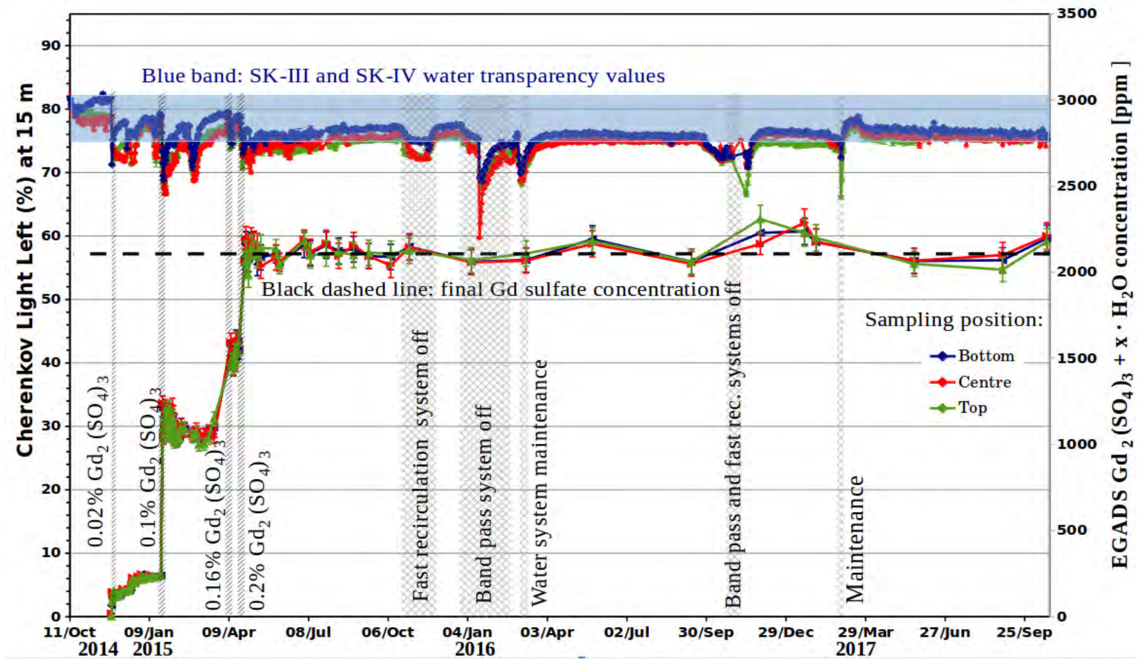

Fig. 18. Cherenkov light left at 15 m for Gd loaded water in EGADS until September 2017. The horizontal blue band are the typical values for SK-III and SK-IV. The vertical lines shows the injection dates where we also indicate the concentration (% in mass) in the 200-ton tank. The black dashed line shows the final expected concentration.

Fig. 19. Cherenkov light left at 15 m for Gd loaded water in EGADS since December 2017. The horizontal blue band are the typical values for SK-III and SK-IV. The vertical lines shows the injection dates where we also indicate the concentration (% in mass) in the 200-ton tank. The black dashed line shows the final expected concentration.

$Gd_2(SO_4)_3 \cdot 8H_2O$ (gadolinium sulfate octahydrate) was dissolved into the detector, since then the SK-Gd phase of operations has been started.

The first loading and SK-Gd Water System

The first loading of 13 tons of $Gd_2(SO_4)_3 \cdot 8H_2O$, roughly 10% of the final target concentration, was done from July 14 to August 17, 2020. During the loading, water was continuously recirculated at a rate of 60 m^3/h. In order to replace the pure water to Gd loaded water, the water was extracted from the top of the detector and mixed with $Gd_2(SO_4)_3 \cdot 8H_2O$ to create a 0.02% solution of the Gd compound before injecting it into the bottom of the detector as shown in Figure 20.

The SK-Gd water system was newly designed and constructed for this project. It has three components: 1) Gd dissolving system to dissolve $Gd_2(SO_4)_3 \cdot 8H_2O$ into the detector water, 2) the pretreatment system to remove impurities from Gd loaded water before it mixed to the main recirculation line, and 3) the water recirculation system to circulate and continuously purify the resulting 50 kilotons of Gd-loaded water. The new system is rather simpler than the old pure water

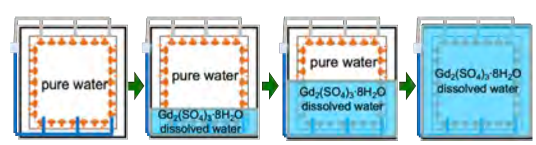

Fig. 20. Gadolinium loading scheme.

system. It mainly consists of UV system to remove bacteria, ion exchange resin to remove dissolved ions, while simultaneously preserving the dissolved gadolinium (Gd^{3+}) and sulfate (SO_4^{2-}) ions in solution, and ultra filtration modules to remove particulates. Water from the detector was continuously circulated and purified before, during, and after the Gd loading.

Figure 21 shows the cumulative mass of $Gd_2(SO_4)_3 \cdot 8H_2O$ during the first loading. As shown in the figure, the loading was very stable up to the target value of 13.2 tons, which corresponded to 5426 kg of Gd in the 50 kilotons of SK water (0.011% Gd concentration).

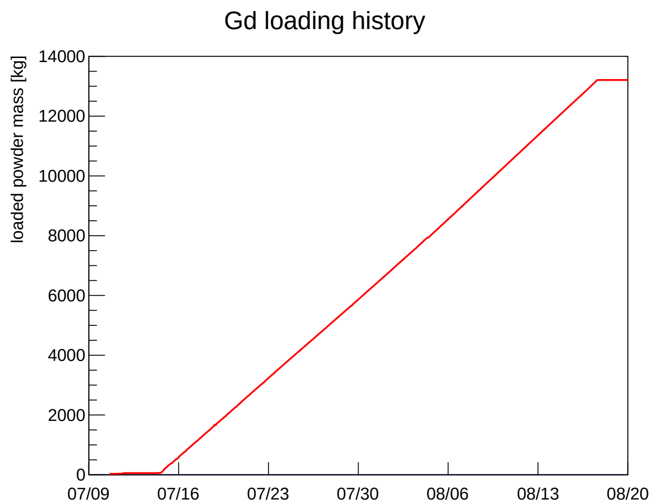

Fig. 21. The weight of $Gd_2(SO_4)_3 \cdot 8H_2O$ powder loaded into SK during 2020 as a function of time. the weight reached the target of 13.2 tons on August 17.

Detector status

Water Transparency

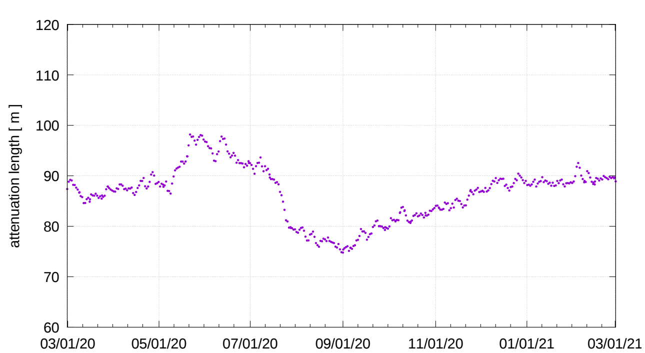

Fig. 22. The light attenuation length as a function of time (from March 1, 2020, to March 1, 2021. From April 29, 2020). It should be noted that before the first loading, the setting temperature of the supply water to the bottom of the tank was lowered in order to simulate the Gd-loading water flow.

Figure 22 shows the time variation of measured Cherenkov light attenuation length in the SK tank. The attenuation length was measured by analysing cosmic ray through-going muon events. It is about 90 meters just before loading Gd in the SK tank on July 14, 2020. After starting the first loading, the attenuation length began to decrease until the end of August 2020, and it reached a minimum value of around 75 m. Then, it had returned to almost 90 m at the beginning of December, 2020. The attenuation length became as long as it had been during the pure water phases of SK with water recirculation at the rate of 120 m^3/h.

$Gd_2(SO_4)_3 \cdot 8H_2O$ Concentration in the SK Detector

During the loading period, daily water sampling was done from calibration ports to monitor the loading status and Gd concentration at the various positions in the detector. Figure 23 shows the time evolution of conductivity near center position as a function of Z. Gd loading started on July 14, but no significant change in the conductivity was observed until July 19 until the Gd water boundary reached to the inner detector. As seen in the figure, a sharp boundary about 2 m thick existed between the Gd loaded layer (>100 μS/cm) and the pure water layer (<1 μS/cm). The boundary moved up about 1.5 m/day in agreement with the rate of water flow in the detector. By checking the clear boundary between the Gd-loaded and pure water can be seen through the loading, it was possible to monitor the loading status and the spatial uniformity of the Gd concentration over the 35 days it took to reach the top of the detector.

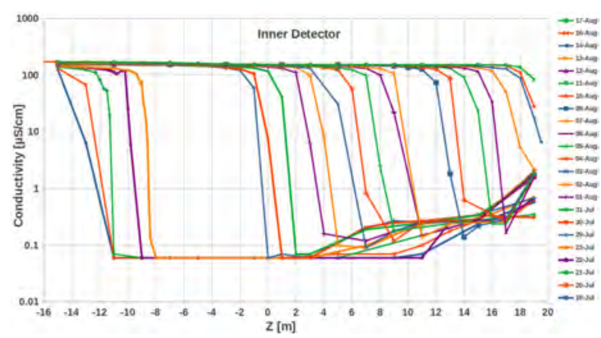

Fig. 23. Conductivity vs. Z position in the inner detector during the loading (there was a problem in the sampling system between July 21 and 29 which correspond to the gap in the figure).

The Gd concentration measurements with an Atomic Absorption Spectrometer (AAS) were also conducted on samples taken from the detector. Figure 24 shows the latest available AAS measurements (from samples taken on March 25, 2021) in in the inner detector region. It can be seen that the concentration had became completely homogeneous and the average of $Gd_2(SO_4)_3 \cdot 8H_2O$ concentration is found to be value of 271 ± 4 ppm. Taking into account the eight water molecules associated with the $Gd_2(SO_4)_3 \cdot 8H_2O$, this AAS result corresponds to Gd concentration in the SK water of 114 ± 2 ppm.

The gadolinium concentration can be measured using a radioactive neutron source because the Gd concentration in water correlates with the neutron capture time constant: a higher concentration makes a shorter capture time. Using an Am-Be neutron calibration source, the neutron capture time constant was confirmed to be stable in time within statistical errors, as shown by data taken between September and November 2020 (Fig. 25). It is also stable at several depths within SK. An av-

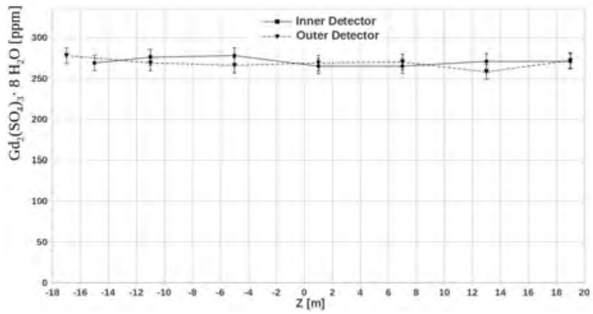

Fig. 24. Latest AAS-measured $Gd_2(SO_4)_3 \cdot 8H_2O$ concentration vs. Z position in the inner detector and the outer detector from samples taken on March 25, 2021, showing the complete homogeneous Gd concentration throughout the detector.

erage neutron capture life time during the period is obtained as 115.6 $\pm$0.6 μs, which corresponds to a Gd concentration of 109.1 ± 1.2 (stat. only) ppm, as expected for this level of doping.

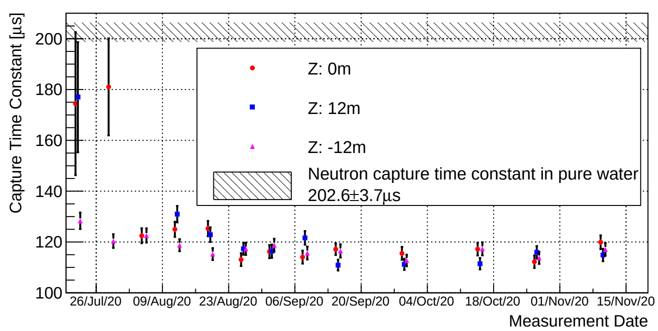

Fig. 25. The measured neutron capture time constant in SK after the loading obtained from the analysis of Am/Be source calibration data. The shaded band corresponds the neutron capture time constant in pure water.

Conclusion of SK-Gd project

In the summer of 2020, 13.2 tons of $Gd_2(SO_4)_3 \cdot 8H_2O$ was dissolved into Super-Kamiokande. Since then, the new phase of SK has been started to study many physics targets such as the supernova relic neutrinos. During this Gd loading, by controlling the Gd concentration and the water temperature, laminar flow of water in the tank was successfully achieved and the pure-water was replaced to the Gd loaded water efficiently from the bottom of the tank. The Gd concentration throughout the tank became homogeneous shortly after the loading. The transparency of the Gd-loaded water was dropped by 20% but improved after starting water recirculation with 120 t/h using the new SK water system. After a three month of commissioning phase, the transparency became as good as that in the experiment's previous pure water phases. The Gd concentration in the SK water was measured to be 114 ± 2 ppm by AAS and 109.1 ± 1.2 (stat. only) ppm. They are both consistent with the expectation for this level of doping.

T2K EXPERIMENT

[Spokesperson : Atsuko Ichikawa] Tohoku University

The Tokai to Kamioka (T2K) experiment [1] is a long baseline neutrino oscillation experiment: a man-made beam of neutrinos is used to do precise studies of the oscillations of neutrinos. Accelerated protons are used to produce the neutrinos in the J-PARC center in the Ibaraki prefecture, which then travel 295 km to reach the Super-Kamiokande (Super-K) detector in the Gifu prefecture where they can be detected after oscillations. A complex of near detectors located 280 meters away from the proton target is used to monitor the neutrino beam, and constrain systematic uncertainties on the neutrino fluxes and interactions. T2K was the first long baseline experiment to use the off-axis beam technique [2]: the beam is not aimed directly at Super-K, but in a direction making a 2.5° angle with the far detector direction. This gives increased sensitivity to neutrino oscillations while reducing the backgrounds by producing a narrow band neutrino beam centered on the energy corresponding to the first maximum of the $\nu_\mu \rightarrow \nu_e$ oscillation probability.

T2K realized the first observation of the appearance of a flavor of neutrinos through oscillation by detecting electron neutrinos in a beam of neutrinos produced in the muon flavor [3]. After achieving this milestone, the experiment has been using its ability to produce a beam of either neutrinos or anti-neutrinos to compare the oscillations of neutrinos and their antiparticles. This allows to study the main remaining open questions in neutrino oscillations (CP symmetry and ordering of the neutrino mass states) by looking at the differences between the oscillations $\nu_\mu \rightarrow \nu_e$ and $\bar{\nu}_\mu \rightarrow \bar{\nu}_e$. At the same time, T2K's physics goals include the precise measurement of the neutrino oscillation parameters θ_{23} and Δm^2_{32} through a precise study of the pattern of disappearance of the muon neutrinos in conjunction with the data used to study the oscillation to the electron flavor. The experiment additionally performs searches for physics beyond the standard model, such as oscillations due to sterile neutrinos and CPT violation. Finally, the near detectors are used to perform a wide range of neutrino and anti-neutrino cross-section measurements.

In J-PARC, protons are accelerated to 30 GeV by a series of three accelerators, and hit a 1.9 interaction-length graphite target. The collisions produce hadrons, in particular charged pions and kaons, which are focused by three electromagnetic horns. The hadrons then go through a 96m long decay tunnel where they decay in flight into neutrinos. A beam dump at the end of the decay tunnel stops the remaining hadrons, while high energy muons (5 GeV/c or higher) can pass through this beam dump and are measured to provide a first, indirect monitoring of the neutrino beam. The horns can be used either with a positive current (ν-mode), in which case the beam is mainly made of ν_μ, or with a negative current ($\bar{\nu}$-mode) which gives a mainly $\bar{\nu}_\mu$ beam.

The near detectors are separated into two groups. On the axis of the beam, the INGRID detector, made of fourteen identical modules is used to monitor the beam direction and rate stabilities. Each module is made of an succession of iron plates to provide large target mass (7.1 tons per module) alternating with scintillator planes for detection. Using the number of events reconstructed in each module, the beam direction can be measured daily with better than 0.4 mrad accuracy. Located in the direction of Super-K, the off-axis detector ND280 is made of several detectors located inside a 0.2T magnet. The higher precision of those off-axis detectors allow to do more detailed measurements of the unoscillated neutrino beam. In neutrino oscillation analyses, the ND280 is used to provide information on the ν_μ and $\bar{\nu}_\mu$ unoscillated spectra directed at SK, constrain the dominant backgrounds, and constrain the combination of flux and interaction cross sections.

The far detector, Super-K, is a 50 kton water Cherenkov detector, shielded from atmospheric muons by 1000 m of rock, or 2700 meters-water-equivalent (m.w.e.) mean overburden. To select events corresponding to the T2K beam, Super-K is synchronized via GPS to the J-PARC beamline. Hit information within $\pm 500\mu s$ from the beam arrival timing are used for T2K data analysis. Events where only one ring was reconstructed (corresponding to one charged particle above Cherenkov threshold) are used in oscillation analysis. Those events are separated into muon-like and electron-like events based on the light pattern of this ring, and additional selection cuts are applied to produce samples enriched in certain interaction modes.

To study neutrino oscillations, the data observed at the far detector are compared to the predictions of the three-flavor oscillation model for different values of the oscillation parameters. To this end, a model of the experiment is constructed: the fluxes of the different flavors of neutrinos reaching the detectors are predicted by a series of simulations, and the interactions of ν and $\bar{\nu}$ in the detectors are simulated using the NEUT Monte Carlo event generator [8]. First, the flux and properties of the proton beam reaching the target are measured by the proton beam line monitors. Interactions of the protons in the graphite target and production of secondary hadrons are then simulated using the FLUKA package [4]. Measurements from hadron production experiments, in particular NA61/SHINE [5], are used to tune this part of the simulation and the out-of-target interactions. The propagation and decay in flight of the hadrons in the decay tunnel are then simulated using the GEANT3 and GCALOR [6] packages. The predictions from this model are compared to the data observed in the near detectors to tune the predictions for the far detector by constraining the model parameters. The result of this near detector fit provides the initial values and uncertainties of the flux and interaction model parameters used in the far detector analysis to measure parameters describing neutrino oscillations.

T2K started collecting physics data in January 2010, and has now completed its 11th run. This year data were taken for the first time with gadolinium dissolved in Super-K water following the upgrade of the detector for the SK-Gd project. The data from this run 11 have not yet been used for physics analyses, but their quality was checked and confirmed the proper functioning of the experiment with this new setting. The data used for the analyses presented here correspond to the period before gadolinium loading, and represent a total of 1.99×10^{21} protons on target (POT) in ν-mode and 1.65×10^{21} POT in $\bar{\nu}$-mode. The details of the data used in the far detector analysis (slightly lower due to data quality cuts) can be found in table 5. Over this period, the event rates and the beam direction were found to be consistent with the expectations and stable by the measurements of the muon monitor and the on-axis near detector. In particular, the beam direction remained stable well within the ± 1mrad target. During run 10, stable operation at 515 kW was achieved.

Table 5. T2K data taking periods and integrated numbers of protons on target (POT) used in the far detector analysis. The numbers for run 11 are still under preparation and have not been included.

Run Period	Dates	$\times 10^{20}$ POT ν	$\times 10^{20}$ POT $\bar{\nu}$
Run 1	Jan.2010 - Jun.2010	0.32	–
Run 2	Nov.2010 - Mar.2011	1.11	–
Run 3	Mar.2012 - Jun.2012	1.60	–
Run 4	Oct.2012 - May.2013	3.60	–
Run 5	May.2014 - Jun.2014	0.24	0.51
Run 6	Oct.2014 - Jun.2015	0.19	3.55
Run 7	Feb.2016 - May.2016	0.48	3.50
Run 8	Oct.2016 - Apr.2017	7.17	–
Run 9	Oct.2017 - May.2018	0.20	8.79
Run 10	Oct.2019 - Feb.2020	4.73	–
Total	**Jan.2010 - Feb.2020**	**19.66**	**16.35**

A selection of results obtained during FY2020 is presented below.

T2K measurements of muon neutrino and antineutrino disappearance using 3.13×10^{21} *protons on target*

T2K reported in [7] an updated measurement of the parameters θ_{23} and Δm^2_{32}, which govern the disappearance of muon neutrinos and antineutrinos in the three-flavor PMNS neutrino oscillation model at T2K's neutrino energy and propagation distance. Utilizing the ability of the experiment to run with either a mainly neutrino or a mainly antineutrino beam, muon-like events from each beam mode are used to measure these parameters separately for neutrino and antineutrino oscillations. This allows to test the standard three flavor oscillation model, which assumes CPT conservation, and in which ν_μ and $\bar{\nu}_\mu$ have identical survival probabilities for vacuum oscillations. At T2K's beam energy and baseline, the effect of the neutrinos propagating through matter on the muon neutrino survival probability is very small. Therefore, if the oscillation probabilities for neutrinos and antineutrinos differ by significantly more than expected, this could be interpreted as possible CPT violation and/or nonstandard interactions

Two analyses are presented here: the first one is a three-flavor analysis, in which the oscillation probabilities for ν_μ and $\bar{\nu}_\mu$ are calculated using the standard PMNS formalism, but with independent parameters to describe ν_μ and $\bar{\nu}_\mu$ oscillations, i.e., $\bar{\theta}_{23} \neq \theta_{23}$ and $\overline{\Delta m^2_{32}} \neq \Delta m^2_{32}$, where the barred parameters affect the antineutrino probabilities. As the dataset used does not constrain the other PMNS parameters, they are assumed to be the same for ν_μ and $\bar{\nu}_\mu$.

While it allows the ν_μ and $\bar{\nu}_\mu$ parameters to take different values, this three-flavor analysis does not allow oscillation probability values not allowed by the PMNS formalism. To test consistency with the PMNS formalism, an analysis in which the oscillation probability is allowed to exceed the maximum possible PMNS value is also presented. In this analysis, the probability for muon neutrino disappearance is approximated using a "two-flavor"-only oscillation formula with an effective mixing angle and mass splitting that takes into account the information known about "three-flavor" mixing. In practice, a modified version of the canonical two-flavor oscillation formula is used [9]:

$$P_{\nu_\mu \to \nu_\mu}(P_{\bar{\nu}_\mu \to \bar{\nu}_\mu}) \approx 1 - \alpha(\bar{\alpha}) \sin^2\left(\frac{1.27\Delta m^2 [eV^2] L[km]}{E[GeV]}\right)$$

where α plays the role of the well-known effective two- flavor mixing angle, $\sin^2(2\theta)$, but is allowed to take values larger than 1.

In the three-flavor analysis, the best-fit values obtained for the parameters describing neutrino oscillations are $\sin^2(\theta_{23}) = 0.51^{+0.06}_{-0.07}$ and $\Delta m^2_{32} = 2.47^{+0.08}_{-0.09}$ eV$^2/c^4$, and those describing antineutrino oscillations are $\sin^2(\bar{\theta}_{23}) = 0.43^{+0.21}_{-0.05}$ and $\overline{\Delta m^2_{32}} = 2.50^{+0.18}_{-0.13}$ eV$^2/c^4$, assuming normal neutrino mass ordering. Figure 26 shows the confidence intervals on the oscillation parameters applying to ν_μ overlaid on those for the parameters applying to $\bar{\nu}_\mu$. As the parameters for ν_μ and $\bar{\nu}_\mu$ show no significant incompatibility, this analysis provides no indication of new physics.

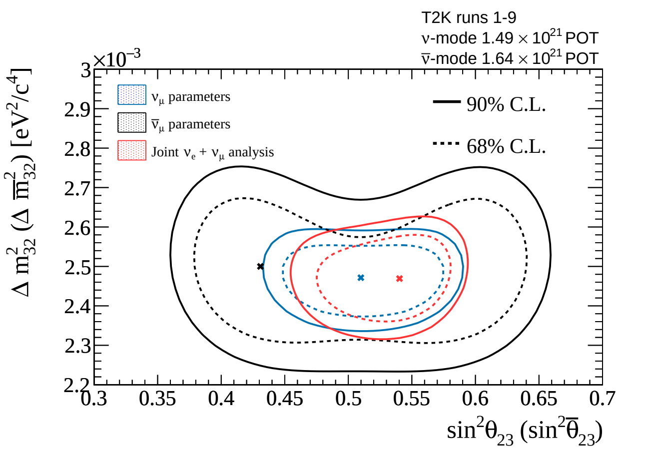

Fig. 26. 68% and 90% confidence intervals on $\sin^2(\theta_{23})$ and Δm^2_{32} (blue) and $\sin^2(\bar{\theta}_{23})$ and $\overline{\Delta m^2_{32}}$ (black) from the three-flavor analysis described here. Also shown are equivalent intervals on $\sin^2\theta_{23}$ and Δm^2_{32} (red) from a joint fit to muon-like and electron-like T2K data described in [10].

The best-fit values obtained on the effective two-flavor oscillation parameters are $\Delta m^2 = 2.49^{+0.08}_{-0.08}$ eV$^2/c^4$, $\alpha = 1.008^{+0.017}_{-0.016}$, $\overline{\Delta m^2} = 2.51^{+0.15}_{-0.14}eV^2/c^4$, $\bar{\alpha} = 0.976^{+0.029}_{-0.029}$. Fig. 27 shows the 68% and 90% confidence intervals for (Δm^2, α) and ($\overline{\Delta m^2}$, $\bar{\alpha}$). Both the 1σ confidence intervals include values of $\alpha(\bar{\alpha}) \leq 1.0$, indicating no significant disagreement between data and standard physical PMNS neutrino oscillations. We also see good compatibility between the parameters affecting neutrinos and antineutrinos.

In conclusion, it was found in both analyses that the neutrino and antineutrino oscillation parameters are compatible

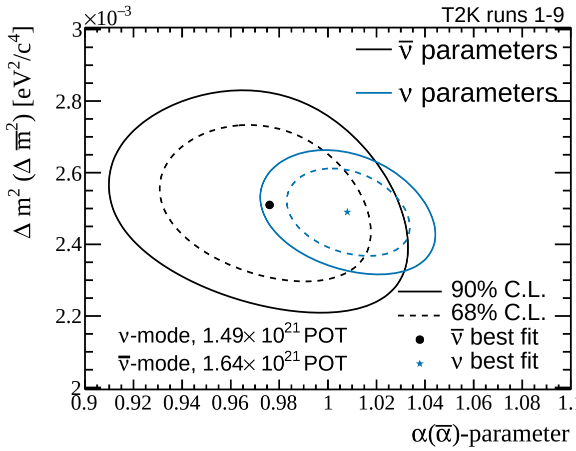

Fig. 27. 68% and 90% confidence intervals on the two-flavor analysis parameters affecting neutrinos (Δm^2,α), and antineutrinos ($\overline{\Delta m^2}$,$\bar{\alpha}$).

with each other, and that the T2K data are compatible with the PMNS framework.

Measurement of the charged-current electron (anti-)neutrino inclusive cross-sections at the T2K off-axis near detector ND280

The measurement of the $\nu_\mu \to \nu_e$ (and $\bar{\nu}_\mu \to \bar{\nu}_e$) oscillations - which is the main goal of the T2K experiment - is affected by two main background sources. The first is the intrinsic ν_e and $\bar{\nu}_e$ beam contaminations and the second is the neutral current (NC) π^0 production, where the π^0 can mimic an electron from a charged-current (CC) ν_e or $\bar{\nu}_e$ interaction at the far detector, Super-Kamiokande. In addition, the $\nu_\mu \to \nu_e$ ($\bar{\nu}_\mu \to \bar{\nu}_e$) appearance signal is predicted by using a predominantly ν_μ ($\bar{\nu}_\mu$) sample, which relies on the knowledge of the ν_e ($\bar{\nu}_e$) cross-section relative to the ν_μ ($\bar{\nu}_\mu$). The modelling of signal and backgrounds is strongly depending on the neutrino cross-sections and the near detector is crucial for measuring them.

T2K published a new measurement of the charged current (CC) ν_e and $\bar{\nu}_e$ inclusive cross-sections [11]. The CC-ν_e cross-section was already measured by T2K in 2014 [12], but the new work presented here follows a different approach to measure the cross-sections: the differential cross-sections are measured in a model independent way as a function of electron and positron kinematics (momentum and scattering angle), the quantities which are measured in the near detector. For the differential cross-section extraction, this work uses a binned likelihood fit with control samples to tune the backgrounds instead of an iterative matrix inversion method [13]. The likelihood fit method is preferred as the correction of detector smearing effects is independent of the signal model used in the simulation and it allows in-depth validation of the background tuning and of the extracted results. Events with momentum below 200 MeV/c were not considered in the 2014 results. This background enriched region can be used for fit validation studies and it is used in the current work. Additionally, T2K has doubled the neutrino data and collected a significant amount of anti-neutrino data since the 2014 measurements. The measurement of the CC-$\bar{\nu}_e$ inclusive cross-section is the first such measurement since Gargamelle in 1978 [14].

Prior to fitting the data, the signal and background events are varied under different model assumptions to create pseudo datasets generated from variations of nominal MC (toy experiments). These pseudo datasets are used to check the fit performance, possible biases, over-constraining the nuisance parameters and the impact of nuisance parameters to the signal normalization parameters and understand the dependencies on signal and background models. In addition, the cross-sections are measured using two generators to test different model assumptions. The results are in good agreement with all the tests providing confidence that our measurements are free from model dependencies.

The differential cross-section results in electron and positron momentum, $d\sigma/dp$, using NEUT (5.3.2) or GENIE (2.8.0) as input MC are shown in Figure 28 and they are in agreement with the predictions. The CC-ν_e cross-sections are expected to be larger in anti-neutrino running mode since the neutrino energy spectrum peaks at higher energy and it is much broader with larger contribution from higher energy neutrinos. Differences between the results using either NEUT or GENIE simulations are expected due to small differences in the efficiency corrections and small differences in the muon, proton and other backgrounds which are kept constant in the fit. The cross-section results are dominated by the statistical uncertainty, especially in RHC. The statistical uncertainty is estimated by fixing all the nuisance parameters to their post-fit nominal values and repeating the fit.

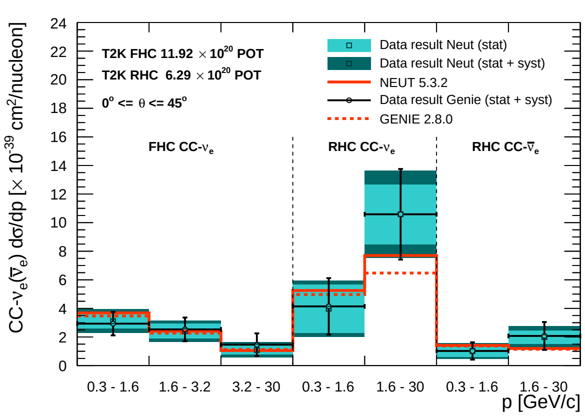

Fig. 28. Inclusive cross-section results in $d\sigma/dp$ in a limited phase-space ($p > 300$ MeV/c and $\theta \leq 45°$) for CC-ν_e in neutrino (FHC) and anti-neutrino (RHC) running modes, and CC-$\bar{\nu}_e$ in anti-neutrino running mode (RHC).

The cross-section results were also compared with more recent neutrino generator models using NEUT 5.4.0, GENIE 2.12.10 and NuWro 19.02. The best agreement was observed with NEUT 5.4.0.

Bibliography

[1] K. Abe *et al.* (T2K Collaboration), Nucl. Instrum. Meth. A **659**, 106 (2011).

[2] D. Beavis, A. Carroll, I. Chiang, *et al.*, Long Baseline Neutrino Oscillation Experiment at the AGS (Proposal E889), 1995. Physics Design Report, BNL 52459.

[3] K. Abe *et al.* (T2K Collaboration), Phys. Rev. Lett. **112**, 061802 (2014).

[4] T. Bhlen *et al.*, Nucl. Data Sheets **120**, 211 (2014).

[5] N. Abgrall et al. (NA61/SHINE Collaboration), Eur. Phys. J. C **76**, 84 (2016).

[6] C. Zeitnitz and T. A. Gabriel, Proceedings of International Conference on Calorimetry in High Energy Physics (World Scientific, Corpus Christi, Texas, 1992), ISBN 9789810213039, pp. 394-404.

[7] K. Abe *et al.* (T2K Collaboration), Phys. Rev. D **103**, L011101 (2021)

[8] Y. Hayato, Acta Phys. Pol. B **40**, 2477 (2009).

[9] Hiroshi Nunokawa, Stephen Parke, and Renata Zukanovich Funchal, Phys. Rev. D **72**, 013009 (2005)

[10] K. Abe *et al.* (T2K Collaboration), Nature, 2020, 580(7803), pp. 339344

[11] K. Abe *et al.* (T2K Collaboration), J. High Energ. Phys. 2020, **114** (2020)

[12] K. Abe *et al.* (T2K Collaboration), Phys. Rev. Lett. **113**, 241803 (2014)

[13] G.D'Agostini Nucl. Instrum. Meth. A **362** (1995) 487-498

[14] Gargamelle collaboration, Nuclear Physics **B133** (1978) 205-219

XMASS EXPERIMENT

[Spokesperson : Shigetaka Moriyama]
Kamioka Observatory, ICRR, the University of Tokyo

Introduction

The XMASS project is designed to detect dark matter, neutrinoless double beta decay, and ^{7}Be/pp solar neutrinos using highly-purified liquid xenon (LXe) scintillator in an ultra-low radioactivity environment [1]. The advantages of using LXe are a large amount of scintillation light yield, scalability of the size of the detector mass, an easy purification to reduce internal radioactive backgrounds (BGs), shielding ability against radiations from outside of the detector due to a high atomic number ($Z = 54$). The detector with $\sim$830 kg of LXe has been constructed in September 2010. After completion of the construction, commissioning data was taken from December 2010 to May 2012. We published results from searches for some dark matters [2, 3, 4], solar axions [5], and two-neutrino double electron capture on ^{124}Xe [6]. We also studied a possibility to detect galactic supernova neutrinos via coherent elastic neutrino-nucleus scattering [7].

During the commissioning data-taking, we found that a majority of events at low energy originated from radioactive contamination in the aluminum seal of the photomultiplier tube (PMT) window. In order to minimize the BG contribution, detector refurbishment was conducted. The contaminated parts of PMTs were covered by copper rings and plates in order to stop scintillation lights and radiations caused by its contamination. PMT windows were cleaned by nitric acid and copper parts were electropolished in order to remove possible surface contamination. After a year of detector refurbishment, data-taking resumed in November 2013 with background significantly reduded and continued for more than five years. We then completed the data taking in February 2019. We have published results from the searches for annual modulation from dark matters [8, 9], for solar Kaluza-Klein axions [10], for two-neutrino double electron capture on ^{124}Xe [11], for dark matter through elastic-scattering [12], for hidden photons [13], for inelastic-scattering off ^{129}Xe [14], for sub-GeV dark matter [15], and for exotic neutrino-electron interactions [16].

In the following sections, we introduce the XMASS-I detector briefly and report the latest physics results from the XMASS data collected after the refurbishment.

The XMASS-I detector

XMASS-I is a single phase LXe scintillator detector located underground (2700 m water equivalent) at the Kamioka Observatory [17]. Fig. 29 shows a schematic drawing of the XMASS-I detector. It contains $\sim$830 kg of LXe in an active region. The volume is viewed by 630 hexagonal and 12 cylindrical Hamamatsu R10789 PMTs arranged on an 80 cm diameter pentakis-dodecahedron support structure. These PMTs were developed to achieve low background requirement [18]. The largest contributions to the reduction of radioactivity came from the stem and the dynode support. The glass stem was exchanged to the Kovar alloy one and the ceramic support were changed to the quartz one. R10789 is the first model of Hamamatsu Photonics K. K. that adopted these materials for low background purposes and provided a groundbreaking step for further reductions of radioactivity in PMTs. A total photocathode coverage of more than 62% is achieved. The spherical arrays of PMTs are arranged in

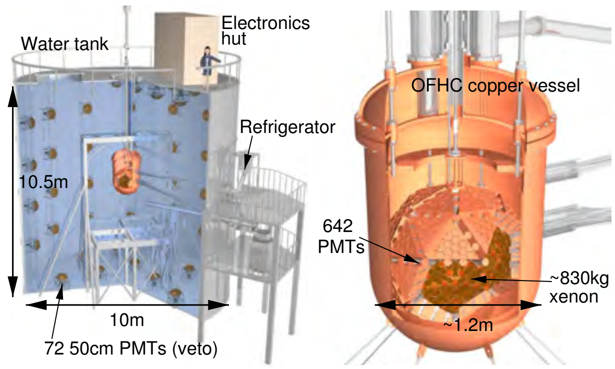

Fig. 29. Schematic drawing of the XMASS-I detector.

a double wall vessel made of oxygen free high conductivity copper [19]. The waveforms in each PMT are recorded with CAEN V1751 waveform digitizers with 1 GHz sampling rate and 10 bit resolution. The detector is calibrated regularly with a ^{57}Co source inserted along the central vertical axis of the detector and external ^{60}Co source. By the data taken with the ^{57}Co source at the center of the detector volume, the photoelectron (PE) yield was determined to be $\sim$14 PE/keV. Two different energy scales were used: keV$_{\rm ee}$ represents an electron equivalent energy, and keV$_{\rm nr}$ denotes the nuclear recoil energy. Scintillation decay time constant was investigated in liquid xenon with the XMASS detector. These are summarized at [20] and [21].

In order to shield the LXe detector from external gammas, neutrons, and muon-induced BGs, the copper vessel was placed at the center of a ϕ10 m$\times$ 10.5 m cylindrical tank filled with pure water. The water tank is equipped with 72 Hamamatsu R3600 20-inch PMTs to provide both an active muon veto and passive shielding against these BGs. XMASS-I is the first direct detection dark matter experiment equipped with such an active water Cherenkov shield. The LXe and water Cherenkov detectors are hence called an Inner Detector (ID) and an Outer Detector (OD), respectively.

Search for exotic neutrino-electron interactions using solar neutrinos [16]

We have searched for exotic neutrino-electron interactions that could be produced by a neutrino millicharge, by a neutrino magnetic moment, or by dark photons using solar neutrinos in the XMASS-I liquid xenon detector. We observed no significant signals in 711 days of data and obtained constraints on the exotic neutrino-electron interactions.

The electric charge of neutrinos is assumed to be zero in the Standard Model (SM). In general, the existence of a neutrino millicharge would give hints on models beyond the SM. In a simple extension of the SM with the introduction of the right-handed neutrino ν_R, the neutrino is a Dirac particle and the three neutrino mass eigenstates share a common millicharge due to gauge invariance whether the millicharge is zero or not. Any differences of millicharge among neutrinos and antineutrinos would be an indication of CPT violation. Moreover, it is still of interest to study the neutrino millicharge of each individual neutrino flavor in the unexplored parameter space. Both, experimental searches and astrophysical indirect searches for neutrino millicharge have been performed, but no evidence for neutrino millicharge has been found so far. Solar neutrinos are produced as electron neutrinos, but due to neutrino oscillation at Earth they also contain ν_μ and ν_τ. We search for millicharge in all three neutrino flavors.

The massless neutrinos of the SM do not have any magnetic moment. However, a minimally-extended SM with Dirac neutrino masses predicts a finite neutrino magnetic moment. It is not currently feasible to detect it experimentally because of its smallness. However, other extensions of SM theory yield neutrino magnetic moments at currently observable levels. For example, if the neutrino is a Majorana particle, the transition magnetic moment is estimated to be $O(10^{-12} \sim 10^{-10})\mu_B$ in an extension that goes beyond a minimally-extended SM.

There are many unsolved problems that cannot be explained by the SM, such as neutrino mass and the particle nature of dark matter, and new physics scenarios beyond the SM are required. The hidden sector scenario is one of such scenario. It could contain a dark photon, which might influence the interaction of neutrinos with electrons via dark-photon exchange. The idea that the light vector boson of this hidden sector appears as a dark photon has been around for a long time, and the possibility that it appears at low energy has received wide interest. In the context of one such scenario, we search for a dark photon derived from a gauged $U(1)_{B-L}$ symmetry, for which a noticeable increase of the cross section for electron-recoil from solar neutrino interactions is expected. The mass $M_{A'}$ of the dark photon A' and coupling constant g_{B-L} are already constrained by various experimental and astrophysical analyses.

These considerations motivate us in our search for exotic neutrino interactions. Since solar neutrinos provide the largest available flux, we used them to search for exotic neutrino interactions with the XMASS-I detector. The expected signal spectrum results from the respective electron recoil spectrum in Figure 30 being folded with the detection efficiency of the detector, which is a function of energy.

We analyzed the data, accumulated in the same period as [12], between November 2013 and March 2016. The total livetime is 711 days, which is slightly increased due to the recovery of some data in this analysis. The event-selection criteria were as follows: We required that (1) the ID trigger is not accompanied by an OD trigger, (2) there was no after pulse or Cherenkov event, (3) R(Timing) $<$ 38 cm, and (4) R(PE) $<$ 20 cm, where R(Timing) and R(PE) were the distances from the center of the detector to the reconstructed vertex obtained by timing-based reconstruction and by PE-based reconstruction [17], respectively. The BG components in the fiducial volume were discussed in [12] for $E_{\rm recon} < 30$ keV and in [11] for $E_{\rm recon} > 30$ keV, respectively. The dominant BG component for $E_{\rm recon} < 30$ keV derives from the radioactive isotopes (RI) that existed at the inner surface of the detector. Moreover, the ^{210}Pb accumulated on the inner surface of the detector was taken into account. RI induced surface events were often misidentified as events in the fiducial volume in the event reconstruction.

Based on the BG estimate, we searched for the signatures

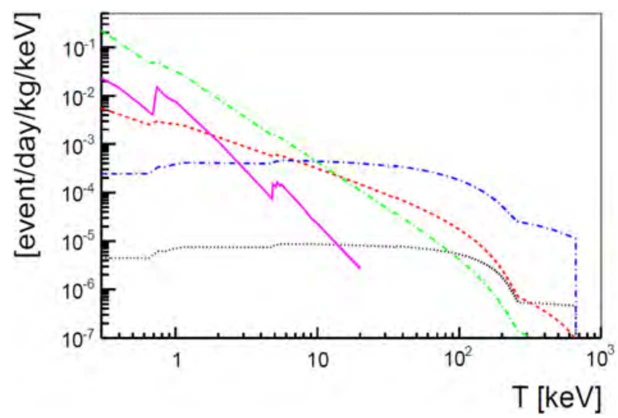

Fig. 30. The deposited energy spectra for neutrino interactions in xenon. The magenta-solid line shows a model where the neutrino has a millicharge ($1.5\times10^{-12}e$). The red-dashed line shows a model where the neutrino has a magnetic moment ($1\times10^{-10}\mu_B$). The green-dash-dotted and blue-dash-dotted line show models where neutrino interacts with electrons through dark photons with $g_{B-L}=1\times10^{-6}$ and $M_{A'}=1\times10^{-3}$ MeV$/c^2$ and with $g_{B-L}=1\times10^{-4}$ and $M_{A'}=10$ MeV$/c^2$, respectively. The black-dotted line shows the Standard Model neutrino-electron weak interaction. The models for atomic effects are RRPA for millicharge and FEA for magnetic moment and dark photons.

of exotic neutrino-electron interactions by fitting the energy spectrum of the data with those of the BG MC and the respective signal MC. The fitting range is 2-15 keV in the neutrino millicharge search, and is 2-200 keV in the dark photon and neutrino magnetic moment searches.

For neutrino millichage case, we found no significant signal excess, which would have been expected around 5 keV, and accordingly we set an upper limit for neutrino millicharge of $5.4 \times 10^{-12}e$ at the 90% confidence level (CL), assuming all three species of neutrino have common millicharge. The best fit χ^2 was obtained at zero millicharge and thus the 90% upper limit was obtained. Figure 31 shows the data and the best-fit signal + BG MC with the signal MC at the 90% CL upper limit. Figure 32 compares our result with those of other experiments.

We searched for a signal excess due to a neutrino magnetic moment, but found no significant excess. The 90% CL upper limit for the neutrino magnetic moment was estimated from the χ^2 probability density function to be $\mu_\nu = 1.8\times10^{-10}\mu_B$.

A signal excess due to a dark photon with $M_{A'}$ in the range from 1×10^{-3} MeV$/c^2$ to 1×10^{3} MeV$/c^2$ was also searched for. Again we found no significant excess. The 90% CL upper limit on the coupling constant as a function of the dark photon mass is shown in Figure 33, together with the limits and allowed region from other experimental and astrophysical analyses.

Development of low-background photomultiplier tubes for liquid xenon detectors [22]

Liquid xenon detectors require efficient read out of scintillation photons. New types of sensors, such as silicon photomultipliers, are being rapidly developed for that purpose, however the PMT still has the main role for upcoming experiments such as XENONnT, LZ, and PandaX. The expected

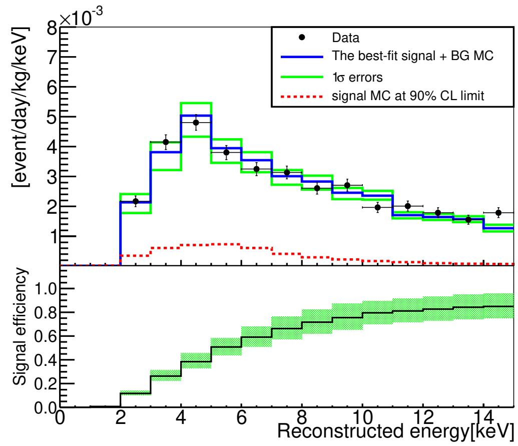

Fig. 31. (Top) The energy distribution after applying all cuts. The black points show the data. The blue histograms show the best-fit signal + BG MC simulation with 1 σ errors shown by the green histograms. The red-dotted histograms show the 90% CL upper limit for the neutrino-millicharge signal. (Bottom) The signal efficiency curve for the millicharge analysis. See text for detail.

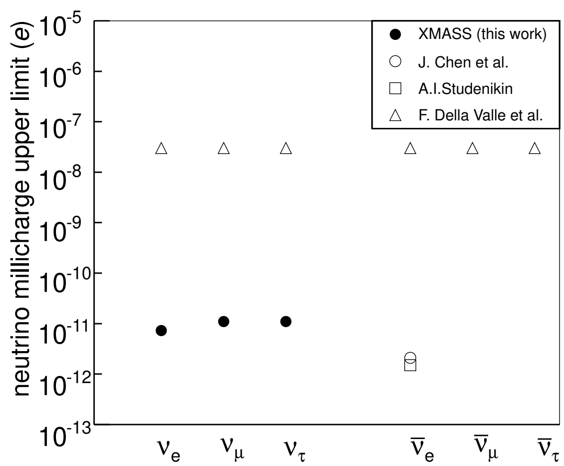

Fig. 32. 90% CL upper limits for neutrino millicharge for each flavor in ours and other experiments. The limit from F. Della Valle *et al.* depends on neutrino mass. It is for neutrino masses less than 10 meV.

signal rate for such LXe dark matter experiments currently is known to be at most one event/ton/year. Since the amount of BG directly impacts the sensitivity of any dark matter search, the BG event rate from the detector components must be as low as possible. This indicates that it is crucial to develop PMTs with still lower BG; lower radioactive impurities (RIs) and better performance. Such improved PMTs will not only be needed to improve dark matter searches, but also be useful in other rare event searches beyond the standard model such as search for neutrinoless double beta decay.

We successfully developed a new PMT with a three-inch diameter, convex-shaped photocathode, R13111. Its prominent features include good performance and ultra-low radioactivity. The convex-shaped photocathode realized a large photon acceptance and good timing resolution. Low radioactivity was achieved by three factors: (1) the glass material was synthesized using low-radioactive-contamination material; (2)

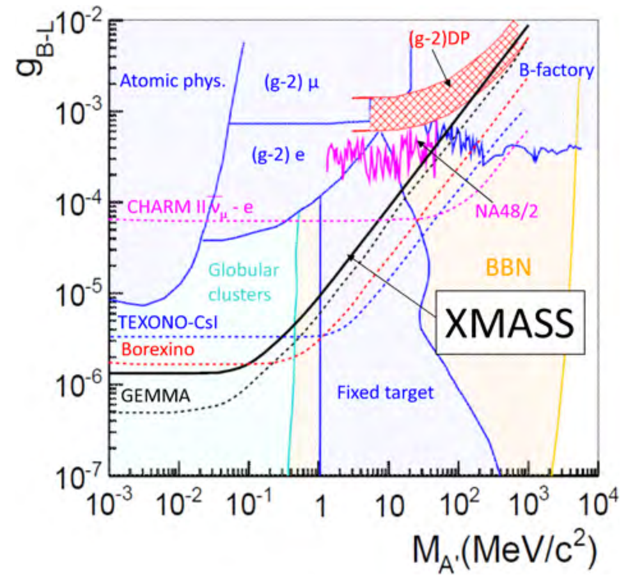

Fig. 33. 90% CL exclusion limits and allowed region on the coupling constant g_{B-L} as a function of the dark photon mass $M_{A'}$. The black-solid line shows the exclusion limit of our analysis (XMASS). The 2σ-allowed-region band from the muon $(g-2)$ experiment is shown as "$(g-2)$ DP" as the red-meshed region. Colored regions have been constrained by other experiments and theoretical considerations.

the photocathode was produced with ^{39}K-enriched potassium; and (3) the purest grade of aluminum material was used for the vacuum seal. As a result each R13111 PMT contains only about 0.4 mBq of ^{226}Ra, less than 2 mBq of ^{238}U, 0.3 mBq of ^{228}Ra, 2 mBq of ^{40}K and 0.2 mBq of ^{60}Co. We also examined and resolved the intrinsic leakage of Xe gas into PMTs that was observed in several older models.

A picture of an R13111 PMT is shown in Figure 34. We adopted a convex-concave shape for the R13111 window. The photocathode is deposited on the window's inside concave surface. Because of this photocathode geometry, the R13111 PMT has a large angular acceptance. The convex geometry of the photocathode also improves the timing resolution, since this geometry makes the photoelectron track length more uniform over the photocathode area.

It is required to measure the RIs of materials we use for PMT production. We used four different low BG HPGe detectors installed underground at Kamioka. We also employed two different mass-spectrometry methods; inductively coupled plasma mass spectrometry and glow-discharge mass spectrometry. We concentrated our efforts at RI reduction on those items that contributed most to the radioactivity of the R10789 PMT [18]: the glass beads used to seal the electrical feedthroughs in the base of the PMT, the potassium compound used in the photocathode production, and the aluminum seal for the entrance window. As a result of this effort we achieved a significantly lower RI contamination for the new R13111 PMT.

We also carried out the RI measurement of PMTs after production. Figure 35 shows the energy spectrum of 13 PMTs with the ^{39}K-enriched photocathode. Table 6 compares the RIs between the R13111 PMT variants in two produc-

Fig. 34. R13111

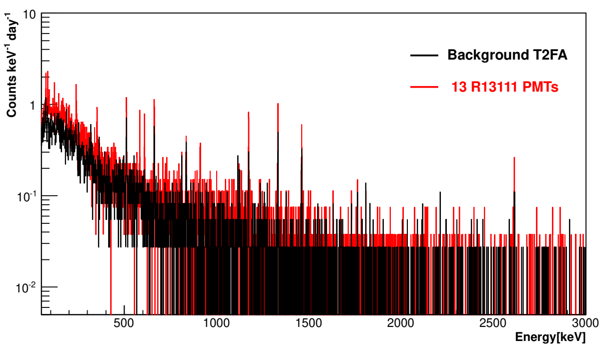

Fig. 35. The energy spectra for 13 R13111 PMTs measured over 27 days (red) with the 36 day BG spectra (black). For the PMTs produced with the ^{39}K-enriched photocathode material. The bin width is 1 keV.

tion years and the R11410 PMT used by XENON1T, PandaX and LUX. Almost all PMT RIs are lowest for our R13111 among these PMTs. Only ^{226}Ra for the 2016 R13111 PMTs is larger than the R11410-10 (LUX) number, though the levels are quite similar.

With its low radioactivity, excellent timing resolution, and large angular acceptance the new R13111 PMT can show highly good performance in future low BG LXe detectors.

Bibliography

[1] Y. Suzuki *et al.*, hep-ph/0008296.

[2] K. Abe *et al.* (XMASS Collaboration), Phys. Lett. B **719** (2013) 78.

[3] H. Uchida *et al.* (XMASS Collaboration), Prog. Theor. Exp. Phys. (2014) 063C01.

[4] K. Abe *et al.* (XMASS Collaboration), Phys. Rev. Lett. **113** (2014) 121301.

[5] K. Abe *et al.* (XMASS Collaboration), Phys. Lett. B **724** (2013) 46.

[6] K. Abe *et al.* (XMASS Collaboration), Phys. Lett. B **759** (2016) 64.

[7] K. Abe *et al.* (XMASS Collaboration), Astropart. Phys. **89** (2017) 51.

[8] K. Abe *et al.* (XMASS Collaboration), Phys. Lett. B **759** (2016) 272.

[9] K. Abe *et al.* (XMASS Collaboration), Phys. Rev. D **97** (2018) 102006.

[10] N. Oka *et al.* (XMASS Collaboration), Prog. Theor. Exp. Phys. **2017** (2017) 103C01.

[11] K. Abe *et al.* (XMASS Collaboration), Prog. Theor. Exp. Phys. **2018** (2018) 053D03.

[12] K. Abe *et al.* (XMASS Collaboration), Phys. Lett. B **789** (2019) 45.

[13] K. Abe *et al.* (XMASS Collaboration), Phys. Lett. B **787** (2018) 153.

[14] T. Suzuki *et al.* (XMASS Collaboration), Astropart. Phys. **110** (2019) 1.

[15] M. Kobayashi *et al.* (XMASS Collaboration), Phys. Lett. B **795** (2019) 308.

[16] K. Abe *et al.* (XMASS Collaboration), Phys. Lett. B **809** (2020) 135741.

[17] K. Abe *et al.* (XMASS Collaboration), Nucl. Instrum. Meth. A **716** (2013) 78.

[18] K. Abe *et al.* (XMASS Collaboration), Nucl. Instrum. Meth. A **922** (2019) 171.

[19] K. Abe *et al.* (XMASS Collaboration), Nucl. Instrum. Meth. A **884** (2018) 157.

[20] H. Takiya *et al.* (XMASS Collaboration), Nucl. Instrum. Meth. A **834** (2016) 192.

[21] K. Abe *et al.* (XMASS Collaboration), JINST **13** (2018) P12032.

[22] K. Abe *et al.* (XMASS Collaboration), JINST **15** (2020) P09027.

Table 6. RI comparison between the R13111 PMT and other PMTs used by other groups. The units are μBq/PMT.

μBq/PMT	^{226}Ra	^{238}U	^{228}Ra	^{40}K	^{60}Co
R13111 in 2015	$(3.8 \pm 0.7)\cdot 10^2$	$<1.6 \cdot 10^3$	$(2.9 \pm 0.6)\cdot 10^2$	$<1.4 \cdot 10^3$	$(2.2 \pm 0.5)\cdot 10^2$
R13111 in 2016	$(4.4 \pm 0.6)\cdot 10^2$	$<1.4 \cdot 10^3$	$(2.0 \pm 0.6)\cdot 10^2$	$(2.0 \pm 0.5) \cdot 10^3$	$(1.3 \pm 0.4)\cdot 10^2$
R11410-21 (XENON1T)	$(5.2 \pm 1.0)\cdot 10^2$	$<1.3 \cdot 10^4$	$(3.9 \pm 1.0)\cdot 10^2$	$(1.2 \pm 0.2) \cdot 10^4$	$(7.4 \pm 1.0) \cdot 10^2$
R11410-10 (PandaX)	$7.2\cdot 10^2$	—	$<8.3\cdot 10^2$	$(1.5 \pm 0.8) \cdot 10^4$	$(3.4 \pm 0.4) \cdot 10^3$
R11410-10 (LUX)	$<4.0\cdot 10^2$	$<6.0 \cdot 10^3$	$<3.0 \cdot 10^2$	$<8.3 \cdot 10^3$	$(2.0 \pm 0.2) \cdot 10^3$

HYPER-KAMIOKANDE

[Co-Spokespersons: Masato Shiozawa[1], Francesca Di Lodovico[2]]
1: Kamioka Observatory, ICRR, The University of Tokyo
2: Department of Physics King's College London

Introduction

The Hyper-Kamiokande (Hyper-K or HK) project is the world-leading international scientific research project hosted by the university of Tokyo and High Energy Accelerator Research Organization (KEK) consisting of a next generation underground water Cherenkov detector and upgraded Japan Proton Accelerator Research Complex (J-PARC) neutrino beam.

The supplementary budget for FY2019 including the first-year construction budget for Hyper-K project was approved by the Japanese Diet on January 2020 and the Hyper-K project has officially started. In May 2020, the University of Tokyo and KEK signed a memorandum of understanding (MoU) which aimed to strengthen the existing MoU between Institute for Cosmic Ray Research (ICRR), UTokyo and Institute of Particle and Nuclear Studies (IPNS), KEK by establishing official organizations to promote the Japan-led Hyper-Kamiokande international scientific research project.

Figure 36 shows a schematic drawing of the Hyper-K cylindrical detector. The detector is filled with 0.260 million metric tons of ultra pure water, which serves an order of magnitude larger fiducial mass of 0.188 million metric tons than Super-K, equipped with newly developed high-sensitivity photosensors, and a high-intensity neutrino beam produced by an upgraded J-PARC accelerator facility. It provides an enormous potential to discover leptonic charge-parity (CP) violation by observing neutrino and anti-neutrino beams from J-PARC, investigate the Grand Unified Theory by exploring proton decay, and determine the neutrino mass ordering by observing atmospheric neutrinos combining beam data. Hyper-K will also have far better capabilities to observe solar neutrinos and neutrinos from other astronomical sources than those of predecessor experiments.

The Hyper-K international collaboration consists of about 440 researchers from 93 institutes in 19 countries. Technical details were published as a design report in May 2018 with various physics reaches [1]. The detector technology has been developed based upon the successful Super-K experiment and feasibility studies have been completed by international group. The Hyper-K construction has started since the end of FY2019 and its operation plans to start in 2027.

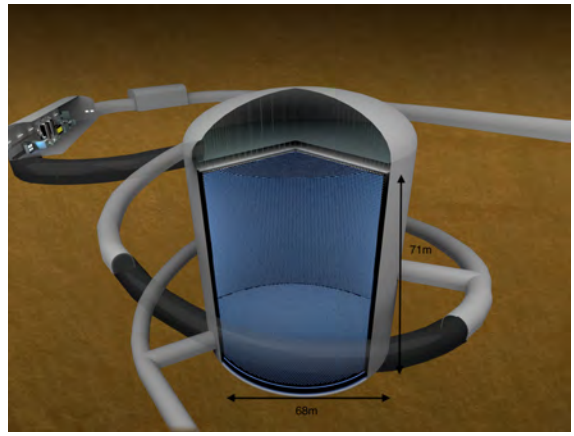

Fig. 36. Schematic view of the Hyper-K water tank.

Construction of the entrance yard

The first step of the Hyper-K construction is the construction of the entrance yard. The entrance yard is a base for the excavation work and is used as a place for necessary facilities such as a concrete plant, storage for excavated rocks, and parking lots.

As the preparation of the yard, the construction of the new temporary prefectural road, the procedure of prefectural road relocation, the preparation of the construction road, and the installation of the wastewater treatment facility have been completed in FY2020. In order to proceed the construction safely, it was required to relocate the prefectural road and to realize grade separation for the prefectural road and the construction road.

After finishing required facilities installations, the tunnel excavation work is scheduled to start from May 2021. From 2022 to the middle of 2024, a huge cavity is to be excavated. After a water tank lining, a PMT installation, and water injection, and the detector operation start is scheduled to start in 2027.

Geological survey FY2020

The geological condition at the HK site has been investigated since the early 2000s by inspection of existing mine tunnels, diamond drill holes, and seismic surveys. From these survey results we have pinned down the cavern position.

In FY2020, another larger geological survey was conducted for more detailed information aiming to: 1. check the validity of the site, 2. identify local conditions such as failures and cracks, 3. extract the physical properties of the bedrock for local geological modeling.

Two adits (total length of 98m) and six boreholes (to-

Fig. 37. The entrance yard at Mar. 26, 2021. The blue building on the right is the wastewater treatment facility. The blue bridge over that facility is part of the new prefectural road. The construction road pass through under the bridge. The excavated rocks and construction drainage are carried by this road without interfering with the prefectural road. The tunnel entrance is at the other end of this construction road.

tal length of 734m) were newly excavated and various in-situ/laboratory tests have been carried out to extract physical properties of the surrounding bedrock. The survey results show the geological condition at the planned site seems suitable for excavation of the HK cavern. The rock quality is favorable over a wide area, no major faults crossing the main cavern was found. Several cracks and aplite layers that can affect the behavior of roof bedrock of the dome section have been identified. Such information and the measured physical properties, Young's modulus, shear strength, compressive strength, and in-situ stress state, are to be used as the basic inputs for the local geological model required from the excavation work.

Fig. 38. The geological survey at HK site. Left: The adit wall visual inspection. Right: Bedrock shearing test.

Photosensors and support structure mockup

A Cherenkov light in a ultra pure water is detected by 40,000 newly developed photomultiplier tubes (PMTs), R12860 by Hamamatsu Photonics K.K., with 40% photo-coverage. It was significantly upgraded from the R3600 PMT used in Super-K due to an improved dynode structure using a box-and-line type and optimized curvature glass as shown in Fig. 39.

The total detection efficiency of R12860 for single photon is twice higher than that of the Super-K PMT owing to 1.4 times higher quantum efficiency (about 30%) and greatly improved photoelectron collection efficiency. The timing and charge resolutions at single photoelectron also becomes much better as 1.1 ns and 35% which can be compared with 2.1 ns and 53% of the Super-K PMT, respectively. These outstanding

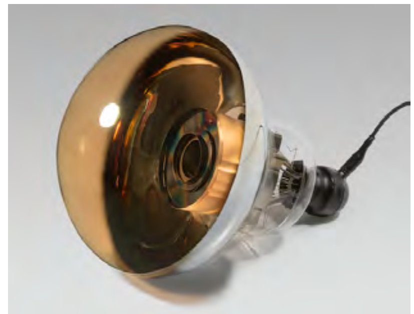

Fig. 39. New 50 cm photomultiplier tube with a box-and-line dynode (R12860, Hamamatsu Photonics K.K.).

improvements enhance Hyper-K detector performance and its physics reaches.

Moreover, pressure tolerance of PMT was improved up to the 125 m water depth, so that new PMT can be used under about 70 m depth of the detector water. To prevent a chain reaction of imploding PMTs caused by the unlikely event of a single PMT implosion, every PMT in the Hyper-K water tank will be housed in the shockwave prevention cover. The test for first prototype cover has been already performed and successfully confirmed the cover prevents the chain implosion at 80 m water depth.

Mass production of R12860 PMT began in October 2020. 300 PMTs have been delivered by the end of FY2020, from FY2021 delivery of about 300 PMTs for every month is scheduled. For storage and inspection of the PMTs, a facility with enough space and air conditioner has been prepared near the tunnel entrance. Inspection of the delivered PMTs started in the facility. Visual inspection for bulb and waterproof quality, signal check for signal property and dark rate, and long term stability check for all the first 1000 PMTs are planned. Optimization of the checks is ongoing.

Fig. 40. First 144 mass production R12860 PMTs delivery to the site for storage.

Physics

Hyper-K will have capability to measure the magnitude of the CP violation with high precision, which could explain the baryon asymmetry in the Universe. Figure 41 shows an expected significance of the CP violation discovery by ten years operation. Hyper-K covers the 76% of δ_{CP} parameter space with 3σ or more significance, and 57% of the parameter space with 5σ or more. More than 7σ significance will be expected if $\delta_{CP} = -90°$ as suggested by T2K [2] and NOνA [3] results.

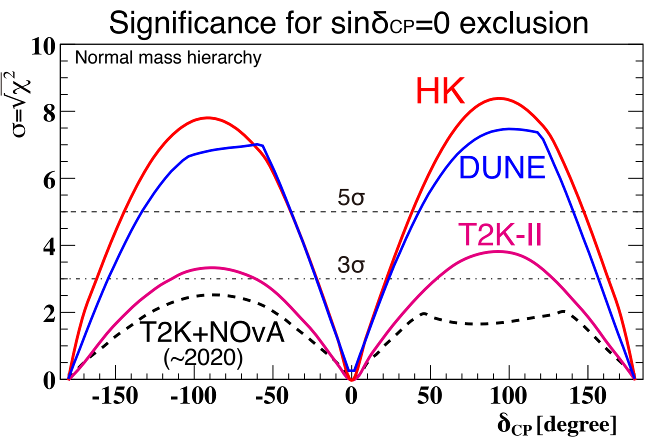

Fig. 41. Significance of the leptonic CP violation discovery with a 10-year observation in Hyper-K (HK) as a function of the unknown CP phase assuming the normal neutrino mass hierarchy. Ongoing and planned long baseline experiments are superimposed [4, 5].

A proton decay $p \to e^+\pi^0$ is an important signal favored by many Grand Unified Theory models with a prediction close to the current limit of the proton decay life time. Figure 42 shows reconstructed invariant mass distributions for $p \to e^+\pi^0$ search after applying the event selection cuts. High sensitive Hyper-K PMTs result in strong background (atmospheric neutrinos) reduction and $p \to e^+\pi^0$ search in Hyper-K is expected to be "background-free" particularly in the free-proton enhanced signal region. Figure 43 shows the 3σ discovery potential for the $p \to e^+\pi^0$ mode as a function of year. Hyper-K is an only realistic proposal which can go beyond the proton lifetime of 1×10^{35} years.

As well as the supernova burst neutrino that was successfully observed in Kamiokande at once, undiscovered supernova relic neutrinos, accumulated by past all supernovae since the beginning of the universe, are interesting events to explore the history of heavy elements and the onset of stellar formation. Figure 44 shows the expected number of events as a function of year.

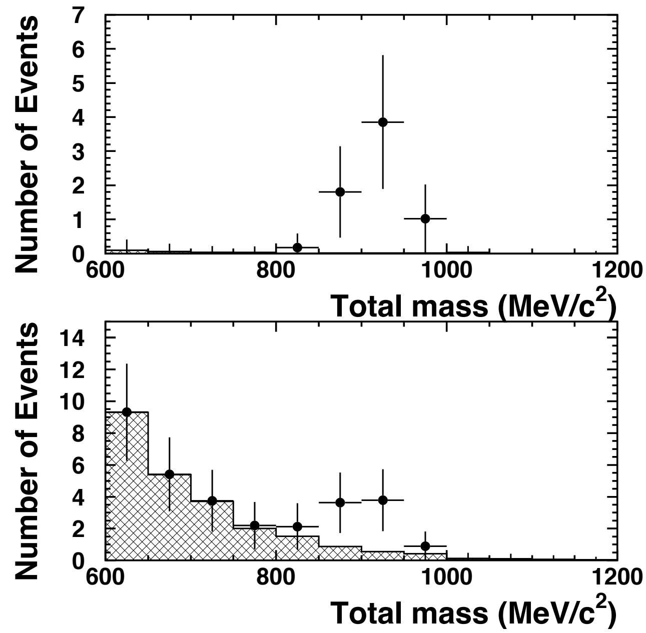

Fig. 42. Reconstructed invariant mass distribution of events passing all steps of the $p \to e^+\pi^0$ event selection except the invariant mass cut with a 10-year exposure in Hyper-K. The hatched histograms show the atmospheric neutrino background and the solid crosses denote the sum of the background and proton decay signal. Here the proton lifetime is assumed to be, 1.7×10^{34} years, just beyond current Super-K limits. The free and bound proton-enhanced signal windows are the upper and lower panels of the plot. The figures are quoted from "Hyper-Kamiokande Design Report" [1].

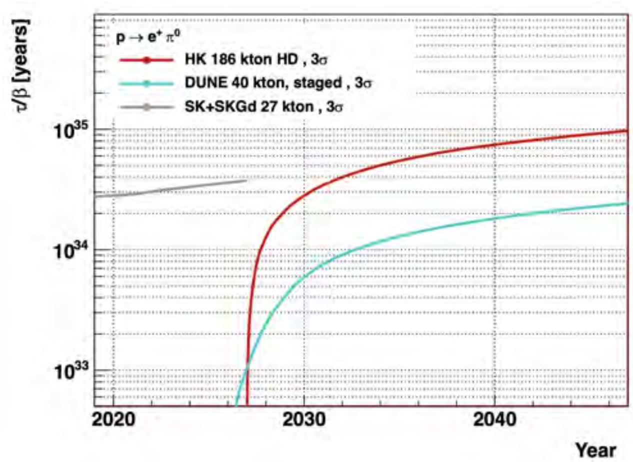

Fig. 43. The $p \to e^+\pi^0$ discovery reach in proton lifetime with 3σ significance as a function of year. It shows Hyper-K (HK) planing to start in 2027, superimposed with the ongoing Super-K (SK) and planned DUNE experiments. The DUNE project assumes 10 kton operation from 2026, toward full 40 kton by increasing 10 kton every year [6].

Bibliography

[1] "Hyper-Kamiokande Design Report," arXiv: 1805.04163.

[2] K. Abe *et al.* [T2K Collaboration], Nature 580, 339-344 (2020).

[3] P. Adamson *et al.* [NOνA Collaboration], Phys. Rev. Lett. 118, 231801.

[4] K. Abe *et al.* [The T2K Collaboration], arXiv:1609.04111 [physics.ins-det].

[5] K. Abe *et al.* [The T2K Collaboration], PTEP **2015**, no. 4, 043C01 (2015).

[6] R. Acciarri *et al.* [The DUNE Collaboration], arXiv:1601.05471 [physics.ins-det].

[7] H. Sekiya [Super-K Collaboration], PoS(ICHEP2016) 982 (2016).

[8] ICRR News (2016), `http://www.icrr.u-tokyo.ac.jp/2016/`

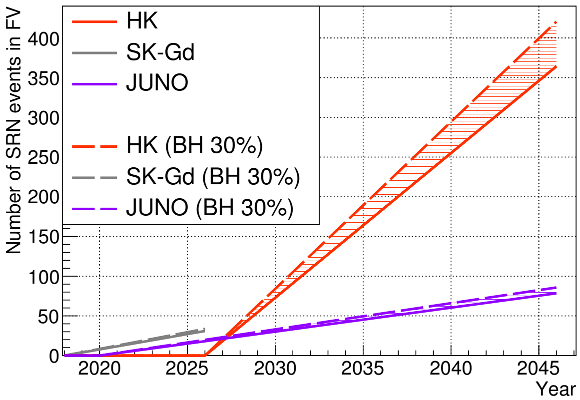

Fig. 44. The accumulated number of supernova relic neutrino events as a function of year assuming that effective temperature of neutrinos inside supernova is 6 MeV. The JUNO experiment and SK-Gd are also plotted [7, 8, 9, 10]. The solid line assumes no black hole formation while the dashed line assumes that 30% of core–collapse stars form a black hole.

06/30101400.html.

[9] F. An *et al.* [JUNO Collaboration], J. Phys. G **43**, no. 3, 030401 (2016).

[10] Yu-Feng LI, Presentation at ”Workshop on Supernova at Hyper-Kamiokande” (2017).

HIGH ENERGY COSMIC RAY DIVISION

Overview

There are three major experimental research activities in the High Energy Cosmic Ray Division, the study of high energy gamma rays and the development of the next generation gamma-ray telescopes by the Cherenkov Cosmic Gamma Ray group, the study of extremely high energy cosmic rays by the Telescope Array (TA) group, and the study of very high energy cosmic rays and gamma rays by the Tibet ASγ group.

Other activities, such as experiments utilizing the Akeno observatory, the Norikura observatory, the Mt. Chacaltaya observatory (jointly operated with Bolivia) are closely related to inter-university joint research programs. Also an all-sky high resolution air-shower detector (Ashra) is in partial operation on the Hawaii island. The High Energy Astrophysics group created in the fiscal year 2009 aims to explore various high energy astrophysical phenomena, through theoretical and observational approaches.

The CANGAROO telescopes had been in operation in South Australia since 1992, with a 3.8 m small telescope and then with four 10 m telescopes. The major scientific objective was the study of Very High Energy (VHE) gamma-ray sources in our galaxy in the southern hemisphere. The mission of these telescopes was completed and the CANGAROO observation site was closed in 2011.

For further development of VHE gamma-ray astronomy, the Cherenkov Cosmic Gamma Ray group is working on the design study and development and construction of the next generation international ground-based gamma-ray observatory CTA which will offer an order of magnitude better sensitivity than currently running Cherenkov telescopes, three times better angular resolution, and wider energy coverage from 20 GeV to 100 TeV or higher. The construction of the first Large-Sized Telescope (LST) was completed on the CTA-North site in La Palma in 2018. High Energy Astrophysics Facility in Canarias was established as a base for the project in April, 2019.

At the Akeno observatory, a series of air shower arrays of increasing geometrical sizes were constructed and operated to observe extremely high energy cosmic rays (EHECRs). The Akeno Giant Air Shower Array (AGASA) was operated from 1991 to January 2004 and covered the ground area of 100 km^2 as the world largest air shower array. In 13 years of operation, AGASA observed a handful of cosmic rays exceeding the theoretical energy end of the extra-galactic cosmic rays (GZK cutoff) at around 10^{20} eV.

The Telescope Array (TA), a large plastic scintillator array with air fluorescence telescopes, has been constructed in Utah, USA, which succeeds AGASA and measures the EHECRs with an order of magnitude larger aperture than that of AGASA for the further study of EHECRs. The full-scale TA is accumulating data as the largest array viewing the northern sky and observed the energy spectrum with high statistics, which is in good agreement with the GZK suppression and found evidence for anisotropy of arrival directions of EHECRs. The TAx4, which is aimed at quadrupling TA, was partially constructed by March of 2019.

An air shower experiment aiming to search for celestial gamma-ray point sources started in 1990 with Chinese physicists at Yangbajing (Tibet, 4,300 m a.s.l.). This international collaboration is called the Tibet ASγ Collaboration. An extension of the air shower array was completed in 1995 and an emulsion chamber has been combined with this air shower array since 1996 to study the primary cosmic rays around the knee energy region. After successive extensions carried out in 1999, 2002 and 2003, the total area of the air shower array amounts to 37,000 m^2. The sun's shadow in cosmic rays affected by the solar magnetic field was observed for the first time in 1992, utilizing its good angular resolution at multi-TeV energy region. The group added underground water Cherenkov muon detector to detect cosmic gamma rays above 100 TeV. The group is planning to construct a new air shower array, called ALPACA, to cover the sky in the Southern hemisphere, and started the construction of its partial array in Bolivia in 2019.

The High Energy Astrophysics group is conducting theoretical researches on fundamental processes responsible for non-thermal particle acceleration in various astrophysical environments, including first-order diffusive shock acceleration, second-order stochastic acceleration in shock downstream regions, modification of shock structure by pick-up interstellar neutrals, as well as injection processes of suprathermal particles. In addition to these theoretical works, R/D studies for radio observations of pulsars and cosmic ray air showers are also being made.

Cherenkov Cosmic Gamma-Ray Group

CTA Project (Cherenkov Telescope Array)

CTA-Japan Consortium

[Spokespersons : M. Teshima and H. Kubo]

Collaboration list:

Institute for Cosmic Ray Research, The University of Tokyo, Chiba, Japan; Department of Physics, Aoyama Gakuin University, Tokyo, Japan; Department of Physics, Hiroshima University, Hiroshima, Japan; Hiroshima Astrophysical Science Center, Hiroshima University, Hiroshima, Japan; Faculty of Science, Ibaraki University, Ibaraki, Japan; Institute of Particle and Nuclear Studies, High Energy Accelerator Research Organization (KEK), Ibaraki, Japan; Department of Physics, Konan University, Hyogo, Japan; Faculty of Medical Engineering and Technology, Kitasato University, Kanagawa, Japan; Graduate School of Science and Technol-

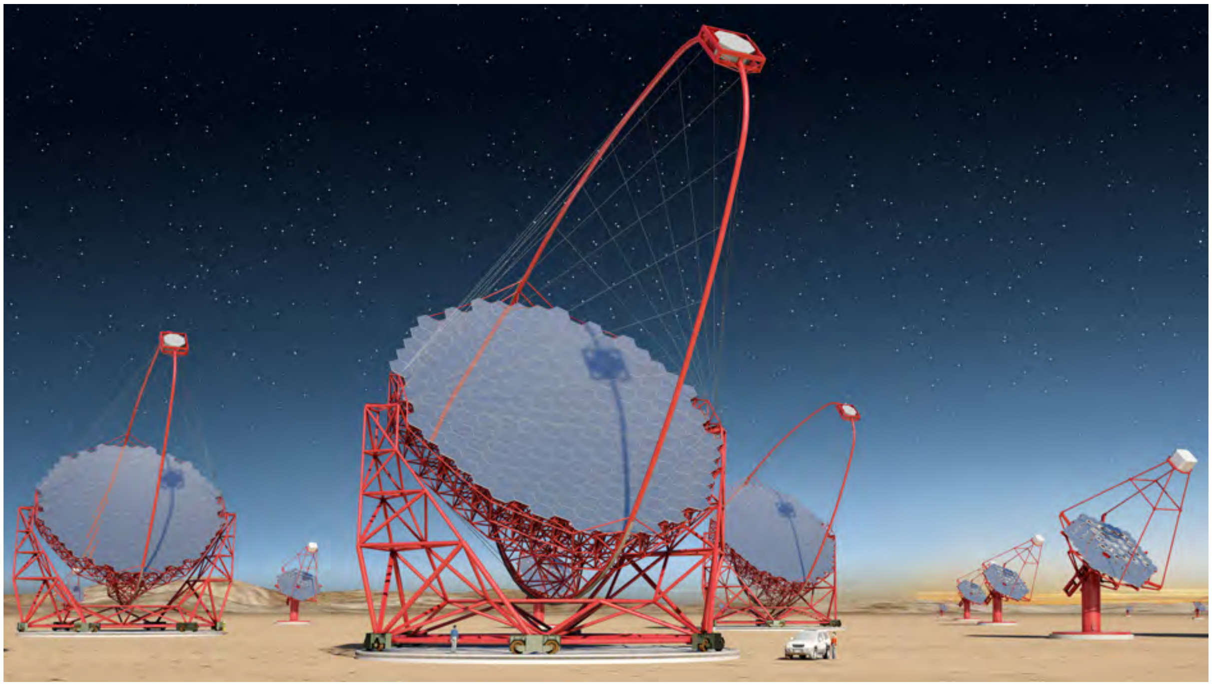

Fig. 1. Artist view of the CTA observatory. CTA consists of three types of telescopes, Large Size Telescopes (23 m diameter), Mid Size Telescopes (12 m) and Small Size Telescopes (4 m), and covers the broad energy band from 20 GeV to 100 TeV.

ogy, Kumamoto University, Kumamoto, Japan; Department of Physics, Kyoto University, Kyoto, Japan; Department of Applied Physics, University of Miyazaki, Miyazaki, Japan; Department of Physics, Nagoya University, Aichi, Japan; Solar-Terrestrial Environment Laboratory, Nagoya University, Aichi, Japan; Kobayashi-Maskawa Institute, Nagoya University, Aichi, Japan; Department of Earth and Space Science, Osaka University, Japan; Department of Physics, Kinki University, Osaka, Japan; Astrophysical Big Bang laboratory, RIKEN, Wako, Japan; Department of Physics, Rikkyo University, Tokyo, Japan; Department of Physics, Saitama University, Saitama, Japan; Institute of Space and Astronautical Science, JAXA, Kanagawa, Japan; Department of Physics, Tokai University, Kanagawa, Japan; Faculty of Integrated Arts and Sciences, The University of Tokushima; Department of Astronomy, The University of Tokyo, Tokyo, Japan; Department of Physics, The University of Tokyo, Tokyo, Japan; Faculty of Science and Engineering, Waseda University, Tokyo, Japan; Department of Physics, Yamagata University, Yamagata, Japan; Faculty of Management Information, Yamanashi Gakuin University, Yamanashi, Japan.

CTA Project

During the past years, Very High Energy (VHE) gamma-ray astronomy has made spectacular progress and has established itself as a vital branch of astrophysics. To advance this field even further, we are constructing the Cherenkov Telescope Array (CTA) [6], the next generation VHE gamma ray observatory, in the framework of a worldwide, international collaboration. CTA is the ultimate VHE gamma-ray observatory, whose sensitivity and broad energy coverage will attain an order of magnitude improvement above those of current Imaging Atmospheric Cherenkov Telescopes (IACTs). By observing the highest energy photons known, CTA will clarify many aspects of the extreme Universe, including the origin of the highest energy cosmic rays in our Galaxy and beyond, the physics of energetic particle generation in neutron stars and black holes, as well as the star formation history of the Universe. CTA will also address critical issues in fundamental physics, such as the identity of dark matter particles and the nature of space and time.

VHE gamma rays from 100 GeV to 10 TeV can be observed with ground-based current IACTs. The history of VHE gamma ray astronomy began with the discovery of VHE gamma rays from the Crab Nebula by the Whipple Observatory in 1989. To date, the current generation IACTs featuring new technologies, such as H.E.S.S., MAGIC, and VERITAS, have discovered more than 200 Galactic and extragalactic sources of various types.

CTA is designed to achieve superior sensitivity and performance, utilizing established technologies and experiences gained from the current IACTs. The project is presently in its pre-construction (prototyping) phase, with international efforts from Japan, US, and EU countries. It will consist of several 10s of IACTs of three different sizes (Large Size Telescopes, Mid Size Telescopes, and Small Size Telescopes). With a factor of 10 increase in sensitivity (1 mCrab $\sim 10^{-14}$erg s^{-1} cm^{-2}), together with a much broader energy coverage from 20 GeV up to 300 TeV, CTA will bring forth further dramatic advances for VHE gamma-ray astronomy. The discovery of more than 1000 Galactic and extragalactic sources is anticipated with CTA.

CTA will allow us to explore numerous diverse topics in physics and astrophysics. The century-old question of the origin of cosmic rays is expected to be finally settled through detailed observations of supernova remnants and other Galactic objects along with the diffuse Galactic gamma-ray emission, which will also shed light on the physics of the interstellar medium. Observing pulsars and associated pulsar wind nebulae will clarify physical processes in the vicinity of neutron stars and extreme magnetic fields. The physics of accretion onto supermassive black holes, the long-standing puzzle of the origin of ultra-relativistic jets emanating from them, as well as their cosmological evolution, will be addressed by extensive studies of active galactic nuclei (AGN). Through dedicated observing strategies, CTA will also elucidate many aspects of the mysterious nature of gamma ray bursts (GRBs), the most energetic explosions in the Universe. Detailed studies of both AGNs and GRBs can also reveal the origin of the highest energy cosmic rays in the Universe, probe the cosmic history of star formation including the very first stars, and provide high precision tests of theories of quantum gravity. Finally, CTA will search for signatures from elementary particles constituting dark matter with the highest sensitivity yet. Realisation of the rich scientific potential of CTA is very much feasible, thanks to the positive experiences gained from the current IACTs.

The CTA-Japan consortium [1] is contributing particularly to the construction of the Large Size Telescopes (LSTs, Fig.2) and is involved in their development. The LST covers the low energy domain from 20 GeV to 3 TeV and is especially important for studies of high redshift AGNs and GRBs. The diameter and area of the mirror are 23 m and 400 m^2, respectively, in order to achieve the lowest possible energy threshold of 20 GeV. All optical elements and detectors require high specifications, such as high reflectivity, high collection efficiency, high quantum efficiency, ultra-fast digitization of signals, and so on. For this purpose, CTA-Japan has developed high quantum efficiency photomultipliers and ultrafast readout electronics (Fig. 3), and high precision segmented mirrors (Fig. 4). On the strength of their experiences gained from the construction of the MAGIC telescope, Max-Planck-Institute for Physics in Munich is responsible for the design of the 23-m diameter telescope structure, based on a carbon fiber tube space frame. The LSTs require very fast rotation (180 degrees in 20 seconds) to promptly observe GRBs. The first LST (LST1) has been built in the CTA North, La Palma, Spain, in 2018, and now in the engineering run. Three more LSTs will be built until 2023, then four more LSTs in the CTA South are expected to be built in the ESO site in Paranal, Chile.

The first telescope LST1 has been regularly operated since January 2020, and has already shown an excellent performance as expected, even in a single telescope mode, through the observation of Crab Nebula, Crab Pulsar, and nearby Active Galactic Nuclei. These results certify LST1 achieved the design performance expected by Monte Carlo simulations. The Critical Design Review of LST was held by CTAO engineers and external experts from high energy physics. The phase diagram of the Crab Pulsar observation is shown in Fig. 6, which certifies the low threshold energy of LST1 and also the accuracy of the recorded event timings. The location of the LST array in the CTA North has an overlap with MAGIC telescopes, which will allow us to perform the cross-calibration between LST and MAGIC telescopes and to operate the three telescopes together in the early phase of the construction.

Fig. 2. Large Size Telescope (23 m diameter) designed by Max–Planck-Institute for Physics. CTA Japan is contributing to the design and and construction of the imaging camera at the focal plane, ultrafast readout electronics, and high precision segmented mirrors.

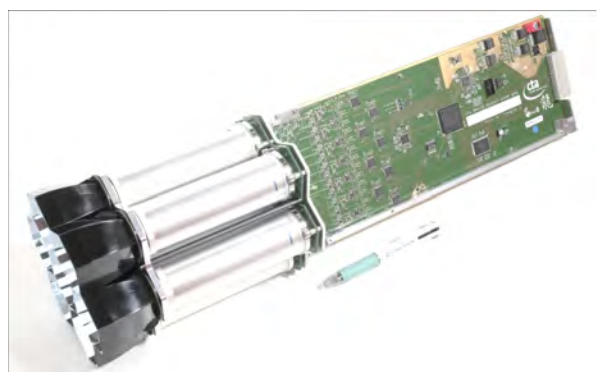

Fig. 3. Camera cluster for the Large Size Telescope (LST) developed by CTA-Japan. This cluster consists of seven high quantum efficiency photomultipliers (R11920-100), CW High Voltages, pre-amplifier, Slow Control Board, DRS4 Ultra fast waveform recording system and Trigger. The LST camera can be assembled with 265 of these clusters, cooling plates and camera housing.

The Cherenkov Cosmic Gamma Ray group is also operating the MAGIC Telescopes [10] on La Palma, Canary Islands (See the next subsection). This facility is used not only for scientific observations but also for technological development toward the future observatory CTA.

Bibliography

[1] CTA Consortium website: `http://www.cta-observatory.jp/` and `http://www.cta-observatory.org/`.

[2] Science with the Cherenkov Telescope Array, arXiv:1709.07997

[3] The Cherenkov Telescope Array potential for the study

Fig. 4. The high precision segmented mirrors for the Large Size Telescope (LST) developed by CTA-Japan in cooperation with Sanko Co.LTD. The mirror is made of a 60-mm thick aluminum honeycomb sandwiched by 3-mm thin glass on both sides. A surface protection coat consisting of the materials SiO_2 and HFO_2 is applied to enhance the reflectivity and to elongate the lifetime.

Fig. 5. The Large Size Telescope prototype (LST-1) constructed at Observatory de Roque de los Muchachos is now in the engineering run. The diameter of dish and mirror surface area are 23 m and 400 m^2.

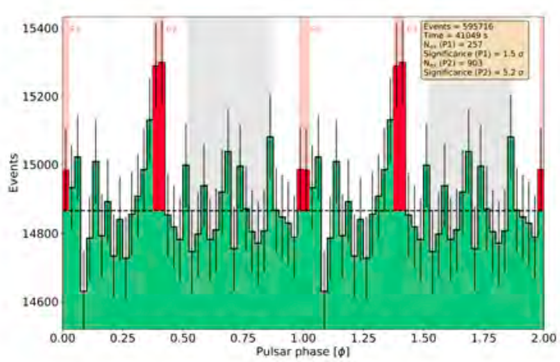

Fig. 6. Phase diagram of Crab Pulsar as measured by LST1. The pulsar is known to emit pulses of gamma rays during phases P1 and P2. The energy threshold in this observation is estimated about 40-50 GeV.

Fig. 7. MAGIC Stereo System with two Cherenkov telescopes of 17 m diameters, so far achieved the threshold energy of 25 GeV with the sum trigger. It locates near the mountain top of the Roque de los Muchachos on the Canary Island of La Palma. Two telescopes are located with the distance of 85 m.

of young supernova remnants, Astropart. Phys. 62 (2015) 152-164.

[4] Introducing the CTA concept, The CTA Consortium, Astropart. Phys. 43 (2013) 3-18.

[5] Gamma-ray burst science in the era of the Cherenkov Telescope Array, S. Inoue et al., Astropart. Phys. 43 (2013) 252-275.

[6] Design Concepts for The Cherenkov Telescope Array, The CTA Consortium, Exper. Astron. 32 (2011) 193-316.

[7] Status of Very High Energy Gamma Ray Astronomy and Future Prospects, M. Teshima, The Astronomical Herald, 104 (2011) 333-342.

[8] Design Study of a CTA Large Size Telescope, Proc. of ICRC2012 at Beijing China, M. Teshima, arXiv:1111.2183.

[9] Introducing the CTA Concept, B. Acharya et al., Astroparticle Physics, 34 (2013) 3.

[10] MAGIC Collaboration website: `http://magic.mppmu.mpg.de/`.

MAGIC

The MAGIC Collaboration has built in 2004 a first large atmospheric imaging Cherenkov telescope, MAGIC-I, with a mirror surface of 236 m^2 and equipped with photomultiplier tubes of optimal efficiency. In 2009, a second telescope of essentially the same characteristics was added; MAGIC-II was installed at a distance of 85 m from MAGIC-I. With the accent of these instruments on large mirror surface and best light collection, cosmic gamma-rays at an energy threshold lower than any existing or planned terrestrial gamma-ray telescope have become accessible. So far achieved has been a threshold of 25 GeV. The Japanese group has joined the MAGIC collaboration since 2010, and contributed to the operation, observations and data analyses. The MAGIC telescopes are upgraded with new cameras, electronics and partially new mirrors in 2012, and are now operated with an unprecedented sensitivity by an international collaboration of about 165 scientists from 24 institutes and consortia from 12 countries.

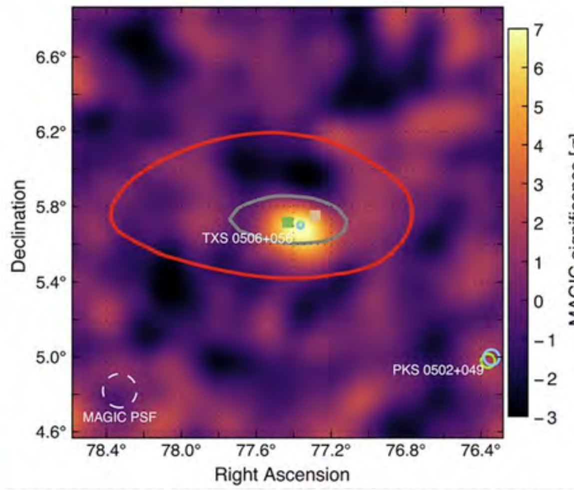

Fig. 8. Sky position of IceCube-170922A in the equatorial coordinate with contour of 50% and 90% confidence level overlaying the gamma-ray colour contour map observed by MAGIC (7 sigma in the peak) [5].

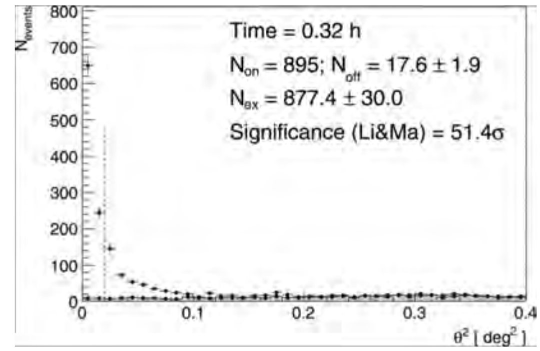

Fig. 9. Significance of the γ-ray signal, 51 sigma, between T_0 + 62 s and T_0 + 1,227 s for GRB 190114C [2].

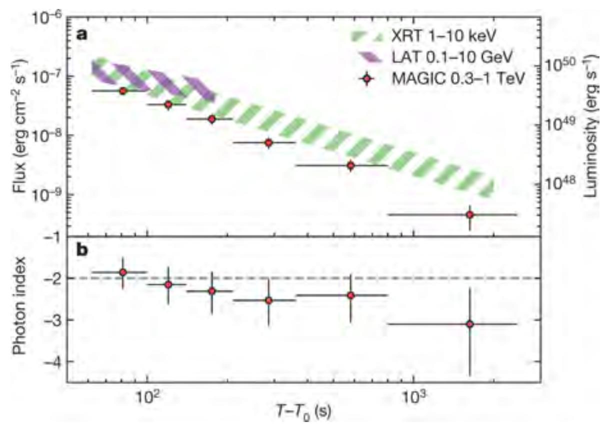

Fig. 10. Light curves in the kiloelectronvolt, gigaelectronvolt and teraelectronvolt bands, and spectral evolution in the teraelectronvolt band for GRB 190114C [2].

The recent highlights from MAGIC are, 1) The first detection of the Gamma Ray Burst GRB 190114C with the ground-based gamma-ray telescope MAGIC [1], [2], [3], 2) Observation of sub-TeV gamma rays from the IceCube 170922A [4], [5] (Fig. 8), 3) the successful observation of pulsed gamma ray signal from the Crab pulsar up to TeV regime [6], 4) the discoveries of the most distant blazers 3S 0218+35 with the redshift of 0.944 and PKS 1441+25 with the redshift of 0.939 [7], 5) the observation of the very fast flare of 1-min time scale from the blazar inside Perseus cluster, IC310 [8]. These results brought new questions on the pulsar emission mechanism, the EBL energy density, and gamma ray emission mechanism from the supermassive blackholes or vicinity of them.

In January 2019, the MAGIC telescopes, for the first time, observed the TeV Gamma-Ray Burst GRB 190114C with the redshift of 0.42 [1],[2], [3]. MAGIC telescopes started observing the GRB at T_0 + 57 seconds after receiving the alert from the SWIFT-BAT satellite. The observation shows the 100 times higher flux of gamma rays than the Crab Nebula at T_0 + 80 sec, and the resultant statistical significance of gamma-rays was more than 50 sigma (Fig. 9). The highest-energy photon reaches above 1 TeV, and the observed spectrum after the EBL de-absorption did not show any roll-off feature in the energy spectrum [2]. This observation will require the new gamma-ray emission mechanism in the GRB to explain the TeV emission, possibly the inverse Compton emission. The light curve shows the power-law decay $t^{-1.6}$, which is surprisingly parallel to the X-ray lightcurve measured by XRT [2] (Fig. 10). The observation shows spectacular features in the energy spectrum and lightcurve. It is worth mentioning that the energetics of the TeV emission is comparable with that of the X-ray emission. The two bump structure in the spectral energy distribution can be fit consistently with the Synchroton Self-Compton model as shown in Fig. 11 [3].

In fiscal year 2020, there were public relation activities related to GRB 190114C, such as a TV program in NHK broadcasted in May 2020. MAGIC published a followup paper about GRB 190114C, a constraint on Lorentz invariance violation using the data of the GRB [9]. After the GRB 190114C related works were settled, we came back to other works stalled. One of such works is a hint of detection from GRB 160821B. The GRB is a short GRB at $z = 0.162$, which is the closest GRB observed by MAGIC (before 190829A), and it has a kilonova emission reported in 2019. After informed of the report, we have revised the modeling of the TeV flux suggested by MAGIC data, revealing that the Synchrotron Self-Compton model does not work well for this GRB [10]. This result shows an importance of continuing GRB observations to increase the number of detections both for long and short GRB types.

Bibliography

[1] The first detection of a GRB at sub-TeV energies; MAGIC detects the GRB190114C., ATEL # 12390.

[2] Teraelectronvolt emission from the γ-ray burst GRB 190114C, Nature 575, 455 (2019).

[3] Observation of inverse Compton emission from a long γ-ray burst; MAGIC collaboration et al. Nature 575, 459 (2019).

[4] First-time detection of VHE gamma rays by MAGIC from a direction consistent with the recent EHE neutrino

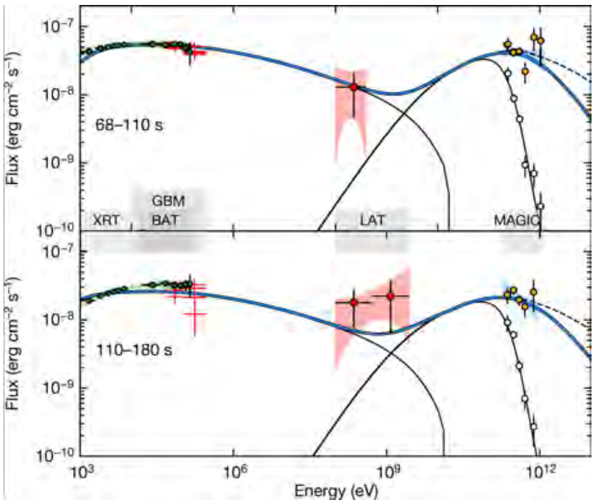

Fig. 11. Modelling of the broadband spectra in the time intervals 68-110 s and 110-180 s for GRB 190114C [3].

event IceCube-170922A, ATel #10817.

[5] Multimessenger observations of a flaring blazar coincident with high-energy neutrino IceCube-170922A, Science 12 July 2018, Science.eaat1378.

[6] Phase-resolved energy spectra of the Crab pulsar in the range of 50-400 GeV measured with the MAGIC telescopes, the MAGIC Collaboration, Aleksić et al. A&A 540 (2012) A69.

[7] Discovery of Very High Energy Gamma-Ray Emission from the distant FSRQ PKS 1441+25 with the MAGIC telescopes, ATEL # 7416.

[8] Black hole lightning due to particle acceleration at subhorizon scales, the MAGIC collaboration, Science 346 (2014) 1080-1084.

[9] Bounds on Lorentz Invariance Violation from MAGIC Observation of GRB 190114C, the MAGIC collaboration, PRL 125 (2020) 021301.

[10] MAGIC Observations of the Nearby Short Gamma-Ray Burst GRB 160821B, the MAGIC collaboration, ApJ 908 (2020) 90.

Other Activities

As a test bench for domestic R & D activities of future ground-based gamma-ray observatory projects, an old atmospheric Cherenkov telescope of 3 m diameter was repaired and then placed at the Akeno Observatory in November 2010. This telescope shown in Figure 12 (Akeno telescope, hereafter) is currently the only atmospheric Cherenkov telescope located in Japan [1]. We have developed an R & D imaging camera system with the Akeno telescope since 2009, the purpose of which is to make a battery-powered data acquisition system for a future mobile imaging atmospheric Cherenkov telescope array [2]. The system consists of 32 PMTs, of which detected Cherenkov light signals are read out by only four GHz-sampling analog memory ASICs.

Fig. 12. Akeno atmospheric Cherenkov telescope of 3 m diameter, located in the Akeno Observatory.

We have also been planning to observe the optical Crab pulsar utilizing some central PMTs of the above system. The purpose of this study is to investigate the efficient acceleration site of the Crab Nebula in a microscopic way with simultaneous observations of radio and optical pulses passing through the nebula plasma. The first observations were performed in January 2020 after developing a dedicated pulse counting system, but they were quite affected by clouds [3]. We therefore tried again in the fiscal year 2020 and could this time accumulate about 10 hr data with a good condition. These data are still under analysis.

Bibliography

[1] M. Ohishi et al., Proc. of 33rd Internat. Cosmic Ray Conf. (Rio de Janeiro), 587 (2013).

[2] T. Yoshikoshi et al., Proc. of 34th Internat. Cosmic Ray Conf. (The Hague), 887 (2015).

[3] S. Takeoka, Master's thesis, Ritsumeikan University (2020).

TA: Telescope Array Experiment

Spokespersons (S. Ogio[1], C.C.H. Jui[2])

1 : Graduate School of Science, Osaka City University
2 : Dept. of Physics and Astronomy, University of Utah

Collaborating Institutions:

Chiba Univ., Chiba, Japan; Chubu Univ., Kasugai, Japan; ERI,

Univ. of Tokyo, Tokyo, Japan; Ewha W. Univ., Seoul, Korea; Hiroshima City Univ., Hiroshima, Japan; Hanyang Univ., Seoul, Korea; ICRR, Univ. of Tokyo, Kashiwa, Japan; INR, Moscow, Russia; Inst. of Phys, Czech Acad. of Sci., Prague, Czech Republic; IPMU, Univ. of Tokyo, Kashiwa, Japan; Kanagawa Univ., Yokohama, Japan; KEK/IPNS, Tsukuba, Japan; Kochi Univ., Kochi, Japan; Kyoto Univ., Kyoto, Japan; Loyola Univ., Chicago, USA; Moscow M.V. Lomonosov State University, Moscow, Russia; NICT, Tokyo, Japan; QST, Chiba, Japan; Osaka Electro-Comm. Univ., Neyagawa, Japan; Osaka City Univ., Osaka, Japan; RIKEN, Wako, Japan; Ritsumeikan Univ., Kusatsu, Japan; Saitama Univ., Saitama, Japan; Shibaura IT, Tokyo, Japan; Shinshu Univ., Nagano, Japan; SKKU, Suwon, Korea; Tokyo City Univ., Tokyo, Japan; Tokyo Inst. of Tech., Tokyo, Japan; Tokyo Univ. of Science, Noda, Japan; ULB, Brussels, Belgium; UNIST, Ulsan, Korea; Univ. of Nova Gorica, Nova Gorica, Slovenia; Univ. of Utah, Salt Lake City, USA; Univ. of Yamanashi, Kofu, Japan; Yonsei Univ., Seoul, Korea

Introduction

The Telescope Array (TA) is the largest Ultra-High Energy Cosmic Ray (UHECR) observatory in the northern hemisphere. The main aim of TA is to explore the origin and nature of UHECRs by measuring the energy spectrum, arrival direction distribution and mass composition. The TA collaboration consists of approximately 130 researchers from USA, Russia, Korea, Belgium, Czech, Slovenia and Japan.

The TA detector consists of a surface array of 507 plastic scintillator detectors (SD) and three stations of fluorescence detectors (FD). It is located in the desert, approximately 200 km south of Salt Lake City in Utah in USA. The SDs were deployed on a square grid with 1.2-km spacing, and the SD array covers an area of approximately 700 km^2. Each SD has two layers of 1.2-cm-thick scintillator with an area of 3 m^2. The full operation of SDs started in March 2008. The duty cycle is approximately 95% on average. One northern FD station at the MD site uses 14 refurbished HiRes telescopes. Two southern FD stations at the BR and LR sites were built newly each with 12 telescopes. The MD FD views 3° - 31° and the BR and LR FDs view 3° - 33° above horizon. All three FD stations started the observation in November 2007, and have duty cycles of approximately 10%.

The TA Low-Energy extension (TALE) enables detailed studies of the energy spectrum and composition from $\sim 10^{16}$ eV upwards. The main aim of TALE is to clarify the expected transition from galactic cosmic rays to extragalactic cosmic rays and the comparison of the data with Monte Carlo (MC) simulation that takes into account the results of the latest LHC experiments. The TALE detector is located north of the TA site (MD site). This FD station consists of 10 refurbished HiRes telescopes. The TALE FD views 31° - 59° in elevation angle. The TALE detectors are located at the northern corner of the TA detectors. The TALE FD operation was commenced in the spring of 2013. The TALE SD array consists of 80 plastic scintillation counters (40 SDs at 400-meter spacing and 40 SDs at 600-meter spacing), which are almost the same as the TA SDs and the same as the TAx4 SDs. A new wireless LAN

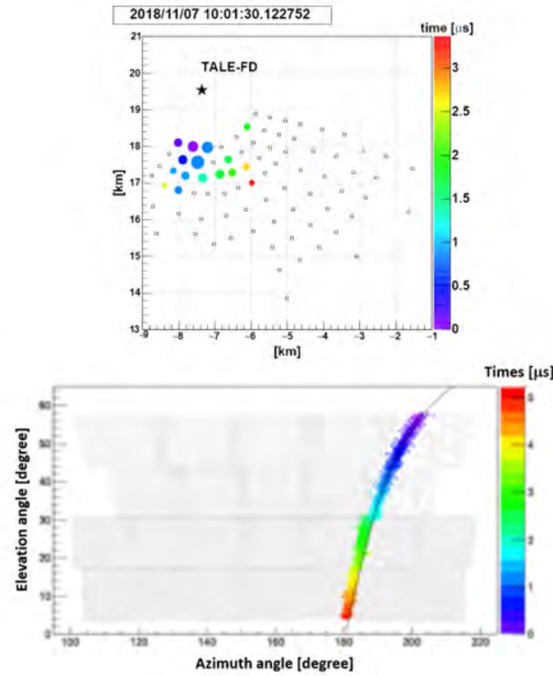

Fig. 13. An example of a TALE hybrid event. (a) The SD footprint. The size and color of each SD show the relative signal strength and arrival time. (b) FD event display. For each PMT, the circle size is proportional to the amount of collected light. The circle color represents the relative tube time.

module is used for the TALE and TAx4 SDs because the one used in TA was out of production. PMTs with quantum efficiency larger than those of TA SDs are used for the TALE and TAx4 SDs. The wireless communication protocol was changed from the transmission control protocol (TCP) to the user datagram protocol (UDP), permitting us to use the new wireless LAN module. The layout of the wavelength shifting (WLS) fibers was optimized and the total length of the WLS fibers is reduced by 67% for the cost reduction by keeping the number of photoelectrons for 1 MIP peak. The TALE SD array was completed in February 2018 and is in stable operation. The mode energy of TALE hybrid events is $10^{16.3}$ eV. There is a plan to install additional 50 SDs with 200-meter spacing near the TALE FD station to observe even lower-energy cosmic rays, for which the mode energy is $10^{15.5}$ eV. The TALE statuses were reported in [1]. Fig. 13 is an example of a TALE hybrid event that was detected simultaneously with FD and SDs.

The Non-Imaging CHErenkov (NICHE) array is planned to have graded spacings, ranging from 100 meters to 400 meters. The NICHE Prototype Array consists of 14 counters each with a 3-inch PMT that collects non-imaging air-Cherenkov light, which started stable observation in May 2018 [3]. The array is situated 600-1000 m from the TALE FD. NICHE and TALE work together as a hybrid detector for cosmic rays with energies in the range between 10^{15} eV and $10^{18.5}$ eV.

TA found evidence for intermediate-scale anisotropy of arrival directions of cosmic rays with greater than 5.7×10^{19} eV. With enhanced statistics, it is expected to observe the structure of the hotspot along with other possible excesses and point sources along with the correlations with extreme phenomena

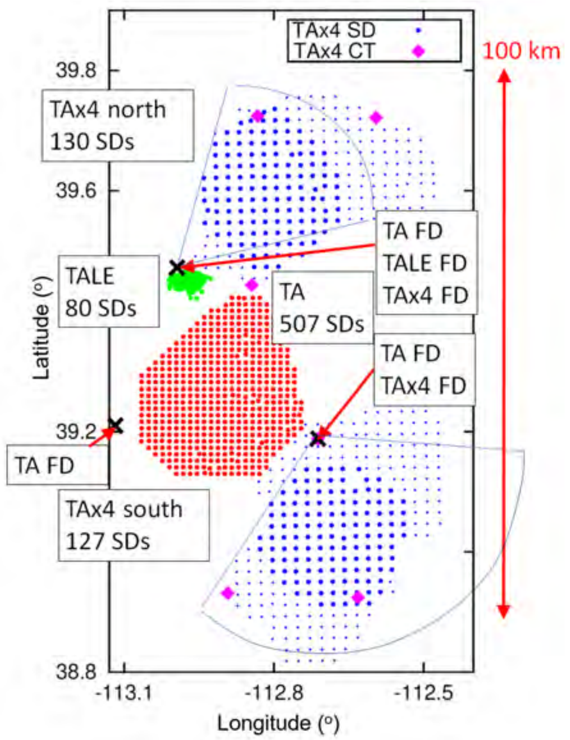

Fig. 14. The layout of the proposed TAx4. The array of 507 SDs (red filled circles on the left) is the original TA SD array. There are three TA FD stations (MD to the north, LR to the west, and BRM to the east of the TA SD array) with black cross symbols. The array of surface detectors (green) to the north of the TA SD array is the TALE SD array. The additional TAx4 500 surface detectors (blue) are located in separate lobes on the northeast and southeast sides of the TA SD array. The 257 large blue filled circles denote deployed SDs, whereas remaining blue dots denote SDs to be deployed. Additional two FD stations with refurbished HiRes telescopes for the TAx4 are located at the MD and BRM FD sites and view to the northeast and southeast as denoted each by the blue frame of the fan. Purple diamond symbols denote TAx4 communications towers.

in the nearby universe. TA proposed to quadruple the effective area of the TA SD aperture including the existing TA SD array (TAx4) by installing additional 500 counters of the current TALE SD design on a square grid with wider, 2.08-km spacing between each. The layout of TAx4 is shown in Fig. 14 together with TALE.

The 257 SDs were deployed in February and March 2019. The total area of the SD array including the original TA array has been increased by a factor of 2.5. The new SD array started the data acquisition in April 2019. Since the new SD array is divided into two lobes, two FD stations are required to overlook each lobe in order to increase the number of hybrid events for the measurement of X_{max} and to confirm the energy scale. These FD stations consist of refurbished HiRes telescopes: four telescopes at the MD site and eight telescopes at the BR site. The TAx4 FD station at the northern site was constructed and started the stable observation in June 2018. The TAx4 FD at the southern site was constructed and started the observation in 2019. The recent status of TAx4 was reported in [4]. Fig. 15(a), (b) and (c) show the footprint, time fit and lateral fit result for a typical TAx4 SD event, respectively.

Due to the pandemic of COVID-19, we suspended all the

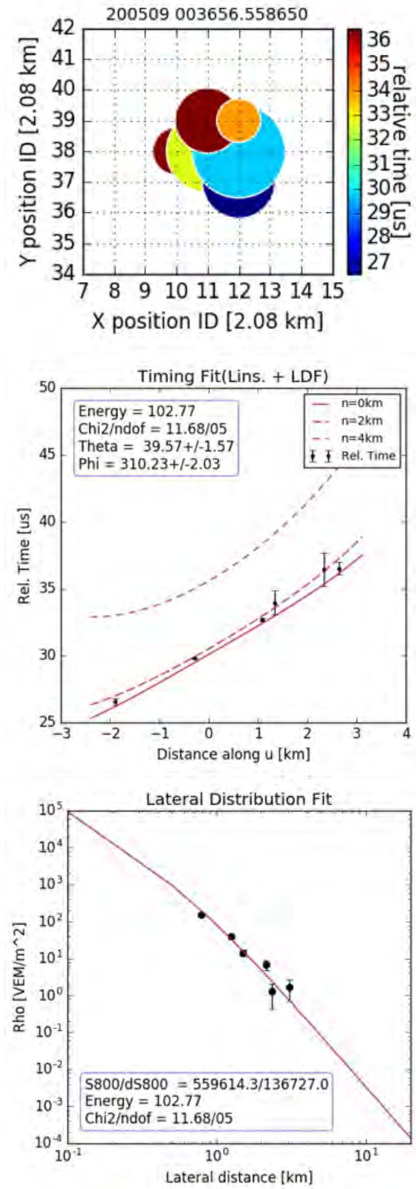

Fig. 15. A typical TAx4 SD event. (a) The footprint of an observed air-shower event.The horizontal and vertical axes denote the SD position IDs in the east-west and north-south directions, respectively. Circle centers correspond to the SD positions. Circle areas are proportional to the logarithmic sizes of signals. Colors denote arrival times at the detectors. (b) SD time fit. The SD times are plotted versus distance along the shower axis on the ground (u-axis). Solid, long-dash and dash lines represent the fit expectation times for SDs that would lie directly on the u-axis, 2 km and 4 km off the u-axis, respectively. (c) Lateral distribution fit. The SD charge densities are plotted versus the lateral distance from the shower axis. Solid line represents the fit curve.

FD operations and the dispatch of researchers from Japan in March of 2020. The TA MD FD and TAx4 MD FD resumed their observations in June of 2020, The TAx4 BR FD started the stable operation in July of 2020. The TALE FD resumed the operation in December 2020. One shift person stays at the TA MD FD and other FDs are operated remotely. The array of SDs are operated because each SD is self-sustaining with solar system for power supply and wireless LAN for communication. The maintenance on site are performed by the persons in

Utah such as a local employee, the staffs and students of the University of Utah and designated vendors.

The results from TA published in refereed journal papers in Japanese fiscal year 2020 are reported below.

Composition

TALE monocular FD $X_{\rm max}$

Using Cherenkov light signal and air fluorescence light from extensive air showers, the TALE FD measures the properties such as energy spectrum and $X_{\rm max}$ (atmospheric depth of shower maximum) in the energy range of $10^{15.3}$ (2 PeV) - $10^{18.3}$ (2 EeV). The TALE FD data collected over a period of $\sim$4 years between June 2014 and November 2018 is used to measure $X_{\rm max}$ of cosmic-ray air showers [5]. The total effective time is approximately 2700 hours. The $X_{\rm max}$ elongation rate of the data is shown with those of four different MC primaries (H, He, N (CNO) and Fe) in Fig. 16a. The result of a broken fit is shown in Fig. 16b. The break in the $X_{\rm max}$ elongation rate is seen approximately at $10^{17.2}$ eV, which is likely correlated with the observed break ($10^{17.04\pm0.03}$ eV) in the TALE energy spectrum [6]. The reconstructed TALE average $X_{\rm max}$ data are smoothly connected to those of TA [7].

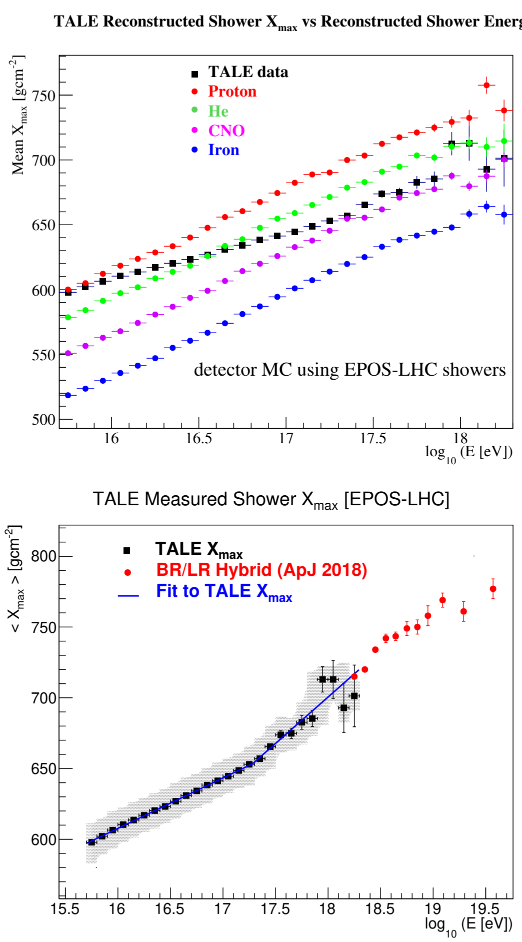

Fig. 16. a) The average $X_{\rm max}$ values of the reconstructed TALE FD events (black) as a function of shower energy together with those of four MC primaries (proton (red), helium (green), nitrogen (violet) and iron (blue)). b) The average $X_{\rm max}$ of the TALE FD events (black) as a function of shower energy together with that of the TA hybrid events (red). A broken line fit to the average TALE $X_{\rm max}$ as a function of energy is shown.

Proton-air cross section from TA

UHECRs provide the highest energy sources in the universe to measure the proton-air cross section [8]. It is assumed that the tail of the $X_{\rm max}$ distribution is dominated by proton air showers. It allows the measurement of the inelastic proton-air cross section. Using the data collected by the TA BR and LR FDs with SDs in hybrid mode for nearly nine years [7], $\sigma^{\rm inel}_{\rm p-air}$ is measured to be 520.1 $\pm$ 35.8 (stat) $^{+25.3}_{-42.9}$ (sys) mb at $\sqrt{s} = 73$ TeV. The total proton-proton cross section is deduced from Glauber formalism and is obtained to be $\sigma^{\rm tot}_{\rm pp}$ = 139.4 $^{+23.4}_{-21.3}$ (stat) $^{+15.7}_{-25.4}$ (sys) mb. The result is shown in Fig. 17 in comparison with previously reported results by UHECR experiments. The results from high-energy models and UHECR experiments continue to show that the cross section increases with increasing energy.

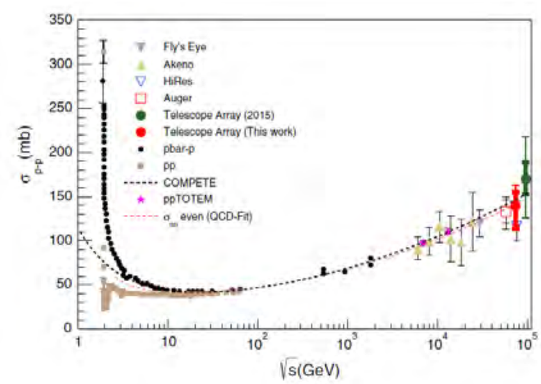

Fig. 17. A compilation of the proton-proton cross section as a function of the center of mass energy, including the statistical (thin) and systematical (thick) error bars, together with previous results by UHECR experiments along with the recent result from LHC by TOTEM at $\sqrt{s}$ - 7 and 13 TeV. The dashed red curve is the BHS fit, and the dashed black curve is the fit by the COMPETE Collaboration.

Search for UHE neutrinos

TA presented the search for neutrinos using the first nine years of the TA SD data [9], employing multivariate analysis with the classifier based on the Boosted Decision Tree (BDT) classifier [10]. Proton-neutrino classifier is built upon 16 observables related to the properties of the shower front and lateral distirubution function. There are no neutrino candidates found in the data set in the energy range $E > 10^{18.0}$ eV. The 90% confidence level upper limit on the single flavor diffuse neutrino flux for $E > 10^{18}$ eV is 1.85×10^{-6} GeV cm^{-2} s^{-1} sr^{-1}).

Arrival Directions of UHECRs

Supergalactic structure of energy-angle correlations for UHECRs

UHECRs with a wide energy range from one source is expected to form a multiplet (arrival directions correlated with energy) in a wedge by deflections of coherent and random magnetic fields as shown in Fig. 18. TA tested the hypothesis of a large-scale supergalactic cosmic-ray multiplet structure for UHECR energies greater than 10^{19} eV as follows and published the result in [11].

The Kendall's τ ranked correlation is described as

$$\tau = \frac{2}{n(n-1)} \sum_{j<k} \text{sign}\left[\frac{x_j - x_k}{y_j - y_k}\right]. \quad (5)$$

Here, x and y are energy and angular distance respectively, and n is the number of cosmic-ray events. A negative correlation is consistent with the expectation that the deflection by magnetic field for cosmic-ray events increases as energy decreases.The schematic diagram of the wedge of UHECR drift and diffusion deflected by coherent and random magnetic fields is shown in Fig. 18.

The resulting energy-angle correlations for seven years of the TA SD data is shown in Fig. 19a. The mean τ correlation is shown inside equal solid angle bins parallel to the supergalactic plane in Fig. 19b. The resultant parabolic fit curvature is a = (2.45 ± 0.15)× 10^{-4} with a minimum at supergalactic latitude (SGB) of $-0.5°$. The seven year data post-trial significance of this supergalactic structure of multiplets appearing by chance, on an isotropic sky, is found to be 4.2σ. For 10 years of data, the parabolic curvature fit to the mean τ correlation for SGB is a = (1.60 ± 0.09)× 10^{-4} with a minimum at 1.1° SGB. The 10 years of data post-trial significance is 4.1σ.

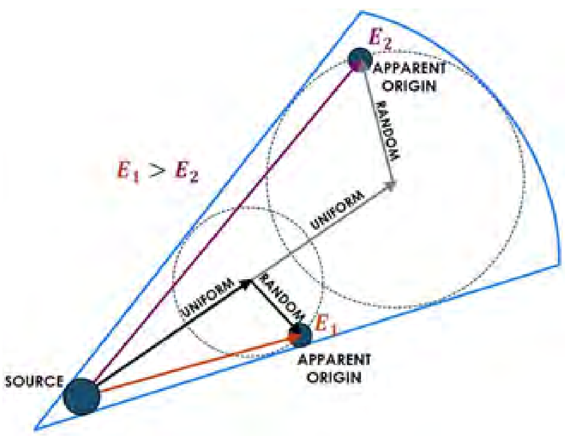

Fig. 18. Schematic diagram showing the wedge of drift and diffusion of UHECRs deflected by coherent and random magnetic fields. A purpule line represents the spherical arc of an event with lower energy (E_2), whereas a red line represents an event with higher energy (E_1). Dashed circles denote the rms deflections by random magnetic fields.

Search for Large-scale Anisotropy on UHECR Arrival Directions

Motivated by the detection of a significant dipole structure in the arrival directions of UHECRs with energies greater than 8 EeV reported by Auger, we search for a large-scale anisotropy of cosmic rays above 8.8 EeV using 11 years of TA data [12]. A dipole structure in a projection of the R.A. is fitted with an amplitude of 3.3% ± 1.9% and a phase of 131° ± 33°. The 99% confidence-level upper limit on the amplitude is 7.3%. The fitted result for TA is compatible with both an isotropic distribution and the dipole structure reported by Auger.

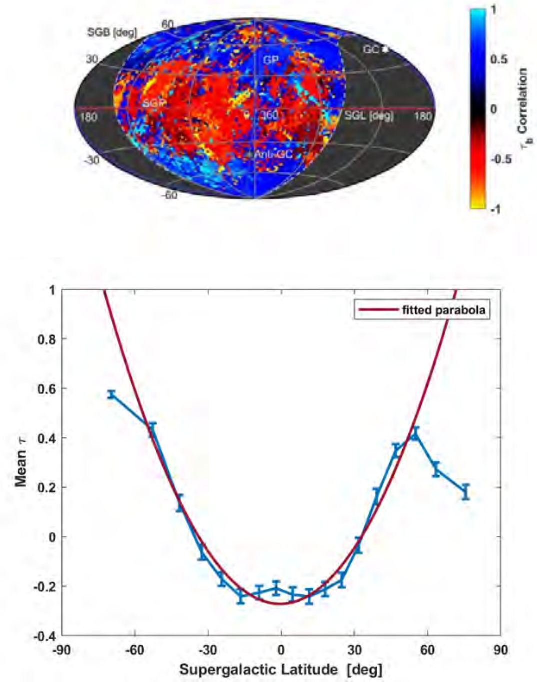

Fig. 19. Preliminary result of seven year data. (a) Hammer-Aitoff projection of the correlation strength τ for all grid points in the supergalactic coordinates. Negative correlations expected for magnetic deflections are apparent around the supergalactic plane. Red and blue solid curves indicate the supergalactic plane (SGP) and galactic plane (GP), respectively. Hexagrams indicate the galactic center (GC) in white and antigalactic center (nti-GC) in gray. (b) Mean τ inside equal solid angle binds of supergalactic latitude (SGB).

Interdisciplinary research

Observations of the Origin of Downward Terrestrial Gamma-Ray Flashes

We report the first close, high-resolutioon observations of downward-directed terrestrial gamma-ray flashes (TGFs) detected by the TA detector in conjunction with broadband VHF interferometer and fast electric field change measurements of the parent discharge [13].

Other analyses

Other analyses are ongoing towards ICRC2021 as follows: For TA,

- TA hybrid analysis for the measurement of energy spectrum and $X_{\max}$ using data recorded by hybrid trigger that helps to perform SD data collection when an FD detects a shower event especially below $10^{18.5}$ eV, where the SD self-trigger efficiency decreases rapidly
- Update on cosmic-ray mass composition with the TA SD data, implementing the Boosted Decision Trees (BDT) [10] techniques that are trained using a set of compostion-sensitive observables for Monte-Carlo sets of iron nuclei as "signal" and protons as "background"
- Mass composition anisotropy with the TA SD data, implementing the above-mentioned BDT techniques.

- TA energy spectrum measurement and its declination dependence for the break point energies around the highest energy region with detailed systematic study
- Update on the anisotropy of the spectrum of cosmic rays above 10^{19} eV with respect to super-galactic plane (SGP) (for the region within $\pm$ 30° from SGP and the rest)
- Variations in cosmic-ray shower intensity using the TA SDs during thunderstorms and implications for large-scale electric field changes using CORSIKA MC simulations
- Combined fit of an astrophysical model of UHECR sources to the cosmic-ray spectrum using the TA SD data and the composition using the TA FD data in stereo mode
- Update on a cluster of UHECR events above 5.7×10^{19} eV, called the TA hotspot, and a search for a new UHECR excess
- Study on the atmospheric transparency of TA FD observation by the CLF (Central Laser Facility), especially for annual fluctuations in atmospheric transparency at the TA site
- FOV (Field Of View) direction and spot size calibration of TA FD using UV-LED light source mounted on the UAV (Unmanned Aerial Vehicle) with an accuracy of 0.02°

For lower energy cosmic rays,

- Cosmic-ray energy spectrum in the 2nd knee region measured with the TALE SDs
- Cosmic-ray composition in the 2nd knee region measured with the TALE hybrid detector
- Energy spectrum and X_{max} of cosmic rays above the knee region measured with the NICHE Prototype Array

For TAx4,

- Reconstruction of cosmic-ray air-shower events measured by the surface detectors of the TAx4 experiment, the comparison between data and MC simulation, and the measurement of the energy spectrum
- The TAx4 FD performance, data/MC comparisons and the monocular energy spectrum
- TAx4 hybrid trigger data analysis towards the calibration of cosmic-ray energy firstly measured with the TAx4 SDs and the measurement of X_{max} especially below (a few)$\times10^{19}$ eV, where the SD self-trigger efficiency decreases rapidly

As working groups (WG) with other collaborations,

- Energy spectrum WG from Auger and TA
- Anisotropy of UHECR arrival directions from Auger and TA: a search for correlation of UHECR arrival directions with nearby galaxies, and large scale anisotropy
- Combined analysis of the measurements of muons in air showers from nine experiments

Future plans

Test observations with the prototypes of the next-generation UHECR detectors at the TA BR site such as EUSO-TA [14, 15] for the JEM-EUSO mission [16] in space, and FAST [17] and CRAFFT [18] as low-cost wide-area ground detectors were suspended in 2020 due to COVID-19. Discussions are also underway for the next-generation observatories, to measure the properties of the highest-energy cosmic rays with unprecedented accuracy in the future such as TA2 and GCOS (The Global Cosmic Ray Observatory).

Summary

The TA detector consists of 507 SDs and three FD stations. It has started the operation in 2008 and has been operated stably. The TALE FD has commenced in 2013. The TALE SD array for cosmic rays with energies down to $\sim10^{16}$ eV was completed in 2018 and is in stable operation. The NICHE Prototype Array with 14 counters is in operation. The construction of the SD array near the TALE FD is also planned to observe cosmic rays with energies down to $\sim10^{15}$ eV. In 2019, 257 of the planned 500 TAx4 SDs have been deployed and are in operation. Of the two TAx4 FDs, one was operational in 2018 and the other in 2019.

The result of TALE monocular FD X_{max} was published in [5]. Its elongation rate shows the break at $10^{17.2}$ eV, which is likely correlated with the break ($10^{17.04}$ eV) in the TALE energy spectrum [6]. The TALE X_{max} result is smoothly connected to the result of X_{max} from the TA BR/LR hybrid data [7].

An update on proton-air cross section measurement using the TA BR/LR hybrid data for nearly nine years was published [8]. The result from UHECR experiments continues to show a rising cross section with energy.

TA searched for neutrinos using the first nine years of the TA SD data and obtained the upper limit of neutrino flux for $E > 10^{18}$ eV [9].

Evidence for supergalactic structure of energy-angle correlations for cosmi rays above 10^{19} eV was found with its post-trial significance of $\sim4\sigma$.

Motivated by a dipole analysis for UHECRs above 8 EeV reported by Auger, we search for a large-scale anisotropy for UHECRs above 8.8 EeV using 11 years of TA data [12]. A dipole structure in a projection of the R.A. is fitted with an amplitude of 3.3% $\pm$ 1.9%. and a phase of 131° $\pm$ 33°. The TA result is compatible with both an isotropic distribution and the dipole structure reported by Auger.

As an interdisciplinary research, the first close, high-resolution observations of downward-directed TGFs detected by the TA observatory was reported in conjuncton with VHF interferometer and fast electric field change measurements of the parent discharge [13].

Discussions for the next-generation observatory to measure the properties of the highest-energy cosmic rays with unprecedented precision in the future are underway such as TA2 and GCOS (The Global Cosmic Ray Observatory)

Bibliography

[1] S. Ogio *et al.*, "TA experiment 355 : General report on the TALE experiment 6", 2021 Annual JPS Meeting; K. Sato *et al.*, "TA experiment 357 : Cosmic ray energy spectrum in the 2nd knee region measured by the TALE-SD array", 2021 Annual JPS Meeting; K. Fujita *et al.*, " TA experiment 356: Data analysis observed with TALE experiment hybrid detector", 2021 Annual JPS Meeting.

[2] D. Bergman *et al.*, "First Results from NICHE and the NICHE-TALE Hybrid Detector", Pos(ICRC2019)189.

[3] R. Tsuda *et al.*, "TA experiment 363: Reconstruction of air shower events observed with j-NICH by DNN", 2021 Annual JPS Meeting.

[4] H. Sagawa *et al.*, "TA experiment 352 : Report on the TAx4 experiment 8", 2021 Annual JPS Meeting; K. Fujisue *et al.*, "TA experiment 353 : Monte Carlo simulation for TAx4-SD array analysis", 2021 Annual JPS Meeting; S.W. Kim *et al.*, "TA experiment 354: Analysis of TAx4 hybrid trigger and events", 2021 Annual JPS Meeting.

[5] R.U. Abbsi *et al.*, "The Cosmic-Ray Composition between 2 PeV and 2 EeV Observed with the TALE Detector in Monocular Mode", Astrophysical Journal, 909:178 (17pp), 2021.

[6] R.U. Abbasi *et al.*, "Cosmic-Ray Energy Spectrum between 2 PeV and 2 EeV Observed with the TALE detector in monocular mode", Astrophysical Journal 865:74 (18pp), 2018; arXiv:1803.01288 [astro-ph.HE].

[7] R.U. Abbasi *et al.*, "Depth of Ultra High Energy Cosmic Ray Induced Air Shower Maxima Measured by the Telescope Array Black Rock and Long Ridge FADC Fluorescence Detectors and Surface Array in Hybrid Mode", Astrophysical Journal 858:76 (27pp), 2018.

[8] R.U. Abbasi *et al.*,"Measurement of the proton-air cross section with Telescope Array's Black Rock Mesa and Long Ridge fluorescence detectors, and surface array in hybrid mode", Physical Review D 102, 062004 (13pp), 2020.

[9] R.U Abbasi *et al.*, "Search for Ultra-High-Energy Neutrinos with the Telescope Array Surface Detector", Journal of Experimental and Theoretical Physics, 131, 255-264, 2020.

[10] R.E. Schapire, "The strength of weak learnability", Mach. Learn. 5 (July, 1990) 197-227.

[11] R.U. Abbasi *et al.*, "Evidence for a Supergalactic Structure of Magnetic Deflection Multiplets of Ultra-high-energy Cosmic Rays", Astrophysical Journal 899:86 (13pp), 2020.

[12] R.U. Abbasi *et al.*, "Search for Large-scale Anisotropy on Arrival Directions of Ultra-high-energy Cosmic Rays Observed with the Telescope Array Experiment", Astrophysical Journal 898:L28 (5pp), 2020.

[13] J.W. Belz *et al.*, "Observations of the Origin of Downward Terrestrial Gamma-Ray Flashes", Journal of Geophysical Research: Atmospheres, 125, 1-26, 2020.

[14] L.W. Piotrowski *et al.*, "Results and status of the EUSO-TA detector", Pos(ICRC2019)388.

[15] F. Bisconti *et al.*, "EUSO-TA ground based fluorescence detector: analysis of the detected events", Pos(ICRC2019)197.

[16] M. Bertaina "Search for Ultra High Energy Cosmic Rays from Space - The JEM-EUSO Program", Pos(ICRC2019)192.

[17] T. Fujii, "Observing ultra-high energy cosmic rays with prototypes of the Fluorescence detector Array of Single-pixel Telescopes (FAST) in both hemispheres", Pos(ICRC2019)259.

[18] Y. Tameda *et al.*, "The status and performance of Cosmic Ray Air Fluorescence Fresnel lens Telescope (CRAFFT) for the next generation UHECR obsevatory", Pos(ICRC2019)435.

Tibet ASγ Experiment

[Spokesperson: M. Takita]

ICRR, The Univ. of Tokyo, Kashiwa, Chiba 277-8582

1. Experiment

The Tibet air shower experiment has been successfully operated at Yangbajing (90°31′ E, 30°06′ N; 4300 m above sea level) in Tibet, China since 1990. It has continuously made a wide field-of-view (approximately 2 steradian) observation of cosmic rays and gamma rays in the northern sky.

The Tibet I array was constructed in 1990 and it was gradually upgraded to the Tibet II by 1994 which consisted of 185 fast-timing (FT) scintillation counters placed on a 15 m square grid covering 36,900 m^2, and 36 density (D) counters around the FT-counter array. Each counter has a plastic scintillator plate of 0.5 m^2 in area and 3 cm in thickness. All the FT counters are equipped with a fast-timing 2-inch-in-diameter photomultiplier tube (FT-PMT), and 52 out of 185 FT counters are also equipped with a wide dynamic range 1.5-inch-in-diameter PMT (D-PMT) by which we measure up to 500 particles which saturates FT-PMT output, and all the D-counters have a D-PMT. A 0.5 cm thick lead plate is put on the top of each counter in order to increase the counter sensitivity by

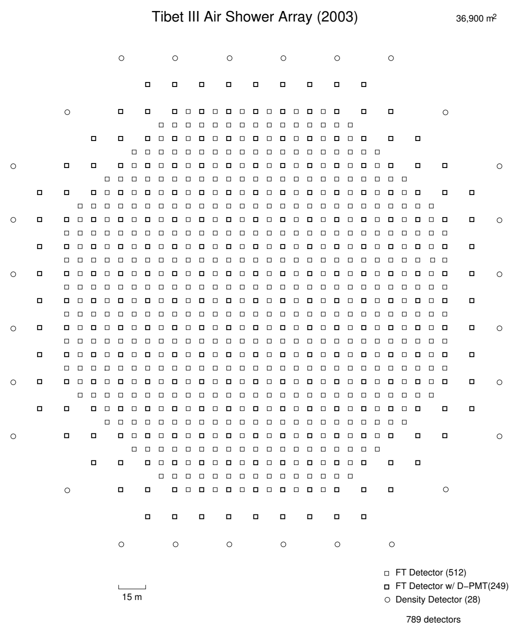

Fig. 1. Schematic view of Tibet III.

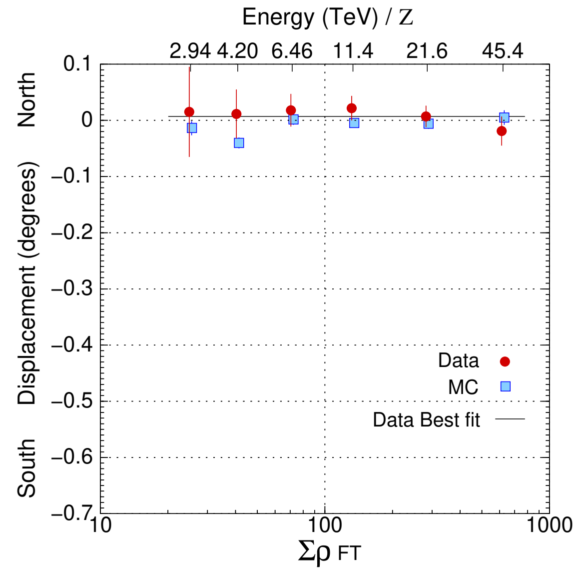

Fig. 2. From [1]. The Moon's shadow center displacement from the apparent position in the north-south direction as a function of energy, observed by Tibet III.

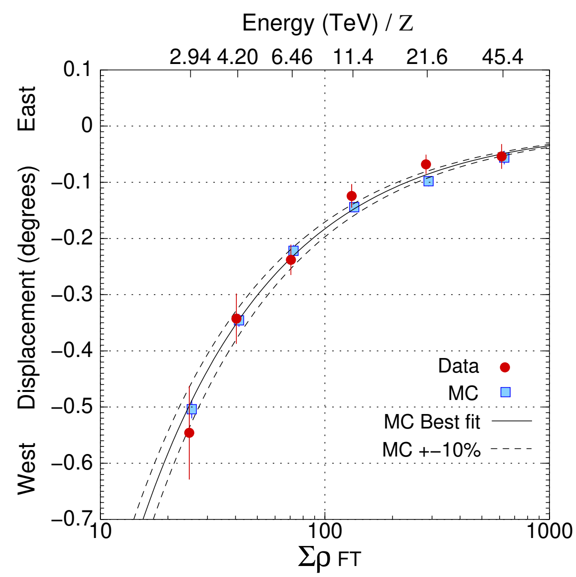

Fig. 3. From [1]. The Moon's shadow center displacement from the apparent position in the east-west direction as a function of energy, observed by Tibet III.

converting gamma rays into electron-positron pairs in an electromagnetic shower. The mode energy of the triggered events in Tibet II is 10 TeV.

In 1996, we added 77 FT counters with a 7.5 m lattice interval to a 5,200 m^2 area inside the northern part of the Tibet II array. We called this high-density array Tibet HD. The mode energy of the triggered events in Tibet HD is a few TeV.

In the late fall of 1999, the array was further upgraded by adding 235 FT-counters so as to enlarge the high-density area from 5,200 m^2 to 22,050 m^2, and we call this array and further upgraded one Tibet III. In 2002, all of the 36,900 m^2 area was covered by the high-density array by adding 200 FT-counters more. Finally we set up 56 FT-counters around the 36,900 m^2 high density array and equipped 8 D-counters with FT-PMT in 2003. At present, the Tibet air shower array consists of 761 FT-counters (249 of which have a D-PMT) and 28 D-counters as in Fig. 1.

The performance of the Tibet air shower array has been well examined by observing the Moon's shadow (approximately 0.5 degrees in diameter) in cosmic rays. The deficit map of cosmic rays around the Moon demonstrates the angular resolution to be around 0.9° at a few TeV for the Tibet III array. The pointing error is estimated to be better than $\sim 0.01^\circ$, as shown in Fig. 2, by displacement of the shadow center from the apparent center in the north-south direction, as the east-west component of the geomagnetic field is very small at the experimental site. On the other hand, the shadow center displacement in the east-west direction due to the geomagnetic field enables us to spectroscopically estimate the energy scale uncertainty at ± 12 % level, as shown in Fig. 3. Thus, the Tibet air shower experiment introduces a new method for energy scale calibration other than the conventional estimation by the difference between the measured cosmic-ray flux by an air shower experiment and the higher-energy extrapolation of cosmic-ray flux measured by direct measurements by balloon-borne or satellite experiments.

In 2007, a prototype 100-m^2 underground water Cherenkov muon detector was successfully constructed in Tibet to demonstrate the technical feasibility, cost estimate, validity of our Monte Carlo simulation. Data analyses demonstrate that our MC simulation reproduces real data quite reasonably.

After the success of the prototype underground muon detector, we added a large underground muon detector (MD) array and the experimental configuration was changed starting from February 2014. The current array consists of 597 plastic scintillation detectors with an area of 0.5 m^2 as shown by small dots in Fig. 4, covering an area of 65,700 m^2. The Tibet MD array (3,400 m^2 in total area) consists of 64 water-Cherenkov-type detectors located at 2.4 m underground of the AS array as shown by open squares in Fig. 4. Each detector is a waterproof concrete cell filled up with water of 1.5 m in depth, 7.35 m $\times$ 7.35 m in area, equipped with a 20-inch-diameter downward-facing photomultiplier tube (PMT) on the ceiling. The inner walls and floor have a white Tyvek sheet lining to efficiently gather catoptric water Cherenkov light. The electromagnetic component is shielded by the soil overburden which corresponds to $\sim$19 radiation lengths. The energy threshold for muons is approximately 1 GeV. A photon induced air shower has much less muons compared with a cosmic-ray induced one. The Tibet MD array enables us to significantly discriminate a cosmic-ray background event from a photon signal by means of counting the number of muons in an air shower.

2. Physics Results

Our current research theme is classified into 4 categories:

(1) TeV celestial gamma-ray point/diffuse sources,

(2) Chemical composition and energy spectrum of primary cosmic rays in the knee energy region,

(3) Cosmic-ray anisotropy in the multi-TeV region with high precision,

(4) Global 3-dimensional structure of the solar and interplanetary magnetic fields by observing the Sun's shadow in cosmic rays.

We will introduce a part of the results obtained in this fiscal year[2].

The supernova remnant (SNR) G106.3+2.7 is an extended source located in the northern Galactic Plane. At the northeast edge of G106.3+2.7, exists the so-called "Boomerang" pulsar wind nebula (PWN) G106.65+2.96, which is powered by an energetic (E = 2.2 $\times$ 10^{37} erg s^{-1}) pulsar PSR J2229+6114 of age 10.5 kyr. The radio and X-ray pulsations of PSR J2229+6114 were observed with a period of 51.6 ms. The gamma-ray counterpart of PSR J2229+6114 was detected as 0FGL J2229.0+6114 by the Fermi Large Area Telescope, and its gamma-ray pulsations above 100 MeV were detected by Fermi as well as AGILE. Upper limits were set on the flux of PWN G106.65+2.96 between 100 GeV and 1 TeV by MAGIC. PSR J2229+6114 and SNR G106.3+2.7 could belong to the same supernova explosion, and the radial velocity measurements of molecular material and atomic hydrogen suggested a distance of $\sim$ 0.8 kpc to the whole system.

Milagro reported on a gamma-ray source MGRO J2228+61 coincident with PSR J2229+6114 at 35 TeV. VERITAS also detected gamma- ray emissions above 1 TeV from the supernova remnant (SNR) G106.3+2.7 with a flux of $\sim$5 % Crab and named the source VER J2227+608. Of late, HAWC observed G106.3+2.7 and reported a best-fit spectrum with an error band above 40 TeV. The centroid of VER J2227+608, 0.4? away from PSR J2229+6114 in the southwest direction, is consistent with that of MGRO J2228+61 and the HAWC centroid within statistical and systematic uncertainties. Fermi observed this source in the GeV energy region and found that the source positon is coincident with that of the molecular cloud.

A photon induced air shower contains much less muons compared with a cosmic-ray induced air shower. Therefore, the MD array enables us to distinguish a photon signal event from a cosmic-ray induce background event. Using the AS and MD arrays, we analyzed the air shower data and muon data during 719 live days from February 2014 to May 2017.

Figure 4 (a) and (b) show the event display and the lateral distribution, respectively, of a typical photon-like event observed with $E = 251$ TeV from the Crab nebula[3]. The total uncertainty of the energy ΔE is defined as the quadratic sum of the absolute energy-scale error (12%) [1] and the energy resolution estimated by using MC events with the same θ and core distance from the array center (R). The ΔE of the 251 TeV photon-like event is estimated to be $^{+45}_{-43}$ TeV.

We reconstruct the arrival direction of an air shower by means of the relative timing information recorded at each scintillation detector. The color scale and circle size in Fig. 4 (a) stand for the relative timing (t) and the number of particle density (ρ) in an air shower. In the first place, we estimate the air shower core location weighted by ρ. The arrow head position and direction in the figure indicate the estimated core position and azimuthal direction. The t's in the air shower front are fitted by a conical shape, and its cone angle is optimized by the MC simulation depending on the air shower size. The angular resolutions (50% containment) are estimated to be approximately 0.5° and 0.2° for 10 TeV and 100 TeV photon, respectively.

The secondary particles in an air shower deposit energy, which is proportional to ρ, in a scintillator. The ρ at each detecto r is defined as the PMT output charge divided by the single particle peak which is monitored every 20 minutes to correct temperature dependence of each detector gain. The energy of each air shower is reconstructed using the lateral distribution of ρ, above 10 TeV. Figure 4 (b) shows an example of the lateral distribution of ρ. As an energy estimator, we use $S50$[4], which is defined as ρ at a distance of 50 m from the air shower axis in the best-fit Nishimura-Kamata-Greisen (NKG) function. The energy resolutions with $S50$, which depend on air shower core location and zenith angle, are roughly estimated to be 40% at 10 TeV and 20% at 100 TeV. On the other hand, the energy below 10 TeV was estimated directly from $\Sigma\rho$ corresponding to the sum of of the particle density measured by each scintillatoin detector, as the number of hit detectors is too low to fit $S50$. The absolute energy scale uncertainty is estimated to be 12 by the westward displacement of the Moon shadow position.

The electromagnetic cascade in the air shower is strongly suppressed by the bremsstrahlung process in the overburden,

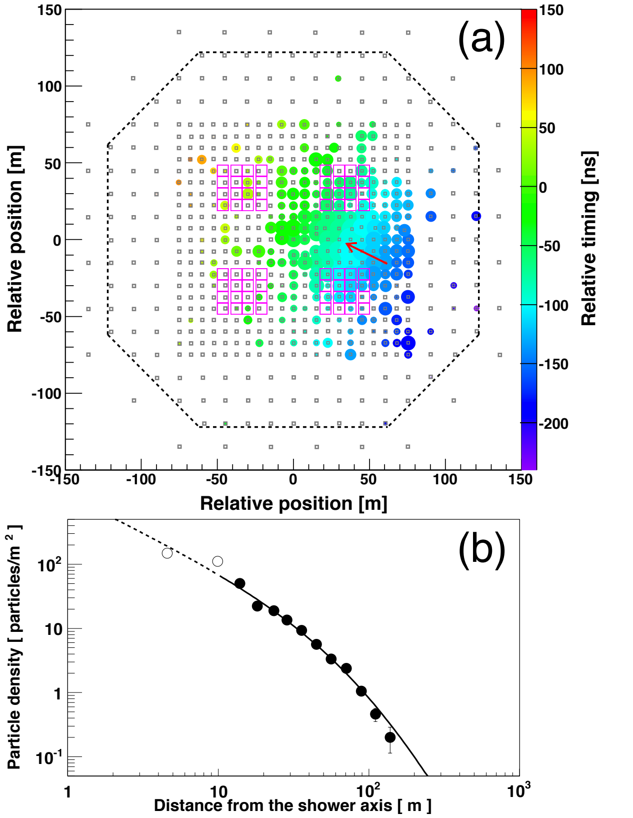

Fig. 4. From Ref.[3], references therein. (a) An event display of the observed photon-like AS of energy 251 TeV. The size and color of each circle represent the logarithmic particle density and the relative timing in each detector, respectively. The arrow head and direction indicate the AS core location and incident direction, respectively. Dots and open squares denote scintillation detectors and underground MDs, respectively. The enclosed area by the dashed line indicates the fiducial area of the AS array. (b) Lateral distribution of the photon-like shower event in panel (a). The solid circles and curve show the experimental data and fitting result by the Nishimura-Kamata-Greisen (NKG) function to the data recorded by detectors more than 10 m apart from the AS axis. The dashed curve and open circles are an extrapolation of the NKG function fitting and the unused data within 10 m from the AS axis.

while muons and a part of hadronic components penetrate into the underground MD array. The number of detected particles at an MD (N_μ) is defined as the output charge divided by the single muon peak which is monitored every 20 minutes. The sum of detected particles in all MDs (ΣN_μ) is used as a parameter to separate between photon and cosmic-ray induced air showers.

An event trigger is issued at any 4-fold coincidence with detectors recording more than 0.6 particles within the area enclosed by the dashed lines in Fig. 4. At air shower energies smaller than 10 TeV, we employ the same selection criteria and estimate the event energy as in the previous work[1], except for the MD selection criterion. At air shower energies greater than 10 TeV, we employ the following event selections: (1) zenith angle of arrival direction (θ) should be $\theta < 40^\circ$; (2) number of available detectors for the air shower reconstruction should be ≥ 16; (3) among 6 detectors recorded with the largest ρ's, 5 should be contained in the fiducial area enclosed by the dashed lines in Fig. 4; (4) $\log(S50)$ should be > -1.2; (5) age parameter (s) in the best-fit NKG function should be $0.3 < s < 1.3$. (6) ΣN_μ should be $\Sigma N_\mu < 0.15(\Sigma\rho)^{2.8}$ or $\Sigma N_\mu < 3.6 \times 10^{-4}(\Sigma\rho)^{1.4}$, where $\Sigma\rho$ is the sum of particle density measured by the AS array. The MD cut is optimized for photon detection by our MC simulation.

To estimate the background contribution from cosmic rays, we adopt the Equi-Zenith Angle method which is the same as our previous works [1]. The background counts are estimated from the number of events averaged over 20 off-source bins of the same size as the on-source bin located at the equi-zenith angle. The radius of the on/off-source bin is set to $R_{\rm sw}(\Sigma\rho) = 6.9/\sqrt{\Sigma\rho}$ (deg.). In order to efficiently extract signals in the higher energy region at low background level, the lower limit of $R_{\rm sw}$ is set to 0.5°, which corresponds to $\sim 90\%$ containment of photons above 100 TeV.

To generate air shower events in the atmosphere, Employed are the CORSIKA code v7.4000 with EPOS-LHC for the high-energy hadronic interaction model and FLUKA code v2011.2b for the low-energy hadronic interaction model. The very-high-energy photons at the top of atmosphere are inputted, assuming the power-law spectrum with a differential index -2.9 above 0.3 TeV. The generated secondary particles in an air shower are fed into the detector response simulation for the AS array developed based on the GEANT4 code v4.10.00. The MC simulation for the MD array considering the overburden has been developed based on the GEANT4 code. The electromagnetic and hadronic cascades by the secondary particles in the overburden, as well as the ray tracing of Cherenkov lights emitted in the water cells are simulated by the GEANT4 code. The number of photoelectrons detected in the 20-inch PMT is converted to N_μ referring to the single muon peakin each cell. The muon cut is determined to maximize the figure of merit $N_\gamma^{\rm MC}/\sqrt{N_\gamma^{\rm MC} + N_{\rm CR}^{\rm DATA}}$, where $N_\gamma^{\rm MC}$ and $N_{\rm CR}^{\rm DATA}$ denote the expected number of photons by the MC and the number of background events in the data after the muon cut. The photon-like events are defined as the remaining events after the muon cut.

Figure 5 shows the detection significance map around G106.3+2.7 above 10 TeV, with smoothing by the search window size. The map is consistent with a symmetrical 2D Gaussian function, and the centroid of gamma-ray emissions (a red filled star with a red position error circle) is at (R.A., Dec.) $= (336.82^\circ \pm 0.16_{\rm stat}, 60.85^\circ \pm 0.10_{\rm stat})$, coincident with a nearby molecular cloud location revealed by CO emissions (green contours) overlying the black radio contours of the SNR and away from PSR J2229+6114 by 0.44° in the southwest direction. Our source location is also consistent with those of VERITAS and HAWC. Assuming the distance of 800 pc from the Earth to both PSR J2229+6114 and SNR G106.3+2.7, the distance from the pulsar to the source location obtained by this work is estimated at 6 pc. Our source location deviates from the pulsar location at a confidence level of 3.1σ, based on the error of 0.14° including statistical errors as well as systematic ones. While the location of the HAWC centroid is consistent with both those of the Boomerang pulsar and the molecular cloud location, the centroids of VERITAS and Fermi are coincident with the location of molecular cloud as well as our source location.

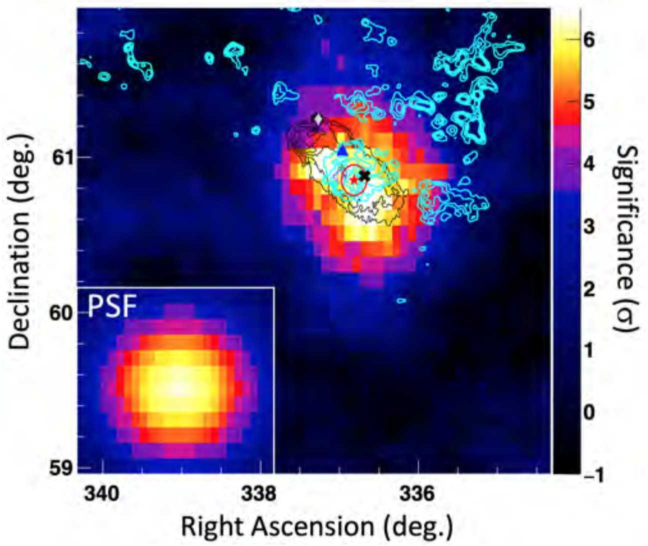

Fig. 5. From Ref.[2], references therein. Distribution of events as a function of the square of the incident angle (ϕ^2) measured around G106.3+2.7. The red filled star with a 1σ statistical position error circle is our source location, while the magenta open cross, the black X mark and the blue filled triangle are the centroids determined by VERITAS, Fermi and HAWC. The black contours represent 1420 MHz radio emissions from the Dominion Radio Astrophysical Observatory Synthesis Telescope, and the cyan contours represent CO emissions from the Five College Radio Astronomy Observatory survey. The gray filled diamond at the northeast corner of the black contours indicates the pulsar PSR J2229+6114. The inset figure shows our point spread function (PSF).

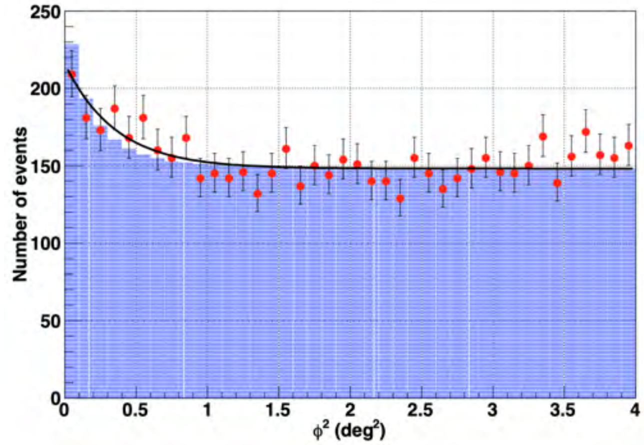

Fig. 6. From Ref.[2], references therein. Projected angular distribution of events observed above 10 TeV. The horizontal axis ϕ^2 is the square of the opening angle between the estimated event arrival direction and our source location. The red filled circles are the experimental data with the best-fit black solid curve. The purple histogram is the expected event distribution by MC simulations assuming a point-like gamma-ray source.

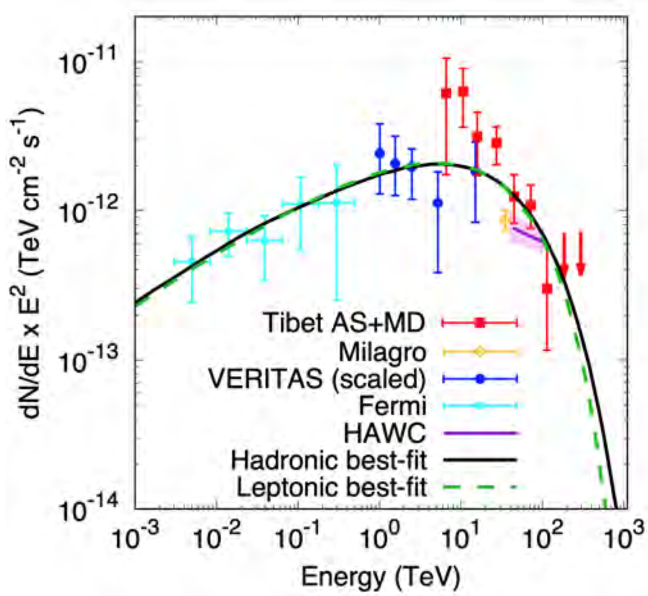

Fig. 7. From Ref.[2], references therein. Differential gamma-ray energy spectrum of SNR G106.3+2.7. Red filled squares (Tibet AS+MD) represent data measured by this work with two 99 % C.L. upper limits (downward red arrows), VERITAS (deep-blue filled circles), Fermi (sky-blue crosses), Milagro (an orange open diamond) and HAWC (a purple solid line with a shaded light purple area indicating the 1 σ statistical error band). VERITAS's data points are raised by a factor of 1.62 from the original value. The black solid (green dashed) line is the best-fit curve of the hadronic (leptonic) model for the combined data points of Tibet AS+MD, VERITAS and Fermi.

Figure 6 shows the distribution of the number of observed events above 10 TeV as a function of the opening angle between the measured arrival direction and our source location. Fitting the data with a Gaussian function + N_{BG} , assuming our point spread function is 0.35° above 10 TeV and N_{BG} = 148 is the number of background events, we estimate the 1 σ extent of the source to be $\sigma_{EXT} = 0.24° \pm 0.10°_{stat}$, consistent with that estimated by VERITAS of 0.27° (0.18°) along the major (minor) axis.

Figure 7 shows the differential gamma-ray energy spectrum (red filled squares and two red downward arrows for two upper limits). The detection significance above 10 TeV is 6.1σ. Our gamma-ray energy spectrum can be fitted by a single power law from 6 to 115 TeV as $d\mathrm{N}/d\mathrm{E} = (N_0/40\ \mathrm{TeV})^{-\Gamma}$ with $N_0 = (9.5 \pm 1.6_{stat}) \times 10^{16}$ [cm^{-2} s^{-1} TeV^{-1}] and $\Gamma = 2.95 \pm 0.17_{stat}$ (χ^2/ndf = 2.5/5). The systematic error in N_0 is estimated to be +40 %/-31 %, resulting from the 12 % uncertainty in the absolute energy scale determination. Our spectrum is consistent with the HAWC spectrum. The flux data points of VERITAS (blue filled circles) are raised by a factor of 1.62 to account for the spill-over of gamma-ray signals outside their window size. Our three flux data points below 20 TeV overlapping the energy range covered by the VERITAS flux points are statistically consistent with 1.62 times VERITAS's original best-fit value at the 1.5σ level.

As to the physical mechanism of the gamma-ray emission we fit the multi-wavelength gamma- ray energy spectrum using the naima package. For the energy spectrum of the parent particles, we assume a power-law spectrum with an exponential cut off , $E\ {-\alpha}\exp\ (E/E_{cut})$. In the hadronic model, we get E_{cut}~0.5 PeV and α~1.8. The value α falls between that predicted in the standard diffusive shock acceleration (α = 2) and the asymptotic limit of the very efficient proton acceleration (α = 1.5). The total energy of protons with energies 1 GeV (0.5 PeV) is estimated to be $\sim 5.0 \times 10^{47}$ erg (3.0×10^{46} erg) for a target gas density of 10 cm^{-3}. One might argue that, considering the estimated SNR age of 10 kyr, PeV protons escape the SNR much earlier than the present time in the standard theory of cosmic-ray acceleration. Given that $E_{\mathrm{cut}}\sim$0.5 PeV and that the maximum energy of protons remaining inside an SNR is proportional to $\tau^{-0.5}$ where τ is the SNR age, protons should be accelerated up to $\sim$1.6 PeV at τ = 1 kyr in the case of G106.3+2.7. This suggests that the acceleration of protons at G106.3+2.7 should be efficient enough to push their maximum energy up to $\sim$1.6 PeV during the SNR free expansion phase. In addition, G106.3+2.7 has a dense molecular cloud nearby indispensable for accelerated protons to produce TeV gamma rays via π^0 production. With $\alpha\sim$1.8, the proton energy spectrum does not appear softened, implying that protons may not be able to escape the SNR easily due to the suppression of the diffusion coefficient. Future observations of G106.3+2.7 could provide useful information for these theoretical studies on its mechanisms of particle acceleration and confinement.

In the leptonic model, we get $E_{\mathrm{cut}}\sim$190 TeV, $\alpha\sim$2.3 and the SNR magnetic field strength of $\sim$9 μG. The total energy of relativistic electrons with energies 10 MeV is estimated to be $\sim 1.4 \times 10^{47}$ erg. Considering the synchrotron cooling, we estimate that electrons need to be accelerated freshly within 1 kyr if they originate from the SNR, and that electrons provided by the Boomerang PWN are not likely to produce the observed gamma-ray emission in view of the energy budget and the gamma-ray morphology.

Generally, the energy spectrum of hadronically-induced gamma rays rises steeply below $\sim$200 MeV and approximately follows the energy spectrum of parent particles above a few GeV, resulting in a characteristic "π^0-decay bump" in the gamma-ray spectrum. Hopefully, future multi- wavelength observations would establish the hadronic origin of gamma-ray emissions from SNR G106.3+2.7.

Anyway, this is the first detection of gamma rays in the 100 TeV region from an overlapping region between a supernova remnant and a molecular cloud.

3. Other Activities

The emulsion-pouring facilities can meet the demands for making any kind of nuclear emulsion plates which are used for cosmic ray or accelerator experiments. The thermostatic emulsion-processing facilities are operated in order to develop nuclear emulsion plates or X-ray films. Using these facilities, it is also possible to make and develop emulsion pellicle in 600-micron thickness each. In this way, these facilities have been open to all the qualified scientists who want to carry out joint research programs successfully. Of recent, however, the shrinking demand for the facilities let us decide that we should suspend calls for joint research programs to utilize the emulsion-pouring facilities, starting from 2012.

4. Ongoing Research Plans with MD

(1) Chemical composition of primary cosmic rays making the knee in the all-particle energy spectrum

Fig. 8. YAC2 set up at Yangbajing.

We have measured the energy spectra of primary cosmic-ray protons, helium, all particles around the knee energy region. The main component responsible for making the knee structure in the all particle energy spectrum is heavier nuclei than helium. The next step is to identify the chemical component making the knee in the all particle energy spectrum. We have a plan to install an Yangbajing Air shower Core detector array (YAC) near the center of Tibet III to distinguish the chemical component making the knee. We completed construction of YAC2 (124 detectors over $\sim$500m^2 in area), as is shown in Fig. 8, and started data-taking in 2014. YAC2 aims at mainly studying the energy spectra of proton and helium components in the knee energy region.

(2) Gamma-ray astronomy in the 100 TeV region

For the purpose of detecting high-energy cosmic gamma rays with an air shower array, a large underground muon detecter[5] is very effective to reduce cosmic-ray background.

We added a large ($\sim$3,400 m^2) underground water Cherenkov muon detector (Tibet-MD) array under the present Tibet air shower array (Tibet AS $\sim$65,700 m^2). By Tibet AS + MD, we aim at background-free detection of celestial point-source gamma rays around 100 TeV with the world-best sensitivity and at locating the origins (PeVatrons) of cosmic rays accelerated up to the knee (PeV) energy region in the northern sky. The measurement of cut off energies in the energy spectra of such gamma rays in the 100 TeV region may contribute significantly to understanding of the cosmic- ray acceleration limit at SNRs. Search for extremely diffuse gamma-ray sources by Tibet AS + MD, for example, from the galactic plane or from the Cygnus region may be very intriguing as well. Above 100 TeV, the angular resolution of Tibet AS with 2-steradian wide field of view is 0.2° and the hadron rejection power of Tibet MD is typically 1/1000.

In addition to unknown point-like sources, we expect to detect established sources in the 100 TeV region: TeV J2032+4130, HESS J1837-069, Crab, MGRO J2019+37, MGRO J1908+06, Milagro candidate sources, Mrk421, Mrk501 are sufficiently detectable and Cas A, HESS J1834-

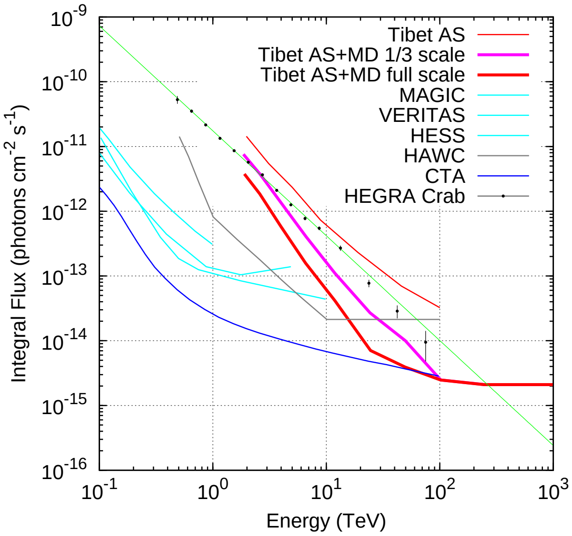

Fig. 9. Sensitivity to point-like gamma-ray sources with Tibet AS+MD (see,Tibet AS+MD 1/3 scale) by pink curve.

087,LS I+63 303, IC443 and M87 are marginal.

Furthermore, our integral flux sensitivity to diffuse gamma rays will be very high. We hope that the diffuse gamma rays from the Cygnus region reported by the Milagro group and also diffuse gamma-rays from the galactic plane will be detected. Diffuse gamma-rays of extragalacitic origin may be an interesting target as well.

Development of Monte Carlo simulation is under way for comparison with real data. Various analysis tools are also extensively being developed. According to the simulation, the sensitivity of the current configuration (Tibet AS + MD) is demonstrated in Fig. 9.

As is described in the text, we succeeded in first detection of photons with energies above 100 TeV from Crab in the world, opening a new energy (sub-PeV) window in astronomy. The hightest energy photon has the world-record energy of 450 TeV approximately. Analyses are under way in search of other sub-PeV gamma-ray sources.

Bibliography

Papers in refereed journals

[1] "Multi-TeV Gamma-Ray Observation from the Crab Nebula Using the Tibet-III Air Shower Array Finely Tuned by the Cosmic-Ray Moon's Shadow", M. Amenomori *et al.*, Astrophysical Journal, **692** , 61-72 (2009).

[2] "Potential PeVatron supernova remnant G106.3+2.7 seen in the highest-energy gamma rays", M. Amenomori*et al.*, Nature Astronomy, **5** 460-464 (2021).

[3] "First Detection of Photons with Energies beyond 100 TeV from an Astrophysical Source", M. Amenomori*et al.*, Physical Review Letters, **123** :051101-1-6 (2019).

[4] "Energy determination of gamma-ray induced air showers observed by an extensive air shower array", K. Kawata*et al.*, Experimental Astronomy, **44** 1-9 (2017).

[5] "Exploration of a 100 TeV gamma-ray northern sky using the Tibet air-shower array combined with an underground water-Cherenkov muon-detector array", T.K. Sako *et al.*, Astroparticle Physics, **32** , 177-184 (2009).

The Tibet ASγ Collaboration

M. Amenomori[1], Y. W. Bao[2], X. J. Bi[3], D. Chen[4*], T. L. Chen[5], W. Y. Chen[3], Xu Chen[3], Y. Chen[2], Cirennima[5], S. W. Cui[6], Danzengluobu[5], L. K. Ding[3], J. H. Fang[3,7], K. Fang[3], C. F. Feng[8], Zhaoyang Feng[3], Z. Y. Feng[9], Qi Gao[5], Q. B. Gou[3], Y. Q. Guo[3], Y. Y. Guo[3], H. H. He[3], Z. T. He[6], K. Hibino[10], N. Hotta[11], Haibing Hu[5], H. B. Hu[3], J. Huang[3], H. Y. Jia[9], L. Jiang[3], H. B. Jin[4], K. Kasahara[12], Y. Katayose[13], C. Kato[14], S. Kato[15], K. Kawata[15], W. Kihara[14], Y. Ko[14], M. Kozai[16], Labaciren[5], G. M. Le[17], A. F. Li[18,8,3], H. J. Li[5], W. J. Li[3,9], Y. H. Lin[3,7], B. Liu[19], C. Liu[3], J. S. Liu[3], M. Y. Liu[5], W. Liu[3],
Y.-Q. Lou[20,21,22], H. Lu[3], X. R. Meng[5], K. Munakata[14], H. Nakada[13], Y. Nakamura[3], H. Nanjo[1], M. Nishizawa[23], M. Ohnishi[15], T. Ohura[13], S. Ozawa[24], X. L. Qian[25], X. B. Qu[26], T. Saito[27], M. Sakata[28], T. K. Sako[15*], J. Shao[3,8], M. Shibata[13], A. Shiomi[29], H. Sugimoto[30], W. Takano[10], M. Takita[15], Y. H. Tan[3], N. Tateyama[10], S. Torii[31], H. Tsuchiya[32], S. Udo[10], H. Wang[3], H. R. Wu[3], L. Xue[8], Y. Yamamoto[28 2], Z. Yang[3], Y. Yokoe[15], A. F. Yuan[5], L. M. Zhai[4], H. M. Zhang[3], J. L. Zhang[3], X. Zhang[2], X. Y. Zhang[8], Y. Zhang[3], Yi Zhang[33], Ying Zhang[3], S. P. Zhao[3], Zhaxisangzhu[5] and X. X. Zhou[9]

[1]Department of Physics, Hirosaki University, Hirosaki 036-8561, Japan
[2]School of Astronomy and Space Science, Nanjing University, Nanjing 210093, China
[3]Key Laboratory of Particle Astrophysics, Institute of High Energy Physics, Chinese Academy of Sciences, Beijing 100049, China
[4]National Astronomical Observatories, Chinese Academy of Sciences, Beijing 1 00012, China
[5]Physics Department of Science School, Tibet University, Lhasa 850000, China
[6]Department of Physics, Hebei Normal University, Shijiazhuang 050016, China
[7]University of Chinese Academy of Sciences, Beijing 100049, China
[8] Institute of Frontier and Interdisciplinary Science and Key Laboratory of Particle Physics and Particle Irradiation (MOE), Shandong University, Qingdao 2 66237, China
[9]Institute of Modern Physics, SouthWest Jiaotong University, Chengdu

*2 deceased

610031, China
[10]Faculty of Engineering, Kanagawa University, Yokohama 221-8686, Japan
[11]Faculty of Education, Utsunomiya University, Utsunomiya 321-8505, Japan
[12]Faculty of Systems Engineering, Shibaura Institute of Technology, Omiya 330-8570, Japan
[13]Faculty of Engineering, Yokohama National University, Yokohama 240-8501, Japan
[14]Department of Physics, Shinshu University, Matsumoto 390-8621, Japan
[15]Institute for Cosmic Ray Research, University of Tokyo, Kashiwa 277-8582 , Japan
[16]Institute of Space and Astronautical Science, Japan Aerospace Exploratio n Agency (ISAS/JAXA), Sagamihara 252-5210, Japan
[17]National Center for Space Weather, China Meteorological Administration, Beijing 100081, China
[18]School of Information Science and Engineering, Shandong Agriculture Univ ersity, Taian 271018, China
[19]Department of Astronomy, School of Physical Sciences, University of Scie nce and Technology of China, Hefei, Anhui 230026, China
[20]Department of Physics and Tsinghua Centre for Astrophysics (THCA), Tsing hua University, Beijing 100084, China
[21]Tsinghua University-National Astronomical Observatories of China (NAOC) Joint Research Center for Astrophysics, Tsinghua University, Beijing 100084, Ch ina
[22]Department of Astronomy, Tsinghua University, Beijing 100084, China
[23]National Institute of Informatics, Tokyo 101-8430, Japan
[24]National Institute of Information and Communications Technology, Tokyo 1 84-8795, Japan
[25]Department of Mechanical and Electrical Engineering, Shangdong Managemen t University, Jinan 250357, China
[26]College of Science, China University of Petroleum, Qingdao 266555, China
[27]Tokyo Metropolitan College of Industrial Technology, Tokyo 116-8523, Jap an
[28]Department of Physics, Konan University, Kobe 658-8501, Japan
[29]College of Industrial Technology, Nihon University, Narashino 275-8575, Japan
[30]Shonan Institute of Technology, Fujisawa 251-8511, Japan
[31]Research Institute for Science and Engineering, Waseda University, Tokyo 169-8555, Japan
[32]Japan Atomic Energy Agency, Tokai-mura 319-1195, Japan
[33]Key Laboratory of Dark Matter and Space Astronomy, Purple Mountain Obser vatory, Chinese Academy of Sciences, Nanjing 210034, China
(The Tibet ASγ Collaboration as of 2020)

ALPACA Project

[Spokesperson: M. Takita]
ICRR, The Univ. of Tokyo, Kashiwa, Chiba 277-8582

Cosmic rays are supposed to be accelerated up to the knee energy (PeV) region at supernova remnants (SNRs) in our galaxy. Therefore, we naturally expect gamma rays at 100 TeV energies, which originate in π^0 decays produced by the accelerated cosmic rays interacting with matter surrounding the SNRs. However, on-going experiments focus on measuring gamma rays in the 1 - 10 TeV region. The gamma-ray emission of electron origin might be highly suppressed above 10 TeV due to rapid decrease of inverse-Compton cross section by the Klein-Nishina effect as well as synchrotron radiation energy loss in the strong magnetic field around the SNRs. The detection and spectral measurement of gamma rays in the 100 TeV region from their celestial sources, together with multi-wavelength (radio, X-ray, gamma-ray) observations, will be an important experiment enabling us to discriminate between the two processes (cosmic-ray/electron origins), to locate the acceleration site (PeVatron which accelerate cosmic rays up to PeV energies) of cosmic rays and to verify the standard acceleration model of cosmic rays. Furthermore, diffuse gamma rays from the Fermi bubbles recently reported by the Fermi-LAT group and sub-PeV neutrino events[1] detected by IceCube suggests that the Fermi bubbles be a PeVatron candidate. Similarly, the energy spectrum of diffuse gamma rays from the extended region around the galactic center marginally measured by HESS up to approximately 10 TeV also strongly indicates existence of PeVatron[2], from which we expect to detect gamma rays at 100 TeV energies. Thus, a wide field-of-view gamma-ray imaging at 100 TeV energies in the southern sky, where the HESS sources, the Fermi bubbles and the galactic center are located within field of view, will be a key experiment.

Fig. 1. From Ref.[3]. Experimental site for the ALPACA experiment, Chacaltaya Plateau ia (4,740 m above see level, 16°23’ S, 68°08’ W), near Mount Chacaltaya, in Bolivia.

5. Experiment

The ALPACA[3],[4] (Andes Large area PArticle detector for Cosmic ray physics and Astrophysics) is a cosmic-ray experiment with a large surface air shower array with a large underground muon detector array The experimental site (approximately 500 m$\times$500 m $\sim$250,000 m^2 in total area) is located on a flat high land called Chacaltaya Plateau (4,740 m above sea level, 16°23’ S, 68°08’ W), as shown in Fig. 1, around Mount Chacaltaya, near La Paz, Bolivia. In some part in this area, our detectors will be constructed.

We plan to set up a 5,400 m^2 underground (approximately one to a few meters) muon detector array (MD) and an 83,000 m^2 air shower array (AS). MD of water Cherenkov type is composed of eight pools with each pool (approximately 1 m deep) containing twelve 56 m^2 unit detectors. AS is made up of 401 1 m^2 plastic scintillation counters at 15 m spacing.

The AS field of view is roughly 2 steradian. The expected angular resolution of AS is approximately 1 degree at 5 TeV and 0.2 degrees around 100 TeV for gamma rays. For 100 TeV gamma rays, the AS energy resolution is estimated to be ~20-25 %. The hadron rejection power of MD is more than 99.9 % at 100 TeV, while keeping most of gamma-ray events. Long-term detector stability, angular resolution, pointing accuracy and energy scale can be calibrated by the cosmic-ray shadow in the Moon as well as by some of the bright stable TeV gamma ray sources in the southern sky.

6. Covered Physics

Our reserch target is divided into four in ALPACA:

1. Measurement of high-energy (5 TeV – 1 PeV) cosmic gamma rays.

2. Measurement of cosmic ray energy spectra around the Knee energy region (100 TeV – 100 PeV).

3. Measurement of cosmic ray anisotropy $>$ 5 TeV at sidereal time frame.

4. Measurement of the Sun shadow in cosmic rays $>$ 5 TeV.

We aim at low-background detection of celestial gamma rays in the 100 TeV region with the world-best sensitivity (an order of magnitude better than any previous/existing experiments) and at locating the origins of cosmic rays accelerated up to the knee energy region in the southern sky. Presuming a Crab-like gamma-ray source extending up with power-law index -2.6 located in the southern sky, the ALPACA experiment is sensitive to the source with ~15 % Crab intensity during one calendar year, as is demonstrated in Fig. 2.

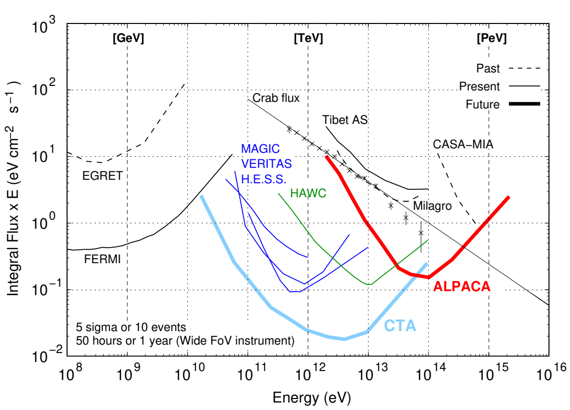

Fig. 2. Sensitivity of ALPACA to high-energy gamma-ray point source. Experimental data points are from HEGRA. The ALPACA sensitivity is evaluated from Ref.[8].

The AS + MD in the southern hemisphere will be a unique/complementary experiment to on-going experiments (FERMI, CALET, DAMPE, HESS, VERITAS, MAGIC, Tibet ASγ, HAWC, LHAASO) and future projects (CTA, SWGO) in this field, which are either located in the northern hemisphere or aiming at gamma-ray astronomy below 10 TeV region, or having narrow field-of-view, or not expected to start operation in the near future (within 10 years). Thus, the new energy window in the 100 TeV region observing gamma rays with wide field-of-view will be opened first in the southern sky by the ALPACA experiment. We expect to detect established more than a dozen of sources, i.e., young SNRs (SN1006, RX J1713.7-3946, RX J0852.0-4622), Pulsar Wind Nebulae, the galactic center, etc) in the 100 TeV region, some of which may be cosmic-ray PeVatron candidates. Furthermore, our wide field-of-view sensitivity to diffuse gamma rays allows us to study extremely diffuse gamma-ray sources which are difficult to detect by IACTs. The diffuse gamma rays from the Fermi bubbles recently reported by the Fermi-LAT group may be clearly detected, if they extend up to the 100 TeV region. Similarly, detection of diffuse gamma rays above 100 TeV from extended region from the galactic center is promising, where the gamma-ray energy spectrum strongly suggests existence of PeVatron. Detection and spectral measurement of gamma rays in the 100 TeV region from these celestial sources, together with multi-wavelength (radio, X-ray, gamma-ray) observations, are key points enabling us to discriminate between the two processes (cosmic-ray/electron origins), to locate the acceleration site of cosmic rays and to examine the standard acceleration model of cosmic rays. In astronomical point of view, we pioneer the ultra-high energy (above 100 TeV) gamma-astronomy in the southern sky. Besides, gamma-ray emission from near-by extragalactic sources, e.g. M87, Cen A, gamma rays of dark matter origin, those from the Sun disk recently obseved by Fermi[9] may be interesting subjects.

We also aim at measuring energy spectra of proton, helium and iron components separately around the knee energy region with the new AS + MD. The standard cosmic-ray acceleration model at SNR predicts the knee energy of each nucleus component being proportional to Z (atomic number). We can discriminate proton and iron components by MD, as an iron nucleus produces approximately 2 times more muons than a proton with the same energy. Thus, the cosmic-ray acceleration scenario (SNR shock acceleration) will be verified by observing the linearly Z(atomic number)-dependent knee(=bent) positions of proton, helium, iron components around the knee energy region.

Precise cosmic-ray anisotropy measurement at sidereal time frame in the TeV energy region in the southern sky provides unique data for the community to understand the magnetic field structure in the heliosphere. The ALPACA experiment gives complementary data in the TeV region to those from IceCube above a few tens of TeV.

Furthermore, measurement of the Sun shadow in cosmic rays above the TeV energy region in the southern hemisphere also helps understand the modeling of the magnetic fields between the Sun and the Earth, complementary to the observations in the northern hemisphere.

7. ALPAQUITA

As a proto-type experiment, the ALPAQUITA[4], [6] air shower array which is ∼25 % of the ALPACA air shower array in area is being constructed at the experimental site, Chacaltaya Plateau. The containers including materials and equipments necessary to construct the ALPAQUITA air shower array arrived at La Paz, Bolivia in early 2019. The main infrastructures including electricity, experimental hut, fence, cable guide drains were ready in 2020. A part of the ALPAQUITA air shower array was set up, as is seen in Fig. 3. Due to COVID19 problems, the construction of ALPAQUITA air shower array was stopped during 2020. We aim at completing construction of the ALPAQUITA air shower array under which we will add a ∼900-m^2 muon detector array in 2021 in the earliest case.

Fig. 3. ALPAQUITA air shower array under construction, as of autumn 2019.

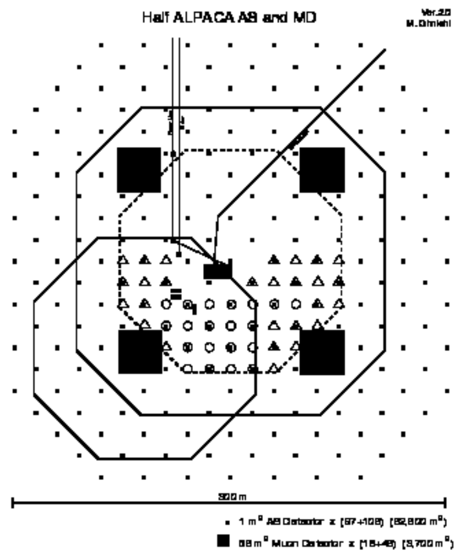

Fig. 4. Schematic view of the ALPACA(half) experiment. The small black squares indicate 200 1 m^2 plastic scintillation detectors at 21m spacing, forming an air shower array with 83,000 m^2 in area.The black large rectangles indicate four underground muon detector pools, each of which contains sixteen 56 m^2 muon detector units. The total area of the underground muon detector array is 3,600 m^2. The area enclosed in the lower-left octagon represents ALPAQUITA.

8. ALPACA(half)

The budget which affords to construct approximately half of ALPACA was funded in 2020. We replanned to set up ALPACA(half), a 3,600 m^2 underground (approximately one to a few meters) muon detector array (MD) and an 83,000 m^2 air shower array (AS), shown in Fig. 4. MD of water Cherenkov type is composed of four pools with each pool (approximately 1 m deep) containing sixteen 56 m^2 unit detectors. AS is made up of 200 1 m^2 plastic scintillation counters at 21 m spacing. The performace of ALPACA(half) for cosmic gamma rays above 100 TeV is expected to be similar to that of ALPACA.

We will finish contruction of ALPACA(half) in 2022, in the ealiest case, assuming the COVID-19 problems will be solved as early as possible.

Bibliography

Papers and references

[1] C. Lunardini et al., PRD, **92**, 021301-1-5 (2015).

[2] A. Abramoswski et al., Nature, **531**, 476 (2016).

[3] M. Takita for the ALPACA Collaboration, THE EUROPEAN PHYSICAL JOURNAL, **145**, 01002-1-3, (2017).

[4] C. Calle et al, Proc. of ICRC2019, POS(ICRC2019)779, Madison, WI, U.S.A, July 24-August 1, (2019).

[5] C. Calle et al, Proc. of ICRC2019, POS(ICRC2019)711, Madison, WI, U.S.A, July 24-August 1, (2019).

[6] C. Calle et al, Proc. of TAUP2018, Journal of Physics: Conference Series,1468 (2020) 012091 (2020).

[7] F. Aharonian et al., ApJ, **614**, 897 (2004)

[8] T. K. Sako et al., Astroparticle Physics, **32**, 177 (2009).

[9] C. Y. Kenny et al., arXiv:1508.06276v1.

The ALPACA Collaboration, as of 2020

C. A. H. Condori,[a] E. de la Fuente,[b,m,z] A. Gomi,[c] K. Hibino,[d] N. Hotta,[e] I. Toledano-Juarez,[f] Y. Katayose,[c] C. Kato,[g] S. Kato,[h] K. Kawata,[h] W. Kihara,[g] Y. Ko,[g] T. Koi,[i] H. Kojima,[j] D. Kurashige,[k] J. Lozoya,[l] F. Orozco-Luna,[m] R. Mayta,[n] P. Miranda,[a] K. Munakata,[g] H. Nakada,[c] Y. Nakamura,[o] Y. Nakazawa,[p] C. Nina,[a] M. Nishizawa,[q] S. Ogio,[n,r] M. Ohnishi,[h] T. Ohura,[c] S. Okukawa,[c] A. Oshima,[s]

M. Raljevich,[a] H. Rivera,[a] T. Saito,[t] T. Sako,[h] T. K. Sako,[h] S. Shibata,[s] A. Shiomi,[p] M. Subieta,[a] N. Tajima,[u] W. Takano,[d] M. Takita,[h] Y. Tameda,[v] K. Tanaka,[w] R. Ticona,[a] H. Torres,[x] H. Tsuchiya,[y] Y. Tsunesada,[n,r] S. Udo,[d] K. Yamazaki,[s] and Y. Yokoe[h] (The ALPACA Collaboration)

[a]Instituto de Investigaciones Físicas, Universidad Mayor de San Andres, La Paz 8635, Bolivia
[b]Departamento de Fisica, CUCEI, Universidad de Guadalajara, Blvd. Marcelino Garcia Barragan #1421, esq Calzada Olimpica, C.P. 44430, Guada lajara, Jalisco, Mexico
[c]Faculty of Engineering, Yokohama National University, Japan
[d]Faculty of Engineering, Kanagawa University, Japan
[e]Faculty of Education, Utsunomiya University, Japan
[f]Doctorado en Ciencias Fisicas, CUCEI, Universidad de Guadal ajara, Blvd. Marcelino Garcia Barragan #1421, esq Calzada Olimpica, C.P. 44430 , Guadalajara, Jalisco, Mexico
[g]Department of Physics, Shinshu University, Japan
[h]Institute for Cosmic Ray Research, The University of Tokyo, Japan
[i]College of Engineering, Chubu University, Japan
[j]Faculty of Engineering, Aichi Institute of Technology, Japan
[k]Graduate School of Engineering Science, Yokohama National U niversity, Japan
[l]Departamento de Ciencias de la Informacion y Desarrollo Tec nologico, Cutonala, Universidad de Guadalajara, Av. 555 Ejido San Jose Tateposc o, Nuevo Perif. Ote., 45425, Tonala, Jalisco, Mexico
[m]Doctorado en Tecnologias de la Informacion, CUCEA, Univer sidad de Guadalajara, Periferico Norte 799, Nucleo Universitario los Belenes, 4 5100, Zapopan, Jalisco, Mexico
[n]Graduate School of Science, Osaka City University, Japan
[o]Institute of High Energy Physics, Chinese Academy of Scienc e, Shijingsham, Beijing 100049, China
[p]College of Industrial Technology, Nihon University, Japan
[q]National Institute of Informatics, Japan
[r]Nambu Yoichiro Institute of Theoretical and Experimental P hysics, Osaka City University, Japan
[s]College of Engineering, Chubu University, Japan
[t]Tokyo Metropolitan College of Industrial Technology, Japan
[u]Institute of Physical and Chemical Research, Japan
[v]Faculty of Engineering, Osaka Electro-Communication University, Japan
[w]Graduate School of Information Sciences, Hiroshima City University, Japan
[x]Coordinacion General de Servicios Administrativos e Infraes tructura Tecnologica (CGSAIT), Universidad de Guadalajara, Av. Juarez 976, 4410 0, Guadalajara, Jalisco, Mexico
[y]Japan Atomic Energy Agency, Japan
[z]Departamento de Fisica, CUCEI, Universidad de Guadalajara, Blvd. Marcelino Garcia Barragan #1421, esq Calzada Olimpica, C.P. 44430, Guada lajara, Jalisco, Mexico

High Energy Astrophysics Group

[Spokesperson: K. Asano]

ICRR, The Univ. of Tokyo, Kashiwa, Chiba 277-8582

Overview

The high energy astrophysics group has been making theoretical studies of violent astrophysical phenomena, in which nonthermal cosmic-ray particles are being accelerated. Targets of the group's study include high energy astrophysical objects such as supernova remnants/explosions, pulsars, pulsar wind nebulae, black hole/neutron star mergers, jets from active galactic nuclei (AGNs), and gamma-ray bursts (GRBs). We especially study the formation of relativistic outflows, particle acceleration in jets, emission mechanisms of electromagnetic waves or neutrinos, and electromagnetic counterparts for compact binary mergers. Our research carries the multi-messenger astronomy forward, which probes astronomical phenomena through collaborating observations of electromagnetic waves, cosmic rays, neutrinos, and gravitational waves. Gravitational-wave astronomy is also our target. We have been probing the formation history of massive stars from the early universe to the present time with the observation results by gravitational-wave detectors.

Research Topic 1: TeV Afterglow of Gamma-Ray Bursts GRB 190114C

Gamma-ray burst (GRB) 190114C at redshift $z = 0.4245$ is the first gamma-ray burst detected with imaging atmospheric Cerenkov telescopes (IACTs). MAGIC Collaboration reported gamma-ray detection in the energy range of 0.2–1 TeV from 62 s to 2454 s after the trigger by the Swift-BAT. The spectral component in this energy range is naturally interpreted as the synchrotron self-Compton (SSC) emission from the afterglow caused by electrons accelerated at a blastwave, because the photon energy is significantly larger than the maximum photon energy expected by synchrotron radiation.

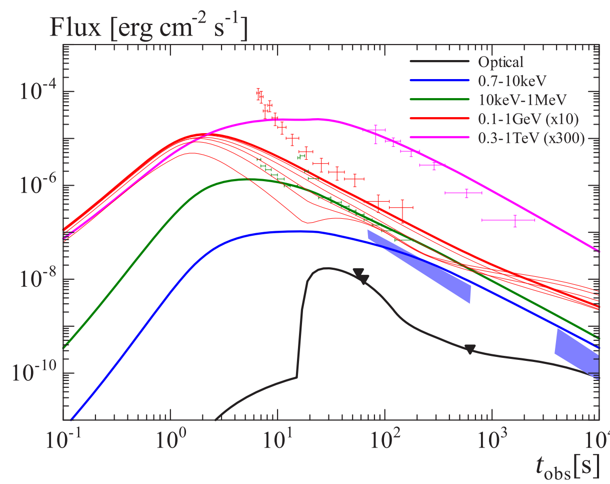

Fig. 1. Model light curves for GRB 190114C. The thick lines show the model with $\eta = 1$, where $\eta \geq 1$ is the acceleration efficiency parameter, to which the acceleration time of electrons is proportional. The red thin lines show the light curves for 0.1–1 GeV with $\eta = 10, 100, 1000, 3000$, and 10,000, decreasing the flux. The optical bump at ~ 20–100 s is the reverse-shock component we set manually.

This can constrain microscopic parameters of the shock-heated plasma emitting non-thermal emission. Focusing on the early afterglow of this event, we numerically simulate the spectrum and multi-wavelength light curves (Figure 1) using a time-dependent code. Our results show that the electron acceleration timescale at the highest energies is likely shorter than 20 times the gyroperiod to reproduce the GeV gamma-ray flux and its spectral index reported by *Fermi*. This gives an interesting constraint on the acceleration efficiency for Weibel-mediated shocks. Our results show that the acceleration timescale can be much shorter than the simple estimate supported by the state-of-art PIC simulations. The maximum energy of non-thermal electrons would need to be regulated by another mechanism rather than the diffusive process seen in the early stage of the Fermi acceleration in the PIC simulations.

We also constrain the number fraction of non-thermal electrons $f_{\rm e}$, and the temperature of the thermal electrons. It is natural that only a fraction of electrons are accelerated by the shock and the rest of electrons remain as the thermal component, which is especially the case for mildly relativistic shocks. The early optical emission can be explained by the thermal synchrotron emission with $f_{\rm e} <\sim 0.01$. On the other hand, the X-ray light curves restrict efficient energy transfer from protons to the thermal electrons, and $f_{\rm e} \sim 1$ is required if the energy fraction of the thermal electrons is larger than $\sim 10\%$. The parameter constraints obtained in this work give important clues to probing plasma physics with relativistic shocks.

Research Topic 2: A Jet-Bases Emission Model of M87*

The Event Horizon Telescope (EHT) observed M87 in 2017 observation campaign and detected the BH shadow surrounded by bright ring-like emission (EHTC 2019a-e). However, throughout their theoretical interpretation, no emission from the strongly magnetized jet is assumed and, thus, its contribution to the observed ring image was not thoroughly studied yet.

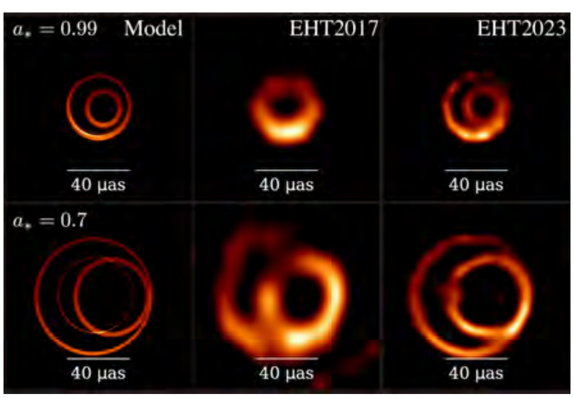

Fig. 2. Black hole shadow images formed by the jet-bases emission for the model with black hole spin $a_* = 0.99$ (top) and 0.7 (bottom). Left, center, and right panels display the theoretical images, synthetic images assuming EHT 2017 array, and those assuming forthcoming EHT observation in 2023, respectively.

We, therefore, calculated the image of the bases of the relativistic jet using our general relativistic, radiative transfer code RAIKOU. For the model with the BH spin $a_* = 0.99$, the direct image of the counter-jet and strong gravitational lense image (i.e., photon ring) reproduces ring with diameter $\sim 40\mu$as observed by EHT 2017 observation (Figure 2). This indicates that the ring image in M87* may contain the important feature of the jet bases in addition to the photon ring. We find that forthcoming EHT observations (EHT 2023) can resolve the stagnation-ring image and may enable us to explore the enigmatic plasma-injection mechanism into the relativistic jet.

Research Topic 3: Kilonova Emission

A number of gravitational-wave events from binary mergers possibly including neutron stars were reported in the third observation runs of the ground-based detector network. We predicted the kilonova lightcurve models in various setups based on the latest numerical relativity simulations and radiative transfer simulations, and discussed the property of the progenitor employing our kilonova lightcurve models.

On 2019 August 14 advanced LIGO and advanced Virgo have reported the detection of GWs from a black hole-neutron star (BH-NS) merger, which is referred to as S190814bv. Although no significant EM counterpart was found, upper limits in the nearly whole sky localization region of the event are obtained by their efforts. Based on the observational upper-limits, we derived the upper limit to the ejecta mass of S190814bv, a black hole-neutron star merger candidate, through the radiative transfer simulations for kilonovae with the realistic ejecta density profile as well as the detailed opacity and heating rate models (Figure 3).

We found that the limits to the ejecta mass strongly depend on the viewing angle. For the face-on observations ($\leq 45°$), the total ejecta mass should be smaller than $0.1 M_\odot$ for the average distance of S190814bv ($D = 267$ Mpc), while larger mass is allowed for the edge-on observations. We also discussed the implication for the future observation, showing that the *iz*-band observation deeper than 22 mag within 2 d after the GW trigger is crucial to detect the BH-NS kilonova with the total ejecta mass of $0.06 M_\odot$ at the distance of $D = 300$ Mpc. We pointed out that a strong constraint on the NS mass-radius relation can be obtained if the future observations put the upper limit of $0.03 M_\odot$ to the dynamical ejecta mass for a BH-NS event with the chirp mass $<\sim 3 M_\odot$ and effective spin $>\sim 0.5$.

The early kilonova emission from NS mergers is investigated by deriving the line opacity table for the highly ionized r-process elements based on atomic structure calculations. In this work, we show that that existing bolometric and multicolor data of GW170817 can be naturally explained by the purely radioactive model, while the early-phase luminosity is sensitive to the structure of the outer ejecta.

Research Topic 4: Supernova Explosion

Massive stars end their lives with core-collapse supernova (CCSN) explosions. Its explosion energy is $\sim 10^{51}$ erg, and the ultimate energy source is the released gravitational energy when the star collapses to form a neutron star (NS). A star whose mass is larger than $8 M_\odot$ forms an iron core or an ONeMg core at its center at the end of its evolution. This core eventually becomes gravitationally unstable and experiences the gravitational collapse. When the central density reaches the nuclear density, the collapse is halted by the nuclear repulsive force. Then the bounce shock is launched. This bounce

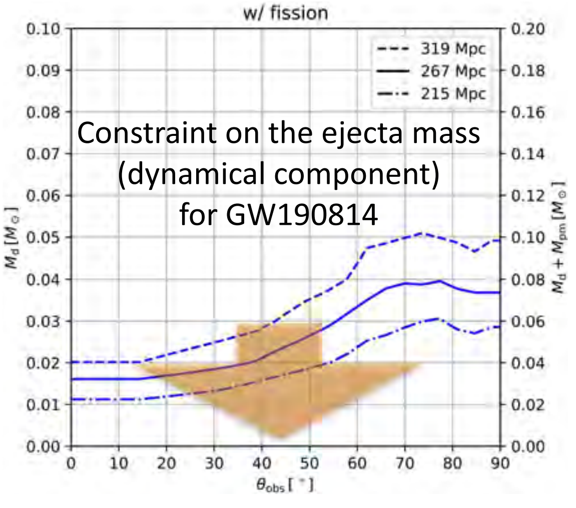

Fig. 3. Upper limit to the dynamical ejecta mass, M_d, and the total ejecta mass, $M_d + M_p$, as a function of viewing angle, θ_{obs}, consistent with the observational upper limits.

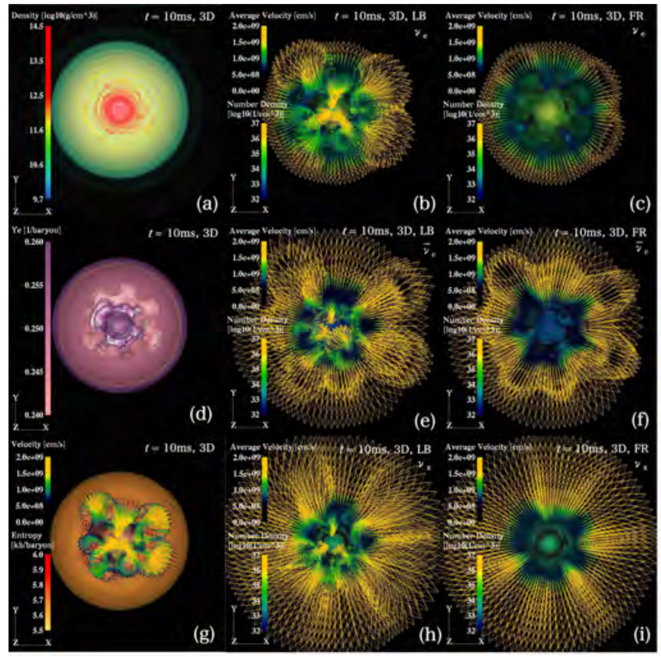

Fig. 4. The snapshots for the 3D BRH simulation at 10 ms after the core bounce. The left column shows the density (top), electron fraction Y_e (middle), and entropy by volume rendering and velocity by arrows (bottom). The middle column shows the neutrino number density (volume rendering) and average velocity (arrows) in the laboratory frame for the electron-type neutrinos ν_e (top), electron-type antineutrinos $\bar{\nu}_e$ (middle), and heavy-lepton-type neutrinos ν_x (bottom). The right column is the same as the middle column except that the fluid rest frame is considered.

shock finally stalls due to the energy loss by the photodissociation of accreting heavy nuclei. The problem is how to revive this stalled shock.

The neutrino heating mechanism is the leading hypothesis for the shock revival. After the core bounce, a proto-neutron star (PNS) is formed at the center. The PNS is the progenitor of the NS. This PNS emits energetic neutrinos, and these neutrinos are absorbed by matter behind the shock. Thanks to the energy supply by this process, the shock revives. This mechanism, however, does not work under spherical symmetry. This is concluded by the simulations which solve the Boltzmann equation for neutrino transport under the spherical symmetry. Currently, multi-dimensional simulations with approximate neutrino transport schemes indicate that the shock revives with the help of the multi-dimensional effects such as turbulence. However, the simulated explosion energy of $\sim 10^{50}$ erg is much smaller than the observed explosion energy. Since the conclusion in spherically symmetric simulations was obtained with the Boltzmann-neutrino-transport simulations, we think that performing the Boltzmann-neutrino-transport is necessary to obtain robust results in multi-dimensions. Therefore, we developed the multi-dimensional Boltzmann-radiation-hydrodynamics (BRH) code for CCSN simulations.

We ran a 3D simulation using the BRH code this year. This simulation covers until 20 ms after the core bounce. It revealed the fully multidimensional behavior of neutrinos with no symmetry (Figure 4) and paved the way for 3D shock revival simulations. Besides, the general relativistic extension of the code was developed. The Boltzmann neutrino transport solver developed this year correctly solves transport in curved spacetimes. This is a key to the first-principle code for CCSN.

Observational signals for CCSN neutrinos were investigated in a practical way. We developed an analytic model for CCSN neutrinos based on the Lane–Emden solution and neutrino diffusion. This model gives a very quick estimate for the PNS radius, mass, and surface structure. We further developed a coherent framework for neutrino detection. This includes the neutrino-radiation-hydrodynamics code for CCSN explosion and neutrino detection at the ground detector, i.e., Super-Kamiokande. The model and framework help us to get physical information of CCSN from future observation of CCSN neutrinos.

Research Topic 5: Gravitational Wave Astronomy

We perform the binary evolution of zero-metal (population III or Pop III) stars by using population synthesis simulations. We find that Pop III binaries tend to be binary black holes (BBHs) with chirp mass $M_{\rm chirp} \sim 30\ M_\odot$ and they can merge at present day due to long merger time. The merger rate densities of Pop III BBHs at $z = 0$ ranges 3.34–21.2 /yr/Gpc^3 which is consistent with the aLIGO/aVIRGO result of 9.7–101 /yr/Gpc^3. These Pop III binaries might contribute to some part of the massive BBH gravitational wave (GW) sources detected by aLIGO/aVIRGO. We also calculate the redshift dependence of Pop III BBH mergers. We find that Pop III low spin BBHs tend to merge at low redshift like LIGO events, while Pop III high spin BBHs do at high redshift, which can be confirmed by future GW detectors such as ET, CE, and DECIGO. These detectors can also check the redshift dependence of BBH merger rate and spin distribution. Our results show that except for one model, the mean effective spin $\langle \chi_{\rm eff} \rangle$ at $z = 0$ ranges 0.02–0.3 while at $z = 10$ it does 0.16–0.64. Therefore, massive stellar-mass BBH detection by GWs will be a key for the stellar evolution study in the early universe.

We show that the total mass of binary black holes from binary Pop III star evolution can be $\sim 150 M_\odot$, which agrees with the mass of the binary black hole GW190521 recently discovered by LIGO/Virgo. Our results show that the primary BH mass distribution of GW190521 like binaries which are made by Pop III binaries. The event rate of such massive stelar binary black hole mergers is estimated as 0.13–0.66 $(\rho_{\rm SFR}/(6\times10^5\ M_\odot/{\rm Mpc}^3))\ Err_{\rm sys}\ {\rm yr}^{-1}\ {\rm Gpc}^{-3}$, where $\rho_{\rm SFR}$ and $Err_{\rm sys}$ are the cumulative comoving mass density of Pop III stars depending on star formation rate and the systematic errors depending on uncertainties in the Pop III binary parameters, respectively. The event rate in our fiducial model with $\rho_{\rm SFR} = 6\times10^5\ M_\odot/{\rm Mpc}^3$ and $Err_{\rm sys} = 1$ is 0.13–0.66 $\rm yr^{-1}\ Gpc^{-3}$, which is consistent with the observed value of 0.02–0.43 $\rm yr^{-1}\ Gpc^{-3}$.

Research Topic 6: Impact of Binary Interactions on the Neutrino Background

Binary interactions, especially mass transfer and mergers, can strongly influence the evolution of massive stars and change their final properties and the occurrence of supernovae. We investigate how binary interactions affect predictions of the diffuse flux of neutrinos. By performing stellar population syntheses including prescriptions for binary interactions, we show that the resulting detection rates of the diffuse supernova neutrino background is enhanced by 15%–20% compared to estimates without binary considerations. A source of significant uncertainty arises due to the presently sparse knowledge of the evolution of rapidly rotating carbon-oxygen cores, especially those created as a result of mergers near the white dwarf to core collapse boundary. The enhancement effect may be as small as a few percent if the effects of rotation in postmerger systems are neglected, or as large as 75% if trends are extrapolated. Our estimates serve to highlight that binary effects can be important.

Research Topic 7: CALET Project

We have joined CALET, CALorimetric Electron Telescope, which is a mission for the Japanese Experiment Module-Exposed Facility (JEM-EF) on the International Space Station. The CALET mission aims at revealing unsolved problems in high energy phenomena of the Universe by carrying out accurate measurements of high energy spectra of electrons, gamma-rays and nuclei.

The energy spectra of carbon and oxygen in cosmic-rays obtained with CALET is shown in Figure 6. The observation period used in this analysis is from October 2015 to October 2019. The energy spectra are measured in kinetic energy per nucleon from 10 GeV$/n$ to 2.2 TeV$/n$ with an all-calorimetric instrument with a total thickness corresponding to 1.3 nuclear interaction length. The observed carbon and oxygen fluxes show a spectral index change of ~ 0.15 around 200 GeV$/n$ established with a significance $> 3\sigma$. They have the same energy dependence with a constant C/O flux ratio 0.911 ± 0.006 above 25 GeV$/n$. The spectral hardening is consistent with that measured by AMS-02, but the absolute normalization of the flux is about 27% lower, though in agreement with observations from previous experiments including the PAMELA spectrometer and the calorimetric balloon-borne experiment CREAM.

Bibliography

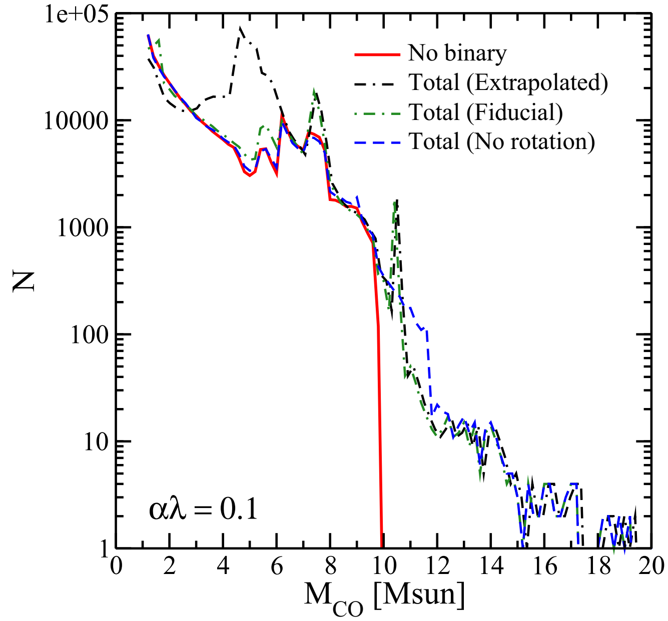

Fig. 5. Distributions of CO mass for our binary population synthesis compared to the case with no binary interactions (red solid). Three types of binary treatment with different postmerger evolution scenarios are shown: extending the study of Limongi et al (black dot-dashed-dashed), our fiducial model (green dot-dashed), and a low version neglecting postmerger rotation (dashed blue). CE parameter is $\alpha\lambda = 0.1$.

Papers in refereed journals

1. Kenta Kiuchi, Kyohei Kawaguchi, Koutarou Kyutoku, Yuichiro Sekiguchi, Masaru Shibata "Sub-Radian-Accuracy Gravitational Waves from Coalescing Binary Neutron Stars in Numerical Relativity. II. Systematic Study on the Equation of State, Binary Mass, and Mass Ratio", Phys. Rev. D, 101, 084006(25pp) (2020).

2. Kyohei Kawaguchi, Masaru Shibata, Masaomi Tanaka "Constraint on the Ejecta Mass for a Black Hole?Neutron Star Merger Event Candidate S190814bv", Astrophys. J., 893, 153(17pp) (2020).

3. Ataru Tanikawa, Tomoya Kinugawa, Jun Kumamoto, Michiko S. Fujii "Formation Rate of LB-1-like Systems through Dynamical Interactions", Pub. Astron. Soc. J., 72, 39(10pp) (2020).

4. Ataru Tanikawa, Takashi Yoshida, Tomoya Kinugawa, Koh Takahashi, Hideyuki Umeda "Fitting Formulae for Evolution Tracks of Massive Stars under Extreme Metal-Poor Environments for Population Synthesis Calculations and Star Cluster Simulations", Mon. Not. Roy. Astro. Soc., 495, 4170-4191 (2020).

5. Masaomi Tanaka, Daiji Kato, Gediminas Gaigalas, Kyohei Kawaguchi "Systematic Opacity Calculations for Kilonovae", Mon. Not. Roy. Astro. Soc., 496, 1369-1392 (2020).

6. V. A. Acciari, S. Ansoldi, L. A. Antonelli, A. Arbet Engels, K. Asano, et al. "Studying the Nature of

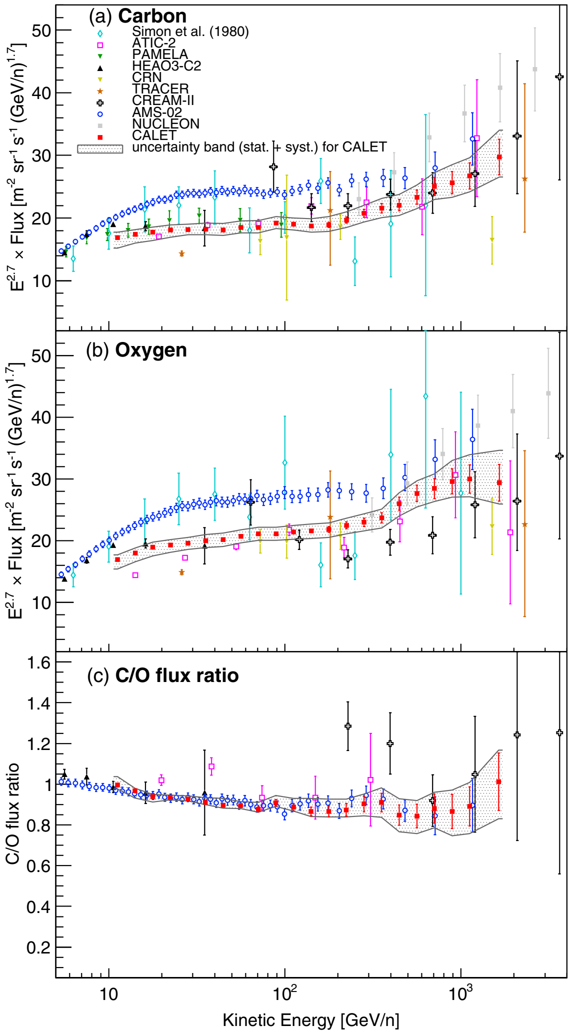

Fig. 6. Cosmic-ray (a) carbon and (b) oxygem spectrum measured by CALET (red points).

the Unidentified Gamma-Ray Source HESS J1841–055 with the MAGIC Telescopes", Mon. Not. Roy. Astro. Soc., 497, 3734-3745 (2020).

7. Smaranika Banerjee, Masaomi Tanaka, Kyohei Kawaguchi, Daiji Kato, Gediminas Gaigalas "Simulations of Early Kilonova Emission from Neutron Star Mergers", Astrophys. J., 901, 29(12pp) (2020).

8. D. Psaltis, et al. "Gravitational Test beyond the First Post-Newtonian Order with the Shadow of the M87 Black Hole", Phys. Rev. Lett., 125, 141104(9pp) (2020).

9. Shotaro Yamasaki, Yuri Lyubarsky, Jonathan Granot, Ersin Göğüş "Spectral Modification of Magnetar Flares by Resonant Cyclotron Scattering", Mon. Not. Roy. Astro. Soc., 498, 484-494 (2020).

10. Akira Harada, Hiroki Nagakura, Wakana Iwakami, Hirotada Okawa, Shun Furusawa, Kohsuke Sumiyoshi, Hideo Matsufuru, Shoichi Yamada "The Boltzmann-Radiation-Hydrodynamics Simulations of Core-Collapse Supernovae with Different Equations of State: the Role of Nuclear Composition and the Behavior of Neutrinos", Astrophys. J., 902, 150(25pp) (2020).

11. Tomoya Kinugawa, Takashi Nakamura, Hiroyuki Nakano "Chirp Mass and Spin of Binary Black Holes from First Star Remnants", Mon. Not. Roy. Astro. Soc., 498, 3946-3963 (2020).

12. Wakana Iwakami, Hirotada Okawa, Hiroki Nagakura, Akira Harada, Shun Furusawa, Kosuke Sumiyoshi, Hideo Matsufuru, Shoichi Yamada "Simulations of the Early Postbounce Phase of Core-Collapse Supernovae in Three-Dimensional Space with Full Boltzmann Neutrino Transport", Astrophys. J., 903, 82(24pp) (2020).

13. V. A. Acciari, S. Ansoldi, L. A. Antonelli, A. Arbet Engels, K. Asano, et al. "Detection of the Geminga Pulsar with MAGIC Hints at a Power-Law Tail Emission beyond 15 GeV", Astron. Astrophys., 643, L14(6pp) (2020).

14. O. Adriani, Y. Akaike, K. Asano, et al. "Direct Measurement of the Cosmic-Ray Carbon and Oxygen Spectra from 10 GeV/n to 2.2 TeV/n with the Calorimetric Electron Telescope on the International Space Station", Phys. Rev. Lett., 125, 251102(7pp) (2020).

15. Katsuaki Asano, Kohta Murase, Kenji Toma "Probing Particle Acceleration through Broadband Early Afterglow Emission of MAGIC Gamma-Ray Burst GRB 190114C", Astrophys. J., 905, 105(9pp) (2020).

16. Yudai Suwa, Akira Harada, Ken'ichiro Nakazato, Kohsuke Sumiyoshi "Analytic Solutions for Neutrino-Light Curves of Core-Collapse Supernovae", Prog. Theo. Exp. Phys., 2021, 013E01(12pp) (2021).

17. A. Acharyya, et al. "Sensitivity of the Cherenkov Telescope Array to a Dark Matter Signal from the Galactic Centre", J. Cos. Astropart. Phys., 01, 057(62pp) (2021).

18. Tomoya Kinugawa, Takashi Nakamura, Hiroyuki Nakano "Formation of Binary Black Holes Similar to GW190521 with a Total Mass of ?150M? from Population V Binary Star Evolution", Mon. Not. Roy. Astro. Soc., 501, L49-L53 (2021).

19. Shunsaku Horiuchi, Tomoya Kinugawa, Tomoya Takiwaki, Koh Takahashi, Kei Kotake "Impact of Binary Interactions on the Diffuse Supernova Neutrino Background", Phys. Rev. D, 103, 043003(13pp) (2021).

20. Kota Hayashi, Kyohei Kawaguchi, Kenta Kiuchi, Koutarou Kyutoku, Masaru Shibata "Properties of the Remnant Disk and the Dynamical Ejecta Produced in Low-Mass Black Hole-Neutron Star Mergers", Phys. Rev. D, 103, 043007(16pp) (2021).

21. Tomoya Kinugawa, Takashi Nakamura, Hiroyuki Nakano "Formation of Mass Gap Compact Object and Black Hole Binary from Population Ⅲ Stars", Prog. Theo. Exp. Phys., 2021, 021E01(11pp) (2021).

22. Masamitsu Mori, Yudai Suwa, Ken'ichiro Nakazato, Kohsuke Sumiyoshi, Masayuki Harada, Akira Harada, Yusuke Koshio, Roger A. Wendell "Developing an End-to-End Simulation Framework of Supernova Neutrino Detection", Prog. Theo. Exp. Phys., 2021, 023E01(21pp) (2021).

23. V. A. Acciari, S. Ansoldi, L. A. Antonelli, A. Arbet Engels, K. Asano, et al. "MAGIC Observations of the Nearby Short Gamma-Ray Burst GRB 160821B", Astrophys. J., 908, 90(11pp) (2021).

24. H. Abdalla, et al. "Sensitivity of the Cherenkov Telescope Array for Probing Cosmology and Fundamental Physics with Gamma-Ray Propagation", J. Cos. Astropart. Phys., 02, 048(63pp) (2021).

25. Tomohisa Kawashima, Kenji Toma, Motoki Kino, Kazunori Akiyama, Masanori Nakamura, Kotaro Moriyama "A Jet-Bases Emission Model of the EHT2017 Image of M87*", Astrophys. J., 909, 168(6pp) (2021).

26. Ryuichiro Akaho, Akira Harada, Hiroki Nagakura, Kohsuke Sumiyoshi, Wakana Iwakami, Hirotada Okawa, Shun Furusawa, Hideo Matsufuru, Shoichi Yamada "Multidimensional Boltzmann Neutrino Transport Code in Full General Relativity for Core-Collapse Simulations", Astrophys. J., 909, 210(17pp) (2021).

27. Ataru Tanikawa, Hajime Susa, Takashi Yoshida, Alessandro A. Trani, Tomoya Kinugawa "Merger Rate Density of Population III Binary Black Holes below, above, and in the Pair-Instability Mass Gap", Astrophys. J., 910, 30(31pp) (2021).

28. K. Akiyama, et al. "First M87 Event Horizon Telescope Results. VII. Polarization of the Ring", Astrophys. J. Lett., 910, L12(48pp) (2021).

29. K. Akiyama, et al. "First M87 Event Horizon Telescope Results. VIII. Magnetic Field Structure near The Event Horizon", Astrophys. J. Lett., 910, L13(43pp) (2021).

30. C. Goddi, et al. "Polarimetric Properties of Event Horizon Telescope Targets from ALMA", Astrophys. J. Lett., 910, L14(54pp) (2021).

31. V. A. Acciari, S. Ansoldi, L. A. Antonelli, A. Arbet Engels, M. Artero, K. Asano, et al. "VHE Gamma-Ray Detection of FSRQ QSO B1420+326 and Modeling of its Enhanced Broadband State in 2020", Astron. Astrophys., 647, A163(19pp) (2021).

Other Activities

Ashra NTA

Combined detection of PeV ν's and γ's from an astronomical accelerator provides indispensable identification of the location and the physics mechanism i.e. $p+\gamma \rightarrow \Delta^+ \rightarrow \pi^0 + p,\ \pi^+ + n$; $p + \text{nucleus} \rightarrow \pi^{\pm,0} + X$, which can clearly reveal the unresolved origin of cosmic rays. Recently several observations suggesting cosmic ray accelerators have been independently made [1, 2, 3]. Such a "multi-particle" paradigm [4] can be performed by Ashra NTA with the single unique detector system [5].

Since 2001, we have been developing the Earth-skimming tau ν (ES-ν_τ) air-shower technique [6], as a promising potential, which can enjoy a large target mass by detecting air-showers (AS's) produced by τ decays in the air. The τ's, produced by ν_τ's that interact with the Earth matter, traverse, and emerge out of a mountain or the ground decaying and generating AS's. Adding to that, the advantages are perfect shielding of cosmic ray secondaries, precise arrival direction determination, and negligible background from atmospheric ν's [7]. The detectors of Ashra-1 and its extension plan NTA can precisely image AS Cherenkov (CE) and fluorescence (FL) light generated from ES-ν_τ and γ AS's in the huge effective volume of air around the mountain in the field of view (FOV) (Figure 7) [8].

The Ashra Phase 1 (Ashra-1) [9] light collector (LC) (Figure 8 Left) achieves the total resolution of 3 arcmin covering FOV of 42° (Figure 8 Right). The key feature is the use of electrostatic rather than optical lenses to generate convergent beams with the 20 inch Photoelectric Lens Imaging tube (PLI) [10] (Figure 8) demagnifying to 1 inch at focal surface, enabling high resolution over a wide FOV [11]. The following trigger readout Photoelectric Image Pipeline (PIP) [12] can image and read out three independent phenomena on different time scales, i.e. AS CE emission (ns), AS FL (μs), and starlight (s), without sacrificing the S/N ratios. We have shown the cosmic ray energy spectrum and the stringent ES-ν_τ limit from the updated Ashra-1 3rd observation period (Obs3) of 1863 hours [13]. The ν_τ with the E_{ν_τ} detection sensitivity of the Ashra-1 LC and the validity of the reconstruction procedure have been well demonstrated.

As another unique advantage of Ashra-1, the wide FOV and parallel trigger with PIP enable us to search for the precursor and very early prompt optical emission from very energetic transient objects like GRBs adding to PeV ν's, γ-rays, and nuclei. To investigate GRB optical emission, we define three specific observational time domains with respect to satellite triggers; precursor ($0<t_0-t_e<24$ hr), prompt ($t_s<t_0<t_e$), and afterglow ($0<t_s-t_0<3$ hr) where t_0 is a satellite trigger time, t_s is the time when the trajectory of the center position of GRB counter part object triggered by the satellite enters into a FOV of an Ashra-1 LC and t_e is the time when it exits the FOV. Through out the observation time for optical flashes and afterglows, we preselected and categorized 32 (33), 5 (5), and 4 (2) GRBs triggers by Swift (Fermi) satellite, which were circulated through Gamma-ray Coordi-

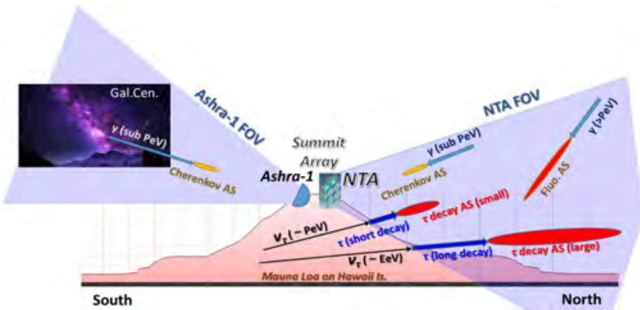

Fig. 7. Concept of imaging observation of PeV ν's, γ-rays, and nuclei with Ashra NTA summit array. For example, Ashra-1 and NTA detectors can simultaneously observe our galactic bulge in their FOV, checking the coincidence of ν's with γ-rays originating from the same objects or regions.

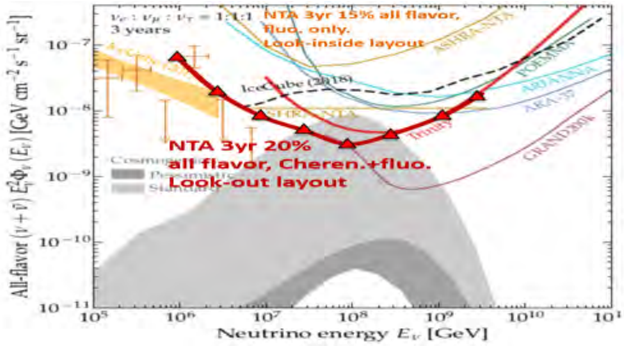

Fig. 9. Neutrino flux sensitivity of NTA including both fluorescence and far-Cherenkov modes, that with only fluorescence mode, and other experiments, neutrino flux predictions, and existing flux constraints. Figure adapted from [8].

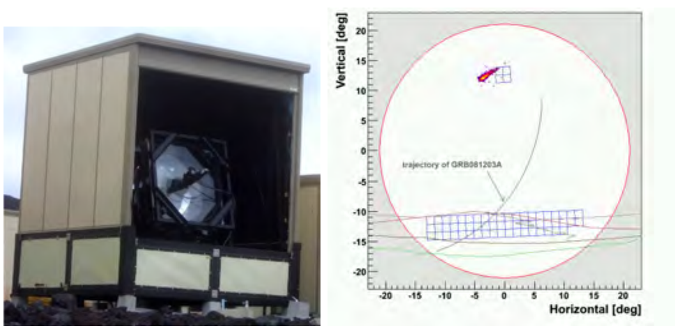

Fig. 8. *Left*: The Ashra-1 light collector (LC) facing Mauna Kea. *Right*: Boundary (large red circle) between the inside (open circle) and outside (hatched area) of the FOV of the LC and the layout of trigger pixel FOVs (blue boxes) for Cherenkov τ shower observation. Attached array of the trigger pixel FOVs (upper four blue boxes) to check the detection sensitivity with ordinary cosmic-ray air showers at a higher elevation, A simulated image of a cosmic-ray air shower readout along the trigger (points), and the trajectory of GRB081203A counterpart (circular arc) [14] are shown.

nates Network (GCN)[15], into the three time domains respectively as optical transient candidates. By optimizing the layout of the NTA stations to enhance the sensitivity for ES-ν_τ's around 1 PeV from the simulation studies [5, 7], four NTA stations will be served on Mauna Loa at 3000 - 3500 m a.s.l. (Summit Array), which watch the air volume surrounding the mountain including the surface. Mauna Loa is the world largest volcano suitable for detecting CE and FL light from τ AS's with both short and long decay lengths and γ AS's as shown Figure 7. Figure 9 shows the neutrino flux sensitivity of NTA with only fluorescence mode, that including far-Cherenkov mode and other experiments, neutrino flux predictions, and existing flux constraints. The NTA neutrino sensitivity can be fairly competitive in PeV-EeV.

As an intermiediate step towards the full NTA project, the combination between Ashra-1 and NTA detector units is planned to realize the comprehensive observation both with TeV-PeV γ-rays and PeV ν's. Six combined Ashra-1 LCs will be realigned for the FOV centers to be on the arc of the galactic center (GC) trajectory maximizing the stereoscopic observation efficiency. The adjacent FOVs of the LCs overlap each other by half, and the distance between the LCs is 80 meters. It results in total rate of the stereoscopic observation can be more than 70% of the trajectory in the sky. The estimated annual observable time of 1150 hours $\times \varepsilon_w$ during nights without moon in the south is more than 50 times better than HESS achieved i.e. 227 hours for Sgr A* in 10 years [2], assuming the weather efficiency $\varepsilon_w \sim 90\%$ according to the Ashra-1 operation.

Another fascinating is the detection of γ-rays with the large zenith-angle (LZA) method. The galactic bulge (GB) has the trajectory in the southern night sky with LZA more than 50 degrees, corresponding to the shower max distance larger than 9 km and the detection threshold energies higher than 16 TeV. Our simulation studies check the cut-off energy in the γ-ray spectrum in the GB or central region. We confirm the LZA method is promising particularly for the PeV γ-ray detection. Once the northward NTA units detect ν's from the same γ-ray objects observed by Ashra-1 LCs, we can argue, more concretely than ever, the physics of the occurrence of γ-rays and ν's [8]. The GB can be considered an intriguing testing site for the discovery of elementary particles predicted by the non-standard theory of particle physics. Observing the combined flux ν and γ-ray can probe and verify non-standard theories such as anomalous reaction cross sections and extra dimensions. In particular, for the heuristic search of dark matter, which is of great significance for the fundamental astroparticle physics, the wide-angle and high-accuracy γ-ray/$i\nu$ composite monitoring by Ashra NTA is extremely powerful. In terms of the detection sensitivity of ν's and γ-rays from the decay of dark matter WIMPS after annihilation, which constitutes the galactic halo, the Ashra NTA project, which monitors large-angle CE and FL in a wide field of view with high precision, surpasses the expected sensitivity of future plans such as large-scale IACTs, ground array detectors and satellite observations in the PeV-EeV region by a factor of 10 to 100 as shown Figure 10 and 11.

Bibliography

[1] M. Aartsen et al., PRL **113**, 101101 (2014).

[2] HESS Collab., Nature **531**, 476 (2016).

[3] IceCube Collab., Science **361**, 147 (2018).

[4] M. Sasaki, ICRR2000 Sat. Sympo., 109 (2000).

[5] M. Sasaki, G. Hou, arXiv:1408.6244 (2014).

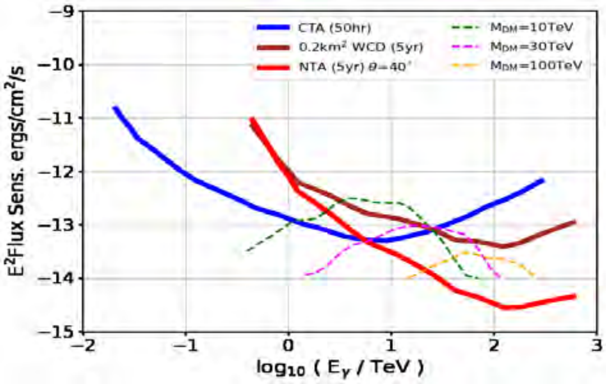

Fig. 10. Flux sensitivities of this Ashra NTA for 5 years comparing with a possible ground-based γ-ray survey observatory (200,000 m^2 WCD) and of CTA as a function of γ-ray energy E_γ for 5 years and 50 hours of observation of the galactic halo, respectively and the predicted DM annihilation rate into τ pairs [16].

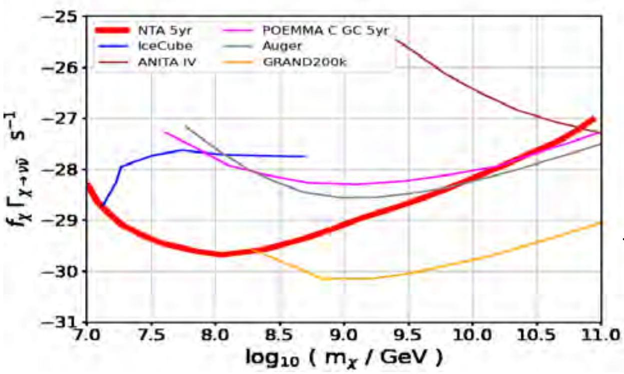

Fig. 11. Sensitivities to dark matter decay width (right) for the τ-pair channels. The 5-year sensitivities of this Ashra NTA, POEMMA, GRAND10k, GRAND200k, ANITA IV, Auger, and IceCube [17]. The proposed Ashra NTA has the highest sensitivity with the air light Earth skimming method in the 10 PeV to sub-EeV region.

[6] M. Sasaki, et al., Astropart. Phys. **19**, 37 (2003).

[7] Y. Asaoka, M. Sasaki, Astropart. Phys. **41**, 7 (2013).

[8] M. Sasaki (Ashra-1/NTA), PoS (ICRC2019) 1003.

[9] M. Sasaki, Prog. Theo. Phys. Suppl. **151**, 192 (2003).

[10] Y. Asaoka, M. Sasaki, NIMA **647**, 34 (2011).

[11] M. Sasaki, et al., NIMA **492**, 49 (2002).

[12] M. Sasaki et al., NIMA **501**, 359 (2003).

[13] S. Ogawa (Ashra-1), PoS (ICRC2019) 970.

[14] Y. Aita, et al., ApJL 736, L12 (2011).

[15] http://gcn.gsfc.nasa.gov/

[16] Engel, K. L., et al. "Astro2020 Science White Paper Searching for TeV Dark Matter in the Milky Way Galactic Center."

[17] Guepin et al., PoS (ICRC2021) 551 (2021)

γI Group

γI Project

γI Consortium
[Spokesperson : R.Enomoto]

Collaboration list:
ICRR, The University of Tokyo, Chiba, Japan: R. Enomoto; National Institute of Technology, Sendai College, Miyagi, Japan: M. Kagaya College of Science, Ibaraki University, Ibaraki, Japan: H. Katagiri; Faculty of Medical Engineering and Technology, Kitasato University, Kanagawa, Japan: H. Muraishi, S. Ishikawa; IPNS, High Energy Accelerator Research Organization, Ibaraki, Japan: M. M. Tanaka; National Cancer Center Hospital East, Chiba, Japan: D. Kano, T. Watanabe;

Shift-invariant gamma-ray imaging by adding a detector rotation function to a high-sensitivity omnidirectional Compton camera[1]

The Compton camera technique is a well-known method of visualizing the distribution of radiation sources that emit gamma rays with energies of approximately 1 MeV. One major disadvantage of this technique is that the reconstructed image is degraded owing to the appearance of artificial uneven structures caused by accumulating rings estimated from each event. In this study, we demonstrated that we can easily achieve shiftinvariant gamma-ray imaging with a drastic reduction in these artificial uneven structures by rotating the Compton camera during the measurement while also applying image sharpening techniques based on the filtered backprojection algorithm used in computed tomography.

Figure 12 shows a picture of the detector. Six scintillators were placed at the vertexes of an octahedron with a side length of 10 cm to obtain uniform acceptance and angular resolution in all directions, even with a small number of elements. Each CsI (Tl) scintillator (cube, 3.5 × 3.5 × 3.5 cm in size) was read out with a super-bialkali photo-multiplier tube (PMT) assembly (Hamamatsu Photonics H11432-100). The signals were fed into a 16-channel flash ADC board (operated at 2.5 MHz) using SiTCP technology. When two hits are coincident above some threshold, a gate signal is generated, and the waveform data stored in the FPGA registers are transferred to a PC via an Ethernet connection. The timing resolution (σ) between two hit counters was 60 ns when 511 keV gamma rays were measured from the ^{22}Na-sealed source. The Compton camera was fixed to a motorized rotation stage (Sigma Koki, OSMS-60YAW), as shown in Fig. 1. The detector rotation stage is controlled by an online computer via USB using an independent program that was also created using Visual C++. The online program that controls the Compton camera can save the rotation angle of a detector for each event by referring to the shared memory when saving the waveform data for each two-fold coincidence event.

To investigate how multiple gamma-ray sources are reconstructed, performance tests were also carried out using two 0.8

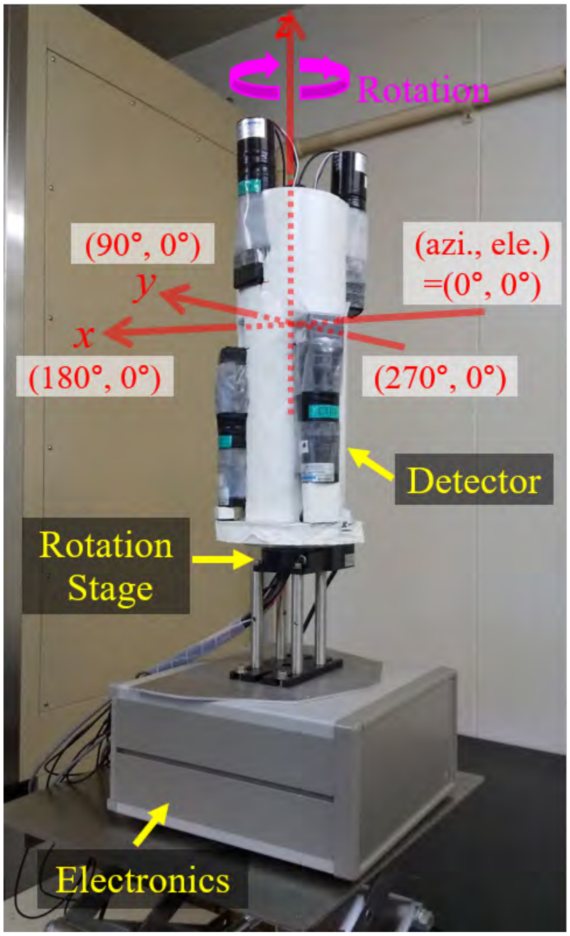

Fig. 12. Photograph of a developed Compton camera with the detector rotation function.

MBq ^{22}Na-sealed sources in different directions at a distance of 1 m from the detector. The measurements were done for 60 min with rotation of the Compton camera from 0 ° to 360 ° every 10 s at angular intervals of 1 ° , assuming continuous detector rotation at a constant speed as in the case of the one radiation source mentioned above. The results are shown in Figs. 13(a)(h), where the image sharpening technique was also applied to the back projection. A drastic reduction in these artificial uneven structures was achived by rotating the Compton camera during the measurement. When the distances between the two sources were 60^o [Figs. 13(a), (e)] and 40^o [Figs. 13(b), (f)], two sources were successfully reconstructed as a superposition of independent point sources. This implies that a shift-invariant gamma-ray imaging is well achievable. Additionally, when the two sources were 30^o apart [Figs. 13(c), (g)], their partial regions were reconstructed by overlapping, but the peak positions were separable. Furthermore, when the distance between the two sources approached 20^o, it became difficult to separate the two sources; instead, they were reconstructed as a distribution with one peak spread in the elevation [Fig. 13(d)] and azimuthal [Fig. 13(h)] directions, respectively. Thus, the angular resolution of this system was slightly less than 30^o in FWHM. In fact, the angular resolution (σ) obtained from 2D Gaussian fitting of the measurement result with one source was 11.7^o in the azimuth and 11.0^o in the elevation direction, which is in good agreement with the above estimation.

Development of an omnidirectional Compton camera using CaF_2(Eu) scintillators to visualize gamma rays with energy below 250 keV for radioactive environmental monitoring in nuclear medicine facilities[2]

We developed an omnidirectional Compton camera for radioactive environmental monitoring which can visualize gamma rays with energy below 250 keV emitted from various radiopharmaceuticals used in nuclear medicine facilities to prevent occupational radiation exposure. An omnidirectional Compton camera based on high light yield scintillators CsI(Tl) or NaI(Tl) developed in our previous studies is a promising system for environmental radiation monitoring because it has a wide field of view and high sensitivity for sub-MeV gamma rays. However, its sensitivity rapidly decreases below 250 keV because photoelectric effect becomes more dominant than the Compton scattering process due to their large effective atomic numbers (approximately 50). Thus, CaF_2(Eu) was adopted, which has both low effective atomic number (approximately 15) and high light yield. Four CaF2(Eu) crystals were arranged symmetrically to achieve a relatively uniform acceptance in all directions. Similarly, the detector rotation technique was adopted to suppress artificial patterns in a reconstructed gamma-ray image because of the small number of crystals. Through experiments in a laboratory and at a nuclear medicine facility, the capability of the camera to visualize gamma rays in energies from 250 keV to 60 keV with reasonable observation time for practical clinical use was confirmed.

Four CaF_2(Eu) crystals manufactured by OHYO KOKEN KOGYO Co., Ltd. are set at the vertexes of a tetrahedron. Each scintillator is used as a scatterer and absorber. This geometrical symmetry facilitates a relatively uniform acceptance in all directions even with the small number of scintillators, and thus, reduces the detector size, weight, and cost. The small number of counters generally makes artificial patterns in an image called ‘‘ ghost ’’ in a reconstructed image. This phenomenon is attributed to the limited number of ring patterns due to the small number of scintillation counters. By rotating the detector during a measurement, the number of ring patterns can increase, i.e., we can increase the effective number of scintillation counters and suppress ghost features. Furthermore a diameter and height of 1 in (2.54 cm) for the crystal size was adopted to achieve both good energy resolution and high detection efficiency. The length of the side of the tetrahedron is set to 6 cm to obtain a moderate angular resolution of approximately 12^o and reasonable sensitivity to reduce observation time. We emphasize that the energy deposit of Compton scattering is always smaller theoretically than that of subsequent photoabsorption for events with incident gamma-ray energy $< m_ec^2/2 = 256$ keV from a simple kinematical argument. Thus, for such energies, we can identify the scintillator in which a gamma ray is Compton scattered and reconstruct an image without false events due to misidentification of those backscattered. Scintillation photons produced in each scintillator are detected with a photomultiplier tube (PMT) as-

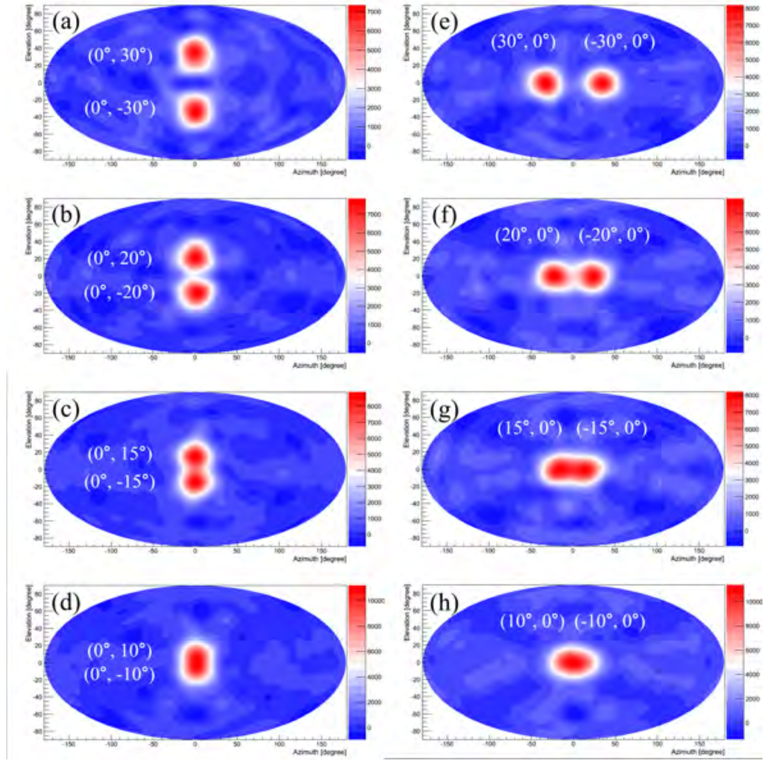

Fig. 13. (Color online) Reconstructed images of 511 keV gamma rays from two ^{22}Na-sealed source sin the various directions (radioactivity: 0.8 MBq each; measurement time: 30 min; distance between detector and source: 1 m). (a) (azimuth, elevation) = (0°, 30^{o}), (0^{o}, $-$ 30^{o}). (b) (0^{o}, 20^{o}), (0^{o}, $-$ 20^{o}). (c) (0^{o}, 15^{o}), (0^{o}, $-$ 15^{o}). (d) (0^{o}, 10^{o}), (0^{o}, $-$ 10^{o}). (e) (30^{o}, 0^{o}), ($-$ 30^{o}, 0^{o}). (f) (20^{o}, 0^{o}), ($-$ 20^{o}, 0^{o}). (g) (15^{o}, 0^{o}), ($-$ 15^{o}, 0^{o}). (h) (10^{o}, 0^{o}), ($-$ 10^{o}, 0^{o}).

sembly (H11432-100, Hamamatsu Photonics K. K.). A Cock-croftWalton high-voltage power supply is installed inside the PMT assembly. The PMT output is charge integrated, amplified and shaped with the time constant of approximately 3 μs in a preamplifier circuit. The voltage signals from the preamplifiers are fed into a 16-channel flash analog-to-digital converter (FADC) board with SiTCP technology. The waveforms of these signals are digitized by FADC chips (sampling speed, 2.5 MHz) and fed into an FPGA. A hit channel is found in the FPGA by comparing a signal voltage with some threshold voltage. A threshold voltage can be set for each channel individually depending on its electronic noise. When two or more channels are above the thresholds coincidently, a gate signal is generated and the waveform data stored in the FPGA registers are transferred to a PC via Ethernet. Fig. 14 shows the photograph of our camera (size, 30 cm × 20 cm × 40 cm; weight, 2 kg).

To demonstrate the capability to visualize gamma rays from actual radiopharmaceuticals in more realistic environment, verification tests were conducted in a nuclear medicine facility using radioactive sources of ^{99m}Tc and ^{111}In in syringes. The length and diameter of the syringes were 95 mm and 7 mm, respectively. The corresponding angular size at 100 cm distance from the detector is 5^{o} ; hence, they can be assumed as a point source for the measurements in this study.

We performed a measurement with two radioactive sources with a total observation time of 9 min. Two photopeaks from ^{111}In were confirmed and the events with 171 $\pm$ 20

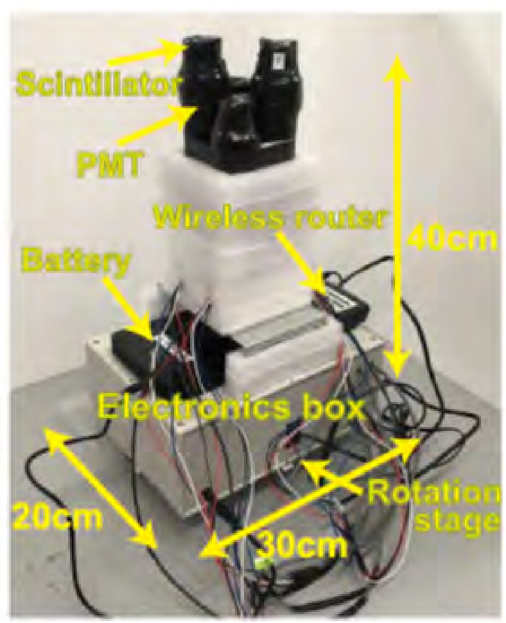

Fig. 14. Photograph of the developed camera.

keV and 245 $\pm$ 20 keV energy were selected. The background was estimated by fitting the total spectrum with two Gaussian functions for two gamma-ray lines and a Gaussian function for the background. A gamma-ray image from ^{111}In is shown in Fig. 15. A 9.5 MBq-source (src 1) was located roughly at the center of the field of view 110 cm from the detector, and the other source (src 2) with 9.3 MBq was placed at the azimuthal angle of 70^o at the distance of 120 cm from the detector. The spatial separation between 2 sources is about 130 cm. The 2 sources were spatially resolved. The expected ratio of gamma-ray intensity is (9.3 MBq/9.5 MBq)(120 cm/110 cm)$^{-2}$ = 0.82, and the ratio of the peak counts between src 2 and src 1 is 0.75 ± 0.09, which is consistent within the statistical error.

Bibliography

[1] Shift-invariant gamma-ray imaging by adding a detector rotation function to a high-sensitivity omnidirectional Compton camera, Hiroshi Muraishi, Ryoji Enomoto, Hideaki Katagiri, Mika Kagaya, Takara Watanabe, Naofumi Narita, Daisuke Kano, Saki Ishikawa, Hiromichi Ishiyama, Japanese Journal of Applied Physics 59(9) 090911-090911 2020/9/1

[2] Development of an omnidirectional Compton camera using CaF_2(Eu) scintillators to visualize gamma rays with energy below 250 keV for radioactive environmental monitoring in nuclear medicine facilities, H. Katagiri;N. Narita;R. Enomoto;H. Muraishi;D. Kano;T. Watanabe; R. Wakamatsu;M. Kagaya;M.M. Tanaka, Nuclear Inst. and Methods in Physics Research, A996, 165133

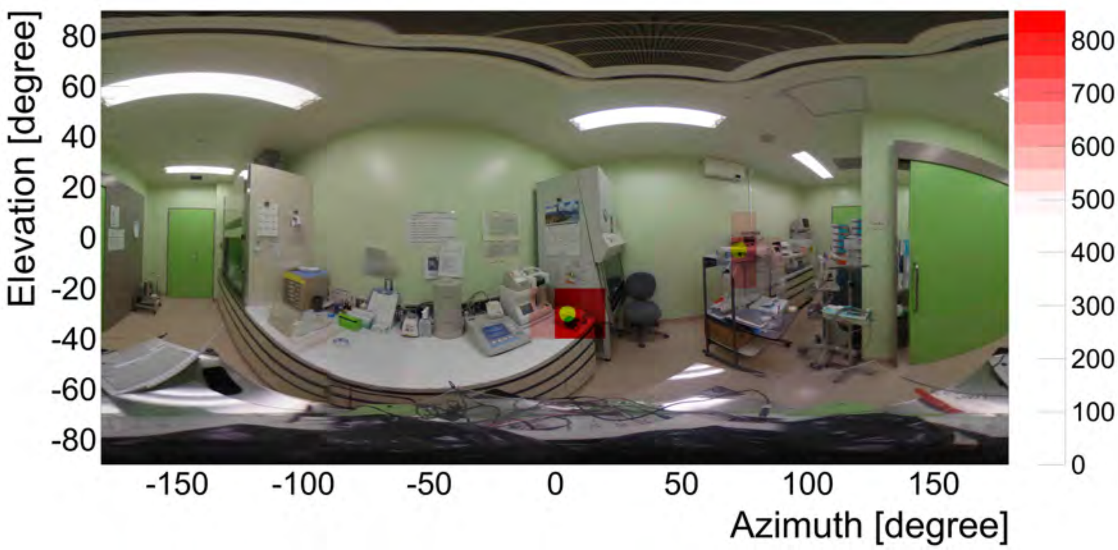

Fig. 15. Gamma-ray all-sky image from ^{111}In sources. The optical image was obtained using a RICOH THETA camera (all-sky optical camera). The figures are shown in equirectangular projection. The red mosaics show the gamma-ray distributions with values $>$ 60 % of the peak value. The source positions are indicated by yellow closed circles.

ASTROPHYSICS AND GRAVITY DIVISION

Overview

Astrophysics and Gravity Division consists of Gravitational Wave Group, The Observational Cosmology Group, Primary Cosmic Ray Group and Theory Group.

The Gravitational Wave Group conducts experimental research of gravitational waves with researchers of gravitational wave experiments and theory in Japan. The main items are the construction of the large-scale cryogenic interferometer (KAGRA) at Kamioka underground and the operation of CLIO. For this purpose, KAGRA observatory was established at the beginning of the fiscal year of 2016 to assist the construction of KAGRA gravitational wave telescope.

The Observational Cosmology Group studies cosmic history based on deep multi-wavelength observations in collaboration with worldwide researchers. This group has started a new optical deep survey project with the wide-field imager of Hyper Suprime-Cam mounted on the Subaru telescope.

Theory Group conducts both theoretical studies of the Universe and astroparticle physics.

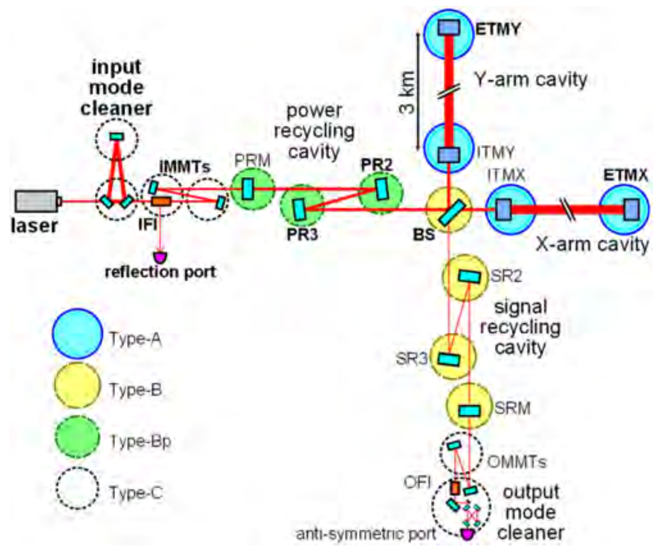

Fig. 1. Schematic view of the bKAGRA interferometer[3]. Type-A, Type-B, Type-Bp, and Type-C are the names of vibration isolation systems for each mirror.

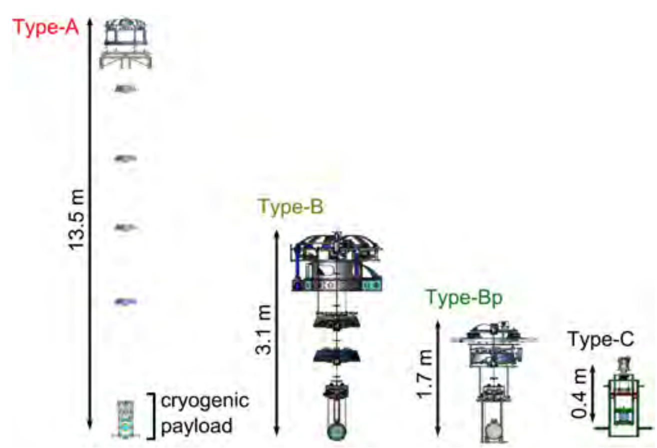

Fig. 2. KAGRA vibration isolation systems[3]. KAGRA equips four kinds of vibration isolation systems as Type-A, Type-B, Type-Bp, and Type-C.

Gravitational Wave Group

KAGRA Project Status

[Spokesperson : Takashi UCHIYAMA]

ICRR, The Univ. of Tokyo, Hida, Gifu 506-1205

Overview

KAGRA, Large-scale Cryogenic Gravitational wave Telescope, aims at detecting gravitational waves and developing gravitational wave astronomy, which was established by the first detection of gravitational waves by LIGO. KAGRA employs a 3 km L-shaped laser interferometer with a cryogenic mirror system placed underground at Kamioka[1]. The KAGRA development is divided into two stages: the initial KAGRA (iKAGRA) and baseline KAGRA (bKAGRA). The iKAGRA interferometer is a simple Michelson interferometer with a 2-Watt laser, room-temperature mirrors, and a simple vibration isolation system. We completed the iKAGRA interferometer with a test run in April 2016[2]. Then we proceeded to bKAGRA.

Figures 1 and 2 show a schematic view of the optical layout of the bKAGRA interferometer and the KAGRA vibration isolation systems. Table 1 shows design parameter of the bKAGRA interferometer[3]. The bKAGRA interferometer will employ a Resonant Sideband Extraction (RSE) interferometer with a 180-Watt laser, cryogenic Sapphire mirrors, and several kinds of vibration isolation systems. The bKAGRA interferometer should attain a sensitivity high enough for the detection of gravitational waves with the help of the high power laser and RSE interferometer to reduce the quantum noise, the cryogenic Sapphire mirrors to reduce the thermal noise, and the vibration isolation systems to reduce the seismic noise. Figure 3 shows designed sensitivities of bKAGRA in the cases of Broadband RSE (BRSE) and of Detuned RSE (DRSE), where the incoherent sum of the fundamental noise sources is assumed. The observation range for an inspiral and merger of neutron-star binary reaches 135 Mpc in BRSE and 153 Mpc in DRSE with the same definition of the observation range as LIGO and Virgo.

Figure 4 shows the international collaborative observation scenario[4]. LIGO conducted Observation 1 (O1) from

Table 1. The design parameters of the bKAGRA interferometer[3].

Arm cavity length	3000 m	Test mass size	$\phi 22\,\mathrm{cm} \times 15\,\mathrm{cm}$
Laser wave length	1064 nm	Mass of test mass	22.8 kg
Input power at PRM	67W	Temperature of test mass	22 K
Arm intra-cavity power	340 kW	Beam radius at test mass	3.5 cm
ITM transmittance	0.4 %	PRC/SRC lengths	66.6 m
PRM transmittance	10 %	Detuning angle	3.5 deg
SRM transmittance	15 %	Homodyne angle	135.1 deg

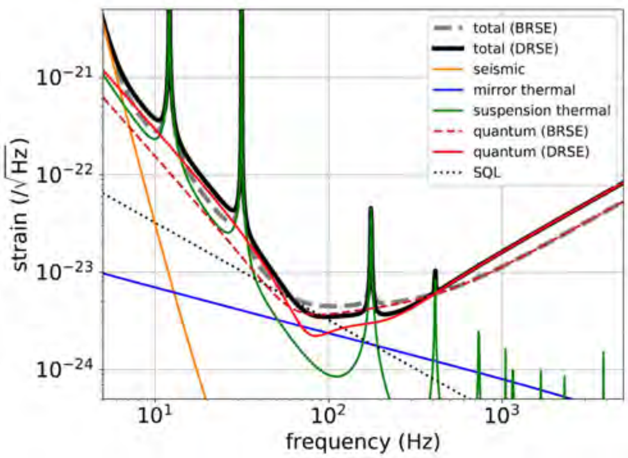

Fig. 3. The designed sensitivity of the bKAGRA interferometer[3]. "total", "seismic", "mirror thermal", "suspension thermal", "quantum", and "SQL" mean total sum of fundamental noise sources shown in this figure, seismic noise including gravity gradient noise, mirror thermal noise, suspension thermal noise, quantum noise, and standard quantum limit, respectively. The figure shows "total" and "quantum noise" in both Broadband RSE (BRSE) and Detuned RSE (DRSE) cases. Observation range for an in-spiral and merger of neutron-star binary reaches 135 Mpc in BRSE and 153 Mpc in DRSE with the same definition of the observation range as LIGO and Virgo.

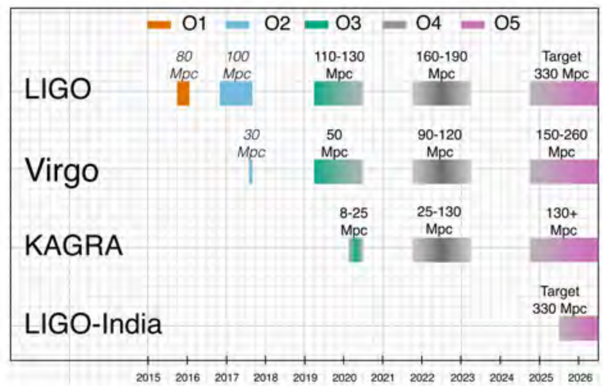

Fig. 4. International observation scenario[4]. LIGO and Virgo started Observation 3 on April 1 in 2019 and it was suspended on March 27, 2020, due to the influence of the COVID-19. The schedule of the next international collaborative observation called O4 is still under discussion and it has been decided that it will only be started after June 2022 at the earliest as of May 2021.

September 12, 2015, to January 19, 2016, and Observation 2 (O2) from November 30, 2016, to August 25, 2017. Virgo joined O2 on August 1, 2017. LIGO and Virgo started Observation 3 (O3) from April 1, 2019. Initially, O3 was planned to continue until the end of April in 2020, but it was suspended on March 27, 2020, due to the influence of the COVID-19[5]. The schedule of the next international collaborative observation called O4 is still under discussion and it has been decided that it will only be started after June 2022 at the earliest as of May 2021.

The KAGRA observatory signed the three documents between LIGO and VIRGO in order to realize international joint observation on October 4, 2019. The documents are the Memorandum of Agreement between VIRGO, KAGRA, and LIGO (main part)[6], Memorandum of Agreement between VIRGO, KAGRA, and LIGO (Attachment A)[7], and Letter of Intent for KAGRA to Join the O3 Run[8]. On the same day, the KAGRA observatory held a completion ceremony.

In FY2019 we started interferometer commissioning works to reach the sensitivity required to join O3. The required sensitivity of 1 Mpc was defined as an observation range of neutron star binary coalescences[8]. KAGRA reached the required sensitivity almost the end of March 2020. Along with the commissioning works the KAGRA observatory carried out several engineering runs and two Observation runs by the end of April 2020. The first observation run was carried out only by KAGRA with the observation range of 0.5 Mpc from February 25 to March 7, 2020. The second observation run was carried out with GEO600 from April 7 to 21, 2020. This observation called O3GK is regarded as an official joint observation with GEO600 by LIGO, VIRGO, and KAGRA. KAGRA was operated in O3GK with the observation range of almost 0.6 Mpc and duty factor of 53 % has achieved. Details of observation runs can be found in the section of "Observation". After the O3GK observation, we restricted activities by the end of May to prevent a spread of COVID-19. Activity restrictions have been gradually relaxed from June, and interferometer upgrades and refurbishment work for O4 are underway accordingly.

We also enhanced the international collaborations with the Einstein Telescope (ET) project, LIGO, Virgo, Korean and other Asian groups mainly based on the JSPS core-to-core program.

The rapidly progressing status of KAGRA were presented in many international conferences. Many papers about the progress of KAGRA were also published [9], [10], [11], [12], [13], [14], [15], [16], [17]. We also presented activities on our web-page.[18]

Bibliography

[1] ”KAGRA: 2.5 generation interferometric gravitational wave detector”, KAGRA collaboration, Nature Astronomy, Vol. 3, January 2019, 35-40

[2] ”Construction of KAGRA: an underground gravitational-wave observatory”, KAGRA collaboration, Prog. Theor. Exp. Phys. 2018, 013F01 (2018)

[3] ”First cryogenic test operation of underground km-scale gravitational-wave observatory KAGRA”, KAGRA collaboration, Class. Quantum Grav. 36 165008 (2019)

[4] ”Prospects for observing and localizing gravitational-wave transients with Advanced LIGO, Advanced Virgo and KAGRA”, Abbott, B.P., Abbott, R., Abbott, T.D. et al. arXiv:1304.0670 [gr-qc]

[5] https://www.ligo.caltech.edu/news/ligo20200326

[6] https://gwdoc.icrr.u-tokyo.ac.jp/cgi-bin/DocDB/ShowDocument?docid=10663

[7] https://gwdoc.icrr.u-tokyo.ac.jp/cgi-bin/DocDB/ShowDocument?docid=10664

[8] https://gwdoc.icrr.u-tokyo.ac.jp/cgi-bin/DocDB/ShowDocument?docid=10813

[9] ”High performance thermal link with small spring constant for cryogenic applications”, Tomohiro Yamada, Takayuki Tomaru, Toshikazu Suzuki, Takafumi Ushiba, Nobuhiro Kimura, Suguru Takada, Yuki Inoue, Takaaki Kajita, Cryogenics 116 (2021) 103280

[10] ”Cryogenic suspension design for a kilometer-scale gravitational-wave detector”, Takafumi Ushiba, Tomotada Akutsu, Sakae Araki, Rishabh Bajpai, Dan Chen, Kieran Craig, Yutaro Enomoto, Ayako Hagiwara, Sadakazu Haino, Yuki Inoue, Kiwamu Izumi, Nobuhiro Kimura, Rahul Kumar, Yuta Michimura, Shinji Miyoki, Iwao Murakami, Yoshikazu Namai, Masayuki Nakano, Masatake Ohashi, Koki Okutomi, Takaharu Shishido, Ayaka Shoda, Kentaro Somiya, Toshikazu Suzuki, Suguru Takada, Masahiro Takahashi, Ryutaro Takahashi, Shinichi Terashima, Takayuki Tomaru, Flavio Travasso, Ayako Ueda, Helios Vocca, Tomohiro Yamada, Kazuhiro Yamamoto, and Simon Zeidler, Class. Quantum Grav. 38 (2021) 085013

[11] ”Vibration isolation systems for the beam splitter and signal recycling mirrors of the KAGRA gravitational wave detector”, KAGRA collaboration, Class. Quant. Grav. 38 (2020) 065011

[12] ”Overview of KAGRA: Calibration, detector characterization, physical environmental monitors, and the geophysics interferometer”, KAGRA collaboration, Progress of Theoretical and Experimental Physics, ptab018

[13] ”Demographic Landscape of the KAGRA collaboration”, Keiko Kokeyama, Chunglee Kim, Joseph M. Fedrow, and Ayaka Shoda, AIP Conference Proceedings 2319, 150001 (2021)

[14] ”Overview of KAGRA : Detector design and construction history”, KAGRA collaboration, Prog. Theor. Exp. Phys. (2020) ptaa125

[15] ”Overview of KAGRA : KAGRA science”, KAGRA collaboration, Prog. Theor. Exp. Phys. (2020) ptaa120

[16] ”Prospects for improving the sensitivity of the cryogenic gravitational wave detector KAGRA”, Yuta Michimura, Kentaro Komori, Yutaro Enomoto, Koji Nagano, Atsushi Nishizawa, Eiichi Hirose, Matteo Leonardi, Eleonora Capocasa, Naoki Aritomi, Yuhang Zhao, Raffaele Flaminio, Takafumi Ushiba, Tomohiro Yamada, Li-Wei Wei, Hiroki Takeda, Satoshi Tanioka, Masaki Ando, Kazuhiro Yamamoto, Kazuhiro Hayama, Sadakazu Haino, Kentaro Somiya, Phys. Rev. D 102, 022008 (2020)

[17] ”Application of independent component analysis to the iKAGRA data”, KAGRA collaboration, Progress of Theoretical and Experimental Physics, 2020, 053F01 (2020)

[18] http://gwcenter.icrr.u-tokyo.ac.jp/en/

Input and Output Optics

[Spokesperson : Osamu MIYAKAWA]

ICRR, The Univ. of Tokyo, Hida, Gifu 506-1205

The input and output optics (IOO) of KAGRA consists of the pre-stabilization laser (PSL), auxiliary locking system (ALS), input optics chain, output optics chain. PSL includes the frequency stabilization servo (FSS), intensity stabilization servo (ISS), pre-mode cleaner (PMC), and modulation system for the main interferometer. ALS includes the phase-locking system for the green beam each for X and Y arms, the fiber system, and the locking system for the arm cavities. The input optics chain includes the input mode cleaner (IMC), input Faraday isolator (IFI), and two input mode matching telescopes (MMT). The output optics chain includes the output mode matching telescopes (OMT), output Faraday isolator (OFI), and output mode cleaner (OMC).

In the fiscal year of 2020, KAGRA had an international observation period until the end of April, and then we tried to lock the signal recycling mirror as known as Dual Recycled Fabry-Perot interferometer configuration. As the IOO subsystem, our primary role was to provide stable input and output optics, including a stable laser source. In the last half of FY2020, KAGRA started upgrading the vibration isolation system, and as part of this, the IMC suspensions are being tuned in FY2021 now.

During the commissioning, it was pointed out that angular fluctuations were serious problems that limited the stability of the whole interferometer. Therefore, we are preparing to implement Wave Front Sensors (WFS) to stabilize the angular motion of the IMC.

For the high power laser, a 60W high power laser was installed at the University of Toyama (Fig. 5). Intensity noise and frequency noise have been measured as a part of characterizations. The intensity noise was improved by order of 1 to 1.5 over all frequencies compared with the current laser source used in KAGRA. We can expect more improvement in the intensity noise for O4 and the future. On the other hand, measured frequency noise with a new one was almost the same as the current laser used in KAGRA, and we concluded that there is no problem using this new laser in KAGRA. However, we found that the beam profile may not be so clean, and we are now considering replacing the master seed laser with the new one.

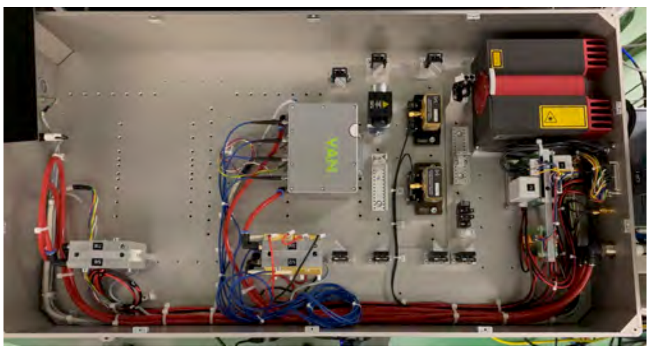

Fig. 5. 60W High power laser located at Toyama Univ. This laser will be installed to KAGRA in the end of 2021.

As for ALS, activities including maintenance have been suspended after the commissioning. This is due to the influence of COVID-19. It was also pointed out that the actuator range of the feedback signal was narrow, so we started discussing to improve this small range issue, and the maintenance scheme for O4.

As for the IFI, there is an existing problem that the height of the optical axis is not correct, and we are considering improving it during the whole KAGRA upgrade that will be performed until FY2021.

There was no doubt that the COVID-19 caused a considerable delay in research in FY2020. In the last half a year, the situation seemed to be improved slightly. We will prepare the IOO system working stably for O4 that will start in FY2022.

Cryogenic system

[Spokesperson : Takafumi USHIBA]
ICRR, The Univ. of Tokyo, Hida, Gifu 506-1205

One of the unique features of KAGRA is the use of cryogenic sapphire mirrors in the 3-km arm cavities.The people working in this group are mainly from the ICRR, KEK and the University of Toyama. Here, we summarize the activity of members of ICRR in FY 2020.

Cryogenic payload A KAGRA sapphire mirror is suspended by a 9-stage suspension and its bottom 4 stages that include sapphire mirror is called cryogenic payload. Figure 6 shows

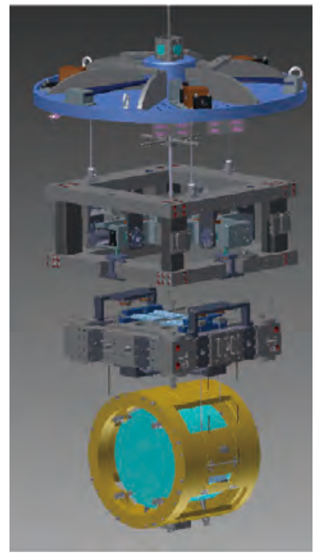

Fig. 6. Schematic view of the cryogenic payload.

the schematic view of the cryogenic payload. Angular and translational motion of these sapphire mirrors must be controlled well for operating them as an interferometer. Therefore, damping and global control of suspension were implemented during international joint observation with GEO600 (O3GK). In the observation run, the local control of the cryogenic sapphire mirrors contaminated the detector sensitivity below 50 Hz. So, we improved the sensors for controlling the cryogenic payloads in FY 2020.

Our cryogenic payload consists of four stages, which are called the platform (PF) stage, Marionette (MN) stage, Intermediate mass (IM) stage, and test mass (TM) stage from the top. One large improvement of sensors for the cryogenic payload is installing optical levers at the marionette stage and platform stage. These optical levers have a lower noise level than the photosensors on the MN stage and IM stage, which limits the sensitivity below 50 Hz during O3GK.

Heatlink vibration isolation system KAGRA cryogenic payload has heatlinks, which are directly connected to cryocoolers, for cooling sapphire mirror to 20 K. Since the cryocooler produces vibrations that are large compared to the ground motion, the vibrations propagating through the heat link may be harmful for the interferometer sensitivity. So, we developed heatlink vibration isolation system (HLVIS) to mitigate not only the horizontal vibrations but also the vertical ones. Figure 7 shows the photo of HLVIS.

HLVIS consists of a three-stage pendulum. Each stage is suspended by four tension springs in order to mitigate not only horizontal vibration but also vertical vibration. Vibration isolation ratio up to 100 Hz was measured at room and cryogenic temperature in FY 2020. We also estimated the effect of the HLVIS in terms of the sensitivity for binary black hole (BH)

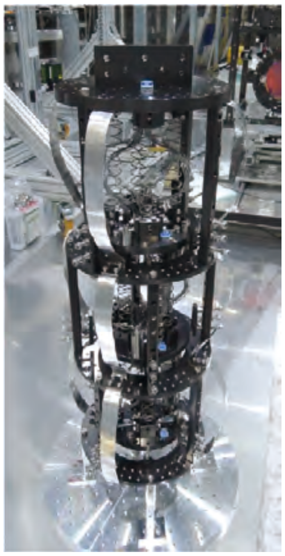

Fig. 7. Photo of the HLVIS.

mergers and found that the HLVIS can improve the sensitivity for 50-50 solar-mass BH mergers by a factor of 2 and 100-100 solar mass BH mergers by a factor of 40.

New design of mirror inclination control system A cryogenic payload has an inclination adjustment system called the moving mass system. The moving mass system consists of three components: a cryogenic compatible stepper motor, an oil-free ball screw, and a copper block. We can drive a copper block by rotating the stepper motor and change the mass balance of the cryogenic payload to tilt the mirror. Basically, this moving mass system workes well but in terms of long-term reliability, there is an issue to be solved. So, we started to re-design the moving mass system, and an initial design was finished and a prototype was fabricated in FY 2019. Then, we checked the performance of the new moving mass in FY 2020.

The new moving mass has a range of about ± 10 mrad and a resolution of several μrad. We also checked the long-term reliability and found that the new moving mass can work at cryogenic temperature after 6000 times operation, Then, the new moving masses were installed to the practical payload at KAGRA site in FY 2020.

Doctoral theses One doctral thesis, *Low-Vibration Conductive Cooling of KAGRA Cryogenic Mirror Suspension*, was accepted in FY 2020.

Master theses One master thesis, *Development of tilt adjustment mechanism for KAGRA cryogenic mirror suspension*, was accepted in FY 2020.

Acknowledgement Mechanical Engineering Center of KEK and Engineering Machine Shop, Faculty of Engineering, University of Toyama make a large contribution through providing many products for our research.

Vibration Isolation System Type-B

[Spokesperson : Fabian Peña Arellano]

ICRR, The Univ. of Tokyo, Hida, Gifu 506-1205

Besides the four Type-A suspensions KAGRA relies on smaller suspensions for other mirrors which are always at room temperature. The Type-B suspension is used for the beam splitter and the three signal recycling mirrors, whereas the Type-Bp is used for the three power recycling mirrors.

Fig. 8. The IP of the beam splitter in the vacuum chamber and the installation team.

As in Type-A suspension, in Type-B suspension, the first vibration isolation stage is the Inverted Pendulum (IP), whose main goal is to passively attenuate the persistent horizontal microseismic motion produced by ocean activity. Typical resonant frequencies for these IPs are between 60 mHz and 80 mHz in order to attenuate the microseismic peak at around 200 mHz. The following three stages, intended for vertical isolation, are three geometric anti-spring filters. The first one lies directly on top of the IP table while the other two hang from it as the masses of a multi-stage pendulum. As in the case of the IP, GAS filters are devices capable of supporting loads of hundreds of kilograms and at the same time achieving resonant frequencies of a few hundreds of millihertz. The horizontal position of the IP and the vertical positions of the GAS filters are measured with Linear Variable Differential Transformers (LVDTs) and are adjusted with coil-magnet actuators which also damp the mechanical resonant motion. The typical resolution of the LVDTs is below 0.2 μm. From the lowermost GAS filter the payload hangs. The payload, which is common to Type-B and Type-Bp suspensions, comprises the optic, its marionette and their respective recoil masses. The recoil mass of the marionette holds local displacement sensors to monitor six degrees of freedom and coil-magnet actuators for damping the resonant modes of oscillation of the suspension itself. The sensors have typical resolutions of about 20 nm. The recoil mass of the mirror holds coil-magnet actuators only and the system relies on an optical lever to monitor the tilt and position of the optic from the ground.

The Type-Bp suspension is shorter and comprises two GAS filters and the payload. The uppermost GAS filter lies directly on the ground while the lowermost one has its own recoil mass in order to attenuate motion which may be excited by the microseismic motion of the ground.

This fiscal year we focused on remedying work towards the O4 observation campaign. In SRM suspension we withdrew a mechanical component that was limiting the moving range of a GAS filter. In the BS and SR3 suspensions we adjusted the amount of ballast mass in a couple of GAS filter stages to move them to suitable heights. We Installed a new stepper motor in the BS suspension and limit switches in all accessible stepper motors in all Type-B suspensions. With the aim of improving the mirror orientation stability of the PR3 and PR2 mirrors, we increased the torque applied to the screws used in the clamps holding the wires from which the mirrors hang. Currently we are in the process of installing in-vacuum thermistors to measure the temperature of all Type-Bp and Type-B suspensions. Soon we will be adjusting the amount of ballast mass in Type-B's Inverted Pendulums in order to optimize their resonant frequencies.

Integrated DAQ/control system using real time computers

[Spokesperson : Shoichi OSHINO]

ICRR, The Univ. of Tokyo, Hida, Gifu 506-1205

In the 2020 fiscal year, we joined the international observation with a power-recycled Fabry-Perot-Michelson interferometer from April 2020. During this observation, we continued to maintain a stable DAQ/control system.

Stable operation with the real-time control system We were planning to upgrade Real-time Code Generator(RCG) in 2020. This important software handles the control of the interferometer and the data acquisition process. However, the configuration that worked well in the test environment did not work in the production environment. Therefore, we started planning to create a larger test bench to build an environment equivalent to KAGRA.

We are creating a new type of I/O chassis. In 2020, we have made a prototype of new type I/O chassis and running various tests. This new I/O chassis will be able to hold four PCI-e expansion cards and will be connected to the computer via MTP optical fiber cables.

We also installed a NAS to store the data acquired by KAGRA. The data, which was previously stored on multiple HDDs, can now be stored in one place. The NAS also provides redundancy to ensure that the data is safely recorded.

Detector Charcterization

[Spokesperson : Takahiro Yamamoto]

ICRR, The Univ. of Tokyo, Hida, Gifu 506-1205

Detector commissioning support The goal of detector characterization is to provide reliable data for gravitational waves searches. For the commissioning test, monitoring various kinds of signals is required. In fact, more than 20,000 signals were acquired in 2020.

The detector characterization group aims to support the improvement of detector sensitivity and to investigate the noise sources. In 2019, we implemented some tools for searching noise correlation between the main interferometer signal and various auxiliary channels. These tools contributed to improving the sensitivity as a factor of $\sim$10,000 from late 2019 to early 2020.

In the final stage of the commissioning test, we determined the normal state of the interferometer and defined the indicator of the observation mode, which means that the interferometer can provide stable data.

Observing data validation In April 2020, an international observing run named O3GK was taken place with KAGRA and GEO600 (Hannover, Germany). As one of the data validation activities, a data quality evaluation was performed. The stability of interferometer control and saturation in detection ports of interferometer signals were checked in the real-time ($\sim$61us interval) process.

Observing data only which passed the data quality check was used for searching GWs. Data quality was also used in order to select used data for evaluating the rate of operation (a.k.a duty factor), the detection range of binary neutron stars and so on. Data quality information was shared with LIGO, Virgo and GEO within 10-seconds long of latency for the co-operative observation and, the web interface shown in Fig.9 was also implemented for O3GK and future observing runs.

Data quality information was archived as part of the measurement data set with main interferometer signals and on the data quality database in California Institute of Technology which is shared with LIGO, Virgo, and KAGRA for the purpose of easy access when GW searches are performed in an offline process. Sharing data quality with other overseas detectors became the first step of joining the international observing run for KAGRA.

Information sharing on the database was implemented with the 1-day cadence during the O3GK observing run and cadence will be planned to shrink a few minutes for providing early alert of GW detections in O4 and future observing runs.

Environment Monitors

[Spokesperson : Takaaki YOKOZAWA]

ICRR, The Univ. of Tokyo, Hida, Gifu 506-1205

Because the typical amplitudes of Gravitational Waves(GWs) are extremely small, small vibration from instruments, small sound from outside of the experimental area and so on can produce noise source contamination that reduces the sensitivity. Major noise sources include environmental disturbances caused by earthquakes, effects from magnetic and acoustic fields, temperature fluctuations, and so on. To evaluate the noise sources, about 100,000 auxiliary channels are recorded by the KAGRA digital system. The

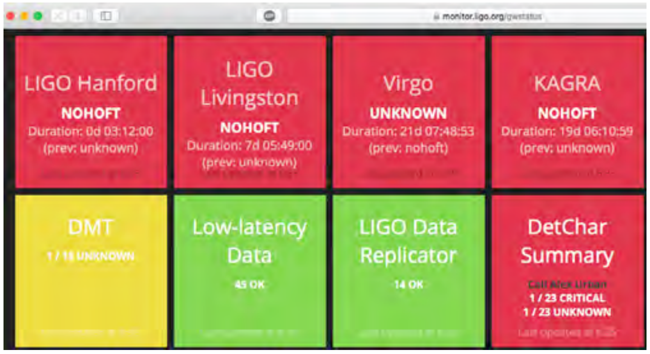

Fig. 9. In order to perform the international observing run, data quality of each detector was shared among the LVK collaboration. This information was available on the web interface with a few second latency during the O3GK observing run.

main purposes of the physical and environmental monitoring are two.

The first is to characterize the underground and cryogenic environment; KAGRA detector has two unique features, underground and cryogenic environment, and those features will be essential in the next-generation detectors. We are collaborating with the Virgo collaborators and evaluated the Newtonian noise in the underground experimental area. And by using the new signal processing method called local Hurst exponent to KAGRA seismometer signals. As a result, we identified the time series of seismometers have different features in XY axis and Z axis and position of the seismometer. This implies we should understand more about the water fluid of Ikenoyama mountain. Also, we have a meeting every month and various topics were discussed.

The second aim is understanding the interferometer noise by environmental monitors. We installed various PEMs, including accelerometers, microphones, magnetometers, thermometers, weather station and so on. Before the O3GK, performed Apr. 2020, we performed the hammering test, in which we produced vibrations in different locations of the interferometer, and evaluated the scattered light and noise path by vibration. As a result, we identified the bellows between IMC and IMM chambers as a weak point and limit the sensitivity around 300 Hz. Also, we performed the acoustic injection test and magnetic field injection with a new method. This result is published to CQG.

Observation

[Spokesperson : Shinji MIYOKI]

ICRR, The Univ. of Tokyo, Hida, Gifu 506-1205

The first formal "solo" observation was performed from February 25 to March 10, 2020, because the sensitivity was less than 1Mpc that was the descoped criteria for joining O3. Some "noise hunting" activities during observation resulted in sensitivity enhancement up to ~590kpc mainly due to displacement noise reduction around 200 Hz by the introduction of the feedforward of MI control signals. The displacement noise was also found to be sensitive to the beam spot positions on mirrors (and/or on injection beam axes). The longest continuous lock was ~9 hours, however, the violent ocean condition sometimes sopped KAGRA operation due to failure of lock acquisition of the FP cavity arms.

From March 11 to April 6 in 2020, more optimization of optical axes and/or beam spots on mirrors, noise contribution check from the frequency and intensity noise and more noise hunting were done. Finally, 1Mpc sensitivity was realized around the end of March mainly due to the displacement noise enhancement around 200 Hz. DRMI was also tried and successfully operated, however, DRFPMI was not realized.

At the same time, unfortunately, the COVID-19 pandemic forced aLIGO and aVirgo to suspend O3 on March 27, 2020. Consequently, KAGRA could not join the network observation with them. However, GEO600, which has already joined O3 and had the same level of sensitivity as KAGRA, was still online. So, GEO600-KAGRA joint observation (named O3GK) was urgently planed according to the KAGRA observation schedule from 17:00 (JST) on April 7 to 09:00 (JST) on April 21. The mean sensitivity in the science mode was 500kpc with a standard deviation of 170kpc. The duty factor, that is the ratio between the period of the science (observation) mode and the total operation period, was 54%. Especially, around April 13~14, the duty cycle was almost zero because the violent ocean condition enhanced micro-seismic noise beyond approximately 1μm/s RMS, and the lock acquisition became completely impossible. Another reason for the low duty cycle was because the mirror alignment control, such as WFS, was not implemented for the main interferometer. An offline analysis for more accurate calibration was done. Data analysis of O3GK together with the GEO600 data for GW signal search is now ongoing. Especially, during the online state of both KAGRA and GEO600, an astronomical gamma-ray burst event named GRB200415A was reported. We are now analyzing our data on this event.

Data Analysis

[Spokesperson : Hideyuki Tagoshi]

ICRR, The Univ. of Tokyo, Kashiwa, Chiba, 277-8582

On October 4, 2019, KAGRA signed a Memorandum of Agreement (MoA) between LIGO and Virgo. The MoA defines the policy of the joint data analysis and the data sharing. Based on this MoA, all data analysis activities are now done jointly with LIGO and Virgo. In LIGO-Virgo-KAGRA (LVK) collaboration, there is a Data Analysis Council (DAC), which is a committee that manages data analysis activities in LVK. Under DAC, there are four working groups regarding gravitational wave signal search, Compact Binary Coalescence working group (CBC), Burst working group (Burst), Continuous Wave Working group (CW), and Stochastic background working group (Stochastic). In LVK, there is also the Operations group that manages various data-related activities. Those include calibration, detector characterization, computing and software, low latency, open data, run planning and so on. In KAGRA, Data Analysis Committee manages data analysis and data-related activities.

KAGRA performed an observing run from April 7th to

20th, 2020 (UTC). Originally, this observation was supposed to be done jointly with LIGO and Virgo at the end of the 3rd observing run of LIGO and Virgo. However, while KAGRA was preparing the observing run, the LIGO and Virgo detectors were forced to terminate operations on March 27, 2020 (UTC) due to the COVID-19 pandemic. Fortunately, however, GEO600 in Germany was operating and continuously taking data. Thus, GEO and KAGRA decided to perform an observing run jointly. In LIGO-Virgo-KAGRA (LVK) collaboration, this observation was officially approved as a joint observation under the LVK framework. Later, this observing run was named "O3GK". After the end of the observing run, offline calibrated h(t) data were produced, and new data files were shared among LVK. Currently, the analysis of O3GK data is underway. The data analysis tasks include all-sky searches for compact binary coalescences (CBC), un-modeled short-duration burst waves (Burst), targeted searches for short and long Gamma Ray Bursts.

We also participated in the joint data analysis of LIGO-Virgo O3 data. These include the parameter estimation of CBC signals, CBC searches targeting short Gamma Ray Burst during O3, and so on.

As one of the main computing resources in KAGRA, the main data server of KAGRA is located at ICRR Kashiwa. It has 2.5PiB data storage. All KAGRA data taken at Kamioka are packed into one file every 32 seconds, and are transferred continuously to the main data server at Kashiwa. Besides this, low latency data transfer is also done by packing only the gravitational wave channel and a few other channels into one file every 1 second. For low latency data transfer, the latency of about 3 seconds is achieved from Kamioka to Kashiwa (this time includes the time necessary for calibration). In order to share the low latency data file among LIGO-Virgo-KAGRA, the low latency data files are also transferred to a server at LIGO Caltech. On the other hand, low latency data files of LIGO and Virgo detectors are transferred from Caltech to the main data server at Kashiwa. GEO data during O3GK were also transferred to Kashiwa.

Bibliography

[1] S. Ueda, K Somiya et al., Class. Quantum Grav. 31 095003 (2014)

[2] K Yamamoto et al., Class. Quantum Grav. 36 (2019) 205009.

Observational Cosmology Group

[Spokesperson : Yoshiaki Ono]

ICRR, The Univ. of Tokyo, Kashiwa, Chiba 277-8582

Large Population of ALMA Galaxies at $z > 6$ with Very High [OIII]88μm *to* [CII]158μm *Flux Ratios: Evidence of Extremely High Ionization Parameter or PDR Deficit?* [1]

In collaboration with the members of National Astronomical Observatory of Japan, University College London, Waseda University, Ehime University, Nagoya University, The University of Tokyo, Kitami Institute of Technology, University of Arizona, Scuola Normale Superiore, The Graduate University for Advanced Studies (SOKENDAI), Museo Storico della Fisica e Centro Studi e Ricerche "Enrico Fermi," and Leiden Observatory.

We present our new Atacama Large Millimeter/Submillimeter Array (ALMA) observations targeting [OIII]88μm, [CII]158μm, [NII]122μm, and dust continuum emission for three Lyman break galaxies at $z = 6.0293 - 6.2037$, identified in the Subaru/Hyper Suprime-Cam (HSC) survey. We clearly detect [OIII] and [CII] lines from all of the galaxies at $4.3 - 11.8\sigma$ levels, and identify multi-band dust continuum emission in two of the three galaxies, allowing us to estimate infrared luminosities and dust temperatures simultaneously. In conjunction with previous ALMA observations for six galaxies at $z > 6$, we confirm that all the nine $z = 6 - 9$ galaxies have high [OIII]/[CII] ratios of $L_{[\mathrm{OIII}]}/L_{[\mathrm{CII}]} \sim 3 - 20$, ~ 10 times higher than $z \sim 0$ galaxies. We also find a positive correlation between the [OIII]/[CII] ratio and the Lyα equivalent width (EW) at the $\sim 90\%$ significance level. We carefully investigate physical origins of the high [OIII]/[CII] ratios at $z = 6 - 9$ using Cloudy, and find that high density of the interstellar medium, low C/O abundance ratio, and the cosmic microwave background attenuation are responsible to only a part of the $z = 6 - 9$ galaxies (Figure 10). Instead, the observed high [OIII]/[CII] ratios are explained by $10 - 100$ times higher ionization parameters or low photodissociation region (PDR) covering fractions of $0 - 10\%$, both of which are consistent with our [NII] observations. The latter scenario can be reproduced with a density bounded nebula with PDR deficit, which would enhance the Lyα, Lyman continuum, and C^+ ionizing photons escape from galaxies, consistent with the [OIII]/[CII]-Lyα EW correlation we find.

Bibliography

[1] Harikane, Y., Ouchi, M., Inoue, A. K., Matsuoka, Y., Tamura, Y., Bakx, T., Fujimoto, S., Moriwaki, K., Ono, Y., Nagao, T., Tadaki, K., Kojima, T., Shibuya, T., Egami, E., Ferrara, A., Gallerani, S., Hashimoto, T., Kohno, K., Matsuda, Y., Matsuo, H., Pallottini, A., Sugahara, Y., Vallini, L. 2020, The Astrophysical Journal, 896, 93

Extremely Metal-Poor Representatives Explored by the Subaru Survey (EMPRESS). I. A Successful Machine Learning Selection of Metal-Poor Galaxies and the Discovery of a Galaxy with $M_* < 10^6 M_\odot$ and $0.016 Z_\odot$ [2]

In collaboration with the members of The University of Tokyo, Carnegie Observatories, National Astronomical Observatory of Japan, Cosmic Dawn Center, University of Copenhagen, University College London, University of Tsukuba, University of Geneva, Subaru Telescope, NSF's National Optical Infrared Astronomy Research Laboratory Ehime University, The Graduate University for Advanced Studies (SOKENDAI), Kitami Institute of Technology, Waseda University, and University of Tsukuba.

We have initiated a new survey for local extremely metal-poor galaxies (EMPGs) with Subaru/HSC large-area (~ 500 deg^2) optical images reaching a 5σ limit of ~ 26 magnitude, about 100 times deeper than the Sloan Digital Sky Survey (SDSS). To select $Z/Z_\odot < 0.1$ EMPGs from ~ 40 million sources detected in the Subaru images, we first develop a machine-learning (ML) classifier based on a deep neural network algorithm with a training data set consisting of optical photometry of galaxy, star, and QSO models. We test our ML classifier with SDSS objects having spectroscopic metallicity measurements, and confirm that our ML classifier accomplishes 86%-completeness and 46%-purity EMPG classifications with photometric data. Applying our ML classifier to the photometric data of the Subaru sources as well as faint SDSS objects with no spectroscopic data, we obtain 27 and 86 EMPG candidates from the Subaru and SDSS photometric data, respectively. We conduct optical follow-up spectroscopy for 10 out of our EMPG candidates with Magellan/LDSS-3+MagE, Keck/DEIMOS, and Subaru/FOCAS, and find that the 10 EMPG candidates are star-forming galaxies at $z = 0.007 - 0.03$ with large Hβ equivalent widths of 104–265 Å, stellar masses of $\log(M_*/M_\odot) = 5.0$–7.1, and high specific star-formation rates of $\sim$300 Gyr^{-1}, which are similar to those of early galaxies at $z \gtrsim 6$ reported recently. We spectroscopically confirm that 3 out of 10 candidates are truly EMPGs with $Z/Z_\odot < 0.1$, one of which is HSC J1631+4426, the most metal-poor galaxy with $Z/Z_\odot = 0.016$ reported ever (Figure 11).

Bibliography

[2] Kojima, T., Ouchi, M., Rauch, M., Ono, Y., Isobe, Y., Fujimoto, S., Harikane, Y., Hashimoto, T., Hayashi, M., Komiyama, Y., Kusakabe, H., Kim, J. H., Lee, C.-H., Mukae, S., Nagao, T., Onodera, M., Shibuya, T., Sugahara, Y., Umemura, M., Yabe, K. 2020, The Astrophysical Journal, 898, 142

Early Low-Mass Galaxies and Star-Cluster Candidates at $z \sim 6-9$ Identified by the Gravitational Lensing Technique and Deep Optical/Near-Infrared Imaging [3]

In collaboration with the members of The University of Tokyo, National Astronomical Observatory of Japan, Sorbonne University, University College London, and National Autonomous University of Mexico.

We present very faint dropout galaxies at $z \sim 6-9$ with a stellar mass $M_\star$ down to $M_\star \sim 10^6 M_\odot$ that are found in deep optical/near-infrared (NIR) images of the full data sets of the Hubble Frontier Fields (HFF) program in conjunction with deep ground-based and Spitzer images and gravitational lensing magnification effects. We investigate stellar populations of the HFF dropout galaxies with the optical/NIR photometry and BEAGLE models made of self-consistent stellar population synthesis and photoionization models, carefully including strong nebular emission impacting on the photometry. We identify 453 galaxies with $M_\star \sim 10^6 - 10^9 M_\odot$. Our best-estimate $M_\star/L_{\rm UV}$ function is comparable to a model of star formation duration time of 100 Myr that is assumed in Bouwens et al. We derive the galaxy stellar mass functions (GSMFs) at $z \sim 6-9$ that agree with those obtained by previous studies with no $M_\star/L_{\rm UV}$ assumptions at $M_\star \gtrsim 10^8 M_\odot$, and that extends to $M_\star \sim 10^6 M_\odot$. Estimating the stellar mass densities $\rho_\star$ with the GSMFs, we find a very slow evolution from $z \sim 9$ to $z \sim 6-7$, which is consistent with the one estimated from star formation rate density measurements. In conjunction with the estimates of the galaxy effective radii $R_{\rm e}$ on the source plane, we have pinpointed four objects with low stellar masses ($M_\star \leq 10^7 M_\odot$) and very compact morphologies ($R_{\rm e} \leq 40$ physical pc) that are comparable with those of globular clusters (GCs) in the Milky Way today (Figure 12). These objects are candidates of star clusters, some of which may be related to GCs today.

Bibliography

[3] Kikuchihara, S., Ouchi, M., Ono, Y., Mawatari, K., Chevallard, J., Harikane, Y., Kojima, T., Oguri, M., Bruzual, G., Charlot, S. 2020, The Astrophysical Journal, 893, 60

Three-dimensional Distribution Map of* H I *Gas and Galaxies around an Enormous Lyα Nebula and Three QSOs at $z = 2.3$ Revealed by the* H I *Tomographic Mapping Technique [4]

In collaboration with the members of The University of Tokyo, Tsinghua University, Kavli Institute for the Physics and Mathematics of the Universe, University of California Santa Cruz, ETH Zurich, University of Utah, Osaka University, University of Nevada, Shinshu University, Waseda University, University of California Santa Barbara, National Astronomical Observatory of Japan, The Graduate University for Advanced Studies (SOKENDAI), Kitami Institute of Technology, and Johns Hopkins University.

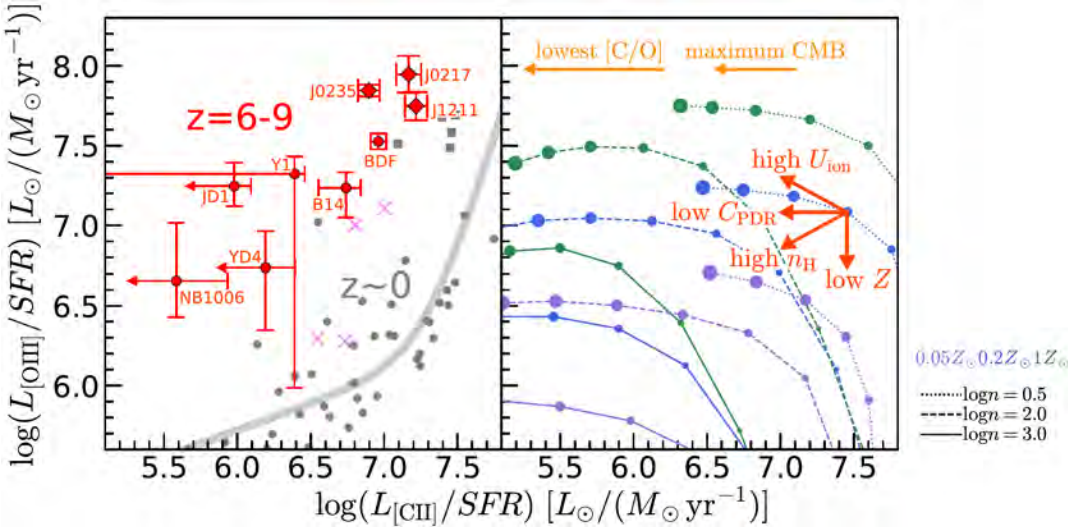

Fig. 10. (Left panel) $L_{\rm [OIII]}/SFR$ and $L_{\rm [CII]}/SFR$ ratios. The red diamonds represent our targets at $z\sim6$, and the red circles are other $z=6-9$ LBGs and LAEs in the literature. The gray squares and circles denote $z\sim0$ galaxies from the Dwarf Galaxy Survey and GOALS, respectively. The magenta crosses show SMGs at $z=4.4$, 6.1, and 6.9 in the literature, respectively. The $L_{\rm [CII]}/SFR$ ratios of the $z=6-9$ galaxies are systematically lower than those of $z\sim0$ galaxies with similar $L_{\rm [OIII]}/SFR$ ratios. (Right panel) Cloudy calculation results for the $L_{\rm [OIII]}/SFR$ and $L_{\rm [CII]}/SFR$ ratios. The purple, blue, and green lines are results for metallicities of $Z=0.05\ Z_\odot$, $0.2\ Z_\odot$, and $1.0\ Z_\odot$, respectively. The dotted, dashed and solid lines correspond to densities of $\log(n_{\rm H}/[{\rm cm}^{-3}])=0.5$, 2.0, and 3.0, respectively. The larger circles indicate higher ionization parameters, from $\log U_{\rm ion}=-4.0$ to -0.5 with a step size of 0.5. The red arrows show directions of the shifts in the $L_{\rm [OIII]}/SFR$-$L_{\rm [CII]}/SFR$ plane by higher ionization parameter, lower PDR covering fraction, higher density, and lower metallicity. The orange arrows indicate maximum shifts in $L_{\rm [CII]}/SFR$ by the lower C/O ratio and the CMB attenuation effect.

We present an IGM HI tomographic map in a survey volume of $16\times19\times131\ h^{-3}$comoving Mpc^3 (cMpc^3) centered at MAMMOTH-1 nebula and three neighboring quasars at $z=2.3$. MAMMOTH-1 nebula is an enormous Lyα nebula (ELAN), hosted by a type-II quasar dubbed MAMMOTH1-QSO, that extends over $1\ h^{-1}$ cMpc with not fully clear physical origin. Here we investigate the HI-gas distribution around MAMMOTH1-QSO with the ELAN and three neighboring type-I quasars, making the IGM HI tomographic map with a spatial resolution of $2.6\ h^{-1}$ cMpc (Figure 13). Our HI tomographic map is reconstructed with HI Lyα forest absorption of bright background objects at $z=2.4-2.9$: one eBOSS quasar and 16 Keck/LRIS galaxy spectra. We estimate the radial profile of HI overdensity for MAMMOTH1-QSO, and find that MAMMOTH1-QSO resides in a volume with fairly weak HI absorption. This suggests that MAMMOTH1-QSO may have a proximity zone where quasar illuminates and photo-ionizes the surrounding HI gas and suppresses HI absorption, and that the ELAN is probably a photo-ionized cloud embedded in the cosmic web. The HI radial profile of MAMMOTH1-QSO is very similar to those of three neighboring type-I quasars at $z=2.3$, which is compatible with the AGN unification model. We compare the distributions of the HI absorption and star-forming galaxies in our survey volume, and identify a spatial offset between density peaks of star-forming galaxies and HI gas. This segregation may suggest anisotropic UV background radiation created by star-forming galaxy density fluctuations.

Bibliography

[4] Mukae, S., Ouchi, M., Cai, Z., Lee, K.-G., Prochaska, J. X., Cantalupo, S., Zheng, Z., Nagamine, K., Suzuki, N., Silverman, J. D., Misawa, T., Inoue, A. K., Hennawi, J. F., Matsuda, Y., Mawatari, K., Sugahara, Y., Kojima, T., Ono, Y., Shibuya, T., Harikane, Y., Fujimoto, S., Chiang, Y.-K., Zhang, H., Kakuma, R. 2020, The Astrophysical Journal, 896, 45

Cosmological 3D HI *Gas Map with HETDEX Lyα Emitters and eBOSS QSOs at* $z=2$*: IGM-Galaxy/QSO Connection and a* $\sim$ *40-Mpc Scale Giant* HII *Bubble Candidate* [5]

In collaboration with the members of The University of Tokyo, National Astronomical Observatory of Japan, The University of Texas at Austin, The Pennsylvania State University, Missouri University of Science and Technology, Max Planck Institute for Extraterrestrial Physics, Rutgers University, Max Planck Institute for Astrophysics, University of Oxford, and University of the Western Cape.

We present cosmological ($30-400$ Mpc) distributions of neutral hydrogen (HI) in the inter-galactic medium (IGM) traced by Lyα Emitters (LAEs) and QSOs at $z=2.1-2.5$, selected with the data of the on-going Hobby-Eberly Telescope Dark Energy Experiment (HETDEX) and the eBOSS survey. We investigate spatial correlations of LAEs and QSOs with HI tomography maps reconstructed from HI Lyα forest absorption in the spectra of background galaxies and QSOs obtained by the CLAMATO survey and this study, respectively. In the cosmological volume far from QSOs, we find that LAEs reside in regions of strong HI absorption, i.e. HI rich, which is consistent with results of previous galaxy-background QSO pair studies. Moreover, there is an anisotropy in the HI-distribution plot of transverse and line-of-sight distances; on

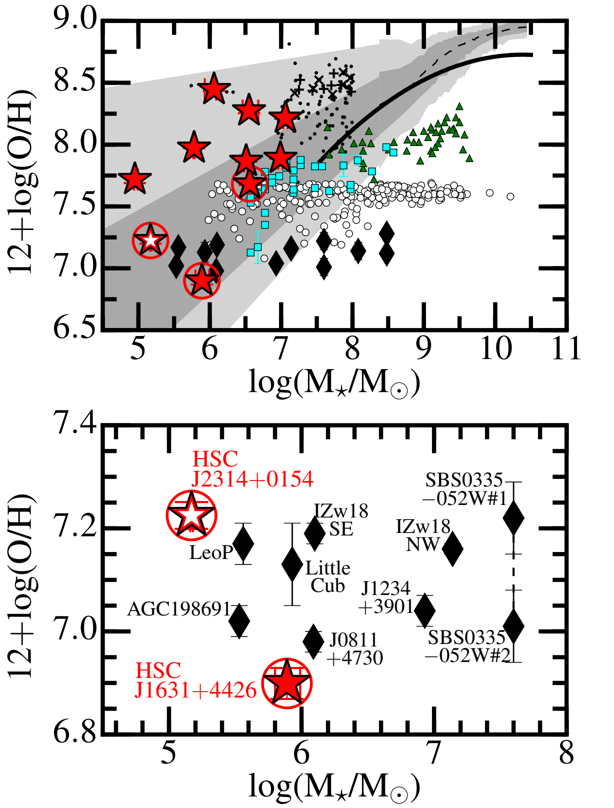

Fig. 11. (Top) Mass-metallicity relation of our metal-poor galaxies. The red stars indicate our HSC-EMPGs and SDSS-EMPGs. The open star is a galaxy whose metallicity is obtained with an empirical relation in the literature. The other symbols are taken from the literature. The solid and dashed lines indicate averaged local SFGs from SDSS data, respectively. The dark gray and light gray shaded regions represent the 68 and 95-percentile distributions of SFGs, although the extrapolation is applied below $\log(M_*/M_\odot)$ =8.4. We also show relatively metal-enriched dwarfs from SDSS (cross and plus), as well as DEEP2 galaxies (dot) in the stellar mass range of $\log(M_*/M_\odot)$ <8.0. Typical metallicity error of our metal-poor galaxies is Δ(O/H)$\sim$0.01 dex. (Bottom) Same as the top panel, but zoom-in around the low-M_*, low-metallicity ends.

average the H I absorption peak is blueshifted by $\sim$ 200 km s^{-1} from the LAE Lyα redshift, reproducing the known average velocity offset between the Lyα emission redshift and the galaxy systemic redshift. We have identified a $\sim$ 40-Mpc scale volume of H I underdensity that is a candidate for a giant H II bubble, where six QSOs and an LAE overdensity exist at $\langle z \rangle = 2.16$ (Figure 14). The coincidence of the QSO and LAE overdensities with the H I underdensity indicates that the ionizing photon radiation of the QSOs has created a highly ionized volume of multiple proximity zones in a matter overdensity. Our results suggest an evolutionary picture where H I gas in an overdensity of galaxies becomes highly photoionized when QSOs emerge in the galaxies.

Bibliography

[5] Mukae, S., Ouchi, M., Hill, G. J., Gebhardt, K., Cooper, E. M., Jeong, D., Saito, S., Fabricius, M., Gawiser, E., Ciardullo, R., Farrow, D., Davis, D., Zeimann, G., Finkelstein, S. L., Gronwall, C., Liu, C., Zhang, Y., Byrohl, C., Ono, Y., Schneider, D. P., Jarvis, M. J., Casey, C. M.,

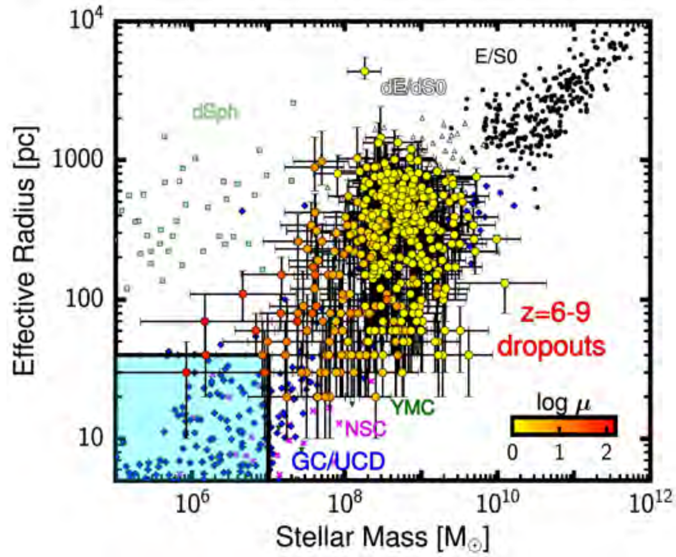

Fig. 12. Effective radius on the source plane, as a function of $M_\star$. Our $z \sim 6-9$ dropouts are presented with the large circles whose colors indicate the magnification factor values that are defined with the color bar at the bottom right. The other symbols show the distributions of the local elliptical/S0 galaxies (E/S0s; black circles), dwarf elliptical/S0 galaxies (dEs/dS0s; gray triangles), dwarf spheroids (dSphs; light-green squares), nuclear star clusters (NSCs; orange crosses), young massive clusters (YMCs; green down-pointing triangles), and globular clusters/ultra-compact dwarfs (GCs/UCDs; blue hexagons) obtained in the literature. The cyan shade presents the region where the local GCs are located. We define the dropouts in this region as early GC candidates.

Mawatari, K. 2020, The Astrophysical Journal, 903, 24

Theory Group

Overview

The theory group is active in elementary particle physics focusing on particle phenomenology, and in astroparticle physics focusing on particle cosmology. In particle physics, the main topics are theoretical studies of dark matter, inflation and extensions of the standard model. In astroparticle physics, the main topics are theoretical studies of inflation, thermal history of the early universe, dark matter, baryogenesis and big-bang nucleosynthesis.

After the discovery of the Higgs boson, the LHC has shown no strong hints on new physics. In this situation, we need to reconsider many ideas of new physics models as well as conventional strategies to search for them. Accordingly, our studies on beyond the Standard Model physics becomes more and more diverse.

Since the LIGO detectors detected the first confirmed gravitational waves (GWs) from colliding black holes on September 14, 2015, new era of GW astronomy began. So far, six GW events were detected by LIGO. Among them is the first detection of GW from binary neutron star. The discovery suggested strongly the existence of kilonova which can produce r-process elements. If they continue to find GW events

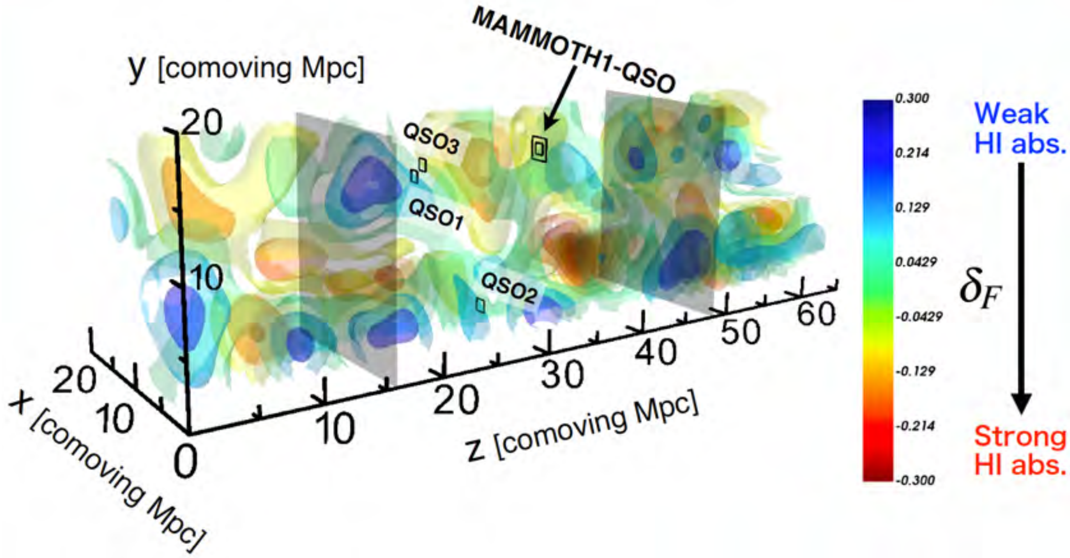

Fig. 13. HI tomographic map reconstructed based on Lyα forest absorption along the sightlines of our background quasar and galaxies in the BQ1 region. Here we present a zoomed map at $z = 2.28$–2.35 to clearly show the HI overdensity distribution around MAMMOTH1-QSO, although we obtain the HI tomographic map in the redshift range of $z = 2.25$–2.40. The spatial axes of R.A., Decl., and z are represented as x, y, and z in co-moving scales, respectively. The color contours show the HI overdensity δ_F, whose maximum (minimum) scale is set to $+0.3$ (-0.3) for visualization, although some regions show higher or lower δ_F values in the range of $-0.6 < \delta_F < 0.4$. The double square indicates the position of MAMMOTH1-QSO. The single squares show the three neighboring quasars, QSOs 1–3. Note that the redshift range between the two gray planes at $z \simeq 2.30$ and $z \simeq 2.33$ correspond to the FWHM of the narrowband filter NB403, which is used in the literature to detect LAEs at $z \simeq 2.30$–2.33 in the BOSS1441 field.

from black holes and neutron stars, their origin becomes one of the most interesting topics.

The supersymmetric (SUSY) extension of the standard model (SM) in the particle physics is considered to be one of the most promising models beyond the standard model. It solves the naturalness problem for the Higgs boson mass term in the standard model, and it is also compatible with the grand unified theories (GUTs). Although no hints of the superparticles have been indicated from the LHC yet, the SUSY models are the most attractive candidates beyond the Standard Model. Our group has been studying phenomenological and cosmological aspects of the SUSY models.

Recent cosmological observations including the Planck data determine precisely the mean densities of matter and baryon in the Universe, and existence of non-baryonic dark matter is established. Weakly interacting massive particles (WIMPs) are considered to be good candidates of the dark matter. They act as the cold dark matter in the structure formation of the universe. Our group has been studying model building for dark matter and detectability in direct and indirect search experiments.

For understanding of the early universe, a role of the elementary particle physics is crucial. Recent progress in the particle physics such as grand unification theories and supersymmetry leads us to a more deeper insight into the fundamental aspects of the early universe. In the inflationary universe, the quantum fluctuations of the scalar field which drives the inflation become the density fluctuations and lead to formation of the structure observed in the present universe. On the other hand cosmology and astrophysics are used to test new theories in particle physics. Such particle cosmology is one of main subjects of our group.

Big Bang Nucleosynthesis (BBN) is one of the most important subjects in modern cosmology. Predicted abundances of the light elements are very sensitive to the cosmological scenario. On the other hand, physics beyond the standard model predicts the new particles which would have existed at the BBN epoch. Such particles may spoil the success of BBN, which leads to constraints on the new particles and the particle physics models.

The grand unified theories predict that our universe undergoes several vacuum phase transitions. In the course of phase transitions topological defects (monopoles, cosmic strings and domain walls) are generally produced depending on symmetries of the vacua. Our group has studied evolution of various topological defects.

Particle Phenomenology

[Spokesperson : M. Ibe]
ICRR, The Univ. of Tokyo, Kashiwa, Chiba 277-8582

Beyond Standard Model

• Cosmic string in Abelian-Higgs model with enhanced symmetry — Implication to the axion domain-wall problem [1]

In collaboration with the members of ICRR, Rikkyo U. and TD-Lee Institute

In our previous work, we found new types of the cosmic string solutions in the Abelian-Higgs model with an enhanced $U(1)$ global symmetry. We dubbed those solutions as the compensated/uncompensated strings. The compensated string

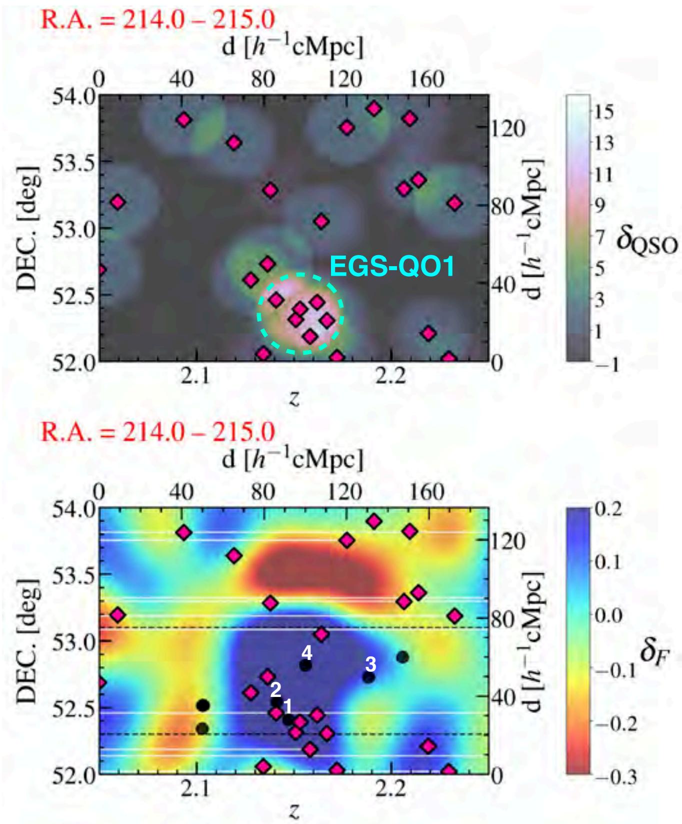

Fig. 14. Top panel: projection of the δ_{QSO} map for a 40 h^{-1} cMpc (R.A. direction) slice in EGS that includes the EGS-QO1 QSO overdensity. The color contours represent the QSO overdensity δ_{QSO}, where white indicates a high δ_{QSO} value. The magenta diamonds represent the foreground QSOs. The dashed circle indicates EGS-QO1, the identified QSO overdensity. Bottom panel: same as the top panel, but for the HI tomography map. The width of the slice, 40 h^{-1} cMpc, is twice as large as the spatial resolution of this map. The color contours represent the HI transmission overdensity δ_F, where the red (blue) color is a negative (positive) δ_F that corresponds to a strong (weak) HI absorption. The white dashed horizontal lines denote the background QSO sightlines. As in the top panel, the magenta diamonds represent the foreground QSOs residing in the slice. The black circles denote the positions of the LAEs. The black dashed lines indicate the edges in declination of the LAE detections covered by the HETDEX survey. Although spatial correlations between objects (QSOs and LAEs) and HI absorption may be identified by visual inspection, one needs quantitative analysis to conclude the reality of the apparent spatial correlations.

is similar to the conventional cosmic string in the Abrikosov-Nielsen-Olesen (ANO) string, around which only the would-be Nambu-Goldstone (NG) boson winds. Around the uncompensated string, on the other hand, the physical NG boson also winds, where the physical NG boson is associated with the spontaneous breaking of the enhanced symmetry. Our previous simulation in the 2+1 dimensional spacetime confirmed that both the compensated/uncompensated strings are formed at the phase transition of the symmetry breaking. Non-trivial winding of the physical NG boson around the strings potentially causes the so-called axion domain-wall problem when the model is applied to the axion model. In this paper, we perform simulation in the 3+1 dimensional spacetime to discuss the fate of the uncompensated strings. We observe that the evolution of the string-network is highly complicated in the 3+1 dimensional simulation compared with that seen in the previous simulation. Despite such complications, we find that the number of the uncompensated strings which could cause can be highly suppressed at late times. Our observation suggests that the present setup can be applied to the axion model without suffering from the axion domain-wall problem.

• Proton Decay in Product Group Unification [2]

In collaboration with the members of ICRR and TD-Lee Institute

Product group unification is an attractive alternative to simple grand unification. It solves the infamous doublet-triplet splitting problem and the dimension-5 proton decay problems without introducing any fine-tuning. Furthermore, the matter multiplets are still embedded into unified SU(5) representations. In this paper, we discuss proton decay of the simplest product group unification model based on SU(5)XU(2)$_H$. We find that the minimal setup of the model has already been excluded by dimension-6 proton decay. We also show that a simple extension of the model, with naturally generated SU(5) incomplete multiplets, can rectify this problem. We find that the proton lifetime will be in reach of coming experiments like DUNE and Hyper-K, when the mass of the incomplete multiplet is associated with the Peccei-Quinn symmetry breaking. In this case, the dark matter may be an admixture of the Wino LSP and the axion.

• Freeze-in generation of lepton asymmetries after baryogenesis in the νMSM [3]

In collaboration with the members of ICRR and EPFL

The νMSM – an extension of the Standard Model by three relatively light singlet Majorana fermions $N_{1,2,3}$ – allows for generation of lepton asymmetry which is several orders of magnitude larger than the observed baryon asymmetry of the Universe. The lepton asymmetry is produced in interactions of $N_{2,3}$ (with masses in the GeV region) at temperatures below the sphaleron freeze out $T < 130$ GeV and can enhance the cosmological production of dark matter (DM) sterile neutrinos N_1 (with mass of the keV scale) happening at $T \sim 200$ MeV due to active-sterile neutrino mixing. In this work we address the question of the magnitude of late-time asymmetry (LTA) generated by the heavy neutral leptons $N_{2,3}$ during their freeze-in at $T \sim 20$ GeV and study how much of it can survive down to the lower temperatures relevant for the sterile neutrino DM creation. We find that this LTA could result in production of a sizeable fraction of dark matter. We also examine a role played by magnetic fields and the Abelian chiral anomaly in generation of LTA, not accounted for in the previous studies. We argue that the production of LTA can be increased significantly and make an estimate of the influence of this effect.

Bibliography

[1] T. Hiramatsu, M. Ibe and M. Suzuki, JHEP **09** (2020), 054 doi:10.1007/JHEP09(2020)054 [arXiv:2005.10421 [hep-ph]].

[2] J. L. Evans, M. Ibe and T. T. Yanagida, Phys. Rev. D **103** (2021) no.3, 035009 doi:10.1103/PhysRevD.103.035009 [arXiv:2009.11448 [hep-ph]].

[3] S. Eijima, M. Shaposhnikov and I. Timiryasov, [arXiv:2011.12637 [hep-ph]].

Dark Matter

• J-factor estimation of Draco, Sculptor and Ursa Minor dwarf spheroidal galaxies with the member/foreground mixture model [1]

In collaboration with the members of ICRR, Kavli IPMU and Tohoku U.

Dwarf spheroidal galaxies (dSphs) are promising targets of indirect detection experiments searching for dark matter (DM) at present universe. Toward robust prediction for the amount of signal flux originating in DM annihilation inside dSphs, a precise determination of DM distributions as well as J-factors of the dSphs is particularly important. In this work, we estimate those of Draco, Sculptor, and Ursa Minor dSphs by an improved statistical method in which both foreground stars and dSph member stars are simultaneously taken into account. We define the likelihood function of the method as the so-called conditional one to remove sampling bias of observed stellar data. This improved method enables us to estimate DM distributions and J-factors of the dSphs directly from observed stellar data contaminated by foreground stars without imposing stringent membership criteria on the measured quantities.

• N-body self-consistent stars-halo modeling of the Fornax dwarf galaxy [2]"

In collaboration with the members of ICRR, ITEP, Kavli IPMU and Lomonosov Moscow State U.

We present nearly self-consistent stellar-halo models of the Fornax dwarf spheroidal galaxy associated with the Milky Way galaxy. Such galaxies are dominated by dark matter and have almost no gas in the system. Therefore, they are excellent objects for N-body modeling that takes into account visible and dark matter halo components. In order to model the dark matter halo inferred from the analysis of the measured velocities of Fornax's stars, we constructed several self-consistent quasi-equilibrium models based on two source code sets. One of them (GalactICS Software, NEMO) deals with the self-consistent distribution function modeling which depends on energy E and vertical component of the angular momentum L_z. The other is included in the AGAMA framework and is based on Schwarzschild's calculation of orbits. It can reproduce the non-spherical self-consistent structure of Fornax as the weighted sum of orbit contributions to the galactic density even though the inferred dark halo parameters come from Jeans analysis which does not require that any distribution functions should be positive. To guess the parameters which make the N-body models close to the visible object we use the stellar-dark matter model of the Fornax galaxy based on hydrodynamic axisymmetric Jeans equations taking into account the velocity anisotropy parameter. Then we studied the evolution of the models by performing N-body simulations with the falcON code in order to test their stability. The variability of the model parameters over time was obtained during simulations. The AGAMA models show the best agreement of the resulting velocity dispersion profiles with the observed data.

• Formation of massive globular clusters with dark matter and its implication on dark matter annihilation [3]

In collaboration with the members of ICRR and The University of Western Australia

Recent observational studies of γ-ray emission from massive globular clusters (GCs) have revealed possible evidence of dark matter (DM) annihilation within GCs. It is, however, still controversial whether the emission comes from DM or from milli-second pulsars. We here present the new results of numerical simulations, which demonstrate that GCs with DM can originate from nucleated dwarfs orbiting the ancient MW. The simulated stripped nuclei (i.e., GCs) have the central DM densities ranging from 0.1 to several $M_\odot pc^{-3}$, depending on the orbits and the masses of the host dwarf galaxies. However, GCs born outside the central regions of their hosts can have no/little DM after their hosts are destroyed and the GCs become the Galactic halo GCs. These results suggest that only GCs originating from stellar nuclei of dwarfs can possibly have DM. We further calculate the expected γ-ray emission from these simulated GCs and compare them to observations of ω Cen. Given the large range of DM densities in the simulated GCs, we suggest that the recent possible detection of DM annihilation from GCs should be more carefully interpreted.

• Diversity of Dark Matter Density Profiles in the Galactic Dwarf Spheroidal Satellites [4]

In collaboration with the members of ICRR, Tohoku U. and Chiba U.

The core-cusp problem is one of the controversial issues in the standard paradigm of Λ cold dark matter (ΛCDM) theory. However, under the assumption of conventional spherical symmetry, the strong degeneracy among model parameters makes it unclear whether dwarf spheroidal (dSph) galaxies indeed have cored dark matter density profiles at the centers. In this work, we revisit this problem using non-spherical mass models, which have the advantage of being able to alleviate the degeneracy. Applying our mass models to the currently available kinematic data of the eight classical dSphs, we find that within finite uncertainties, most of these dSphs favor cusped central profiles rather than cored ones. In particular, Draco has a cusped dark matter halo with high probability even considering a prior bias. We also find the diversity of the inner slopes in their dark matter halos. To clarify the origin of this diversity, we investigate the relation between the inner dark matter density slope and stellar-to-halo mass ratio for the sample dSphs and find this relation is generally in agreement with the predictions from recent ΛCDM and hydrodynamical simulations. We also find that the simulated subhalos have anti-correlation between the dark matter density at 150 pc and pericenter distance, which is consistent with the observed one. We estimate their astrophysical factors for dark matter indirect searches and circular velocity profiles, associated with huge uncertainties. To more precisely estimate their dark matter profiles, wide-field spectroscopic surveys for the dSphs are essential.

• Cosmological Constraint on Vector Mediator of Neutrino-Electron Interaction in light of XENON1T Excess [5]

In collaboration with the members of ICRR and Kavli IPMU

Recently, the XENON1T collaboration reported an excess in the electron recoil energy spectrum. One of the simplest new physics interpretation is a new neutrino-electron interaction mediated by a light vector particle. However, for the parameter region favored by this excess, the constraints from the stellar cooling are severe. Still, there are astrophysical uncertainties on those constraints. In this paper, we discuss the constraint on the light mediator from the effective number of neutrino Neff in the CMB era, which provides an independent constraint. We show that Neff is significantly enhanced and exceeds the current constraint in the parameter region favored for the XENON1T excess. As a result, the interpretation by a light mediator heavier than about 1 eV is excluded by the Neff constraint.

• Probing dark matter self-interaction with ultrafaint dwarf galaxies [6]

In collaboration with the members of ICRR, Kavli IPMU and Tohoku U.

Self-interacting dark matter (SIDM) has gathered growing attention as a solution to the small scale problems of the collisionless cold dark matter (DM). We investigate the SIDM using stellar kinematics of 23 ultra-faint dwarf (UFD) galaxies with the phenomenological SIDM halo model. The UFDs are DM-dominated and have less active star formation history. Accordingly, they are the ideal objects to test the SIDM, as their halo profiles are least affected by the baryonic feedback processes. We found no UFDs favor non-zero self-interaction and some provide stringent constraints within the simple SIDM modeling. Our result challenges the simple modeling of the SIDM, which urges further investigation of the subhalo dynamical evolution of the SIDM.

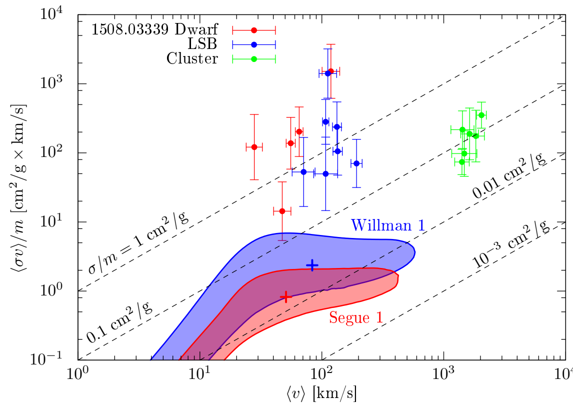

Fig. 15. The 1σ parameter estimation of $\langle v\rangle$-$\langle\sigma v\rangle/m$ based on the MLE for Segue 1 and Willman 1 with the Plummer profile. We also show the SIDM cross section which are favored by the dwarf irregular galaxies (red), low surface brightness galaxies (blue) and clusters (green). The values are subject to $\mathcal{O}(1)$ uncertainties in the thermalized condition.

• Detection capability of the Migdal effect for argon and xenon nuclei with position-sensitive gaseous detectors [7]

In collaboration with the members of ICRR, Kobe U., KMI, Nagoya and Hebrew U.

Migdal effect is attracting interests because of the potential to enhance the sensitivities of direct dark matter searches to the low mass region. In spite of its great importance, the Migdal effect has not been experimentally observed yet. A realistic experimental approach towards the first observation of the Migdal effect in the neutron scattering was studied with Monte Carlo simulations. In this study, potential background rate was studied together with the event rate of the Migdal effect by a neutron source. It was found that a table-top sized $\sim (30\mathrm{cm})^3$ position-sensitive gaseous detector filled with argon or xenon target gas can detect characteristic signatures of the Migdal effect with sufficient rates (O($10^2 \sim 10^3$) events/day). A simulation result of a simple experimental set-up showed two significant background sources, namely the intrinsic neutrons and the neutron induced gamma-rays. These background rates were found to be much higher than those of the Migdal effect in the neutron scattering. As a consequence of this study, it is concluded that the experimental observation of the Migdal effect in the neutron scattering can be realized with a good understanding and reduction of the background.

Bibliography

[1] S. i. Horigome, K. Hayashi, M. Ibe, M. N. Ishigaki, S. Matsumoto and H. Sugai, [arXiv:2002.04866 [astro-ph.GA]].

[2] G. Shchelkanova, K. Hayashi and S. Blinnikov, ApJ, 909, 147 (2021) doi:10.3847/1538-4357/abdd24 [arXiv:2004.11215 [astro-ph.GA]].

[3] H. Wirth, K. Bekki and K. Hayashi, Mon. Not. Roy. Astron. Soc. **496** (2020) no.1, L70-L74

doi:10.1093/mnrasl/slaa089 [arXiv:2005.07128 [astro-ph.GA]].

[4] K. Hayashi, M. Chiba and T. Ishiyama, Astrophys. J. **904** (2020) no.1, 45 doi:10.3847/1538-4357/abbe0a [arXiv:2007.13780 [astro-ph.GA]].

[5] M. Ibe, S. Kobayashi, Y. Nakayama and S. Shirai, JHEP **12** (2020), 004 doi:10.1007/JHEP12(2020)004 [arXiv:2007.16105 [hep-ph]].

[6] K. Hayashi, M. Ibe, S. Kobayashi, Y. Nakayama and S. Shirai, Phys. Rev. D **103** (2021) no.2, 023017 doi:10.1103/PhysRevD.103.023017 [arXiv:2008.02529 [astro-ph.CO]].

[7] K. D. Nakamura, K. Miuchi, S. Kazama, Y. Shoji, M. Ibe and W. Nakano, PTEP **2021** (2021) no.1, 013C01 doi:10.1093/ptep/ptaa162 [arXiv:2009.05939 [physics.ins-det]].

Axions

• On Stability of Fermionic Superconducting Current in Cosmic String [1]

In collaboration with the members of ICRR and Kavli IPMU

Recently, the chiral superconductivity of the cosmic string in the axion model has gathered attention. The superconductive nature can alter the standard understanding of the cosmology of the axion model. For example, a string loop with a sizable superconducting current can become a stable configuration, which is called a Vorton. The superconductive nature can also affect the cosmological evolution of the string network. In this paper, we study the stability of the superconducting current in the string. We find the superconductivity is indeed stable for a straight string or infinitely small string core size, even if the carrier particles are unstable in the vacuum. However we also find that the carrier particle decays in a curved string in typical axion models, if the carrier particles are unstable in the vacuum. Accordingly, the lifetime of the Vorton is not far from that of the carrier particle in the vacuum.

Bibliography

[1] M. Ibe, S. Kobayashi, Y. Nakayama and S. Shirai, JHEP **05** (2021), 217 doi:10.1007/JHEP05(2021)217 [arXiv:2102.05412 [hep-ph]].

Primordial Black Holes

• Constraining Primordial Black Holes with Dwarf Galaxy Heating [1]

In collaboration with the members of ICRR, UCLA, Kavli IPMU, Tohoku U., Osaka U. and RIKEN

Black holes formed in the early universe, prior to the formation of stars, can exist as dark matter and also contribute to the black hole merger events observed in gravitational waves. We set a new limit on the abundance of primordial black holes (PBHs) by considering interactions of PBHs with the interstellar medium, which result in the heating of gas. We examine generic heating mechanisms, including emission from the accretion disk, dynamical friction, and disk outflows. Using the data from the Leo T dwarf galaxy, we set a new cosmology-independent limit on the abundance of PBHs in the mass range $\mathscr{O}(1)M_\odot - 10^7 M_\odot$, relevant for the recently detected gravitational wave signals from intermediate-mass BHs.

Bibliography

[1] P. Lu, V. Takhistov, G. B. Gelmini, K. Hayashi, Y. Inoue and A. Kusenko, Astrophys. J. Lett. **908** (2021) no.2, L23 doi:10.3847/2041-8213/abdcb6 [arXiv:2007.02213 [astro-ph.CO]].

Particle Cosmology

[Spokesperson : M. Kawasaki]
ICRR, The Univ. of Tokyo, Kashiwa, Chiba 277-8582

Inflation

• Chiral Gravitational Waves Produced in a Helical Magnetogenesis Model [1]

In collaboration with the members of ICRR and Titech

We investigate the gravitational wave production induced by the primordial magnetic fields in a parity-violating magnetogenesis model. It is shown that the gravitational waves detectable by LISA, DECIGO or BBO and the magnetic fields strong enough to explain the blazar observation can be simultaneously produced. The magnetic fields and the gravitational waves have the same chirality and their amplitudes are related, which may also be tested by future observations.

• Bipartite temporal Bell inequalities for two-mode squeezed states [2]

In collaboration with the members of ICRR and APC

Bipartite temporal Bell inequalities are similar to the usual Bell inequalities except that, instead of changing the direction of the polariser at each measurement, one changes the time at which the measurement is being performed. By doing so, one is able to test for realism and locality, but relying on position measurements only. This is particularly useful in experimental setups where the momentum direction cannot be probed (such as in cosmology for instance). We study these bipartite temporal Bell inequalities for continuous systems placed in two-mode squeezed states, and find some regions in parameter space where they are indeed violated. We highlight the role played by the rotation angle, which is one of the three parameters characterising a two-mode squeezed state (the other two being the squeezing amplitude and the squeezing angle). In single-time measurements, it only determines the overall phase of the wavefunction and can therefore be discarded, but in multiple-time measurements, its time dynamics becomes relevant and crucially determines when bipartite temporal Bell inequalities can be violated. Our study opens up the possibility of new experimental designs for the observation of Bell inequality violations.

• Statistically-Anisotropic Tensor Bispectrum from Inflation [3]

In collaboration with the members of ICRR, Rikkyo U, MPI, and KMI, Nagoya

We develop a possibility of generating tensor non-Gaussianity in a kind of anisotropic inflation, where a $U(1)$ gauge field is kinetically coupled to a spectator scalar field. Owing to this coupling, the coherent mode of the electric field appears and softly breaks the isotropy of the Universe. We compute the bispectrum of linearly-polarized tensor perturbations sourced by the gauge field and find that it is strongly red-tilted and has distinctive statistical anisotropies including higher-order multipole moments. Interestingly, the tensor bispectra with the specific combinations of linear polarization modes are dominant, and their amplitudes depend on the different sets of multipole moments. This new type of statistically-anisotropic tensor non-Gaussianity can be potentially testable with the upcoming cosmic microwave background B-mode polarization experiments.

• Affleck-Dine inflation in supergravity [4]

In collaboration with the members of ICRR

Affleck-Dine inflation is a recently proposed model in which a single complex scalar field, nonminimally coupled to gravity, drives inflation and simultaneously generates the baryon asymmetry of universe via Affleck-Dine mechanism. In this paper we investigate the supersymmetric implementation of Affleck-Dine inflation in the use of two chiral superfields with appropriate superpotential and Kähler potential. The scalar potential has a similar form to the potential of original Affleck-Dine inflation, and it gives successful inflation and baryogenesis. We also consider the isocurvature perturbation evolving after crossing the horizon, and find that it is ignorable and hence consistent with the observations.

• Detection of isotropic cosmic birefringence and its implications for axionlike particles including dark energy [5]

In collaboration with the members of ICRR and Waseda U.

We investigate the possibility that axion-like particles (ALPs) with various potentials account for the isotropic birefringence recently reported by analyzing the Planck 2018 polarization data. For the quadratic and cosine potentials, we obtain lower bounds on the mass, coupling constant to photon g, abundance and equation of state of the ALP to produce the observed birefringence. Especially when the ALP is responsible for dark energy, it is possible to probe the tiny deviation of dark energy equation of state from -1 through the cosmic birefringence. We also explore ALPs working as early dark energy (EDE), which alleviates the Hubble tension problem. Since the other parameters are limited by the

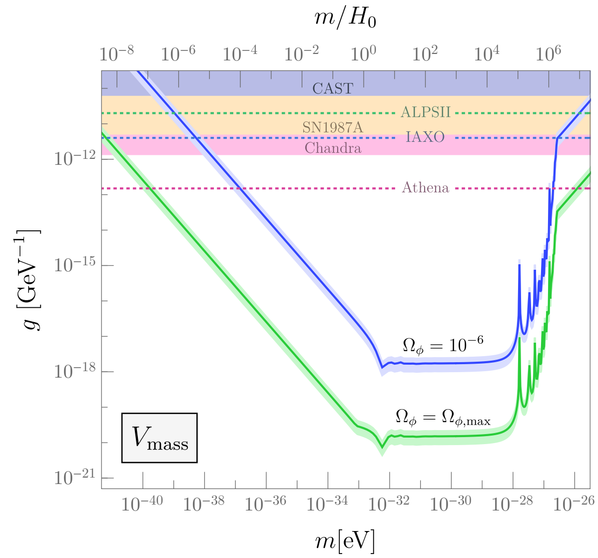

Fig. 16. *The ALP-photon coupling constant g inferred by the isotropic birefringence $\bar{\alpha} = 0.35 \pm 0.14$ deg versus the ALP mass m for the quadratic potential $V_{\rm mass}(\phi) = m^2\phi^2/2$. The green line corresponds to the maximum energy fraction, whereas the blue line shows the case with $\Omega_\phi = 10^{-6}$. The shaded regions are excluded by the measurements of CAST (blue), SN1987A (orange), and Chandra (pink). We also plot the projected sensitivities of the future experiments, ALPSII, IAXO, and Athena, from top to bottom as dotted lines.*

EDE requirements, we narrow down the ALP-photon coupling to $10^{-19}\,\mathrm{GeV}^{-1} \lesssim g \lesssim 10^{-16}\,\mathrm{GeV}^{-1}$ for the decay constant $f = M_{\rm pl}$. Therefore, the Hubble tension and the isotropic birefringence imply that g is typically the order of f^{-1}, which is a non-trivial coincidence.

• Power spectrum in stochastic inflation [6]

In collaboration with the members of ICRR and APC

We compute the power spectrum of curvature perturbations in stochastic inflation. This combines the distribution of first crossing times through the end-of-inflation surface, which has been previously studied, with the distribution of the fields value at the time when a given scale crosses out the Hubble radius during inflation, which we show how to compute. This allows the stochastic-δN formalism to make concrete contact with observations. As an application, we study how quantum diffusion at small scales (arising e.g. in models leading to primordial black holes) affects the large-scale perturbations observed in the cosmic microwave background. We find that even if those sets of scales are well separated, large effects can arise from the distortion of the classical relationship between field values and wavenumbers brought about by quantum diffusion near the end of inflation. This shows that cosmic microwave background measurements can set explicit constraints on the entire inflationary potential down to the end of inflation.

Bibliography

[1] S. Okano and T. Fujita, JCAP **03** (2021), 026 doi:10.1088/1475-7516/2021/03/026 [arXiv:2005.13833 [astro-ph.CO]].

[2] K. Ando and V. Vennin, Phys. Rev. A **102** (2020) no.5, 052213 doi:10.1103/PhysRevA.102.052213 [arXiv:2007.00458 [quant-ph]].

[3] T. Hiramatsu, K. Murai, I. Obata and S. Yokoyama, JCAP **03** (2021), 047 doi:10.1088/1475-7516/2021/03/047 [arXiv:2008.03233 [astro-ph.CO]].

[4] M. Kawasaki and S. Ueda, JCAP **04** (2021), 049 doi:10.1088/1475-7516/2021/04/049 [arXiv:2011.10397 [hep-ph]].

[5] T. Fujita, K. Murai, H. Nakatsuka and S. Tsujikawa, Phys. Rev. D **103** (2021) no.4, 043509 doi:10.1103/PhysRevD.103.043509 [arXiv:2011.11894 [astro-ph.CO]].

[6] K. Ando and V. Vennin, JCAP **04** (2021), 057 doi:10.1088/1475-7516/2021/04/057 [arXiv:2012.02031 [astro-ph.CO]].

Axions

• Probing axionlike particles via cosmic microwave background polarization [1]

In collaboration with the members of ICRR and Osaka U., Res. Ctr. Nucl. Phys.

Axion-like particles (ALPs) rotate the linear polarization of photons through the ALP-photon coupling and convert the cosmic microwave background (CMB) E-mode to the B-mode. We derive the relation between the ALP dynamics and the rotation angle by assuming that the ALP ϕ has a quadratic potential, $V = m^2\phi^2/2$. We compute the current and future sensitivities of CMB observations to the ALP-photon coupling g, which can reach $g = 4\times10^{-21}\,\mathrm{GeV}^{-1}$ for $10^{-32}\,\mathrm{eV} \lesssim m \lesssim 10^{-28}\,\mathrm{eV}$ and extensively exceed the other searches for any mass $m \lesssim 10^{-25}\,\mathrm{eV}$. We find that the fluctuation of the ALP field at the observer, which has been neglected in previous studies, can induce significant isotropic rotation of the CMB polarization. The measurements of isotropic and anisotropic rotation allow us to put bounds on relevant quantities such as the ALP mass m and the ALP density parameter Ω_ϕ. In particular, if LiteBIRD detects anisotropic rotation, we obtain the lower bound on the tensor-to-scalar ratio as $r > 5\times10^{-9}$.

• Resonant gravitational waves in dynamical Chern-Simons-axion gravity [2]

In collaboration with the members of ICRR Kyoto U. and MPA

In this paper, we consider dynamical Chern-Simons gravity with the identification of the scalar field coupled though the Pontryagin density with the axion dark matter, and we discuss the effects of the parametric resonance on gravitational waves (GWs). When we consider GWs in a coherently oscillating axion cloud, we confirm that significant resonant amplification of GWs occurs in a narrow frequency band, and the amplification is restricted to the late epoch after the passage of the incident waves. We also identify the condition that an axion cloud spontaneously emits GWs. Once we take into account the randomness of the spatial phase distribution of the axion oscillations, we find that the amplification is suppressed compared with the coherent case, but significant amplification of GWs can still occur. We also examine whether or not the amplification of GWs is possible in the present universe, taking into account the history of the universe. We find that resonant amplification is difficult to be tested from GW observations in the standard scenario of the axion DM model, in which the axion is the dominant component of DM. However, there is some parameter window in which the resonant amplification of GWs might be observed, if the axion is subdominant component of DM, and the axion cloud formation is delayed until the Hubble rate becomes much smaller than the axion mass.

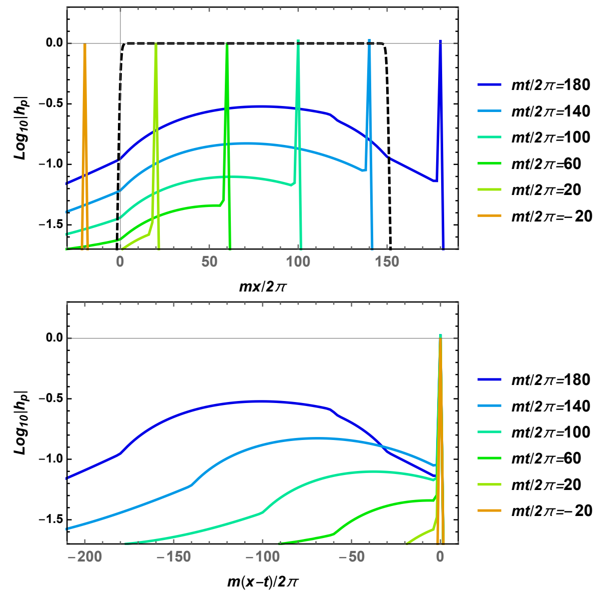

Fig. 17. *The time evolution of the wave packet. The top panel shows how the wave packet propagates in the axion cloud, while the horizontal axes is $m(x-t)/2\pi$ in the bottom panel such that the original center of the wave packet is overlapped. The black dashed line in the top panel denotes the distribution of the axion amplitude $|\varepsilon(x)|$ whose plateau value is 0.03. The resonant amplification is significant in the coherent axion cloud but it takes place only in the causal future and slightly on the tip of the wave packet.*

• Oscillons of Axion-Like Particle: Mass distribution and power spectrum [3]

In collaboration with the members of ICRR and Tokyo U.

In string theory, the simultaneous existence of many Axion-Like Particles (ALPs) are suggested over a vast mass range, and a variety of potentials have been developed in the context of inflation. In such potentials shallower than quadratic, the prominent instability can produce localized dense objects, oscillons. Because of the approximate conservation of their adiabatic invariant, oscillons generally survive quite long, maybe up to the current age of the universe in the case of ultra-light ALPs with $m \sim 10^{-22}$ eV. Such oscillons can have significant effects on the evolution of the recent universe. In this paper, we investigate the oscillons of the pure-natural type potential by classical lattice simulation to explore the key quantities necessary for phenomenological application: the number density of oscillons, the oscillon mass distribution, the energy ratio of oscillons to the ALP field, and the power spectrum. Then, we evolve these values in consideration of the analytic decay rate.

• Probing Oscillons of Ultra-Light Axion-like Particle by 21cm Forest [4]

In collaboration with the members of ICRR and Tokyo U.

Ultra-Light Axion-like Particle (ULAP) is motivated as one of the solutions to the small scale problems in astrophysics. When such a scalar particle oscillates with an $\mathcal{O}(1)$ amplitude in a potential shallower than quadratic, it can form a localized dense object, oscillon. Because of its longevity due to the approximate conservation of the adiabatic invariant, it can survive up to the recent universe as redshift $z \sim \mathcal{O}(10)$. The scale affected by these oscillons is determined by the ULAP mass m and detectable by observations of 21cm line. In this paper, we examine the possibility to detect ULAP by 21cm line and find that the oscillon can enhance the signals of 21cm line observations when $m \lesssim 10^{-19}$ eV and the fraction of ULAP to dark matter is much larger than 10^{-2} depending on the form of the potential.

Bibliography

[1] T. Fujita, Y. Minami, K. Murai and H. Nakatsuka, Phys. Rev. D **103** (2021) no.6, 063508 doi:10.1103/PhysRevD.103.063508 [arXiv:2008.02473 [astro-ph.CO]].

[2] T. Fujita, I. Obata, T. Tanaka and K. Yamada, Class. Quant. Grav. **38** (2021) no.4, 045010 doi:10.1088/1361-6382/abce49 [arXiv:2008.02764 [gr-qc]].

[3] M. Kawasaki, W. Nakano, H. Nakatsuka and E. Sonomoto, JCAP **01** (2021), 061 doi:10.1088/1475-7516/2021/01/061 [arXiv:2010.09311 [astro-ph.CO]].

[4] M. Kawasaki, W. Nakano, H. Nakatsuka and E. Sonomoto, [arXiv:2010.13504 [astro-ph.CO]].

Primordial Black Holes

• NANOGrav Results and LIGO-Virgo Primordial Black Holes in Axionlike Curvaton Models [1]

In collaboration with the members of ICRR, Chicago U., CERN and TD-Lee Inst.

We discuss a possible connection between the recent NANOGrav results and the primordial black holes (PBHs) for the LIGO-Virgo events. In particular, we focus on the axion-like curvaton model, which provides a sizable amount of PBHs and GWs induced by scalar perturbations around the NANOGrav frequency range. The inevitable non-Gaussianity of this model suppresses the induced GWs associated with PBHs for the LIGO-Virgo events to be compatible with the NANOGrav results. We show that the axion-like curvaton model can account for PBHs for the LIGO-Virgo events and the NANOGrav results simultaneously.

• Gravitational waves from type II axion-like curvaton model and its implication for NANOGrav result [2]

In collaboration with the members of ICRR

The recent report of NANOGrav is gathering attention since its signal can be explained by the stochastic gravitational waves (GWs) with $\Omega_{\rm GW} \sim 10^{-9}$ at $f \sim 10^{-8}$Hz. The PBH formation scenario is one of the candidates for the NANOGrav signal, which can simultaneously explain the observed $30M_\odot$ black holes in the binary merger events in LIGO-Virgo collaboration. We focus on the type II axion-like curvaton model of the PBH formation. In type II model the complex field whose phase part is the axion rolls down from the origin of the potential. It is found that type II model achieves the broad power spectrum of the density perturbations and can simultaneously explain the LIGO-Virgo events and the NANOGrav signal. We also improve the treatment of the non-Gaussianity of perturbations in our model to accurately estimate the amplitude of the induced GWs.

Bibliography

[1] K. Inomata, M. Kawasaki, K. Mukaida and T. T. Yanagida, Phys. Rev. Lett. **126** (2021) no.13, 131301 doi:10.1103/PhysRevLett.126.131301 [arXiv:2011.01270 [astro-ph.CO]].

[2] M. Kawasaki and H. Nakatsuka, JCAP **05** (2021), 023 doi:10.1088/1475-7516/2021/05/023 [arXiv:2101.11244 [astro-ph.CO]].

Dark Matter

• Ultralight vector dark matter search with auxiliary length channels of gravitational wave detectors [1]

In collaboration with the members of ICRR, Tokyo U., Garching, Max Planck Inst.

Recently, a considerable amount of attention has been given to the search for ultralight dark matter by measuring the oscillating length changes in the arm cavities of gravitational wave detectors. Although gravitational wave detectors are extremely sensitive for measuring the differential arm length changes, the sensitivity to dark matter is largely attenuated, as the effect of dark matter is mostly common to arm cavity test masses. Here, we propose to use auxiliary length channels, which measure the changes in the power and signal recycling cavity lengths and the differential Michelson interferometer length. The sensitivity to dark matter can be enhanced by exploiting the fact that auxiliary interferometers are more asymmetric than two arm cavities. We show that the sensitivity to $U(1)_{B-L}$ gauge boson dark matter with masses below 7×10^{-14} eV can be greatly enhanced when our method is applied to a cryogenic gravitational wave detector KAGRA, which employs sapphire test masses and fused silica auxiliary mirrors. We show that KAGRA can probe more than an order of magnitude of unexplored parameter space at masses around 1.5×10^{-14} eV, without any modifications to the existing interferometer.

• Improved sensitivity of interferometric gravitational wave detectors to ultralight vector dark matter from the finite light-traveling time [2]

In collaboration with the members of ICRR, Wisconsin U., Madison, Tokyo U. and Garching, Max Planck Inst.

Recently several studies have pointed out that gravitational-wave detectors are sensitive to ultralight vector dark matter and can improve the current best constraints given by the Equivalence Principle tests. While a gravitational-wave detector is a highly precise measuring tool of the length difference of its arms, its sensitivity is limited because the displacements of its test mass mirrors caused by vector dark matter are almost common. In this Letter we point out that the sensitivity is significantly improved if the effect of finite light-traveling time in the detector's arms is taken into account. This effect enables advanced LIGO to improve the constraints on the $U(1)_{B-L}$ gauge coupling by an order of magnitude compared with the current best constraints. It also makes the sensitivities of the future gravitational-wave detectors overwhelmingly better than the current ones. The factor by which the constraints are improved due to the new effect depends on the mass of the vector dark matter, and the maximum improvement factors are 470, 880, 1600, 180 and 1400 for advanced LIGO, Einstein Telescope, Cosmic Explorer, DECIGO and LISA respectively. Including the new effect, we update the constraints given by the first observing run of advanced LIGO and improve the constraints on the $U(1)_B$ gauge coupling by an order of magnitude compared with the current best constraints.

Bibliography

[1] Y. Michimura, T. Fujita, S. Morisaki, H. Nakatsuka and I. Obata, Phys. Rev. D **102** (2020) no.10, 102001 doi:10.1103/PhysRevD.102.102001 [arXiv:2008.02482 [hep-ph]].

[2] S. Morisaki, T. Fujita, Y. Michimura, H. Nakatsuka and I. Obata, Phys. Rev. D **103** (2021) no.5, L051702 doi:10.1103/PhysRevD.103.L051702 [arXiv:2011.03589 [hep-ph]].

Big Bang Nucleosynthesis

• Big Bang Nucleosynthesis constraints on sterile neutrino and lepton asymmetry of the Universe [1]

In collaboration with the members of ICRR, Kavli IPMU and UCLA

We consider the cosmological effects of sterile neutrinos with the masses of $150-450$ MeV. The decay of sterile neutrinos changes the thermal history of the Universe and affects the energy density of radiation at the recombination and the big bang nucleosynthesis (BBN) results. We derive severe constraints on the parameters of sterile neutrinos from the primordial abundances of helium-4 and deuterium. We also find that in a particular model the constraints can be considerably relaxed by assuming a large lepton asymmetry in the active neutrinos. In this case, the consistent parameters result in $N_{\rm eff}\simeq3.2-3.4$ and can alleviate the Hubble tension.

• Big-bang nucleosynthesis with sub-GeV massive decaying particles [2]

In collaboration with the members of ICRR, KEK, UC Berkeley and Tokyo U.

We consider the effects of the injections of energetic photon and electron (or positron) on the big-bang nucleosynthesis. We study the photodissociation of light elements in the early Universe paying particular attention to the case that the injection energy is sub-GeV and derive upper bounds on the primordial abundances of the massive decaying particle as a function of its lifetime. We also discuss a solution of the ^{7}Li problem in this framework.

Bibliography

[1] G. B. Gelmini, M. Kawasaki, A. Kusenko, K. Murai and V. Takhistov, JCAP **09** (2020), 051 doi:10.1088/1475-7516/2020/09/051 [arXiv:2005.06721 [hep-ph]].

[2] M. Kawasaki, K. Kohri, T. Moroi, K. Murai and H. Murayama, JCAP **12** (2020), 048 doi:10.1088/1475-7516/2020/12/048 [arXiv:2006.14803 [hep-ph]].

OBSERVATORIES and A RESEARCH CENTER

Location of the Institute and the Observatories

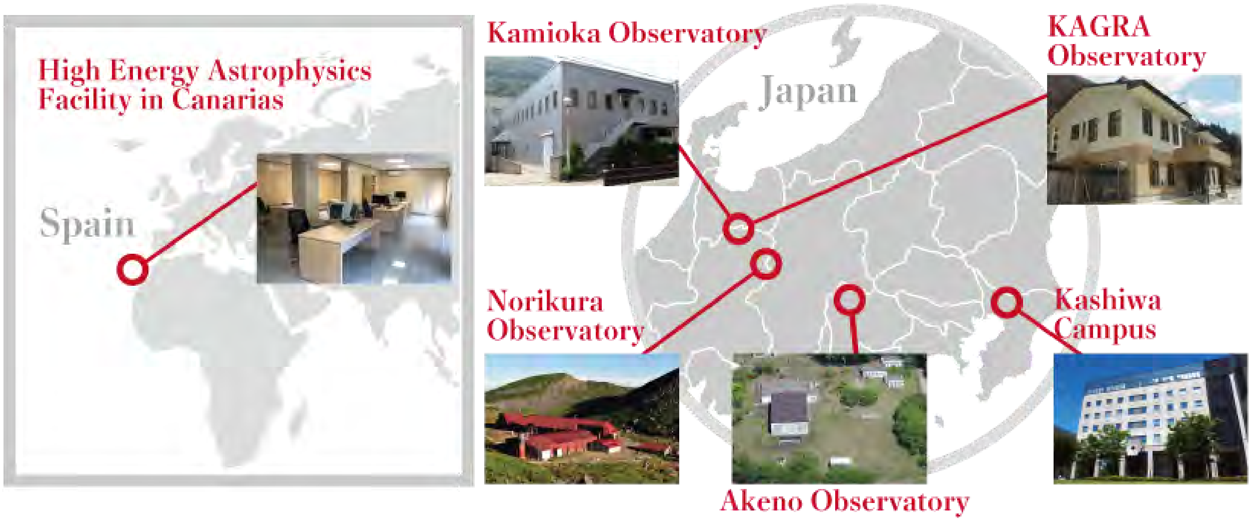

Norikura Observatory

Location:	Norikuradake, Nyukawa-cho, Takayama-shi, Gifu Prefecture 506-2100
Telephone (Fax):	+81-50-3730-3809
Telephone (satellite):	+81-90-7721-5674
Telephone (car):	+81-90-7408-6224

Akeno Observatory

Location:	5259 Asao, Akeno-machi, Hokuto-shi, Yamanashi Prefecture 408-0201
Telephone / Fax:	+81-551-25-2301 / +81-551-25-2303

Kamioka Observatory

Location:	456 Higashi-mozumi, Kamioka-cho, Hida-shi, Gifu Prefecture 506-1205
Telephone / Fax:	+81-578-85-2116 / +81-578-85-2121

KAGRA Observatory

Location:	238 Higashi-mozumi, Kamioka-cho, Hida-shi, Gifu Prefecture 506-1205
Telephone / Fax:	+81-578-85-2343 / +81-578-85-2346

Research Center for Cosmic Neutrinos

Location:	5-1-5 Kashiwanoha, Kashiwa, Chiba Prefecture 277-8582
Telephone / Fax:	+81-4-7136-3138 / +81-4-7136-3115

High Energy Astrophysics Facility in Canarias

Location:	C/Via Lactea, s/n E-38205 La Lagua - Tenerife Espana

NORIKURA OBSERVATORY

Introduction

Norikura Observatory (36.10°N and 137.55°E) was founded in 1953 and attached to ICRR in 1976. It is located at 2770 m above sea level, and is the highest altitude manned laboratory in Japan (Fig. 1). Experimental facilities of the laboratory are made available to all the qualified scientists in the field of cosmic ray research and associated subjects. The AC electric power is generated by the dynamo and supplied throughout the observatory. The observatory can be accessed easily by car and public bus in summer (July-September). The 60th anniversary of Norikura Observatory was celebrated in 2013.

Fig. 1. Norikura Observatory

Norikura Observatory gave manned operation to the observations by the qualified scientists all the year until the year 2003. However, the feasibility of the automatic operation of Norikura Observatory during winter period has been tested since winter 2004 in order to study the possibilities to reduce maintenance and labor costs without causing serious inconveniences for the researches. A long-distance (∼40km) wireless LAN system (11M bps) was set up in 2003. Two new easy-to-handle and easy-to-maintain dynamos of 115 KVA each, as shown in Fig. 2 were installed in 2004 as well. The unmanned operation of Norikura Observatory has been mostly successful in winter, during which the battery backed-up solar panels and/or wind power generators kept supplying the electricity to the wireless LAN and on-going cosmic-ray experiments.

Present major scientific interests of the laboratory is focused on the modulation of high energy cosmic rays in the interplanetary space associated with the solar activity, the generation of energetic particles by the solar flares, and the particle acceleration mechanism in thunderclouds, all of which require long-term observation. These researches have been carried out by the group of user universities, where ICRR provides them with laboratory facility. A part of the facility has been open for the environmental study at high altitude such as aerosol-related mechanism in the atmosphere, observation of total ozone and UV solar radiation, for botanical study in the high-altitude environment, etc..

Fig. 2. A dynamo of 115KV.

Cosmic Ray Physics

Space weather observation

Space weather observation is actively made by a 25 m^2 muon hodoscope at Norikura Observatory[1],[2],[3],[4],[5],[6],[7],[8],[9],[10]. Mt. Norikura muon hodoscope has started operation in May, 1998 and successfully observed a clear precursory signature of the interplanetary shock arrival at Earth. With its improved angular resolution of muon incident direction, the detector succeeded for the first time to observe a loss-cone signature which is an intensity deficit within a narrow cone around the interplanetary magnetic field (IMF). The observation of the loss-cone precursor gives us unique information for the space weather forecast and for understanding the interplanetary disturbances in near Earth space.

Following this successful observation, we installed a small muon hodoscope in Kuwait City, Kuwait as the fourth detector in our Global Muon Detector Network (GMDN) with other three multidirectional muon detectors in Nagoya (Japan), Hobart (Australia), and São Martinho (Brazil). The GMDN has started operation in March, 2006 monitoring the intensity of ∼ 50 GeV cosmic rays over an entire sky around Earth. The cosmic ray observations using muon detector are complementary to observations with neutron monitors monitoring a lower energy range below ∼ 10 GeV and the observations with GMDN have a great advantage particularly in precise measurement of the cosmic ray anisotropy, i.e. the dependence of intensity on incident direction in space, which gives us valuable information of the spatial distribution of the cosmic ray density in three dimensions. The Mt. Norikura muon hodoscope and GMDN have revealed the dynamic variations of the anisotropy which give us important information of the space weather. It has been already confirmed that the GMDN can measure the rapid variation of the anisotropy in the “cosmic ray burst" observed in June 2015 in 10 minute time resolution. The Kuwait muon hodoscope was enlarged three times in March 2016 and one minute data are now available from all of four detectors in the GMDN enabling us to analyze the anisotropy in 1 minute time resolution.

Recently, we also developed the method of the correction of the atmospheric temperature effect on muon count rate by using the GMDN data. This is a significant step, because it makes possible for the first time the analysis of the long-term variation of $\sim$ 50 GeV cosmic ray density (i.e. isotropic intensity) which was possible so far only for cosmic ray below $\sim$ 10 GeV using the neutron monitor data nearly free from the temperature effect. We have already published the long-term variation of the anisotropy observed by Nagoya muon detector.

Solar neutron observation

Observation of solar neutrons in solar cycle 24 has continued at Norikura Observatory of ICRR since fiscal 2007 to understand the acceleration mechanism of high energy ($>$100 MeV) ions associated with solar flares[11]. These neutrons are produced by the interaction between accelerated ions and the solar atmosphere. Neutrons are not reflected by the interplanetary magnetic field, and thought to be more informative than accelerated ions themselves to study the acceleration mechanism at the solar surface. Solar neutron events detected on the ground are rare, and about 10 events were reported before solar cycle 24. The group led by Institute for Space-Earth Environmental Research, Nagoya University has operated a worldwide network of 7 solar neutron telescopes in the world. The solar neutron telescope operated at Norikura Observatory has an area of 64 m^2, which is largest among the 7 stations. The solar neutron telescope at Norikura consists of plastic scintillation detector and proportional counters. The neutron is detected when a recoil proton is produced in the scintillator, and the energy of the recoil proton is measures. Proportional counters are used both to veto charged particles and measure the direction of recoil protons. The telescope is operated by solar power during the winter period when the Norikura observatory is closed.

Solar cycle 24 was its maximum in February 2014 and has decreased its activity since then. We searched for solar neutron signals from the world-wide network of the solar neutron telescopes between January 2010 and December 2014 when the large ($\geq$X1.0 class) solar flare occurred. No solar neutron event was detected by this search. We statistically studied the relation between upper limits of the neutron flux and the energy of soft X-rays during the solar flare. This comparison was also made for the successful detections of solar neutrons before solar cycle 24. The conclusion from this study is that the total energy obtained by neutrons during solar flare does not exceed 0.1 % of the total energy of soft X-rays.

Relativistic electron acceleration in thunderstorm electric field and high-energy atmospheric phenomena at lightning

The Gamma-Ray Observation of Winter THundercloud (GROWTH) collaboration is aiming at revealing high-energy atmospheric phenomena occurring at lightning and in thunderstorms[12],[13],[14],[15],[16]. The project started in 2006 and has detected bremsstrahlung gamma rays from relativistic electrons accelerated by strong electric fields in winter thunderstorms. This gamma-ray radiation events were named "long burst" by our group (as known as gamma-ray glow), which lasts for a minute time-scale corresponding with passage of a thundercloud above our detectors. Winter thunderstorms observed along the Japan sea are ideal targets for our observation campaigns thanks to its low altitude of the cloud base and frequent energetic lightning, while observations of summer thunderclouds at mountain tops are also important to measure the phenomena very close to or even inside thunderstorms. Our collaboration has used the Mount Norikura cosmic ray observatory to study the long bursts, and successfully recorded events.

The GROWTH collaboration newly launched multi-point mapping observation campaigns in 2015. The primary purpose is to study life cycle of the electron acceleration sites in thunderstorms comparing with weather-monitoring data. Another purpose of the project is to reveal mysterious "short burst" events, which have been sometimes detected in our past observations, associated with lightning discharges with its duration shorter than a second. Financially supported by the ICRR joint research programme, academic crowdfunding "academist", and JSPS/MEXT KAKENHI grant, we have developed portable and high-performance radiation detectors. In FY2016 and FY2017, the collaboration deployed radiation detectors at the Mt. Norikura cosmic ray observatory. So far, there is no detection of "long burst" nor "short burst" events from summer thunderclouds during the two years. However, we successfully used these summer campaigns as pilot observations toward the winter campaigns to check our operation and capability of the detectors. The Norikura observations are also educationally important as a training yard for Ph.D students in the team. In 2017 winter, our new mapping system at Kashiwazaki, Niigata, provided us a chance to solve the mystery of the short burst. This phenomena is revealed to be photonuclear reaction triggered by gamma rays from a lightning discharge. This discovery was selected, by the Physics World, as one of the top 10 breakthrough in the physics field in 2017. We are now trying to develop the "high-energy atmospheric physics" of lightning and thunderstorms, a new interdisciplinary field combining the gamma-ray and radio observations.

Study of Secondary Cosmic Rays from Thundercloud at Mt. Norikura

In order to study the relativistic electron acceleration mechanism by thundercloud-derived electric field and the relation between thunder and cosmic-ray air shower, we started an experiment in 2015, mainly using gamma-ray detectors at Norikura Observatory of Institute for Cosnic Ray Research, the University of Tokyo. This experiment consists of gamma-ray detectors, a lightning sensor, an electric field meter, a weather monitor, and an air shower array. Gamma-ray detectors using three crystals, NaI, CsI, and BGO respectively, cover the energy range over 3 orders of magnitude from 70 keV to 120 MeV as a whole.

Observation period: 22 days from August 24 to September 14, 2015

During this time, the thundercloud did not pass, and no gamma-ray burst derived from thundercloud was detected. However, the gamma ray detector was able to observe gamma rays derived from radon of less than 3 MeV as expected during rainfall. Also, gamma ray detectors using CsI and BGO for detecting gamma rays of 3 MeV or more did not observe an increase in gamma rays of 3 MeV or more. This means that gamma rays from radon can be distinguished from contributions from other gamma rays not derived from radon, and it can be expected that these detectors can operate normally even when they are installed at an altitude about 4000 m for a certain future project.

Observation period: 30 days from July 19 to September 16, 2016 (excluding the summer season)

No direct lightning strike event occurred during the observation period, but 6 atmospheric electric field fluctuations exceeding 30 kV/m, which seemed to be an influence of thunder cloud passage, were observed. In one of the events, it seems there was a lightning strike in the vicinity.

Observation period: 41 days from July 31 to September 9, 2017

Unfortunately, during this observation period there was no lightning strike nearby, but it was observed that the thundercloud passed several times. Currently, the data at the time of the thundercloud passing is being analyzed in detail (Fig. 3).

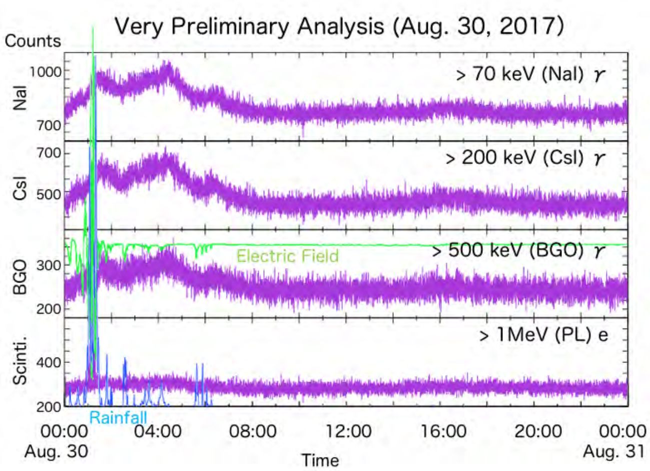

Fig. 3. Electric field (green), rainfall (blue), count value (purple) of each detector at the time of thundercloud passing.

Study of gamma ray bursts from mountain-top thunderclouds

We observed gamma ray bursts that arise in relation to thunderclouds at the Norikura Observatory of ICRR(2,770 m above sea level)[17],[18],[19],[20]. Measurement was carried out by placing PANDA64 detector outdoors of the observatory. The detector is made of 64-module plastic scintillators(total mass about 640 kg) developed for reactor operation monitoring. Our measurement has unprecedented features including high statistics, good energy response, direction sensitivity and neutron identification.

Long-duration persistent bursts were observed 12 times in 54 days from July to September 2014 and their energy spectrum extended up to 25 MeV in the largest burst. The duration of the bursts ranged from a few to ten minutes. Since these bursts were found in the energy range higher than 3 MeV, they were not attributed to the rain fallout of radon and its daughter nuclei.

According to the thundercloud information provided by the Japan Meteorological Agency, the bursts were observed when there was thunder activity near the observatory. The observation is qualitatively in good agreement with thundercloud radiation bursts previously observed in mountain areas or coastal areas of the Sea of Japan.

Monte Carlo simulation showed that the bremsstrahlung γ-rays by source electrons with monochromatic energy of 40–80 MeV falling downwards from altitude of 400–1000 m produced the observed total energy spectra of the bursts well. It is supposed that secondary cosmic ray electrons, which act as seed, were accelerated in electric field of thunderclouds and multiplied by relativistic runaway electron avalanche.

The estimated energy of the source electrons was higher than that of the bursts we previously observed at Ohi Power Station at sea level. Additionally, estimated electron flux at the estimated source height was remarkably lower than that of the Ohi site. These results give new restrictions to the model of electron acceleration and multiplication process in electric field of thunderclouds.

Development of high energy proton irradiation technique for devices used in spaceship

Space exploration is presently interesting in business field. Ion beam irradiation verification for devices to be mounted on spaceships is required to simulate cosmic rays expected in the universe to estimate lifetime of these devices[21],[22],[23],[24].

Flux estimation technique of primary ion beam in wide range from an accelerator is needed In this kind of cosmic ray simulation field. The desired flux of the ion beam for this kind of field is between 10^2 and 10^6 protons$\cdot$cm^{-2} $\cdot$s^{-1} in typical proton cases. Plastic scintillators can be used in lower intense region to count direct primary ions, while ionization chambers can be used in higher intense region to count ionization caused by primary ions. But there have been no definite modalities available to measure throughout this whole intensity region.

One of the candidate techniques is to measure secondary γ-ray intensity emitted through a beam transport, which has nearly a maximum energy of the primary ion beam around 100 MeV for this kind of simulation field. This technique has a feature that detector components do not occupy the beam path and the presence of the detector do not influence the main simulation field at all.

NaI(Tl) scintillator system for high energetic γ-ray measurement which had been used in previous thunder lightning γ-ray measurement was used. This system has a 5-inch NaI(Tl) scintillator with NT100GPS pulse hight analysis system of Laboratory Equipment. Ion beam accelerator experiments using 100 MeV proton beam were carried out at the Wakasa Wan Energy Research Center (WERC). Background measurements were carried out at Norikura Observatory of ICRR in summer, where one can expect high energetic γ-ray, which has the similar energy region compared to the accelerator field of this study. EFM100 atmospheric electric field monitor system of Boltek was added at Norikura to measure accidental high energetic γ-rays caused by thunder lightning.

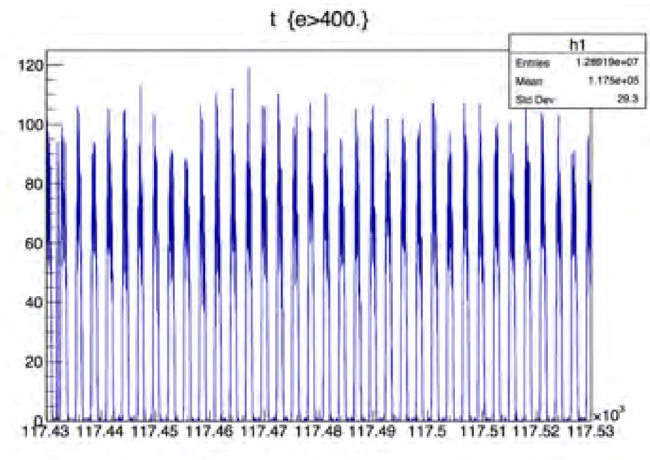

Fig. 4. Time structure of γ-ray above 3 MeV at WERC 100 MeV proton beam delivery. Vertical axis shows γ intensity (events/ms) while horizontal shows time after beginning of the operation (s).

As shown in Fig.4 of a time structure of γ-ray during 100 MeV proton beam delivery duration obtained at WERC, the result clearly shows that this measurement system can distinguish the beam ON/Off, while this system is still in verification for a quantitative discussion. The dead time of the system should be defined.

In the meantime, thunder lightning events were searched using data obtained at Norikura. No events have been distinguished. The whole data at Norikura show a stable condition of the whole system for a couple of months.

With the help of this study, the trial to carry out cosmic ray simulation at the ion beam accelerator facility (WERC) has been successfully carried out. One will keep trying to estimate the quantitative property of the system in ion beam environment.

Development of high energy proton irradiation technique for devices used in spaceship

Aircraft crew are exposed to elevated levels of cosmic rays at aviation since the dose rate of cosmic rays increases with altitude. The occupational doses of aircraft crew have generally been evaluated by model calculation. It is necessary to verify the calculation with measurements to maintain accuracy and credibility of dose assessment. The purposes of this study were to construct a compact and inexpensive cosmic-ray neutron monitoring system which was based on a rem-counter at Norikura Observatory (2770 m above sea level), and to examine the feasibility of it. The monitoring system was installed in the Norikura Observatory in 2014. It consisted of an extended-energy neutron rem counter with wide energy range from 25 meV to 5 GeV, a custom-made data logger connected to LAN, and a battery power unit. The measured data was received in National Institute of Radiological Science in Chiba-city via the ICRR network. This monitoring system succeeded in continuous monitoring more than ten months twice during 2014 to 2016. The averaged counting rate was about 1 count per minute, which was equivalent to neutron ambient dose equivalent rate of about 15 nSv/h by the preliminary evaluation. It is a future problem to reveal the cause of the reduction in counting rate seen over from November to April.

Evaluation of Response to the Gamma-ray of the Emulsion Telescope (2007, 2013)

GRAINE project (Gamma-Ray Astro-Imager with Nuclear Emulsion) has been developing the observation of cosmic γ-ray in the energy range 10 MeV–100 GeV with precise (0.08° at 1–2 GeV), polarization-sensitive, large-aperture-area ($\sim$10 m^2) balloon-borne telescope using nuclear emulsion film[25],[26],[27],[28],[29],[30],[31]. Under the development of the telescope, we performed test observation at Norikura Observatory (2770 m a.s.l.) in 2007 and 2013 using prototype emulsion telescope in order to confirm detection performance using atmospheric γ-ray.

2007 test was the first trial of the detection to the γ-ray spread wide incoming angle. We established configuration of the telescope and its analysis scheme. Based on this experience, we finalized the design of the first balloon-borne emulsion telescope and performed 1st balloon experiment (GRAINE 2011) at the Taiki Aerospace Research Field of JAXA in June 2011.

In 2013 test, we introduced self-produced nuclear emulsion gel film with higher volume occupancy of silver bromide crystals with respect to conventional ordinary gel in order to improve track finding efficiency as well as signal-to-noise ratio. We obtained high ($>$ 97%) track finding efficiency in a single film and confirmed γ-ray detection capability at 100 MeV energy region (Figure 5).
Based on this experience, we performed 2nd balloon experiment (obs/Norikura/GRAINE 2015) in Japan-Australia JAXA collaborative balloon experiment at the Alice Springs balloon-launching station in May 2015.

Environmental Study

Aerosol sampling at Mt. Norikura

Aerosol in the atmosphere has been sampled since 2013 at the Norikura observing site using air-samplers to investigate the production of cosmogenic nuclide ^{7}Be in a free troposphere above 2 km in the altitude. The aerosol size distribution of ^{7}Be was measured for the aerosols sampled by an Andersen sampler enable to separate aerosols to nine classes from 0.43 μm to 11 μm. The 81.7% of ^{7}Be was covered with the aerosol sizes less than 1.1 μm and the ^{7}Be with the aerosol sizes above 1.1 μm decrease with an exponential function. The ^{7}Be concentration at Mt. Norikura was approximately 9.4 times greater than that at the ground level in Yamagata-city (Fig.6.). Its ratio is almost consistent to a simulated ratio 8.8 of ^{7}Be productions due to secondary cosmic rays in the atmosphere by EXPACS. This experimental result is useful for an estimation of altitude distribution of cosmogenic nuclide.

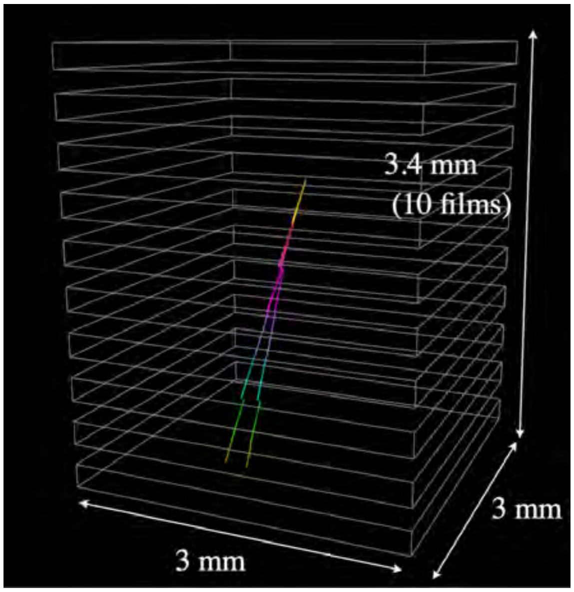

Fig. 5. 3-D view of $\gamma \to e^+ + e^-$ detected in the chamber employed in the observation test at Norikura Observatory. The reconstructed energy of this event was 160 MeV.

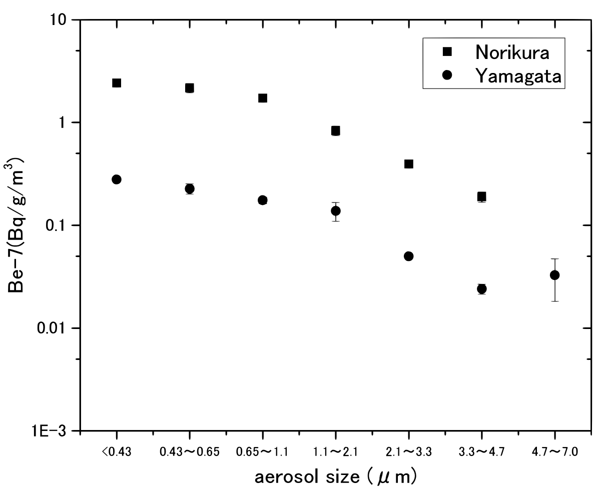

Fig. 6. ^{7}Be concentration as a function of aerosol size

Adaptation of alpine plants to severe environmental conditions

Trees in the alpine regions experience harsh conditions including strong winds, low temperatures, desiccation, and heavy snow. Thus, plants growing in such regions are predicted to have adaptations to these environmental stressors. Through the inter-university research of ICRR, we obtained an opportunity to intensively study plant responses to environmental factors. We identified several characteristics unique to alpine plants, some of which contradict conventional knowledges[32],[33],[34].

1. Adaptation of leaf cuticles in sub-alpine fir (Abies mariessii) at the alpine tree-line

Leaf browning and death are frequently observed in evergreen conifers at the alpine tree-line. These are thought to due to increased transpiration caused by a thinner cuticle and/or mechanical damage to the cuticle by wind-blown snow and ice particles. However, in the sub-alpine fir (Abies mariessii) at Mt. Norikura, mechanical damage was not observed, and the cuticle was rather thick, which may be an adaptation against overwintering at the alpine regions.

2. Embolism of sub-alpine fir (Abies mariessii) at the alpine tree-line

Trees at high altitudes experience severe embolism (loss of xylem conductivity for water) during winters, which is attributed to the entrapment of air in xylem conduits during frost-drought. However, in the sub-alpine fir (Abies mariessii) at Mt. Norikura, air-filled conduits were not observed even in severely-embolized (complete loss of conductivity) shoots. Rather, the pits (valves of partitions inter-conduits) closed before the severe frost-drought in mid-winter, thereby resulting in severe-embolism (complete loss of conductivity). Thus, by pit (valve) cloure, shoots could maintain water in the xylem throughout the winter, which is thought to be an adaptation against lethal filling of air in the conduits during severe frost-drought.

3. Photosynthesis of Haimatsu (Pinus pumila)

At wind-exposed sites on Mt. Norikura, photosynthesis in Haimatsu was suppressed by lower mesophyll CO_2 conductance, and not by stomatal closure.

Investigation of alpine plants on Mt. Norikura

We studied mainly the following three researches on Mt. Norikura after 2012[35],[36],[37],[38],[39],[40],[41],[42],[43],[44],[45],[46],[47],[48],[49].

1) Long-term monitoring and community assembly of alpine plants

We made 40 plots for long-term monitoring of alpine vegetation because climate change possibly affects distributions of alpine plants. We also examined the community assembly process of alpine plants at the 40 plots from the view points of habitat filtering and limiting similarity. Habitat filtering and limiting similarity relate environmental conditions and interspecific competition, respectively. It is suggested that habitat filtering is more important than limiting similarity for the community assembly of alpine plants.

2) Soil respiration rates along an altitudinal gradient

This study investigated seasonal changes of soil respiration rates from forest soil along an altitudinal gradient (1600 m to 2800 m above sea level). The soil respiration rate positively correlated with soil temperatures and forest biomass. It is suggested that forest productivity is an important factor for soil respiration rates.

3) Genetic differentiation of Solidago virgaurea complex

Plant species distributed along wide altitudinal or latitudinal gradients show phenotypic variation due to their heterogeneous habitats. This study investigated whether phenotypic variation in populations of the Solidago virgaurea complex along an altitudinal gradient is caused by genetic differentiation. Population genetic analyses with microsatellite markers were used to infer the genetic structure and levels of gene flow between populations. However, the population genetic analysis suggested an extremely low level of genetic differentiation of neutral genes among the nine populations. This study suggests that genome regions responsible for adaptive traits may differ among the populations despite the existence of gene flow and that phenotypic variation of the S. virgaurea complex along the altitudinal gradient is maintained by strong selection pressure.

Bibliography

[1] " Solar neutron events in association with large solar flares in November 2003", Watanabe, K. *et al.*, Adv. Space Res., **38**, 425–430, 2006.

[2] K. Munakata, M. Kozai, P. Evenson, T. Kuwabara, C. Kato, M. Tokumaru, M. Rockenbach, A. Dal Lago, R. R. S. Mendonca, C. R. Braga, N. J. Schuch, H. K. Al Jassar, M. M. Sharma, M. L. Duldig, J. E. Humble, I. Sabbah, and J. Kota, " Cosmic Ray Short Burst Observed with the Global Muon Detector Network (GMDN) on June 22, 2015 " , Astrophys. J., 862:170 (9pp), 2018 (August 1).

[3] R. R. S. Mendonca, C. R. Braga, E. Echer, A. Dal Lago, M. Rockenbach, N. J. Schuch,, K. Munakata, "Deriving the solar activity cycle modulation on cosmic ray intensity observed by Nagoya muon detector from October 1970 until December 2012 " , Proc. IAU Sympo., 328, 1-4 (IAU-16-IAUS328-0453), 2016 (October 20).

[4] R. R. S. Mendonca, C. R. Braga, E. Echer, A. Dal Lago, K. Munakata, T. Kuwabara, M. Kozai, C. Kato, M. Rockenbach, N. J. Schuch, H. K. Al Jassar, M. M. Sharma, M. Tokumaru, M. L. Duldig, J. E. Humble, P. Evenson, I. Sabbah, " Temperature effect in secondary cosmic rays (muons) observed at ground: analysis of the global muon detector network data " , Astrophys. J., 830:88 (25pp), 2016 (October 20). Cited by 2.

[5] M. Kozai, K. Munakata, C. Kato, T. Kuwabara, M. Rockenbach, A. Dal Lago, N. J. Schuch, C. R. Braga, R. R. S. Mendon, H. K. Al Jassar, M. M. Sharma, M. L. Duldig, J. E. Humble, P. Evenson, I. Sabbah, and M. Tokumaru, " Average spatial distribution of cosmic rays behind the interplanetary shock– Global Muon Detector Network observations " , Astrophys. J., 825:100 (19pp), 2016 (July 10). Cited by 7.

[6] D. Ruffolo1, A. Saiz, P.-S. Mangeard, N. Kamyan, P. Muangha, T. Nutaro, S. Sumran, C. Chaiwattana, N. Gasiprong, C. Channok, C. Wuttiya, M. Rujiwarodom, P. Tooprakai, B. Asavapibhop, J. W. Bieber, J. Clem, P. Evenson, and K. Munakata, "Monitoring short-term cosmic-ray spectral variations using neutron monitor time-delay measurements " , Astrophys. J., 817:38 (12pp), 2016 (January 20). Cited by 8.

[7] M. Kozai, K. Munakata, C. Kato, T. Kuwabara, J. W. Bieber, P. Evenson, M. Rockenbach, A. Dal Lago, N. J. Schuch, M. Tokumaru, M. L. Duldig, J. E. Humble, I. Sabbah, H. K. Al Jassar, M. M. Sharma, J. Kota, " The spatial density gradient of galactic cosmic rays and its solar cycle variation observed with the Global Muon Detector Network " , Earth, Planets and Space, 66, 151-158, 2014 (November 14). Cited by 12.

[8] K. Munakata, M. Kozai, C. Kato, J. Kota, " Long term variation of the solar diurnal anisotropy of galactic cosmic rays observed with the Nagoya multi-directional muon detector " , Astrophys. J., 791:22, 1-16, 2014 (August 10). Cited by 19.

[9] M. Rockenbach, A. Dal Lago, N. J. Schuch, K. Munakata, T. Kuwabara, A. G. Oliveira, E. Echer, C. R. Braga, R. R. S. Mendonca, C. Kato, M. Kozai, M. Tokumaru, J. W. Bieber, P. Evenson, M. L. Duldig, J. E. Humble, H. K. Al Jassar, M. M. Sharma, I. Sabbah, " Global muon detector network use d for space weather applications " , Space Sci. Rev., 182, 1-18, 2014 (May 9). Cited by 18.

[10] K. Munakata, " For space weather applications " , Space Sci. Rev., 182, 1-18, 2014 (May 9).

[11] D. Lopez et al., Estimates of the neutron emission during solar flares in the rising and maximum period of solar cycle 24, Astroparticle Physics, 76 (2016) 19-28.

[12] Enoto, T. and Wada, Y. and Furuta, Y. and Nakazawa, K. and Yuasa, T. and Okuda, K. and Makishima, K. and Sato, M. and Sato, Y. and Nakano, T. and Umemoto, D. and Tsuchiya, H, "Photonuclear reactions triggered by lightning discharge", Nature 551, (2017) 481-484.

[13] Dwyer, J. R. and Smith, D. M. and Cummer, S. A., "High-Energy Atmospheric Physics: Terrestrial Gamma-Ray Flashes and Related Phenomena", 173 (2012) 133-196.

[14] Tsuchiya, H. and Enoto, T. and Torii, T. and Nakazawa, K. and Yuasa, T. and Torii, S. and Fukuyama, T. and Yamaguchi, T. and Kato, H. and Okano, M. and Takita, M. and Makishima, K., "Observation of an Energetic Radiation Burst from Mountain-Top Thunderclouds", Physical Review Letters, 102, (2009) 255003.

[15] Wada, Y. and Bowers, G. S. and Enoto, T. and Kamogawa, M. and Nakamura, Y. and Morimoto, T. and Smith, D. M. and Furuta, Y. and Nakazawa, K. and Yuasa, T. and Matsuki, A. and Kubo, M. and Tamagawa, T. and Makishima, K. and Tsuchiya, H., "Termination of Electron Acceleration in Thundercloud by Intracloud/Intercloud Discharge", Geophysical Research Journal 45, (2018) 5700-5707.

[16] Tsuchiya, H. and Enoto, T. and Yamada, S. and Yuasa, T. and Kawaharada, M. and Kitaguchi, T. and Kokubun, M. and Kato, H. and Okano, M. and Nakamura, S. and Makishima, K., "Detection of High-Energy Gamma Rays from Winter Thunderclouds", Physical Review Letters, 99, (2007) 165002.

[17] Yo Kato, “Observational study of thundercloud radiation bursts using a segmented organic scintillator installed at a mounaintop”, Ph.D. thesis, The University of Tokyo, September, 2015.

[18] Y. Kato, “Thundercloud-related radiation bursts observed at a coastal area and a mountaintop using segmented organic scintillators”, Thunderstorms and Elementary Particle Acceleration (TEPA-2015), 5-9 October 2015, Yerevan, Armenia.

[19] Y. Kato, “Development of Plastic Anti-neutrino Detector Array (PANDA)”, Applied Antineutrino Physics(AAP) 2015, 7-8 December 2015, Virginia Tech Research Center, United States.

[20] Y. Kato “Observation of thundercloud radiation bursts using segmented plastic scintillators”, European Geosciences Union General Assembly (EGU), 8-13 April 2018, Austria Center Vienna, Austria.

[21] T. Torii *et al*., ”Gradual increase of energetic radiation associated with thunderstorm activity at the top of Mt. Fuji”, Geophys. Res. Lett 36(13) , 2009.

[22] T. Kuritai *et al*., ”The Status of the synchrotron of the Wakasa Wan Energy Research Center”, Proc. 12th Annual Meeting of the Particle Accelerator Societ of Japan, 288, 2015.

[23] K. Kume, T. Torii, M. Takita and T. Hasegawa, ”Development of a beam fluence measurement technique at atmosphere”, Igaku Butsuri, Vol.36 Suppl.3 178, 2016 (in Japanese).

[24] K. Kume, T. Hasegawa, S. Hatori, M. Takita and H. Tsuji, ”Space engineering application of therapeutic broad beam for cosmic rai simulation”, Igaku Butsuri, Vol.37 Suppl. 112, 2017 (in Japanese).

[25] Satoru Takahashi,Ph.D Thesis (2011) Nagoya University, http://hdl.handle.net/2237/14900.

[26] Hiroaki Kawahara, Master Thesis (2015), Nagoya University.

[27] “GRAINE project: gamma-ray observation with a balloon-borne emulsion telescope”, Hiroki Rokujo on behalf of GRAINE Collaboration, Proceeding of Science KMI2013 (2014) 042.

[28] “GRAINE project: The first balloon-borne, emulsion gamma-ray telescope experiment”, S. Takahashi, S. Aoki, K. Kamada, S. Mizutani, R. Nakagawa, K. Ozaki and H. Rokujo, PTEP 2015 (2015) no.4, 043H01.

[29] “Gamma-Ray Astro-Imager with Nuclear Emulsion, GRAINE (in Japanese)”, Satoru Takahashi, Shigeki Aoki for GRAINE collaboration, Journal of the SPSTJ, Vol,78(2015) No.4, pp.228-234.

[30] “GRAINE 2015, a balloon-borne emulsion γ-ray telescope experiment in Australia”, Satoru Takahashi et al. (GRAINE collaboration), PTEP 2016 (2016) no.7, 073F01.

[31] “GRAINE project, prospects for scientific balloon-borne experiments”, Satoru Takahashi, Shigeki Aoki for GRAINE collaboration, Advances in Space Research, Articles in press.

[32] Nakamoto A., Ikeda T., Maruta E. (2013) Needle browning and death in the flagged crown of Abies mariesii in the timberline ecotone of the alpine region in central Japan. Trees 27:815-825.

[33] Maruta E., Yazaki K.(submitted) Mechanism of embolism as induced by pit closure during winter in subalpine fir (Abies mariesii)on Mt. Norikura.

[34] Nagano S., Nakano T., Hikosaka K., Maruta E. (2013) Pinus pumila photosynthesis is suppressed by water stress in a wind-exposed mountain site. Arctic, Antarctic, and Alpine Research 45:229-237.

[35] Takahashi, K., Hirosawa, T. and Morishima, R. (2012) How the timberline formed: altitudinal changes in stand structure and dynamics around the timberline in central Japan. Annals of Botany 109: 1165-1174.

[36] Takahashi, K. and Okuhara, I. (2013) Forecasting the effects of global warming on radial growth of subalpine trees at the upper and lower distribution limits 3n central Japan. Climatic Change 117: 278-287.

[37] Takahashi, K. and Obata, Y. (2014) Growth, allometry and shade tolerance of understory saplings of four subalpine conifers in central Japan. Journal of Plant Research127: 329-338.

[38] Takahashi, K. (2014) Effects of wind and thermal conditions on timberline formation in central Japan: a lattice model. Ecological Research 29:121-131.

[39] Takahashi, K. and Koike, S. (2014) Altitudinal differences in bud burst and onset and cessation of cambial activity of four subalpine tree species. Landscape and Ecological Engineering 10:349-354.

[40] Takahashi, K. and Murayama, Y. (2014) Effects of topographic and edaphic conditions on alpine plant species distribution along a slope gradient on Mount Norikura, central Japan. Ecological Research 29: 823-833.

[41] Singh, D., Takahashi, K., Park, J. and Adams, J. M. (2016) Similarities and contrasts in the archaeal community of two Japanese mountains: Mt Norikura compared to Mt Fuji. Microbial Ecology 71: 428-441.

[42] Takahashi, K. and Furuhata, K. (2016) Shoot growth and seasonal changes of non-structural carbohydrate concentrations at the upper and lower distribution limits of three conifers. Landscape and Ecological Engineering 12: 239-245.

[43] Takahashi, K. and Tanaka, S. (2016) Relative importance of habitat filtering and limiting similarity on species assemblages of alpine and subalpine plant communities. Journal of Plant Research 129: 1041-1049.

[44] Takahashi, K. and Matsuki, S. (2017) Morphological variations of the Solidago virgaurea L. complex along an elevational gradient on Mt. Norikura, central Japan. Plant Species Biology 32: 238-246.

[45] Kerfahi, D., Tateno, R., Takahashi, K., Cho, H., Kim, H. and Adams, J. M. (2017) Development of soil bacterial communities on volcanic ash microcosms in a range of climates. Microbial Ecology 73: 775-790.

[46] Sakurai, A. and Takahashi, K. (2017) Flowering phenology and reproduction of the Solidago virgaurea L. complex along an elevational gradient on Mt. Norikura, central Japan. Plant Species Biology 32: 270-278.

[47] Dong, K., Moroenyane, I., Tripathi, B., Kerfahi, D., Takahashi, K., Yamamoto, N., An, C., Cho, H., and Adams, J. (2017) Soil nematodes show a mid-elevation diversity maximum and elevational zonation on Mt. Norikura, Japan. Scientific Reports 7: 3028.

[48] Hirano, M., Sakaguchi, S. and Takahashi, K. (2017) Phenotypic differentiation of the Solidago virgaurea complex along an elevational gradient: Insights from a common garden experiment and population genetics. Ecology and Evolution 7: 6949-6962.

[49] Takahashi, K., Otsubo, S. and Kobayashi, H. (2017) Comparison of photosynthetic traits of codominating subalpine conifers Abies veitchii and A. mariesii in central Japan. Landscape and Ecological Engineering 14: 91-97.

AKENO OBSERVATORY

Introduction

The Akeno Observatory is situated in Akeno of Hokuto-city, 20 km northwest of Kofu and 130 km west of metropolitan Tokyo. The location is at the longitude of 138.5°E and the latitude of 35.8°N. The altitude is ∼900 m above sea level. It was established in 1977 as a research center for air shower studies in the very high energy region, and it has been administered by the ICRR as a facility of joint-university-use.

The 40th anniversary of the Akeno Observatory was held in 2017.

Fig. 2. One of the muon detector housings with concrete shielding.

Akeno Air Shower Experiments

The Akeno Air Shower Experiment started in 1979 with an array covering 1 km^2 area (the 1 km^2 array, see Fig.1). The array was enlarged to 20 km^2 in 1984 and was gradually expanded to the Akeno Giant Air Shower Array (AGASA) of approximately 100 km^2 area by 1990. The AGASA was built to detect Ultra-High Energy Cosmic Rays (UHECRs) in the energy range of 10^{20} eV.

Fig. 1. Aerial View of Akeno Observatory and 1 km^2 Array Area

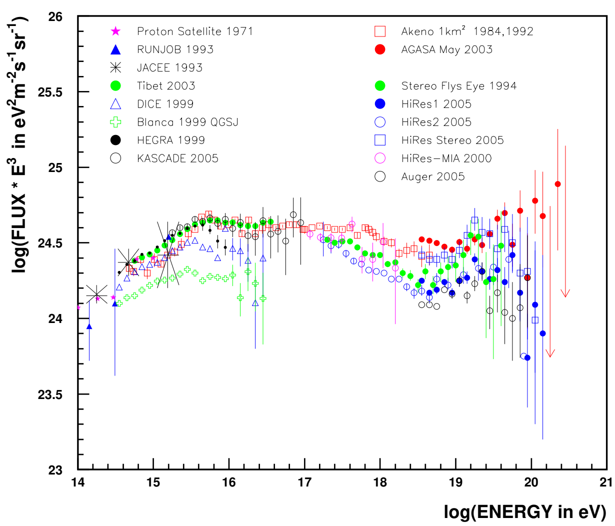

Fig. 3. Akeno energy spectrum measurements for 10^{15} eV - 10^{20} eV.

One of the distinctive features of Akeno experiments is that the measurements were made over five decades of energies well covering 10^{15} eV - 10^{20} eV by using both the surface detector for electromagnetic component, and the shielded detector for muon component (Fig.2). The wide energy coverage was accomplished by the arrays of scintillation detectors of various inter-detector spacings from 3 m to 1 km and with different triggering conditions. This feature of Akeno air shower measurement is well demonstrated in Fig.3, in which the spectra from Akeno 1 km^2 array for $10^{14.5}$ eV - $10^{18.8}$ eV [2] and AGASA for $10^{18.5}$ eV - $10^{20.3}$ eV [3] are plotted.

*[2] M. Nagano et al., J. Phys. **G10**, 1295 (1984); M. Nagano et al., J. Phys. **G18**, 423 (1992).

*[3] M. Takeda et al., Astropart. Phys. **19**, 447 (2003).

AGASA

The AGASA was composed of 111 surface detectors, each with plastic scintillator of 2.2 m^2 area and 5 cm thickness. The counters were deployed with ∼1 km spacing covering the ground area of approximately 100 km^2 in the suburban area of Akeno, outside of the observatory campus. The AGASA served as the largest air shower array in the world since its commissioning in 1990 until it stopped data taking in January 2004, when the construction of the succeeding experiment, Telescope Array (TA), started in Utah. The AGASA was dismantled in 2007 together with other Akeno air shower arrays.

An exposure of 5.8 × 10^{16} m^2 s sr above 10^{19} eV was accumulated by AGASA in 13 years of operation. Extensive air showers with zenith angles smaller than 45° and with core locations inside the array area were used for the analysis. The AGASA reported an extension of the energy spectrum beyond the predicted Greisen-Zatsepin-Kuzmin (GZK) cutoff in 1998 [4] and a total of eleven UHECR events were observed above 10^{20} eV by 2003.

Measurement of UHECRs

Since the AGASA measurement in 1998, the High Resolution Fly's Eye (HiRes) [5], the Pierre Auger Observatory (PAO) [6], and the Telescope Array (TA) [7] measured the energy spectra of UHECRs with higher statistics.

The HiRes observed the UHECR using the fluorescence telescope. The PAO and the TA measure the energy spectra using the surface array consisting of either water tanks (PAO) or plastic scintillators (TA), but the energy scale of the array is determined by the fluorescence telescope using a subset of events observed by the fluorescence telescope and surface array at the same time. The adoption of the energy scale by the fluorescence telescopes is based on its small dependence on the air shower simulation.

The energy spectra above 10^{18} eV by AGASA and other experiments are compiled and compared by the working group represented by UHECR experiments in the UHECR2012 symposium held in 2012 [8]. The result is plotted in Fig.4 with the energy scale of each experiment adjusted to a reference energy, which is set halfway between PAO and TA/HiRes.

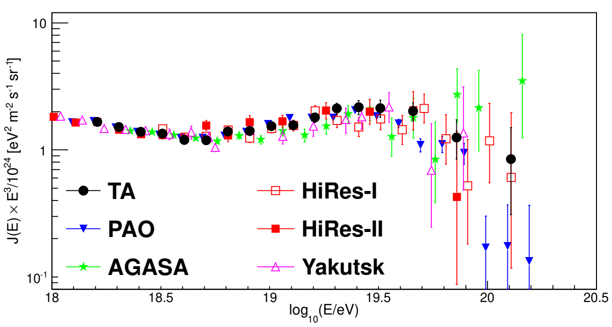

Fig. 4. Compilation of UHECR energy spectra (UHECR2012). The energy scales were adjusted as ×1.10 for PAO, ×0.91 for TA and HiRes, ×0.65 for AGASA and ×0.56 for Yakutsk.

The HiRes, PAO and TA confirmed a flux suppression above approximately $10^{19.7}$ eV. Although the AGASA spectrum does not demonstrate the cutoff structure, the number of events above 10^{20} eV became only two after the energy rescaling, making the claim of the extended spectrum statistically insignificant. The estimate of systematic uncertainty of the energy measurement is approximately 20% for all the experiments, and rescalings for the TA/HiRes and PAO are within this limit. Rescaling of the surface array energy for AGASA and Yaktsuk indicates that there exist larger systematic uncertainties than originally estimated by running the air shower simulation. This difference of energy scale obtained by the surface array and by the fluorescence telescope remains as a basic question in the understanding of the air shower phenomena.

*4 M. Takeda et al., Phys. Rev. Lett. **81**, 1163 (1998).
*5 R.U. Abbasi et al., Phys. Rev. Lett. **100**, 101101 (2008).
*6 J. Abraham et al., Phys. Lett. **B685**, 239 (2010).
*7 T. Abu-Zayyad et al., Astrophys. J. **768**, L1 (2013).
*8 http://indico.cern.ch/conferenceDisplay.py?confId=152124

Recent Research Activities

The study of UHECRs by AGASA in Akeno was succeeded by the TA experiment in Utah, USA since 2008. After the cessation of AGASA, the Akeno Observatory has been used for small scale cosmic ray experiments, astrophysical observations and as a test and maintenance facility by the ICRR and university researchers. Fig.5 shows a recent photograph of the main site of the Akeno Observatory.

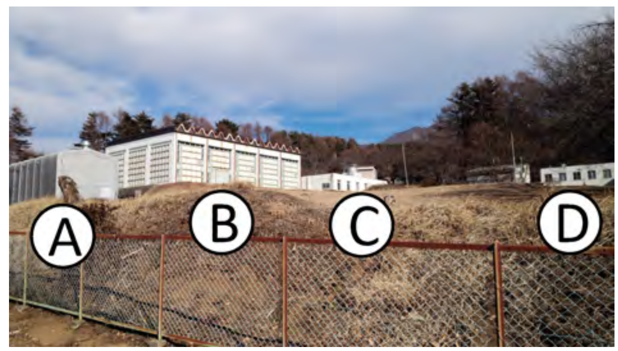

Fig. 5. The main site of the Akeno Observatory. There are the movable tent for a small atmospheric Cherenkov telescope (A), the large experimental hall (B), the research building (C) and the lodging facility (D) from the left.

In 2020, as countermeasures against COVID-19 infection, an air conditioner and a heat-exchange ventilator were installed in the large room of the research building, and a heat-exchange ventilator was installed in the dining room of the lodging facility along with some other measures.

Observation by the multi-color imager for transients, survey and monstrous explosions (MITSuME) by N. Kawai (Tokyo Institute of Technology) et al.

One of the three MITSuME robotic telescopes was installed in the Akeno Observatory in 2003 (Fig. 6). The telescope has an aperture of 50 cm, an FOV of 28' × 28' and is equipped with a tricolor CCD camera capable of $g'R_CI_C$-bands photometry (g':400∼550 nm, Rc:570∼730 nm, Ic:730∼ 850 nm). It is operated remotely from the Tokyo Tech at the Ookayama Campus. Upon receiving a GRB alert, it directs the telescope toward the GRB direction within two minutes, and makes a prompt observation of the GRB and its afterglow. The follow-up observation of GRBs was continued by the MITSuME telescope. Nine events were reported to Gamma-Ray Burst (GRB) Coordinates Network Circular (GCNC).

In order to perform follow-up visible-light observations of gravitational wave objects, the MITSuME participated in J-GEM (Japanese collaboration for Gravitational-wave ElectroMagnetic follow-up) and GROWTH(Global Relay of Observatories Watching Transients Happen) to establish worldwide observation network focusing on the electromagnetic identification of gravitational wave sources as one of scientific themes. The team participated in the follow-up observations of LIGO/Virgo O3 that started in April 2019.

Fig. 6. The dome in which the MITSuME telescope was installed in Akeno.

Fig. 7. The Cherenkov telescope at the tour of the 40th anniversary of the Akeno Observatory in 2017.

Observation of galactic cosmic rays by large area muon telescope by A. Oshima (Chubu University) et al.

Four layers of proportional counter telescopes, each with 25 m^2 area, were installed in three muon houses in Akeno and have been continuously measuring the cosmic ray muons since 2003. Fig. 2 shows one of the three muon houses (M1, M5, M8). The mode energy of the primary cosmic rays is approximately 2.5 GeV corresponding to 2m thick concrete ceiling of the muon house at the latitude of the Akeno Observatory. The measurement in Akeno is combined with a simultaneous measurement by the GRAPES-3 experiment at Ooty in India, and this telescope aims at measuring the modulation effects and anisotropy of galactic cosmic rays in the region of about 100 GeV and detecting trasient phenomena of cosmic rays. It is expected to understand cosmic-ray flow in the universe magnetic field and to obtain a clue to the solution of cosmic-ray propagation. And it is challenging to establish the method of a new space weather observation by simultaneous multi-directional observations with high statistical precision.

In JFY2020, the observations at M5 were stable, except in September and October. The detectors at M1 and M8 needed to be adjusted, but due to the activity restriction caused by the COVID-19 epidemic, the adjustments could not be performed.

Research and development for a small atmospheric Cherenkov telescope at the Akeno Observatory by T. Yoshikoshi (ICRR) et al.

An alt-azimuth telescope with an aperture of three meters (Fig. 7) was setup in the Akeno Observatory for various prototype tests with atmospheric Cherenkov observations of gamma rays on the ground [9]. This telescope is the only telescope to observe atmospherice Cherenkov light emitted from air showers induced by TeV gamma rays in Japan.

In January, 2021, the telescope was used to observe the Crab Pulsar in the visible light region for about ten hours.

Research and development for the Telescope Array observation in Utah by the TA collaboration and others

All the TA fluorescence imaging cameras and a part of the TA surface detectors were assembled in the Akeno Observatory by the TA collaboration team. All the unit mirrors of the TA fluorescence telescope were tested and the atmospheric monitoring lidar of TA using YAG laser was developed. In JFY 2015, the R&D of the surface detectors were performed for the TAx4 project that aims at quadrupling the TA surface detector array in Utah. In August in 2016, 2017 and 2018 the TAx4 and TALE (TA Low Energy extension) scintillator counters were assembled. The assembly of the surface detectors for the TALE-infill array that is described in the TA section was scheduled at the Akeno Observatory in 2020, but due to the COVID-19 epidemic, the assembly had to be postponed.

The tests using facilities in the Akeno Observatory by other subjects were also performed.

*[9] M. Ohishi et al., 33rd ICRC, (Rio deJaneiro), 587 (2013).

KAMIOKA OBSERVATORY

Kamioka observatory is located at 1000 m underground (2700 m water equivalent) in the Kamioka Mine, Gifu prefecture, about 200 km west of Tokyo. The observatory was established in 1995 in order to operate Super-Kamiokande experiment (SK). The underground laboratories are located under Mt.Ikeno-yama and accessible to the experimental site through a 1.7 km horizontal tunnel. The observatory also has surface research buildings and a dormitory located at the distance of 15 minutes drive from the entrance of the underground laboratories.

The Super-Kamiokande experiment had discovered neutrino oscillations through the observations of atmospheric and solar neutrinos (see the section for Neutrino and Astroparticle Division). The atmospheric neutrino oscillation was confirmed by the long baseline neutrino oscillation experiment, K2K, using accelerator neutrino beam, which was conducted between 1999 and 2004. A new long baseline neutrino oscillation experiment (the T2K experiment) using a high intensity beam, 50 times of the K2K neutrino beam, by the J-PARC proton accelerator has started in 2009. In 2011, the experiment has observed 6 ν_e appearance events indicating non-zero θ_{13} which was as yet determined the last neutrino oscillation parameter. From 2014, T2K started taking data using an anti- neutrino beam, and confirmed the disappearance of muon antineutrinos through oscillations. Candidate events for the appearance of electron anti-neutrinos were also found. Additionally, T2K published in 2020 an indication that CP symmetry is not conserved in neutrino oscillations, with the probability of the observations being the results of a random fluctuation if CP symmetry was conserved being less than 5%.

The low cosmic ray flux and low seismic noise environment in the underground site enables us to conduct various researches. There is a 100 m long laser interferometer, which is a prototype of the 3 km gravitational wave antenna (KAGRA). Using the low radioactive background environment in the Kamioka Mine, a dark matter experiment, called XMASS was conducted in Lab-C. The XMASS group constructed a 800kg liquid xenon detector and data were taken from 2010 to 2019. Searches for dark matter interactions and rare phenomena in liquid xenon have been conducted using the obtained data. The R&D study of a tracking type detector for dark matter detection led by the Kobe University group (the NEWAGE experiment) has also been performed in Lab-B. A double beta decay experiment using ^{48}Ca (the CANDLES experiment) led by the Osaka University group has been running in Lab-D. The study to improve the neutrino detection sensitivity by adding gadolinium to Super-Kamiokande (called SK-Gd project) has been performed at Lab-E. A Low background Germanium detector and ICP-MS system are equipped in Lab-1 and Lab-A to measure extremely low radioactive backgrounds. Lab-G area was excavated in 2015 and the SK-Gd equipments which include a Gd dissolving system, a pretreatment system and a Gd-water circulation system were installed in 2016. Other preparations for Gd-loading have been performed including a tank open work to repair the water leak from the SK tank in 2018 and the test of the SK-Gd equipments in 2019. In 2020, SK added soluble Gd salt into the water.

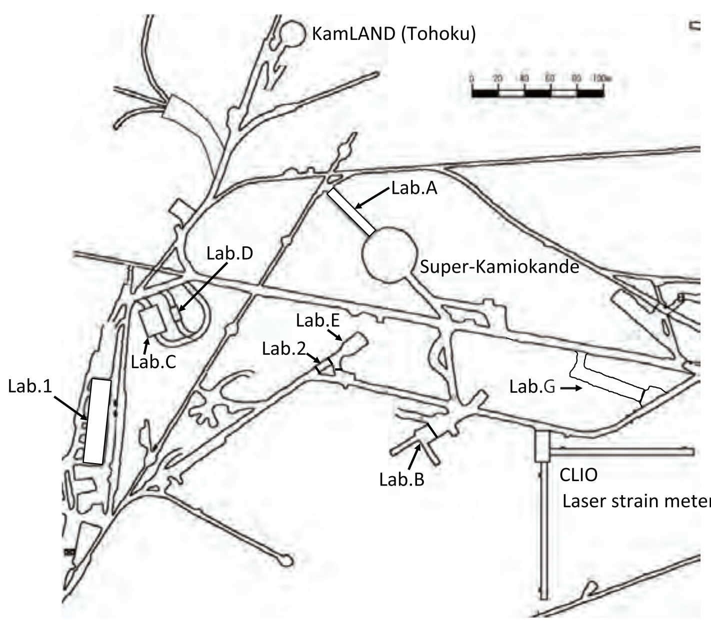

Fig. 1. Kamioka Underground Observatory.

KAGRA OBSERVATORY

KAGRA observatory is located in the Ikenoyama-mountain on the border between Gifu and Toyama prefecture, about 35 km south of Toyama city in Japan. The observatory was established in 2016 in order to operate Large-scale Cryogenic Gravitational Wave Telescope ”KAGRA”. KAGRA itself has a L-shape tunnel facility, and it is located more than 200m under Mt.Ikeno-yama. The corner station of the L-shape tunnel is accessible through a 500-m horizontal access tunnel from Atotsu area. The observatory has its own surface research buildings and rental space in the community center of Hida city located about 5km away from the Atotsu entrance of KAGRA.

KAGRA aims to observe gravitational waves (GWs) as one of observatories of the world GW detection network including Advanced-LIGO, Advanced-Virgo and planned LIGO-India. KAGRA project (formerly named LCGT) was partially approved in 2010 as one of Leading-edge Research Infrastructure Program, and also supported by Program for Promoting Large-scale Science Projects, Subsidy for Facilities Expense and Grants-in-Aid for Scientific Research from Ministry of Education, Culture, Sports, Science and Technology (MEXT).

In the KAGRA project, Institute for Cosmic Ray Research plays a role of a host promoting institute, and National Astronomical Observatory of Japan (NAOJ) and High Energy Accelerator Research Organization (KEK) are the co-host institutions, then more than 417 researchers in 85 institutes and universities in the world are collaborating for construction and data analysis of KAGRA.

The tunnel excavation started in May 2012, and finished in March 2014. After that, the basic laboratory environment was prepared until September 2015. A Michelson interferometer with 3km arm (iKAGRA) was demonstrated in March 2016, and the first engineering run was performed until May 2016. In 2019, all the interferometer components had been installed to complete the KAGRA Observatory that adopts a power recycled Fabry-Perot Michelson type interferometer with the resonant sideband extraction. On February 25th, 2020, KAGRA started its first observation run. After performing the two week observation run ”O3GK” with GEO600 on April 2020, KAGRA will be upgraded and prepared for the joint observation with LIGO and Virgo ”O4” which is expected to start on June 2022.

Fig. 1. Surface Research Building.

Fig. 2. Atotsu Entrance of KAGRA.

RESEARCH CENTER FOR COSMIC NEUTRINOS

The Research Center for Cosmic Neutrinos (RCCN) was established in April 1999. The main mission of this center is to promote researches related to neutrinos based on data from various observations and experiments, and we have provided the occasion to discuss theoretical ideas and experimental results on neutrino physics. Members of this center have been involved in the Super-Kamiokande and T2K experiments, and contributing precise measurements of neutrino oscillations. Also, we have been involved in Hyper-Kamiokande project, and worked on the calculation of the atmospheric neutrino flux to have better predictions of the neutrino flux.

RCCN, together with the computer committee, oversees the operation of the central computer system in ICRR (Fig 1). The computer facility has high performance to analyze huge amount of data, and has been operated without any serious trouble since it was upgraded in 2020. Since 2004, RCCN has been accepted inter-university programs related to activities in the low-background underground facility also (Fig 2). In FY2020, we accepted 8 programs related to these facilities.

We have also contributed holding public lectures. Since JFY2009, ICRR and the Kavli Institute for the Physics and Mathematics of the Universe (Kavli-IPMU) have co-sponsored two public lectures each year. The public lecture held in Spring is co-organized by RCCN and the Public Relation Office of ICRR. In 2020, the lecture scheduled for April was postponed due to the spread of coronavirus infection, but it was held on August 8th due to the change to online. Many audiences listened to the talks given by two scientists entitled as ”Gamma-ray bursts finally seen from the ground with gamma rays” and ”Belle II Experiment-Electron-Positron Accelerator teaches a new world of elementary particles”.

Fig. 1. Photo of the central computer facility in ICRR upgraded in 2014.

Fig. 2. Photo of the low-background underground facility in ICRR.

HIGH ENERGY ASTROPHYSICS FACILITY IN CANARIAS

High Energy Astrophysics Facility in Canarias, established on April 1, 2019 in La Palma, Canary Islands, Spain is the actual base of international collaborations on CTA (Cherenkov Telescope Array) project co-hosted by CTA group of ICRR.

The Cherenkov Telescope Array (CTA) is the next generation ground-based observatory for gamma-ray astronomy at very-high energies, participated by more than 1400 researchers from 31 countries. With more than 100 telescopes located in the northern and southern hemispheres, CTA will be the world ' s largest and most sensitive high-energy gamma-ray observatory. The CTA-Japan consortium is making a significant contribution to the construction of Large-sized Telescopes (LSTs), four proto types of which are planned to construct at northern hemisphere site in La Palma. The first LST was completed and made the first light at the end of December of 2018.

Establishment of the local corporation assets were needed for daily activities such as local procurement and employment to manage and operate the site. High Energy Astrophysics Facility in Canarias was established as a room inside the building of CALP (The Centro de Astrofísica en La Palma), a branch of IAC (Instituto de Astrofisca de Canarias).

Fig. 1. High Energy Astrophysics Facility in Canarias.

APPENDICES

A. ICRR Workshops and Ceremonies

B. ICRR Seminars

C. List of Publications

(a) Papers Published in Journals

(b) Conference Papers (Proceedings)

D. Doctoral Theses

E. Public Relations

(a) ICRR News

(b) Public Lectures

(c) Visitors

F. Inter-University Research Activities

G. List of Committee Members

(a) Board of Councillors

(b) Advisory Committee

(c) Inter-University Research Advisory Committee

H. List of Personnel

A. ICRR Workshops and Ceremonies

Kashiwa Dark Matter Symposium 2020

Date: September 16-19, 2020
Place: Online

Outline: The Kashiwa Dark Matter Symposium 2020 was the second symposium of the series established in 2019. This symposium covered recent processes in searches for Dark Matter (DM) in collider, direct, indirect, and astrophysics studies as well as DM theory. Its goal was to foster collaborations and to explore the complementarity of the different strategies to search for DM.

Due to the COVID-19 pandemic, the symposium was shifted to a virtual format. The talks were held on Zoom and were additionally publicly live streamed on YouTube. To stimulate the discussions, the online tools SpatialChat and Slack were used.

In the collider session, the comprehensive results from the LHC and other experiments and their prospects were reviewed. In the following session of astrophysical constrains on DM, the latest constraints on dark matter distributions in the Milky Way and its satellites as basis for direct and indirect DM searches were presented. As one of the highlight results from 2020, special attention was given to the excess signal claimed by the Xenon 1T project, which was covered by several talks in the direct detection session. In the session of indirect DM searches, the presenters introduced current and future searches in a wide range of electromagnetic wavelengths from X-rays to TeV gamma rays. In a focused session, Axion and Axion-like DM candidates were discussed from theoretical and experimental aspects.

Participants: 290 participants from 33 countries worldwide.

Fig. 1. Kashiwa Dark Matter Symposium 2020

The 7th KAGRA International Workshop (KIW7)

Date: Dec. 18-20, 2020
Place: National Central University, Taiwan and Online

Outline: The 7th KAGRA international workshop (KIW) was held on 18-20 December 2020 in National Central University, Taoyuan City, Taiwan. This workshop is one of the important conferences to discuss the science of KAGRA gravitational wave experiment. However, KIW focuses not only on the KAGRA experiment, but also encompasses other gravitational wave experiments, gravitational wave sciences, and multi-messenger astronomy.

In this workshop, we employed the hybrid style meeting. Local Taiwan people attended National Central University and overseas people joined the online conference system. The unique point of this workshop is parallel sessions. We separated the sessions to experiment, analysis and theory.

We encouraged researchers of both experiment and theory, especially of young generations, to make contributions and exchange the ideas at this conference.

This workshop covered various topics related to gravitational observation; development and characterization of the current and future detector, data analysis, and recent observational results (the results of O3a, from April 2019 to September 2019 by LIGO and Virgo). Finally, the total number of participants of this meeting was 242 from 20 regions. This number is the largest in the previous workshop and three times larger.

*Originally published on KAGRA Scientific Congress Newsletter Issue8 on May 1, 2021.
(https://gwdoc.icrr.u-tokyo.ac.jp/DocDB/0128/L2112871/002/KSCnewsletter8_202105.pdf)

Participants: 242 participants.

Fig. 2. The workshop employs the hybrid style.

Fig. 3. KIW7 group photo

Black Hole Astrophysics with VLBI: Multi-Wavelength and Multi-Messenger Era

Date: Jan. 18-20, 2021
Place: ICRR, The University of Tokyo and Online

Participants: 80 participants.

B. ICRR Seminars

1. September, 11, 2020: Dr. Tomohisa Kawashima (ICRR), ”Probing black hole spacetime and dynamics of accretion flow with relativistic jet via general relativistic multi-wavelength radiative transfer”
2. October, 1, 2020: Dr. Yuichi Harikane (ICRR), ”Subaru/Hyper Suprime-Cam Survey: Statistical Properties of Luminous Galaxies in the Early Universe”
3. October, 9, 2020: Dr. Tomoya Kinugawa (ICRR), ”Remnants of first stars for gravitational wave sources”
4. October, 23, 2020: Dr. Hiroki Yoneda (RIKEN), ”The mystery of the MeV gamma-ray emission from gamma-ray binary systems”
5. November, 27, 2020: Dr. Kenta Hotokezaka (RESCEU), ”Multi-messenger Astrophysics of compact binary and core collapse”
6. December, 18, 2020: Dr. Yoshiyuki Inoue (Osaka University), ”Coronal Magnetic Activity in nearby Active Supermassive Black Holes”
7. December, 21, 2020: Dr. Hiroaki Yamamoto (Caltech), “ LIGO : Past, Present and Future ”
8. January, 22, 2021: Dr. Arun Babu (Universidad Nacional Autonoma de Mexico), ”Cosmic rays: a proxy to study solar transient events”
9. February, 5, 2021: Dr. Marco Casolino (RIKEN), ”The Mini-EUSO experiment on board the International Space Station: first results and perspectives”
10. February, 16, 2021: Dr. Bernard V. Jackson (UC San Diego), ”Heliospheric Remote Sensing Using IPS and Spacecraft Imagery ”

C. List of Publications

(a) Papers Published in Journals

1. ”Measurement of the radon concentration in purified water in the Super-Kamiokande IV detector”, Y. Nakano, T. Hokama. M. Matsubara, M. Miwa, M. Nakahata, T.Nakamura, H. Sekiya, Y.Takeuchi, S.Tasaka, R.A.Wendell, Nucl. Inst. Meth. A, **977** (2020) 164297, Oct. 2020.

2. ”Search for exotic neutrino-electron interactions using solar neutrinos in XMASS-I”, XMASS Collaboration, Physics Letters B **809** (2020) 135741, Aug. 2020.

3. ”Indirect search for dark matter from the Galactic Center and halo with the Super-Kamiokande detector”, The Super-Kamiokande Collaboration, Physical Review D **102**, 072002 (2020), Oct. 2020.

4. ”Search for proton decay via p$\rightarrow e^+\pi^0$ and p$\rightarrow\mu^+\pi^0$ with an enlarged fiducial volume in Super-Kamiokande I-IV”, A. Takenaka et al. (The Super-Kamiokande Collaboration), Phys. Rev. D **102**, 112011 (2020), Dec. 2020.

5. ”Measurement of the anisotropic response of the $ZnWO_4$ crystal for developing the direction sensitive dark matter detector”, K. Ichimura, H. Sekiya et.al, IEEE Transactions on Nuclear Science, Apr. 2020.

6. ”Development of low-background photomultiplier tubes for liquid xenon detectors”, XMASS Collaboration, 2020 JINST **15** P09027, Sep. 2020.

7. ”Measurement of the charged-current electron (anti-)neutrino inclusive cross-sections at the T2K off-axis near detector ND280”, T2K collaboration, J. High Energ. Phys. 2020, 114 (2020), Oct. **2020**.

8. ”First measurement of the charged current$\overline{\nu}_\mu$double differential cross section on a water target without pions in the final state”, T2K collaboration, Phys. Rev. D**102**, 012007(2020), Jul. 2020.

9. ”Simultaneous measurement of the muon neutrino charged-current cross section on oxygen and carbon without pions in the final state at T2K”, T2K collaboration, Phys. Rev. D**101**, 112004(2020), Jun. 2020.

10. ”First combined measurement of the muon neutrino and antineutrino charged-current cross section without pions in the final state at T2K”, T2K collaboration, Phys. Rev. D**101**, 112001(2020), Jun. 2020.

11. ”Search for Electron Antineutrino Appearance in a Long-Baseline Muon Antineutrino Beam”, T2K collaboration, Phys. Rev. Lett.**124**, 161802(2020), Apr. 2020.

12. ”Constraint on the matterantimatter symmetry-violating phase in neutrino oscillations”, T2K collaboration, Nature, 2020,**580**(7803), pp. 339344, Apr. 2020.

13. ”Detection capability of Migdal effect for argon and xenon nuclei with position sensitive gaseous detectors”, Kiseki D Nakamura, Kentaro Miuchi, Shingo Kazama, Yutaro Shoji, Masahiro Ibe, Wakutaka Nakano, Progress of Theoretical and Experimental Physics, ptaa162, Nov. 2020.

14. ”Development of a dual-phase xenon TPC with a quartz chamber for direct dark matter searches ”, Kazufumi Sato, Masaki Yamashita, Koichi Ichimura, Yoshitaka Itow, Shingo Kazama, Shigetaka Moriyama, Kosuke Ozaki, Takumi Suzuki, and Rina Yamazaki, Prog. Theor. Exp. Phys. **2020**, 113H02 , Nov. 2020.

15. ”Energy resolution and linearity of XENON1T in the MeV energy range”, XENON collaboration, Eur. Phys. J. C **80**, 785 (2020), Aug. 2020.

16. ”E. Aprile et al., Observation of Excess Electonic Events in XENON1T”, XENON collaboration, Phys. Rev. D.**102**, 072004 (2020), Oct. 2020.

17. ”Projected WIMP Sensitivity of theXENONnTDark Matter Experiment”, XENON collaboration, JCAP11(**2020**)031, Nov. 2020.

18. ”Improved method for measuring low-concentration radium and its application to the Super-Kamiokande Gadolinium project”, S Ito, K Ichimura, Y Takaku, K Abe, M Harada, M Ikeda, H Ito, Y Kishimoto, Y Nakajima, T Okada, H Sekiya, Progress of Theoretical and Experimental Physics, Volume **2020**, Issue 9, September 2020, 093H02, 44075.

19. ”Evaluation of radon adsorption efficiency values in xenon with activated carbon fibers ”, Y Nakano, K Ichimura, H Ito, T Okada, H Sekiya, Y Takeuchi, S Tasaka, M Yamashita, Progress of Theoretical and Experimental Physics, Volume **2020**, Issue 11, November 2020, 113H01, Nov. 2020.

20. ”Evaluation of gadolinium ’ s action on water Cherenkov detector systems with EGADS”, ll.Marti et al., Nuclear Instruments and Methods in Physics Research Section A, Apr. 2020.

21. ”Neutron-antineutron oscillation search using a 0.37 megaton-years exposure of Super-Kamiokande”, The Super-Kamiokande Collaboration, PHYSICAL REVIEW D **103**, 012008 (2021), Jan. 2021.

22. ”T2K measurements of muon neutrino and antineutrino disappearance using 3.13×10^{21} protons on target”, T2K collaboration, Phys. Rev. D **103**, L011101 (2021), Jan. 2021.

23. ”Development of a Method for Determining the Search Window for Solar Flare Neutrinos”, K. Okamoto et al., Sol. Phys. **295**, 133 (2020), oct. 2020.

24. ”An intermittent extreme BL Lac: MWL study of 1ES 2344+514 in an enhanced state”, MAGIC Collaboration, Mon.Not.Roy.Astron.Soc. , Jun. 2020

25. ”Testing two-component models on very-high-energy gamma-ray emitting BL Lac objects”, MAGIC Collaboration, Astron. Astrophys. **640**, A132, (2020), Jun. 2020

26. ”MAGIC observations of the diffuse γ-ray emission in the vicinity of the Galactic center”, MAGIC Collaboration, Astron. Astrophys. **642** (2020) A190, Jun. 2020

27. ”A search for dark matter in Triangulum II with the MAGIC telescopes”, MAGIC Collaboration, Phys.Dark Univ. **28** (2020) 100529, May. 2020

28. ”The Great Markarian 421 Flare of February 2010: Multiwavelength variability and correlation studies”, Veritas and MAGIC collaboration, Astrophys. J. **890** (2020) 97, Feb. 2020

29. ”Broadband characterisation of the very intense TeV flares of the blazar 1ES 1959+650 in 2016”, MAGIC and Fermi LAT Collaboration, Astron.Astrophys. **638** (2020) A14, Jun. 2020

30. ”MAGIC very large zenith angle observations of the Crab Nebula up to 100 TeV”, MAGIC Collaboration, Astron.Astrophys. **635** (2020) A158, Mar. 2020

31. ”Bounds on Lorentz invariance violation from MAGIC observation of GRB 190114C”, MAGIC Collaboration, Phys.Rev.Lett. **125** (2020) 2, 021301, Jul. 2020

32. ”Unraveling the Complex Behavior of Mrk 421 with Simultaneous X-Ray and VHE Observations during an Extreme Flaring Activity in 2013 April”, MAGIC Collaboration, Astrophys.J.Suppl. **248** (2020) 2, 29, Jun. 2020

33. ”Study of the variable broadband emission of Markarian 501 during the most extreme SwiftSwiftSwift X-ray activity”, MAGIC Collaboration, Astron.Astrophys. **637** (2020) A86, May. 2020

34. ”MAGIC Observations of the Nearby Short Gamma-Ray Burst GRB 160821B”, Acciari et al. (MAGIC Collaboration), Astrophysical Journal, **908**, 90, Feb. 2021

35. ”VHE gamma-ray detection of FSRQ QSO B1420+326 and modeling of its enhanced broadband state in 2020”, MAGIC Collaboration, Astron.Astrophys. **647** (2021) A163, Dec. 2020

36. ”H.E.S.S. and MAGIC observations of a sudden cessation of a very-high-energy γ-ray flare in PKS 1510-089 in May 2016”, HESS, MAGIC collaboration, Astron.Astrophys. **648** (2021) A23, Dec. 2020

37. ”Studying the Nature of the Unidentified Gamma-Ray Source HESS J1841055 with the MAGIC Telescopes”, MAGIC Collaboration, MNRAS, **497**, 3734-3745, Sep. 2020

38. ”Detection of the Geminga Pulsar with MAGIC Hints at a Power-Law Tail Emission beyond 15 GeV”, MAGIC Collaboration, A&A, **643**, L14(6pp), Nov. 2020

39. ”Multiwavelength Variability and Correlation Studies of Mrk 421 during Historically Low X-Ray and γ-Ray Activity in 2015-2016”, MAGIC Collaboration, MNRAS, staa3727, Dec. 2020

40. ”Sensitivity of the Cherenkov Telescope Array to a Dark Matter Signal from the Galactic Centre”, A. Acharyya, et al., JCAP, 01, 057(62pp), Jan. 2021

41. ”Sensitivity of the Cherenkov Telescope Array for Probing Cosmology and Fundamental Physics with Gamma-Ray Propagation”, H. Abdalla, et al., JCAP, 02, 048(63pp), Feb. 2021

42. ”VHE Gamma-Ray Detection of FSRQ QSO B1420+326 and Modeling of its Enhanced Broadband State in 2020”, V. A. Acciari, S. Ansoldi, L. A. Antonelli, A. Arbet Engels, M. Artero, K. Asano, et al., A&A, **647**, A163(19pp), Mar. 2021
43. ”Transverse Single-Spin Asymmetry for Very Forward Neutral Pion Production in Polarized p+p Collisions at $\sqrt{s}$ = 510GeV”, (RHICf Collaboration), Phys. Rev. Lett. **124**, 252501, Jun. 2020
44. ”Measurement of energy flow, cross section and average inelasticity of forward neutrons produced in $\sqrt{s}$ = 13 TeV proton-proton collisions with the LHCf Arm2 detector”, The LHCf Collaboration, JHEP, **2020**, 16 (2020)., Jul. 2020
45. ”Search for Large-scale Anisotropy on Arrival Directions of Ultra-high-energy Cosmic Rays Observed with the Telescope Array Experiment”, R.U. Abbasi et al. (TA collaboration), 2020 ApJL **898** L28, Jul. 2020
46. ”Evidence for a Supergalactic Structure of Magnetic Deflection Multiplets of Ultra-high-energy Cosmic Rays”, R.U. Abbasi et al. (TA collaboration), APJ **899**:86 (13pp), 2020, Aug. 2020
47. ”Measurement of the proton-air cross section with Telescope Array ’ s Black Rock Mesa and Long Ridge fluorescence detectors, and surface array in hybrid mode”, R.U. Abbasi et al. (The Telescope Array Collaboration), Physical Review D **102**, 062004 (13pp) (2020), Sep. 2020
48. ”Search for Ultra-High-Energy Neutrinos with the Telescope Array Surface Detector”, R.U. Abbasi et al. (Telescope Array Collaboration), Journal of Experimental and Theoretical Physics **131**, 255-264 (2020), Sep. 2020
49. ”Observations of the Origin of Downward Terrestrial Gamma-Ray Flashes”, J.W. Belz et al. for the Telescope Array Collaboration, JGR Atmospheres Vol. **125**, Issue 23, 1-26, Oct. 2020
50. ”Using Deep Learning to Enhance Event Geometry Reconstruction for the Telescope Array Surface Detector”, D. Ivanov, O. E. Kalashev, M. Yu. Kuznetsov, G. I. Rubtsov, T. Sako, Y. Tsunesada, Y. V. Zhezher, Mach. Learn.: Sci. and Technol., **2** (2021) 015006, Dec. 2020
51. ”Simulation and experimental validation of optimum read-out electronics design for scintillator bar cosmic ray telescope”, M. Anzorena et al., Nucl. Inst. Meth A **991**,(2021), 165019, Mar. 2021
52. ”The Cosmic-Ray Composition between 2 PeV and 2 EeV Observed with the TALE Detector in Monocular Mode”, R.U. Abbasi et al. (The Telescope Array Collaboration), The Astrophysical Journal, **909**: 178 (17pp), 2021 , Mar. 2021
53. ”Simulation study on the effects of diffractive collisions on the prediction of the observables in ultra-high-energy cosmic-ray experiments”, K. Ohashi, H. Menjo, Y. Itow, T. Sako, and K, Kasahara, PTEP **2021**, 3, 033F01, Feb. 2021
54. ”Polarized radiation and the Emergence of Biological Homochirality on Earth and Beyond”, Noemie Globus, Anatoli Fedynitch, and Roger D. Blandford, Astrophys. J., **910**(2):85, 2021, Mar. 2021
55. ”Impact of the Collision Model on the Multi-messenger Emission from Gamma-Ray Burst Internal Shocks”, Annika Rudolph, Jonas, Heinze, Anatoli Fedynitch, and Walter Winter, Astrophys. J., **893**:72, 2020, Apr. 2020
56. ”The hadronic interaction model Sibyll 2.3d and extensive air showers”, Felix Riehn, Ralph Engel, Anatoli Fedynitch, Thomas K. Gaisser, and Todor Stanev, Phys. Rev. D, **102**(6):063002, 2020, Sep. 2020
57. ”Systematic parameter space study for the UHECR origin from GRBs in models with multiple internal shocks”, Jonas Heinze, Daniel Biehl, Anatoli Fedynitch, Denise Boncioli, Annika Rudolph, and Walter Winter, Mon. Not. Roy. Astron. Soc., **498**(4):5990-6004, 2020, Sep. 2020
58. ”Production of secondary particles in heavy nuclei interactions in supernova remnants”, Maulik Bhatt, Iurii Sushch, Martin Pohl, Anatoli Fedynitch, Samata Das, Robert Brose, Pavlo Plotko, and Dominique M.-A. Meyer, Astropart. Phys., **123**:102490,2020, Dec. 2020
59. ”Constraint on the Ejecta Mass for a Black Hole-Neutron Star Merger Event Candidate S190814bv”, Kyohei Kawaguchi, Masaru Shibata, and Masaomi Tanaka, 2020 ApJ **893** 153, Apr. 2020
60. ”The Boltzmann-Radiation-Hydrodynamics Simulations of the Core-Collapse Supernova with the Different Equations of State: the Role of Nuclear Composition and the Behavior of Neutrinos”, Akira Harada, et al., ApJ **902** 150, Oct. 2020
61. ”Systematic Opacity Calculations for Kilonovae”, Masaomi Tanaka, Daiji Kato, Gediminas Gaigalas, Kyohei Kawaguchi, MNRAS, **496**, 2(2020), Jun. 2020
62. ”Sub-radian-accuracy gravitational waves from coalescing binary neutron stars II: Systematic study on the equation of state, binary mass, and mass ratio”, Kenta Kiuchi, Kawaguchi Kyohei, Koutarou Kyutoku, Yuichiro Sekiguchi, and Masaru Shibata, Phys. Rev. D **101**, 084006, Apr. 2020

63. ”Simulations of the Early Post-Bounce Phase of Core-Collapse Supernovae in Three-Dimensional Space with Full Boltzmann Neutrino Transport”, Wakana Iwakami, Hirotada Okawa, Hiroki Nagakura, Akira Harada, Shun Furusawa, Kosuke Sumiyoshi, Hideo Matsufuru, and Shoichi Yamada, 2020 ApJ **903** 82, Nov. 2020

64. ”Spectral Modification of Magnetar Flares by Resonant Cyclotron Scattering”, Shotaro Yamasaki, Yuri Lyubarsky, Jonathan Granot, Ersin Gogus, MNRAS, **498**, 484-494, Nov. 2020

65. ”Chirp Mass and Spin of Binary Black Holes from First Star Remnants”, Tomoya Kinugawa, Takashi Nakamura, and Hiroyuki Nakano, MNRAS **498**, 3946 - 3963, Nov. 2020

66. ”Formation Rate of LB-1-like Systems through Dynamical Interactions”, Ataru Tanikawa, Tomoya Kinugawa, Jun Kumamoto, and Michiko S. Fujii, PASJ(2020) **72** (3), 39 (110), Apr. 2020

67. ”Fitting Formulae for Evolution Tracks of Massive Stars under Extreme Metal-Poor Environments for Population Synthesis Calculations and Star Cluster Simulations”, Ataru Tanikawa, Takashi Yoshida, Tomoya Kinugawa, Koh Takahashi, and Hideyuki Umeda, MNRAS **495**, 4170-4191, May. 2020

68. ”Probing Particle Acceleration through Broadband Early Afterglow Emission of MAGIC Gamma-Ray Burst GRB 190114C”, Katsuaki Asano, Kohta Murase, Kenji Toma, 2020 ApJ **905** 105, Dec. 2020

69. ”Formation of Mass Gap Compact Object and Black Hole Binary from Population III Stars”, Tomoya Kinugawa, Takashi Nakamura, and Hiroyuki Nakano, PTEP, **2020**, ptaa176, Dec. 2020

70. ”Merger Rate Density of Population III Binary Black Holes below, above, and in the Pair-Instability Mass Gap”, Ataru Tanikawa, Hajime Susa, Takashi Yoshida, Alessandro A. Trani, Tomoya Kinugawa, 2021 ApJ **910** 30, Mar. 2021

71. ”Simulations of Early Kilonova Emission from Neutron Star Mergers”, Smaranika Banerjee, Masaomi Tanaka, Kyohei Kawaguchi, Daiji Kato, and Gediminas Gaigalas, 2020 ApJ **901** 29, Sep. 2020

72. ”Analytic Solutions for Neutrino-Light Curves of Core-Collapse Supernovae”, Yudai Suwa, Akira Harada, Ken ’ ichiro Nakazato, and Kohsuke Sumiyoshi, PTEP**2020** ptaa154, Oct. 2020

73. ”Formation of Binary Black Hole Similar to GW190521 with a Total Mass of $\sim 150 M_\odot$ from Population III Binary Star Evolution”, Tomoya Kinugawa, Takashi Nakamura, and Hiroyuki Nakano, MNRAS **501**, L49-L53 (2021), Dec. 2020

74. ”A Jet-Bases Emission Model of the EHT 2017 Image of M87*”, Tomohisa Kawashima, Kenji Toma, Motoki Kino, Kazunori Akiyama, Masanori Nakamura, and Kotaro Moriyama, 2021 ApJ **909** 168, Mar. 2021

75. ”Properties of the remnant disk and the dynamical ejecta produced in low-mass black hole-neutron star mergers”, Kota Hayashi, Kyohei Kawaguchi, Kenta Kiuchi, Koutarou Kyutoku, Masaru Shibata, Phys. Rev. D **103**, 043007, Feb. 2021

76. ”Multidimensional Boltzmann Neutrino Transport Code in Full General Relativity for Core-collapse Simulations”, Ryuichiro Akaho, Akira Harada, Hiroki Nagakura, Kohsuke Sumiyoshi, Wakana Iwakami, Hirotada Okawa, Shun Furusawa, Hideo Matsufuru, Shoichi Yamada, 2021 ApJ **909** 210, Mar. 2021

77. ”Developing an end-to-end simulation framework of supernova neutrino detection”, Masamitsu Mori, Yudai Suwa, Ken’ ichiro Nakazato, Kohsuke Sumiyoshi, Masayuki Harada, Akira Harada, Yusuke Koshio, Roger A. Wendell, PTEP **2021**, Issue 2, 023E01, Feb. 2021

78. ”Impact of binary interactions on the diffuse supernova neutrino background”, Shunsaku Horiuchi, Tomoya Kinugawa, Tomoya Takiwaki, Koh Takahashi, and Kei Kotake, Phys. Rev. D **103**, 043003, Feb. 2021

79. ”Direct Measurement of the Cosmic-Ray Carbon and Oxygen Spectra from 10 GeV/n to 2.2 TeV/n with the Calorimetric Electron Telescope on the International Space Station”, O. Adriani, Y. Akaike, K. Asano, et al., Phys. Rev. Lett. **125**, 251102, Dec. 2020

80. ”First M87 Event Horizon Telescope Results. VII. Polarization of the Ring”, K. Akiyama, et al., ApJL **910**, L12(48pp), Mar. 2021

81. ”First M87 Event Horizon Telescope Results. VIII. Magnetic Field Structure near The Event Horizon”, K. Akiyama, et al., ApJL **910**, L13(43pp), Mar. 2021

82. ”Polarimetric Properties of Event Horizon Telescope Targets from ALMA”, C. Goddi, et al., ApJL **910**, L14(54pp), Mar. 2021

83. "Gravitational Test beyond the First Post-Newtonian Order with the Shadow of the M87 Black Hole", Dimitrios Psaltis et al. (EHT Collaboration), PRL, **125**, 141104(9pp), Oct. 2020

84. "Potential PeVatron supernova remnant G106.3+2.7 seen in the highest-energy gamma rays", M. Amenomori et. al (Tibet ASgamma Collaboration), Nature Astronomy, **5**, pages 460464 (2021), Mar. 2021

85. "Measurements of radiation from the Fukushima Dai-ichi Nuclear power Plant by the Compton Camera: Estimation of Plant-derived Radioactivity", Ryoji Enomoto, Hideaki Katagiri, Wataru Sato, Ryo Wakamatsu, Hiroshi Muraishi, Mika Kagaya, Takara Watanabe, RADIOISOTOPES, **69**, 189-197 (2020), Jun. 2020

86. "Shift-invariant gamma-ray imaging by adding a detector rotation function to a high-sensitivity omnidirectional Compton camera", Hiroshi Muraishi, Ryoji Enomoto, Hideaki Katagiri, Mika Kagaya, Takara Watanabe, Naofumi Narita, Daisuke Kano, Saki Ishikawa and Hiromichi Ishiyama, Jpn. J. Appl. Phys. **59** 090911, Sep. 2020

87. "Application of the independent component analysis to the iKAGRA data", T.Akutsu et al. (KAGRA Collaboration), PTEP, **2020**, 5, 053F01, May 2020

88. "Reanalysis of the Binary Neutron Star Merger GW170817 Using Numerical-Relativity Calibrated Waveform Models", Tatsuya Narikawa et al., Phys. Rev. Research **2**, 043039, Oct. 2020

89. "Prospects for improving the sensitivity of the cryogenic gravitational wave detector KAGRA", Yuta Michimura et al., Phys. Rev. D, 44036

90. "Overview of KAGRA : KAGRA science", T Akutsu, et al.(KAGRA collaboration), Progress of Theoretical and Experimental Physics, 44055

91. "Overview of KAGRA : Detector design and construction history", T. Akutsu et al.(KAGRA collaboration), Progress of Theoretical and Experimental Physics, 44060

92. "Prospects for observing and localizing gravitational-wave transients with Advanced LIGO, Advanced Virgo and KAGRA", B. P. Abbott, R. Abbott, et al., KAGRA Collaboration, LIGO Scientific Collaboration and Virgo Collaboration (full author paper), Living Reviews in Relativity, 44102

93. "Overview of KAGRA: Calibration, detector characterization, physical environmental monitors, and the geophysics interferometer", T. Akutsu et al. (KAGRA collaboration), PTEP (**2021**) ptab018, Feb. 2021

94. "Vibration isolation systems for the beam splitter and signal recycling mirrors of the KAGRA gravitational wave detector", T. Akutsu et al. (KAGRA Collaboration), 2021 Class. Quantum Grav. **38** 065011, Mar. 2021

95. "Demonstration of a dual-pass differential Fabry-Perot interferometer for future interferometric space gravitational wave antennas", Koji Nagano , Hiroki Takeda, Yuta Michimura, Takashi Uchiyama and Masaki Ando, 2021 Class. Quantum Grav. **38** 085018, Mar. 2021

96. "Cryogenic suspension design for a kilometer-scale gravitational-wave detector", Takafumi Ushiba, Tomotada Akutsu, Sakae Araki, Rishabh Bajpai, Dan Chen, Kieran Craig, Yutaro Enomoto, Ayako Hagiwara, Sadakazu Haino, Yuki Inoue, Kiwamu Izumi, Nobuhiro Kimura, Rahul Kumar, Yuta Michimura, Shinji Miyoki, Iwao Murakami, Yoshikazu Namai, Masayuki Nakano, Masatake Ohashi, Koki Okutomi, Takaharu Shishido, Ayaka Shoda, Kentaro Somiya, Toshikazu Suzuki, Suguru Takada, Masahiro Takahashi, Ryutaro Takahashi, Shinichi Terashima, Takayuki Tomaru, Flavio Travasso, Ayako Ueda, Helios Vocca, Tomohiro Yamada, Kazuhiro Yamamoto, and Simon Zeidler, Class. Quantum Grav. **38** (2021) 085013, 19 March 2021

97. "Reducing orbital eccentricity in initial data of black hole–neutron star binaries in the puncture framework", Koutarou Kyutoku, Kyohei Kawaguchi, Kenta Kiuchi, Masaru Shibata, Keisuke Taniguchi, PHYSICAL REVIEW D, 44201

98. "Early Low-Mass Galaxies and Star-Cluster Candidates at z$\sim$6-9 Identified by the Gravitational Lensing Technique and Deep Optical/Near-Infrared Imaging", Shotaro Kikuchihara, et al., 2020 ApJ **893** 60, Apr. 2020

99. "Large Population of ALMA Galaxies at z$>$6 with Very High [OIII]88μm to [CII]158μm Flux Ratios: Evidence of Extremely High Ionization Parameter or PDR Deficit?", Y. Harikane, et al., APJ **896**:93(2020), Jun. 2020

100. "Extremely Metal-poor Representatives Explored by the Subaru Survey (EMPRESS). I. A Successful Machine-learning Selection of Metal-poor Galaxies and the Discovery of as Galaxy with $M^* < 10^6 M_\odot$ and 0.016 $Z_\odot$", T. Kojima, et al., APJ **898**, 2, id.142(2020), Aug. 2020

101. "Three-dimensional Distribution Map of H I Gas and Galaxies around an Enormous Lyα Nebula and Three QSOs at z = 2.3 Revealed by the H I Tomographic Mapping Technique ", S. Mukae, et al, 2020 ApJ **896** 45, Jun. 2020

102. "RELICS: A Very Large (θ_E~40") Cluster Lens – RXC J0032.1+1808 ", A. Acebron et al., 2020 ApJ **898** 6, Jul. 2020

103. "The Subaru HSC Galaxy Clustering with Photometric Redshift I: Dark Halo Masses Versus Baryonic Properties of Galaxies at $0.3<z<1.4$ ", S. Ishikawa et al., 2020 ApJ **904** 128, Nov. 2020

104. "Faint LAEs near $z>4.7$ CIV absorbers revealed by MUSE", C. Gonzalo Diaz, et al., Monthly Notices of the Royal Astronomical Society, Oct. 2020

105. "Testing an indirect method for identifying galaxies with high levels of Lyman continuum leakage", S. Yamanaka, et al., MNRAS,**498**, 30953114(2020), Aug. 2020

106. "The Mass-Metallicity Relation at z=8: Direct-Method Metallicity Constraints and Near-Future Prospects", T. Jones, et al., APJ **903**:150, Nov. 2020

107. "ALMA twenty-six arcmin2 survey of GOODS-S at one-millimeter (ASAGAO): millimeter properties of stellar mass selected galaxies", Y. Yamaguchi, et al., PASJ(2020) **72** (4), 69 (123), Jun. 2020

108. "The UV Luminosity Function of Protocluster Galaxies at $z\sim4$: the Bright-end Excess and the Enhanced Star Formation Rate Density", K. Ito, et al.,, APJ **899**:5, Aug. 2020

109. "A Wide and Deep Exploration of Radio Galaxies with Subaru HSC (WERGS). III. Discovery of a z = 4.72 Radio Galaxy with the Lyman Break Technique", T. Yamashita, et al., The Astronomical Journal, Volume **160**, Issue 2, id.60, Jul. 2020

110. "Dual supermassive black holes at close separation revealed by the Hyper Suprime-Cam Subaru Strategic Program", J. Silverman, et al., 2020 ApJ **899** 154, Aug. 2020

111. "A detailed study of massive galaxies in a protocluster at z=3.13", K. Shi, et al., 2020 ApJ **899** 79, Aug. 2020

112. "Statistical correlation between the distribution of Lyα emitters and IGM HI at $z\sim2.2$ mapped by Subaru/Hyper Suprime-Cam", Y. Liang, et al., 2021 ApJ **907** 3, 2021 Jan

113. "ALMA Lensing Cluster Survey: an ALMA galaxy signposting a MUSE galaxy group at z=4.3 behind ‘El Gordo’ ", K. I. Caputi, et al., 2021 ApJ **908** 146, 2021 Feb

114. "CHORUS. I. Cosmic HydrOgen Reionization Unveiled with Subaru: Overview", A. K. Inoue, et al., Publ. Astron. Soc. Japan(2020) **72** (6), 101 (117), Nov. 2020

115. "RELICS-DP7: Spectroscopic Confirmation of a Dichromatic Primeval Galaxy at $z\sim7$", D. Pelliccia, et al., 2021 ApJL **908** L30, Feb. 2021

116. "FIR-luminous [CII] emitters in the ALMA-SCUBA-2 COSMOS survey (AS2COSMOS): The nature of submillimeter galaxies in a 10 comoving Mpc-scale structure at $z\sim4.6$", I. Mitsuhashi, et al., 2021 ApJ **907** 122, Feb. 2021

117. "Faint Quasars Live in the Same Number Density Environments as Lyman Break Galaxies at $z\sim4$", H. Uchiyama, et al., 2020 ApJ **905** 125, Dec. 2020

118. "The Faint End of the Quasar Luminosity Function at $z\sim5$ from the Subaru Hyper Suprime-Cam Survey", M. Niida, et al., 2020 ApJ **904** 89, Nov. 2020

119. "A puzzling non-detection of [O III] and [C II] from a $z\approx7.7$ galaxy observed with ALMA", C. Binggeli, et al., A&A **646**, A26 (2021), Feb. 2021

120. "Broadband Selection, Spectroscopic Identification, and Physical Properties of a Population of Extreme Emission-line Galaxies at $3<z<3.7$", M. Onodera, et al., 2020 ApJ **904** 180, Dec. 2020

121. "Observations of the Lyman-α Universe", M. Ouchi, et al., Annual Review of Astronomy and Astrophysics, Volume **58**, pp 617-659 , Aug. 2020

122. "The Mean Absorption-line Spectra of a Selection of Luminous $z\sim6$ Lyman Break Galaxies", Harikane,Y et al., The Astrophysical Journal, Volume **902**, Issue 2, id.117, 12 pp, Oct. 2020

123. "Cosmological 3D H I Gas Map with HETDEX Lyα Emitters and eBOSS QSOs at z = 2: IGM-Galaxy/QSO Connection and a ~40 Mpc Scale Giant H II Bubble Candidate ", S. Mukae et al., The Astrophysical Journal, Volume **903**, Issue 1, id.24, 19 pp., Nov. 2020

124. ”Deep multiredshift limits on Epoch of Reionization 21 cm power spectra from four seasons of Murchison Widefield Array observations”, C. M. Trott et al., Monthly Notices of the Royal Astronomical Society, Volume **493**, Issue 4, p.4711-4727, Apr. 2020

125. ”ALMA uncovers the [C II] emission and warm dust continuum in a z = 8.31 Lyman break galaxy”, T. J. L. C. Bakx et al., Monthly Notices of the Royal Astronomical Society, Volume **493**, Issue 3, p.4294-4307, Apr. 2020

126. ”The Subaru HSC Galaxy Clustering with Photometric Redshift. I. Dark Halo Masses versus Baryonic Properties of Galaxies at $0.3 \le z \le 1.4$”, S. Ishikawa et al., The Astrophysical Journal, Volume **904**, Issue 2, id.128, 26 pp., Dec. 2020

127. ”Subaru High-z Exploration of Low-Luminosity Quasars (SHELLQs) XII. Extended [C II] Structure (Merger or Outflow) in a z = 6.72 Red Quasar”, T. Izumi et al., 2021 ApJ **908** 235, Feb. 2021

128. ”ALMA Lensing Cluster Survey: a strongly lensed multiply imaged dusty system at $z \ge 6$”, N. Laporte et al., NMRAS stab191, Jan. 2021

129. ”Revisiting oscillon formation in the Kachru-Kallosh-Linde-Trivedi scenario”, S. Kasuya, M. Kawasaki, F. Otani and E. Sonomoto, Phys. Rev. D **102**, 043016 (2020), Aug. 2020

130. ”Generation of Primordial Black Holes and Gravitational Waves from Dilaton-Gauge Field Dynamics”, M. Kawasaki, H. Nakatsuka and I. Obata, JCAP05(**2020**)007, 43952

131. ”Gravitational Wave Production right after a Primordial Black Hole Evaporation”, K. Inomata, M. Kawasaki, K. Mukaida, T. Terada and T. T. Yanagida, Phys. Rev. D, **101**, no.12, 123533 (2020), 44373

132. ”Q-ball decay through A-term in the gauge-mediated SUSY breaking scenario”, M. Kawasaki and H. Nakatsuka, JCAP04(**2020**)017, Apr. 2020

133. ”J-factor estimation of Draco, Sculptor and Ursa Minor dwarf spheroidal galaxies with the member/foreground mixture model”, Shun-ichi Horigome, Kohei Hayashi, Masahiro Ibe, Miho N. Ishigaki, Shigeki Matsumoto, MNRAS, **499**,33203337 (2020), Sep. 2020

134. ”Cosmic String in Abelian-Higgs Model with Enhanced Symmetry — Implication to the Axion Domain-Wall Problem”, Takashi Hiramatsu, Masahiro Ibe, Motoo Suzuki, JHEP **2020**, 54 (2020) , Sep. 2020

135. ”Big Bang Nucleosynthesis constraints on sterile neutrino and lepton asymmetry of the Universe”, Graciela B. Gelmini, Masahiro Kawasaki, Alexander Kusenko, Kai Murai, Volodymyr Takhistov, JCAP09(**2020**)051, Sep. 2020

136. ”Big-bang nucleosynthesis with sub-GeV massive decaying particles”, M. Kawasaki, K. Kohri, T. Moroi, K. Murai and H. Murayama, JCAP 12, 048 (**2020**), 44195

137. ”Cosmological Constraint on Vector Mediator of Neutrino-Electron Interaction in light of XENON1T Excess”, Masahiro Ibe, Shin Kobayashi, Yuhei Nakayama, Satoshi Shirai, JHEP2020, Article number: 4 (**2020**), Dec. 2020

138. ”Proton decay and axion dark matter inSO(10) grand unification via minimal leftright symmetry”, Yuta Hamada, Masahiro Ibe, Yu Muramatsu, Kin-ya Oda, Norimi Yokozaki, Eur.Phys.J.C**80**(2020)5,482, Apr. 2020

139. ”Probing Dark Matter Self-interaction with Ultra-faint Dwarf Galaxies”, Kohei Hayashi, Masahiro Ibe, Shin Kobayashi, Yuhei Nakayama, Phys. Rev. D **103**, 023017, Jan. 2021

140. ”Oscillons of Axion-Like Particle: Mass distribution and power spectrum”, Masahiro Kawasaki, Wakutaka Nakano, Hiromasa Nakatsuka, Eisuke Sonomoto, JCAP01(**2021**)061, Jan. 2021

141. ”NANOGrav results and LIGO-Virgo primordial black holes in axion-like curvaton model”, Keisuke Inomata, Masahiro Kawasaki, Kyohei Mukaida, Tsutomu T. Yanagida, Phys. Rev. Lett. **126**, 131301, Mar. 2021

142. ”Detection of isotropic cosmic birefringence and its implications for axion-like particles including dark energy”, Tomohiro Fujita, Kai Murai, Hiromasa Nakatsuka, Shinji Tsujikawa, Phys. Rev. D **103**, 043509, Feb. 2021

143. ”Improved sensitivity of interferometric gravitational wave detectors to ultralight vector dark matter from the finite light-traveling time”, Soichiro Morisaki, Tomohiro Fujita, Yuta Michimura, Hiromasa Nakatsuka, Ippei Obata, Phys. Rev. D **103**, L051702, Mar. 2021

(b) Conference Papers (Proceedings)

1. "Purification of the NaI(Tl) crystal for dark matter search project PICOLON", Kanemitsu, Y.; Chernyak, D.; Ejiri, H.; Fushimi, K.; Hata, K.; Hazama, R.; Ikeda, H.; Imagawa, K.; Inoue, K.; Kozlov, A.; Orito, R.; Shima, T.; Takemoto, Y.; Umehara, S.; Yasuda, K.; Yoshida, S., 16th International Conference on Topics in Astroparticle and Underground Physics (TAUP), SEP 09-13, 2019

2. "Development of low background PMT R13111", Abe, K., XMASS Collaboration, 16th International Conference on Topics in Astroparticle and Underground Physics (TAUP), SEP 09-13, 2019

3. "Study of neutrons associated with neutrino and anti-neutrino interactions on water at T2K", Akutsu, Ryosuke, T2K Collaboration, 16th International Conference on Topics in Astroparticle and Underground Physics (TAUP), SEP 09-13, 2019

4. "ZICOS - Neutrinoless Double Beta Decay experiment using Zr-96 with an organic liquid scintillator -", Fukuda, Yoshiyuki; Moriyama, Shigetaka; Hiraide, Katsuki; Ogawa, Izumi; Gunji, Takahiro; Hayami, Ryohei; Tsukada, Satoru; Kurosawa, Shunsuke, 16th International Conference on Topics in Astroparticle and Underground Physics (TAUP), SEP 09-13, 2019

5. "PICOLON dark matter search similar to Development of highly redio-pure NaI(Tl) scintilltor similar to", Fushimi, Ken-Ichi; Chernyak, Dmitry; Ejiri, Hiroyasu; Hata, Kazumi; Hazama, Ryuta; Hirata, Shoko; Iida, Takashi; Ikeda, Haruo; Inoue, Kunio; Imagawa, Kyoshiro; Kanemitsu, Yuta; Kozlov, Alexandle; Orito, Reiko; Shima, Tatsushi; Takemoto, Yasuhiro; Umehara, Saori; Yoshida, Sei, 16th International Conference on Topics in Astroparticle and Underground Physics (TAUP), SEP 09-13, 2019

6. "Measurement of ambient neutrons in an underground laboratory at Kamioka Observatory and future plan", Mizukoshi, Keita; Taishaku, Ryosuke; Hosokawa, Keishi; Kobayashi, Kazuyoshi; Miuchi, Kentaro; Naka, Tatsuhiro; Takeda, Atsushi; Tanaka, Masashi; Wada, Yoshiki; Yorita, Kohei; Yoshida, Sei, 16th International Conference on Topics in Astroparticle and Underground Physics (TAUP), SEP 09-13, 2019

7. "Characterization of new photo-detectors for the future dark matter experiments with liquid xenon", Ozaki, Kosuke; Kazama, Shingo; Yamashita, Masaki; Itow, Yoshitaka; Moriyama, Shigetaka, 16th International Conference on Topics in Astroparticle and Underground Physics (TAUP), SEP 09-13, 2019

8. "Update of the atmospheric neutrino flux simulation ATMNC for next-generation neutrino experiment", Sato, K.; Itow, Y.; Menjo, H.; Honda, M., 16th International Conference on Topics in Astroparticle and Underground Physics (TAUP), SEP 09-13, 2019

9. "Drift field generation with Cockcroft-Walton voltage multiplier in xenon gas for AXEL 0 nu beta beta search detector", Yoshida, M.; Ban, S.; Hirose, M.; Ichikawa, A. K.; Iwashita, Y.; Kikawa, T.; Minamino, A.; Miuchi, K.; Nakadaira, T.; Nakajima, Y.; Nakamura, K. D.; Nakamura, K. Z.; Nakaya, T.; Obara, S.; Sakashita, K.; Sekiya, H.; Sugashima, B.; Ueshima, K., 16th International Conference on Topics in Astroparticle and Underground Physics (TAUP), SEP 09-13, 2019

10. "Development and performance of the 20 " PMT for Hyper-Kamiokande", Bronner, C.; Nishimura, Y.; Xia, J.; Tashiro, T., 16th International Conference on Topics in Astroparticle and Underground Physics (TAUP), SEP 09-13, 2019

11. "Accuracy improvement of the atmospheric neutrino flux prediction using observed muon spectra at mountain altitude", Honda, Morihiro; Athar, M. Sajjad; Kajita, Takaaki; Kasahara, Katsuaki; Midorikawa, Shoichi; Nishimura, Jun, , 16th International Conference on Topics in Astroparticle and Underground Physics (TAUP), SEP 09-13, 2019

12. "The readout system based on the ultra-fast waveform sampler DRS4 for the Large-Sized Telescope of the Cherenkov Telescope Array", Nozaki, S.; Blanch, O.; Delgado, C.; Gliwny, P.; Hadasch, D.; Inome, Y.; Katagiri, H.; Kubo, H.; Kobayashi, Y.; Mazin, D.; Moralejo, A.; Nogami, Y.; Paoletti, R.; Saito, T.; Sakurai, S.; Sitarek, J.; Takahashi, M.; Teshima, M.; Yamamoto, T., CTA Consortium, 16th International Conference on Topics in Astroparticle and Underground Physics (TAUP), SEP 09-13, 2019

13. "Influence of uncertainty in hadronic interaction models on the sensitivity estimation of Cherenkov Telescope Array", Ohishi, M.; Arbeletche, L.; de Souza, V.; Maier, G.; Bernloehr, K.; Moralejo, A.; Bregeon, J.; Arrabito, L.; Yoshikoshil, T., CTA Consortium, 16th International Conference on Topics in Astroparticle and Underground Physics (TAUP), SEP 09-13, 2019

14. "GRB observations with CTA Large Size Telescopes", Daniela Hadasch, on behalf of the CTA consortium, CTA, Yamada Conference LXXI: Gamma-ray Bursts in the Gravitational Wave Era 2019, 28 Oct - 1 Nov 2019

15. ”Discovery of VHE gamma rays from GRB 190114C”, Koji Noda , A. Berti, S. Covino, S. Fukami, S. Inoue, D. Miceli, E. Moretti, L. Nava, Y. Suda, and I. Vovk, on behalf of the MAGIC Collaboration, MAGIC , Yamada Conference LXXI: Gamma-ray Bursts in the Gravitational Wave Era 2019, 28 Oct - 1 Nov 2019

16. ”Design and production of segment mirrors for the Large-Sized Telescopes of the Cherenkov Telescope Array”, Tomohiro Inada, Satoshi Fukami, Koji Noda, Michiyuki Chikawa, Mika Kagaya, Hideaki Katagiri, Daniel Mazin, Koutaro Obara, Akira Okumura, Takayuki Saito, Masahiro Teshima, Tokonatsu Yamamoto, Tatsuo Yoshida, Ievgen Vovk, CTA, SPIE Astronomical Telescopes + Instrumentation, 14-18 Dec 2020

17. ”Results of ultra-high-energy cosmic rays from the Telescope Array”, Sagawa, H., Telescope Array Collaboration, International Conference on Instrumentation for Colliding Beam Physics, FEB 24-28, 2020

18. ”Innovative astronomical applications with a new-generation relational database”, J. Furusawa et al., SPIE Astronomical Telescopes + Instrumentation, 2020, Online Only

19. ”A machine learning software to estimate morphological parameters of distant galaxies”, T. Shibuya et al., SPIE Astronomical Telescopes + Instrumentation, 2020, Online Only

20. ”The University of Tokyo Atacama Observatory 6.5m telescope: On-sky performance of the near-infrared instrument SWIMS on the Subaru telescope”, M. Konishi et al., SPIE Astronomical Telescopes + Instrumentation, 2020, Online Only

21. ”Enhancement of gravitational waves induced by scalar perturbations due to a sudden transition from an early matter era to the radiation era”, Inomata, Keisuke; Kohri, Kazunori; Nakama, Tomohiro; Terada, Takahiro, 16th International Conference on Topics in Astroparticle and Underground Physics (TAUP), SEP 09-13, 2019

22. ”Gravitational waves induced by scalar perturbations during a gradual transition from an early matter era to the radiation era”, Inomata, Keisuke; Kohri, Kazunori; Nakama, Tomohiro; Terada, Takahiro, 16th International Conference on Topics in Astroparticle and Underground Physics (TAUP), SEP 09-13, 2019

23. ”DANCE: Dark matter Axion search with riNg Cavity Experiment”, Michimura, Yuta; Oshima, Yuka; Watanabe, Taihei; Kawasaki, Takuya; Takeda, Hiroki; Ando, Masaki; Nagano, Koji; Obata, Ippei; Fujita, Tomohiro, 16th International Conference on Topics in Astroparticle and Underground Physics (TAUP), SEP 09-13, 2019

24. ”Dark matter distribution in the Galactic dwarf spheroidal galaxies”, Hayashi, Kohei; Matsumoto, Shigeki; Ibe, Masahiro; Ishigaki, Mino N.; Sugai, Hajime; Horigome, Shun’ichi, 16th International Conference on Topics in Astroparticle and Underground Physics (TAUP), SEP 09-13, 2019

25. ”Axion Dark Matter Search with Interferometric Gravitational Wave Detectors”, Nagano, Koji; Obata, Ippei; Fujita, Tomohiro; Michimura, Yuta, 16th International Conference on Topics in Astroparticle and Underground Physics (TAUP), SEP 09-13, 2019

26. ”Status of KAGRA and its science goals”, Takaaki Kajita

27. ”Radiative Cooling of the Thermally Isolated System in KAGRA Gravitational Wave Telescope”, Tomohiro Yamada and on behalf of the KAGRA collaboration

28. ”Demographic Landscape of the KAGRA collaboration”, Keiko Kokeyama, Chunglee Kim, Joseph M. Fedrow, and Ayaka Shoda, , Proceedings of the 14th Asia-Pacific Physics Conference, Nov 17 - 21, 2019

29. ”Visualization of Low-Level Gamma Radiation Sources Using a Low-Cost, High-Sensitivity, Omnidirectional Compton Camera”, Muraishi, Hiroshi; Enomoto, Ryoji; Katagiri, Hideaki; Kagaya, Mika; Watanabe, Takara; Narita, Naofumi; Kano, Daisuke

D. Doctoral Theses

1. Search for Proton Decay via p$\rightarrow e^+\pi^0$ and p$\rightarrow \mu^+\pi^0$ with an Enlarged Fiducial Mass of the Super-Kamiokande Detector,
TAKENAKA, Akira,
Ph.D Thesis, Mar. 2021

2. Low-Vibration Conductive Cooling of KAGRA Cryogenic Mirror Suspension,
YAMADA, Tomohiro,
Ph.D Thesis, Mar. 2021

3. Stochastic description and quantum aspects of curvature perturbations in the inflationary universe,
ANDO, Kenta,
Ph.D Thesis, Mar. 2021

4. Oscillon formation and 21cm forest by ultra-light axion-like particle,
SONOMOTO, Eisuke,
Ph.D Thesis, Mar. 2021

E. Public Relations

(a) ICRR News

ICRR News is a quarterly publication written in Japanese about scientific and educational activities at ICRR.

Below lists the main topics in the issues published in FY 2020:

No.108 (2020 Summer)

- Features : KAGRA Members' Round-Table Talk
- Features : Press Release Apr. 16, 2020 "T2K Results Restrict Possible Values of Neutrino CP Phase"
- Features : Press Release Jun. 17, 2020 "Observation of Excess Events in the XENON1T Dark Matter Experiment"
- Features : Press Release Jun. 23, 2020 "Transverse single-spin asymmetry for very forward neutral pion production in polarized $p+p$ collisions at $\sqrt{s}$= 510 GeV"
- Reports : The 22nd ICRR x IPMU Public lecture, "Challenge to the Mystery : Extreme Universe and Physics Beyond the Standard Model " : Koji Noda, ICRR Associate Prof., Talks on "Successful Detection of Gamma Ray Burst from MAGIC Telescope"
- Topics : High Precision General Relativity Test Using the Very High Energy Emission from Gamma-Ray Burst GRB 190114c by MAGIC Collaboration
- Topics : CTA Prototype LST-1 Detects Very High-Energy Emission from the Crab Pulsar
- Topics: ICRR's Information Session to Undergraduates Held Online
- Topics: Super-Kamiokande Exhibition in Miraikan Renewed
- Topics : UTokyo and KEK sign MoU to Promote Hyper-Kamiokande Project
- Topics: Former ICRR's Director Yoichiro Suzuki Awarded Persons of Merit from Gifu Prefecture
- Topics: ICRR and Toyama University sign MoU to Promote Research on Gravitational Waves
- Topics: ICRR Catalogue 2020 Published
- Information : Staff reassignment

No.109 (2020 Autumn & Winter)

- Features: Kashiwa Campus Open Days Held Online, About 2000 People Enjoy Online Events
- Features : Press Release on Aug. 21, 2020, "Introduction of Gadolinium into Super-Kamiokande and the Start of New Observations"
- Features : Press Release on Aug. 1, 2020, "Machine Learning Finds a Surprising Early Galaxy –Breaking the Lowest Oxygen Abundance Record"
- Features : Press Release on Oct. 20, 2020, "First Measurement of $\bar{\nu}_{\mu}$and ν_{μ} Charged-current Inclusive Interactions on Water Using a Nuclear Emulsion Detector"

- Reports : The 23rd ICRR x IPMU Public lecture, ”New Epoch of Space Telescopes” : Hideyuki Tagoshi, ICRR Prof., Talks on ”Current Observation of Gravitational-waves”
- Topics: Assistant Prof. Yuichi Harikane Awarded Inoue Research Award for Young Scientists
- Topics: Associate Prof. Takashi Sako Appears and Introduces ICRR’s Researches on JURC Video series
- Topics: Associate Prof. of Musashino Art University Hiroko Miyahara Talks online at Events for Female Students ”Yappari Butsuriga Suki.”
- Topics: Exhibition ”ICRR Now and Then” held at Kashiwa Library
- Topics: ICRR and Tokyo City University Sign Academic Partnership Agreement
- Topics: ICRR Annual Report Published
- Topics: Obituary : Masatoshi Koshiba, Special University Professor, The University of Tokyo
- Information : Staff reassignment
- Information : ICRR Seminar

No.110 (2021 Spring)

- Features : Press Release on Apr. 2, 2021, ”First Detection of Sub-PeV Diffused Gamma Rays from the Galactic Disk: Evidence for Ubiquitous Cosmic Rays Beyond PeV Energies”
- Features : Press Release on Mar. 2, 2021, ”Potential PeVatron Supernova Remnant Seen in the Highest Energy Gamma Rays”
- Features : Press Release on Jan. 25, 2021, ”The Smallest Galaxies in Our Universe Bring More About Dark Matter to Light”
- Features : Press Release on Apr. 9, 2021, ”Enhanced X-ray Emission Coinciding with Giant Radio Pulses from the Club Pulsar”
- Features : Press Release on Apr. 14, 2021, ”Telescope Units in Unprecedented Observations of Famous Black Hole”
- Features : Press Release on Apr. 22, 2021, ”ALMA Discovers Rotating Infant Galaxy with Help of Natural Cosmic Telescope”
- Reports : Science Cafe with Tamarokuto Science Center
- Reports : 2021 Spring School for Undergraduate Students
- Reports : The 24th ICRR x IPMU Public Lecture ”Mystery of the Matter Dominant Universe” : Yoichi Asaoka, Associate Prof. Talks on ”Hyper-Kamiokande to Start Construction”
- Topics : Mr. Otani and Mr. Kato (D2) Awarded Student Presentation Award of Physical Society of Japan in 2020 Autumn Meeting
- Topics : Satellite Office of Kamioka Observatory Opened in Kamioka Branch of Hida City
- Topics : 2021 ICRR Master and Doctor Thesis Workshop Held Online
- Topics : 2020 Research Result Presentation Meeting of ICRR Inter-University Research Program Held Online
- Topics : Shinji Inoue, State Minister for Science and Technology Policy, Visits Super-Kamiokande and KAGRA in Hida City
- Topics : Comments from Director Kajita at the Beginning of 2021 Fiscal Year
- Topics : International Laboratory Established in Kashiwa Campus by CNRS and Four Divisions of The University of Tokyo
- Information : Staff reassignment
- Information : ICRR Seminar

(b) Public Lectures

- ”Public Lecture for JSEC,” Aug. 31, 2020, Online, Takaaki Kajita (ICRR, The University of Tokyo).
- ”Toyama Prefectural Takaoka Minami High School,” Sep. 25, 2020, Takaoka Minami High School, Takaoka-City, Toyama, Takaaki Kajita (ICRR, The University of Tokyo).
- ”Perspective Nuclear Physics in the 21 century,” Sep. 27, 2020, Online, Takaaki Kajita (ICRR, The University of Tokyo).
- ”The 6th Hokkaido University Cross-Departmental Symposium,” Oct. 19, 2020, Online, Takaaki Kajita (ICRR, The University of Tokyo).
- ”Amsterdam University Science Colloquium,” Nov. 3-4, 2020, Online, Takaaki Kajita (ICRR, The University of Tokyo).
- ”Rokko Island High School,” Nov. 11, 2020, Rokko Island High School, Kobe-City, Hyogo, Takaaki Kajita (ICRR, The University of Tokyo).
- ”Future Leaders’ Declaration on ASEAN-Japan Cooperation for International Marine Plastic Waste,” Nov. 14, 2020, Asean-Japan Center, Minato-ku, Tokyo, Takaaki Kajita (ICRR, The University of Tokyo).
- ”Saitama Prefectural Urawa High School,” Nov. 18, 2020, Urawa High School, Saitama-City, Saitama, Takaaki Kajita (ICRR, The University of Tokyo).
- ”Okinawa Institute of Science and Technology Graduate University,” Nov. 27, 2020, OIST, Kunigami-gun, Okinawa, Takaaki Kajita (ICRR, The University of Tokyo).
- ”Public Lecture,” Nov. 28, 2020, OIST, Kunigami-gun, Okinawa, Takaaki Kajita (ICRR, The University of Tokyo).
- ”Hyogo Science and Technology Association,” Dec. 2, 2020, Hotel Crown Palais, Kobe-City, Hyogo, Takaaki Kajita (ICRR, The University of Tokyo).
- ”80th Anniversary of the municipal system of Komatsu City,” Dec. 6, 2020, Komatsu Urara, Komatsu-City, Ishikawa, Takaaki Kajita (ICRR, The University of Tokyo).
- ”Public Lecture commeorating the 110th Anniversary of School’s Founding,” Dec. 22, 2020, Kasukabe Girls High School, Kasukabe-City, Saitama, Takaaki Kajita (ICRR, The University of Tokyo).
- ”Public Lecture for Nakatani Foundation,” Dec. 27, 2020, Online, Takaaki Kajita (ICRR, The University of Tokyo).
- ”Public Lecture,” Jan. 18, 2021, Nihon Club, Chiyoda-Ku, Tokyo, Takaaki Kajita (ICRR, The University of Tokyo).
- ”Future Leaders’ Declaration on ASEAN-Japan Cooperation for International Marine Plastic Waste,” Mar. 16, 2021, Online, Takaaki Kajita (ICRR, The University of Tokyo).
- ”Public Lecture,” Mar. 26, 2021, Chuo-Ku, Tokyo, Takaaki Kajita (ICRR, The University of Tokyo).
- ”Kashiwa Campus Open Day,” Oct. 18, 2020, Online, Takaaki Kajita, Tomohisa Kawashima, Tomohiro Fujita, Kiseki Nakamura (ICRR, The University of Tokyo).
- ”Kashiwa Campus Open Day,” Oct. 17, 2020, Online, Kazumasa Kawata, Sei Kato, Ryo Higuchi (ICRR, The University of Tokyo).
- ”Kashiwa Campus Open Day,” Oct. 17, 2020, Online, Yoshihisa Obayashi, Tomohiro Yamada (KAGRA Observatory, ICRR, The University of Tokyo).
- ”Media Conference,” Feb. 1, 2020, Online, Masatake Ohashi (KAGRA Observatory, ICRR, The University of Tokyo).
- ”Media Conference,” Feb. 1, 2020, Online, Masahiro Teshima (ICRR, The University of Tokyo).
- ”The 22nd ICRR x IPMU Public Lecture,” Aug. 8, 2020, Online, Koji Noda (ICRR, The University of Tokyo).
- ”Public Lecture,” Nov. 28, 2020, Online, Masahiro Teshima (ICRR, The University of Tokyo).
- ”Musashi High School,” Nov. 4, 2020, Musashi High School, Musashino-City, Tokyo, Yoshiaki Ono (ICRR, The University of Tokyo).
- ”Astronomy Pub (Mitaka NETWORK University),” Jul. 18, 2020, Online, Ken Mawatari (ICRR, The University of Tokyo).

- ”Kushiro Children’s Museum Kodomo Yugakukan ,” Aug. 9, 2020, Online, Masami Ouchi (ICRR, The University of Tokyo).
- ”KamiokaLab YouTube Live,” May. 2, 2020, Online, Yoshinari Hayato (Kamioka Observatory, ICRR, The University of Tokyo).
- ”KamiokaLab YouTube Live,” Jul. 5, 2020, Online, Shigetaka Moriyama (Kamioka Observatory, ICRR, The University of Tokyo).
- ”Toyama High School,” Jul. 6, 2020, Toyama High School, Toyama-City, Toyama, Hidekazu Tanaka (Kamioka Observatory, ICRR, The University of Tokyo).
- ”Yamanashi Prefectural Kofu Minami High School,” Jul. 25, 2020, Kofu Minami High School, Kofu-City, Yamanashi, Yosuke Kataoka (Kamioka Observatory, ICRR, The University of Tokyo).
- ”Osaka Prefectural Senri High School,” Oct. 16, 2020, Online, Jun Kameda (Kamioka Observatory, ICRR, The University of Tokyo).
- ”Kashiwa Campus Open Day,” Oct. 18, 2020, Online, Shigetaka Moriyama (Kamioka Observatory, ICRR, The University of Tokyo).
- ”Kashiwa Campus Open Day,” Oct. 23-25, 2020, Online, Kamioka Observatory.
- ”Yamanashi Prefectural Nirasaki High School,” Oct. 21, 2020, Online, Ko Abe (Kamioka Observatory, ICRR, The University of Tokyo).
- ”Public Lecture,” Nov. 7, 2020, Inotani Sekishokan, Masayuki Nakahata (Kamioka Observatory, ICRR, The University of Tokyo).
- ”Public Lecture,” Nov. 21, 2020, Kamioka Community Center, Hida-City, Gifu, Masato Shiozawa (Kamioka Observatory, ICRR, The University of Tokyo).
- ”Live Tour for Super-Kamiokande Open House,” Nov. 22, 2020, Online, Hiroyuki Sekiya (Kamioka Observatory, ICRR, The University of Tokyo).
- ”Public Lecture on Super-K for Super-Kamiokande Open House,” Nov. 22, 2020, Online, Masayuki Nakahata (Kamioka Observatory, ICRR, The University of Tokyo).
- ”Family Tour for Super-Kamiokande Open House,” Nov. 22, 2020, Online, Motoyasu Ikeda (Kamioka Observatory, ICRR, The University of Tokyo).
- ”Super-Kamiokande Open House,” Nov. 22, 2020, Online, Kohei Okamoto, Yuki Kanemura (Kamioka Observatory, ICRR, The University of Tokyo).
- ”Public Lecture on Hyper-K for Super-Kamiokande Open House,” Nov. 22, 2020, Online, Masato Shiozawa (Kamioka Observatory, ICRR, The University of Tokyo).
- ”Worldwide Tour for Super-Kamiokande Open House,” Nov. 22, 2020, Online, Yoshinari Hayato (Kamioka Observatory, ICRR, The University of Tokyo).
- ””What is Super-Kamiokande?” for Super-Kamiokande Open House,” Nov. 23, 2020, Online, Makoto Miura, Takuto Yoshida, Hiromi Nishida (Kamioka Observatory, ICRR, The University of Tokyo).
- ”Q&A session for Super-Kamiokande Open House,” Nov. 23, 2020, Online, Masayuki Nakahata (Kamioka Observatory, ICRR, The University of Tokyo).
- ”Hirameki Tokimeki Science,” Mar. 20, 2021, Online, Masayuki Nakahata, Makoto Miura, Yasuhiro Nakajima, Shintaro Miki (Kamioka Observatory, ICRR, The University of Tokyo).
- ”Science Cafe,” Mar. 27, 2021, Gifu Shinbun sha, Gifu-City, Gifu, Masato Shiozawa (Kamioka Observatory, ICRR, The University of Tokyo).
- ”NHK Culture Center Yokohama Landmark,” Aug. 1, 2020, Online, Masatake Ohashi (KAGRA Observatory, ICRR, The University of Tokyo).
- ”NHK Culture Center Yokohama Landmark,” Aug. 29, 2020, Online, Hideyuki Tagoshi (KAGRA Observatory, ICRR, The University of Tokyo).

- ”NHK Culture Center Yokohama Landmark,” Sep. 12, 2020, Online, Kyohei Kawaguchi (ICRR, The University of Tokyo).
- ”Open College in Hida 2020,” Oct. 3, 2020, Hida Earth Wisdom Center, Takayama-City, Gifu, Masatake Ohashi (KAGRA Observatory, ICRR, The University of Tokyo).
- ”Open College in Hida 2020,” Oct. 3, 2020, Hida Earth Wisdom Center, Takayama-City, Gifu, Kazuhiro Yamamoto (KAGRA Collaborator)(Toyama University).
- ”The 23rd ICRR x IPMU Public Lecture,” Nov. 22, 2020, Online, Hideyuki Tagoshi (KAGRA Observatory, ICRR, The University of Tokyo).
- ”KAGRA Open House,” Nov. 22, 2020, Online, Koseki Miyo, Tomohiro Yamada, Kenta Tanaka (KAGRA Observatory, ICRR, The University of Tokyo).
- ”KAGRA Open House,” Nov. 23, 2020, Online, Shinji Miyoki (KAGRA Observatory, ICRR, The University of Tokyo).
- ”Public lecture for KAGRA Open House,” Nov. 23, 2020, Online, Masatake Ohashi (KAGRA Observatory, ICRR, The University of Tokyo).
- ”Family Tour for KAGRA Open House,” Nov. 23, 2020, Online, Keiko Kokeyama (KAGRA Observatory, ICRR, The University of Tokyo).
- ””What is KAGRA?” for KAGRA Open House,” Nov. 23, 2020, Online, Masayuki Nakano (KAGRA Observatory, ICRR, The University of Tokyo).
- ”Q&A session for KAGRA Open House,” Nov. 23, 2020, Online, Hideyuki Tagoshi, Takashi Uchiyama (KAGRA Observatory, ICRR, The University of Tokyo).
- ”World wide Live Tour for KAGRA Open House,” Nov. 23, 2020, Online, Masayuki Nakano, Fabian Arellano (KAGRA Observatory, ICRR, The University of Tokyo).
- ”An Evening with Nobel Laureates for Tohoku University,” Nov. 25, 2020, Online, Takaaki Kajita (ICRR, The University of Tokyo).
- ”Hida-Kamioka High School,” Oct. 6, 2020, Online, Osamu Miyakawa (KAGRA Observatory, ICRR, The University of Tokyo).
- ”Hida-Kamioka High School,” Oct. 6, 2020, Online, Masatake Ohashi (KAGRA Observatory, ICRR, The University of Tokyo).
- ”Osaka Prefectural Senri High School,” Oct. 16, 2020, Online, Takahiro Yamamoto (KAGRA Observatory, ICRR, The University of Tokyo).
- ”Yamanashi Prefectural Nirasaki High School,” Nov. 4, 2020, Online, Takashi Uchiyama (KAGRA Observatory, ICRR, The University of Tokyo).
- ”Toyama High School,” Jul. 6, 2020, Toyama High School, Toyama-City, Toyama, Keiko Kokeyama, Takaaki Yokozawa (KAGRA Observatory, ICRR, The University of Tokyo).
- ”Aichi Prefectural Meiwa High School,” Oct. 22, 2020, Meiwa High School, Nagoya-City, Meiwa, Masatake Ohashi (KAGRA Observatory, ICRR, The University of Tokyo).
- ”MoU Signing Ceremony,” Oct. 27, 2020, Tokyo City University, Takaaki Kajita (ICRR, The University of Tokyo).

(c) Visitors

Kashiwa Campus (Total: 1 groups, 2 people)

- Junior High and High schools: 0 group
- Universities and Graduate schools: 0 group
- Researchers: 0 group
- Inspections: 0 groups

- Press: 1 groups
- Others: 0 group

KAMIOKA Observatory (Total: 45 groups, 158 people)

- Junior High and High schools: 0 group
- Universities and Graduate schools: 5 groups
- Researchers: 10 groups
- Inspections: 9 groups
- Press: 9 groups
- Others: 12 groups

KAGRA Observatory (Total: 13 groups, 50 people)

- Junior High and High schools: 0 group
- Universities and Graduate schools: 3 groups
- Researchers: 1 groups
- Inspections: 7 groups
- Press: 0 group
- Others: 2 groups

F. Inter-University Research Activities

Numbers of Researchers

		Number of Applications	Number of Adoptions	Number of Researchers
Facility Usage				
Kamioka Observatory	Domestic	46	46	1,211
	International	9	9	49
Akeno Observatory	Domestic	6	6	193
	International	2	2	25
Norikura Observatory		11	11	93
Primary Cosmic rays, Kashiwa underground facility		4	4	20
KAGRA Observatory	Domestic	22	22	591
	International	9	9	63
High Energy Astrophysics Facility in Canarias		11	11	432
Laboratorial Facilities in Kashiwa		1	1	7
Large-Scale Comping System in Kashiwa	Domestic	12	12	237
	International	2	2	7
Conference Facilities in Kashiwa	Domestic	8	8	243
	International	3	3	31
Overseas Facilities (Utah, Tibet and Bolivia)	Domestic	18	18	166
	International	4	4	37
Annual Sums	Domestic	139	139	3,193
	International	29	29	212

Joint Research				
Neutrino and Astroparticle Research	Domestic	46	46	1,221
	International	10	10	59
High Energy Cosmic Ray Research	Domestic	60	60	1,253
	International	10	10	83
Astrophysics and Gravity Research	Domestic	25	25	659
	International	9	9	70
Research Center for Cosmic neutrinos		8	8	70
Annual Sums	Domestic	139	139	3,193
	International	29	29	212

Research Project Titles

1. Astroparticle physics using the Super-Kamiokande detector
2. Study of atmospheric neutrino flux and neutrino oscillations
3. Study of simulation for atmospheric neutrino
4. Studying the Neutrino Mass Hierarchy With Atmospheric Neutrinos
5. Study of flavor identification of atmospheric and beam neutrinos
6. Study of solar neutrino energy spectrum
7. Precise measurement of Day/Night effect for ^8B solar neutrinos
8. Study for Supernova monitor
9. Study of Supernova Relic Neutrinos
10. Elucidation of accidental background events with neutron capturing in water Cherenkov detector

11. Search for proton decay via $e^+\pi^0$ mode
12. Study of proton decay p $\rightarrow \nu K^+$
13. Study in upward-going muons and high energy neutrinos
14. Sidereal daily variation of $\sim$10TeV galactic cosmic ray intensity observed by the Super-Kamiokande
15. Neutrino search associated with astronominal transient events
16. Tokai to Kamioka Long Baseline Experiment T2K
17. Neutrino interaction study using accelerator data
18. Study to improve sensitivity of neutrino oscillation measurement in T2K expriment
19. Joint Oscillation Analysis With the T2K and Super-Kamiokande Experiments
20. Energy calibration for Super-Kamiokande
21. Development of a new LINAC for Super-Kamiokande energy calibration
22. Research and development of computer simulation of Super-Kamiokande detector
23. Development of low concentration radon detection system
24. R&D of Megaton scale water Cherenkov Detector Hyper-Kamiokande
25. Development of the Large Aperture Photodetector for a next-generation neutrino detector
26. Development of software for the next generation neutrino detector
27. Measurement of radon in underground laboratories and evaluation of effects from radon to experiments
28. Study for lowering backgrounds of radioisotopes in large volume detectors
29. Development of a radioactivity assay system for underground experiments
30. Measurement of neutron flux at the Kamioka underground laboratory
31. Trace level radio-activity measurements for SK and underground experiments with an ICP-mass spectrometer
32. RI measurement for SK-Gd project with HPGe detector
33. Generation three direct dark matter search experiment
34. A Search for Dark Matter using Liquid Xenon Detector
35. Detector structure study for future direct dark matter search experiment
36. Development of low radioactivity molecular sieves for dark matter search experiment
37. Study on surface background removal in the dark matter search
38. Research and development for XENONnT and search for dark matter
39. Direction-sensitive dark matter search
40. A study on the near-infrared emission of liquid xenon
41. Study of double beta decay of ^{48}Ca
42. Studies on the background evaluation using laser spectroscopy analysis
43. Integration of crustal activity observation around the Atotsugawa fault
44. Strain, tilt, seismic measurement in Kamioka-mine
45. Searches for neutrinoless double beta decay with high-pressure Xenon gas detector
46. Soft-error-rate estimation for semiconductor device at underground laboratory

47. R&D for a Small Atmospheric Cherenkov Telescope in Akeno Observatory
48. Development of new surface detector for observation of ultra high energy cosmic ray at Telescope Array site
49. Multi-Color Imager for Transients, Survey and Monstrous Explosions
50. Observation of Galactic Cosmic Ray Intensities using Large Area Muon Telescopes
51. Development of Water Cherenkov Muon Detector using Waterproof Sheet
52. Observation of solar neutrons from solar cycle 24 to 25
53. Space weather observation using muon hodoscope at Mt. Norikura
54. Observation of cosmogenic nuclides concentrations at Mt. Norikura
55. Study of secondary cosmic rays from Thundercloud at Mt. Norikura
56. Development of high energy proton irradiation technique for devices used in spaceship
57. Investigation of alpine plants on Mt. Norikura
58. Symbiosis betweem Pinus pumila and Nucifraga caryocatactes on Mt.Norikura
59. Effects of abiotic factors on sporocarp communities of ectomycorrhizal fungi
60. The conservation program of Rock ptarmigan
61. Atmospheric mercury speciation dynamics and mercury wet deposition monitoring at the high-altitude
62. Observational Research on Particle Acceleration and Cosmic-ray Shower in Thunderstorm Electric Fields
63. CTA Project
64. Development of Focal Plane Instrumemnts for the CTA Large Sized Telescope
65. Development of the readout system for the CTA large sized telescopes
66. Engineering runs of the first Large Size Telescope of CTA and construction of LST2-4 in La Palma Canary Islands, Spain
67. Set-up and Commissioning of the onsite data center for CTA North in La Palma, Spain
68. Localization of very high energy gamma-ray emission region in an active galactic nuclei
69. Early phase observations with CTA Large Sized Telescopes
70. Development of the CTA/LST telescope control system
71. Integration and operation of the optical and power systems in CTA LST
72. Development of a system for monitoring characteristics of the CTA-LST PMTs
73. CTA-Japan Physics Research
74. R&D of the measurement of atmospheric transparency at the Telescope Array site
75. The extreme Universe viewed in very-high-energy gamma rays 2020
76. Study of Extremely-high Energy Cosmic Rays by Telescope Array
77. Development of camera for CTA small-sized telescopes
78. CTA Monte Carlo simulation
79. Study of High Energy Gamma-ray Objects with the MAGIC telescope
80. Development of an advanced Compton camera using SOI pixel semiconductor
81. Observing ultrahigh-energy cosmic rays with new fluorescence detectors at Telescope Array site
82. Research and development of surface detectors for the stable run of the TA$\times$4 experiment

83. Study of very high energy cosmic rays around 10^{17} eV with the TALE hybrid experiment
84. Research and development of a Fresnel lens air fluorescence telescope for the next generation UHECR observation
85. The observation of abnormal shower event with lightning by TA surface particle detector
86. Calibration of fluorescence detector optical system with standard light source mounted on UAV
87. Development and analysis of night cloud observation by CCD camera for automatic observation of air fluorescence detector
88. Observation of airshower fluorescence light at the TA FD site by using an Imaging UV telescope
89. Experimental Study of High-energy Cosmic Rays in the Tibet ASγ experiment
90. Study of High Energetic Radiation from Thundercloud in the Altiplano
91. Sidereal daily variation of $\sim$10TeV galactic cosmic ray intensity observed by the Tibet air shower array
92. Study of the composition of cosmic-rays at the Knee
93. A study on variation of interplanetary magnetic field with the cosmic-ray shadow by the sun
94. Air shower observation for high-energy gamma ray and cosmic ray detections at the Chacaltaya Cosmic Ray Observatory
95. Study on High Energy Cosmic Ray Sources by Observation in Space with CALET
96. Design study of a Compton camera for study of cosmic rays
97. Observation with Ashra
98. Integration of the optical fiber trigger system for Ashra
99. comprehensive study of high-energy astrophysical phenomena
100. Development of a new code for cosmic-ray air shower simulation
101. YMAP symposium 2020 (Basic part)
102. Study of solar magnetic fields using the cosmic-ray Sun's shadow observed at the southern hemishpere
103. Cosmic ray interactions in the knee and the highet energy regions
104. Study of Fast Moving Dark Matters and Meteoroids using High Sensitivity CMOS Camera System
105. Development of the local center for the fully remote operation of TA-FD
106. Study of high-energy cosmic-ray anisotropy at the Chacaltaya Cosmic Ray Observatory
107. Research of Large-scale Gravitational wave Telescope (X)
108. Study of Gravitational-wave by cryogenic laser interferometer CLIO in KAMIOKA Mine (IV)
109. Development of High Performance Cryogenic Mirror Control System
110. Construction of KAGRA data transfer and storage system (6)
111. R&D for the intensity stabilization of the laser system in KAGRA
112. Development of scattered light measurement technique and noise reduction for improving sensitivity in KAGRA
113. Development of precision profiler for mirrors of LCGT interferometer 10
114. Development of optical cavity for ultranarrow stable lasers
115. Development of the OMC Mark II for KAGRA
116. Study of signal reconstruction and calibration for the gravitational wave telescope KAGRA (2)
117. Study of Environmental Noise Reduction in KAGRA

118. Calorimetric measurement of absorption coefficient of sapphire at cryogenic temperatures
119. Numerical Simulation of Electro-Magnetic Wave Propagation in Gravitational wave Detector VIII
120. Control and automatic operation for KAGRA
121. Development of a high performance sapphire mirror suspension
122. Research on cryogenic payload for KAGRA
123. Precise geophysical observation at the Kamioka underground site and modeling of crustal activities
124. Promotion of KAGRA scientific collaboration, and development of new methods in gravitational data analysis
125. Study of detector characterization using machine learning
126. Development of KAGRA cryocooler control system for ultra-low vibration
127. Study of the investigation methed for the environmental noises by injection in KAGRA detector
128. Environmental investigation for underground gravity measurement at micro-meter scale
129. Search for poorly modeled gravitational wave signal using KAGRA
130. Cosmic Reionization and Galaxy Formation Probed with Large Optical Near-Infrared Telescopes
131. Evolution of the universe and particle physics
132. Detection of time variations for cosmogenic nucleid Be-7
133. Time profile of radioactive Cs concentration and its aerosol size distribution in local area
134. Development of the observation templates of supernova neutrinos on Super Kamiokande
135. Evaluation of the erupted radioactivities into the environment
136. Behavior of radionuclides in the marine environment
137. Frontier of the planetary material science
138. Precise calculation of the atmospheric neutrino flux
139. CRC workshop for future plans in cosmic ray research
140. Light scattering measurement in the water using the Super-Kamiokande detector
141. Neutron Antineutron Oscillation in Super-Kamiokande
142. New Photogrammetry Calibration and Machine Learning Event Reconstruction for Super-Kamiokande and Hyper-Kamiokande
143. Study of supernova neutrinos in Super-Kamiokande
144. Data Taking, Calibrations, Measurements and Analysis with Super-Kamiokande and SupreK-Gd
145. Tests on mPMT photodetection system for Hyper-Kamiokande Experiment
146. Constraining systematics at T2K and SuperKamiokande oscillation analyses using neutrino-nucleus interaction models
147. Development and testing of cost-effective, high-performance PhotoDetector anti-implosion covers for Hyper-Kamiokande
148. Finalization of the design for the Outer Detector for the Hyper-Kamiokande experiment
149. Photosensors for the Hyper-Kamiokande Experiment
150. Neutrino Telescope Array Light Collector Prototype Test
151. A joint observation of near earth space through $\sim$100 GeV cosmic rays using the Akeno and the GRAPES-3 muon telescope

152. Ultra-high-energy cosmic-ray origin studies with the Telescope Array and TA×4 surface detector
153. Study of the Hotspot in Ultra High Energy Cosmic Rays with a New Large Telescope Array
154. Study of UHECR origin using the TA×4 Fluorescence Detectors
155. Investigating the origin of the diffuse cosmic gamma-ray background in the CTA era
156. 2nd symposium ”Dark Matter searches in the 2020s” (”Kashiwa Dark Matter symposium”)
157. Workshop: Synergies at new frontiers at gamma-rays, neutrinos and gravitational waves
158. Study for Galactic CR origin using the ALPACA air shower array in Bolivia
159. Study of high-energy cosmic rays at a high altitude in Tibet, China
160. Cryogenic Test masses, Isolation, suspension
161. Development of high power KAGRA LASER system
162. Development of calibration and reconstruction system for KAGRA observation
163. Filter cavity experiments for frequency dependent squeezed light source for KAGRA
164. Noise Evaluation and Reduction of Cryogenic Mirror Suspension System in KAGRA
165. Search for astrophysical sources of gamma rays and gravitational waves
166. Eccentric Binary Black Hole Waveform Template: SEOBNREv1 and SEOBNREv1_ROM
167. Collaboration for gravitation wave observatory in study dark matter with compact binary coalescence
168. Implementing Sophisticated Data Analysis Methods on KAGRA Data

G. List of Committee Members

(a) Board of Councillors

KAJITA, Takaaki	ICRR, The University of Tokyo
SHIOZAWA, Masato	ICRR, The University of Tokyo
TAKITA, Masato	ICRR, The University of Tokyo
KAWASAKI, Masahiro	ICRR, The University of Tokyo
HOSHINO, Masahiro	Graduate School of Science, The University of Tokyo
MIYAZONO, Kohei	The University of Tokyo
TOKUSHUKU, Katsuo	Institute of Particle and Nuclear Studies, KEK
AOKI, Shinya	Yukawa Institute for Theoretical Physics, Kyoto University
TSUNETA, Saku	National Astronomical Observatory of Japan
TORII, Shoji	Faculty of Science and Engineering, Waseda University
MORI, Masaki	Ritsumeikan University
YOKOYAMA, Junichi	Research Center for the Early Universe, The University of Tokyo
YAMADA, Toru	Institute of Space and Astronautical Science
ASAI, Shoji	International Center for Elementary Particle Physics, The University of Tokyo
KUSANO, Kanya	Institute for Space-Earth Environmental Research, Nagoya University

(b) Advisory Committee

KAJITA, Takaaki	ICRR, The University of Tokyo
KITANO, Ryuichiro	KEK Theory Center
IOKA, Kunihito	Yukawa Institute for Theoretical Physics, Kyoto University
ISHITSUKA, Masaki	Tokyo University of Science
OZAWA, Kyoichiro	Institute of Particle and Nuclear Studies, KEK
YOKOYAMA, Masashi	Graduate School of Science, The University of Tokyo
TASHIRO, Makoto	Graduate School of Science and Engineering, Saitama University
OGIO, Shoichi	Graduate School of Science, Osaka City University
NISHIJIMA, Kyoshi	Tokai University
ITOW, Yoshitaka	Institute for Space-Earth Environmental Research, Nagoya University
KANDA, Nobuyuki	Graduate School of Science, Osaka City University
NAKAHATA, Masayuki	ICRR, The University of Tokyo
SAGAWA, Hiroyuki	ICRR, The University of Tokyo
KAWASAKI, Masahiro	ICRR, The University of Tokyo
SHIOZAWA, Masato	ICRR, The University of Tokyo
TAKITA, Masato	ICRR, The University of Tokyo
OHASHI, Masatake	ICRR, The University of Tokyo
TESHIMA, Masahiro	ICRR, The University of Tokyo

(c) Inter-University Research Advisory Committee

ITOW, Yoshitaka	Institute for Space-Earth Environmental Research, Nagoya University
ASO, Yoichi	National Astronomical Observatory of Japan
MORI, Masaki	Ritsumeikan University
TAJIMA, Hiroyasu	Institute for Space-Earth Environmental Research, Nagoya University
KUBO, Hidetoshi	Kyoto University
HIBINO, Kinya	Kanagawa University
MIUCHI, Kentaro	Graduate School of Science, Kobe University
TSUNESADA, Yoshiki	Graduate School of Science, Osaka City University
NAKAHATA, Masayuki	ICRR, The University of Tokyo
TAKITA, Masato	ICRR, The University of Tokyo
TAGOSHI, Hideyuki	ICRR, The University of Tokyo
NODA, Koji	ICRR, The University of Tokyo
UCHIYAMA, Takashi	ICRR, The University of Tokyo

H. List of Personnel

Director	KAJITA, Takaaki,		
Vice-Director	NAKAHATA, Masayuki,	SAGAWA, Hiroyuki,	

ICRR HQ in Kashiwa Campus

- High Energy Cosmic Ray Division

Scientific Staff	ASANO, Katsuaki,	ENOMOTO, Ryoji,	HADASCH, Daniela,
	KAWATA, Kazumasa,	KINUGAWA, Tomoya,	KUBO, Hidetoshi,
	MAZIN, Daniil Mihajlovic,	NODA, Koji,	NONAKA, Toshiyuki,
	OGIO, Shoichi,	OHISHI, Michiko,	OHNISHI, Munehiro,
	SAITO, Takayuki,	SAKO, Takashi,	SAKO, Takashi,
	SASAKI, Makoto,	TAKEDA, Masahiro,	TAKITA, Masato,
	TESHIMA, Masahiro,	VOVK, Ievgen,	YAMAMOTO, Tokonatsu,
	YOSHIDA, Tatsuo,	YOSHIKOSHI, Takanori,	
Technical Staff	AOKI, Toshifumi,	INOME, Yusuke,	OHOKA, Hideyuki,
	SEKINO, Koichi,		
Research Fellow	CHIKAWA, Michiyuki,	COLOMBO, Eduardo,	FEDYNITCH, Anatoli,
	FUKAMI, Satoshi,	Haibin Zhang,	HARADA, Akira,
	INADA, Tomohiro,	KAWASHIMA, Tomohisa,	MARQUEZ, Paniagua Patricia,
	NAKAMURA, Yoshiaki,	STRZYS, Marcel,	TAKAHASHI, Mitsunari,
	TAKEISHI, Ryuji,	YAMASAKI, Shotaro	ZHEZHER, Yana Valeryevna,
Secretary	IDOMURA, Takako,	SHIRAGA, Ryoko,	SUGAHARA, Midori,

- Astrophysics and Gravity Division

Scientific Staff	HARIKANE, Yuichi,	IBE, Masahiro,	KAWASAKI, Masahiro,
	ONO, Yoshiaki,	OUCHI, Masami,	
Research Fellow	AOYAMA, Shohei,	EIJIMA, Shintaro,	FUJITA, Tomohiro,
	HAYASHI, Kohei,	MAWATARI, Ken,	TOSHIKAWA, Jun,

Kamioka Observatory

Director	NAKAHATA, Masayuki,		
Scientific Staff	ABE, Ko,	ASAOKA, Yoichi,	BRONNER, Christophe,
	HAYATO, Yoshinari,	HIRAIDE, Katsuki,	IKEDA, Motoyasu,
	ITOW, Yoshitaka,	KAMEDA, Jun,	KATAOKA, Yosuke,
	MARTI MAGRO, Lluis,	MIURA, Makoto,	MORIYAMA, Shigetaka,
	NAKAJIMA, Yasuhiro,	NAKAYAMA, Shoei,	NAKAYA, Tsuyoshi,
	NISHIMURA, Yasuhiro,	PRONOST, Guillaume,	SEKIYA, Hiroyuki,
	SHIOZAWA, Masato,	TAKEDA, Atsushi,	TAKEMOTO, Yasuhiro,
	TANAKA, Hidekazu,	YANO, Takatomi,	
Administrative Staff	SHIMIZU, Akihiko,	YOSHIDA, Takuto,	
Public Relations Staff	TAKENAGA, Yumiko,		
Technical Staff	HIGASHI, Tetsuji,	IMAGAWA, Masahiro,	NOZAWA, Noriyuki,
	ONOUE, Tatsuya,		
Research Administrator	KURACHI, Masafumi,		
Research Fellow	ITO, Hiroshi,	NAKAMURA, Kiseki,	
Secretary	DOI, Kyoko,	KAMIKAWATO, Rie,	MAEDA, Yukari,
	NISHIDA, Hiromi,		

KAGRA Observatory

Director	OHASHI, Masatake,		
Scientific Staff	KAWAGUCHI, Kyohei,	KIMURA, Nobuhiro,	KOKEYAMA, Keiko,
	MIO, Norikatsu,	MIYAKAWA, Osamu,	MIYOKI, Shinji,
	OSHINO, Shoichi,	TAGOSHI, Hideyuki,	TOMARU, Takayuki,
	UCHIYAMA, Takashi,	USHIBA, Takafumi,	YAMAMOTO, Hiroaki,
	YAMAMOTO, Kazuhiro,	YAMAMOTO, Takahiro,	YOKOZAWA, Takaaki,
	YOSHII, Yuzuru,		
Administrative Staff	FUNADA, Shinya,	OKINAKA, Mihoko,	
Technical Staff	FURUTA, Kiyoshi,	KAMIIZUMI, Masahiro,	NAKADA, Kazuo,
	NAKAGAKI, Koji,	NAKANO, Masayuki,	NODE, Ayako,
	OHOKA, Hideyuki,	OMAE, Akio,	SAKAI, Akiko,
	SHIMODE, Katsuhiko,	TAKAHASHI, Masahiro,	TAMORI, Yukio,
	YOSHIMURA, Mitsuharu,		
Public Relations Staff	OBAYASHI, Yoshihisa,		
Research Fellow	MIYO, Koseki,	MORISAKI, Souichiro,	NARUKAWA, Tatsuya,
	OKUTOMI, Koki,	PENA ARELLANO, Fabian,	SAITO, Yoshio,
	SURESH, Jishnu,	SUZUKI, Toshikazu,	TROZZO, Lucia,
	UCHIKATA, Nami,	YUZURIHARA, Hirotaka,	
Secretary	KIKUCHI, Rie,	KUDO, Naomi,	NOJIRI, Midori,
	SAKAMOTO, Eri,		

High Energy Astrophysics Facility in Canarias

Director	TESHIMA, Masahiro,

Research Center for Cosmic Neutrinos

Director	OKUMURA, Kimihiro,		
Scientific Staff	KAJITA, Takaaki,	TASHIRO, Takuya,	TOKANAI, Fuyuki,
Technical Staff	SHINOHARA, Masanobu,		
Research Fellow	AKUTSU, Ryosuke,		
Secretary	KITSUGI, Atsuko,	MASHIMA, Chieko,	

Norikura Observatory

Director	TAKITA, Masato,		
Technical Staff	AWAI, Kyosuke,	HAYAKAWA, Hideaki,	IMANISHI, Hidenori,
	OKAZAKI, Nao,	SHIMODAIRA, Hideaki,	TOMURA, Tomonobu,
	USHIMARU, Tsukasa,		

Akeno Observatory

Director	SAGAWA, Hiroyuki,
Technical Staff	KOBAYASHI, Ryoichi,

Graduate Students

Doctor	ANDO, Kenta,	HIGUCHI, Ryo,	HSIEH, Bin-Hua,
	IWAMURA, Yuki,	KATO, Nobuyuki,	KATO, Sei,
	KIKUCHIHARA, Shotaro,	KOBAYASHI, Shin,	KOBAYASHI, Yukiho,
	MURAI, Kai,	NAKATSUKA, Hiromasa,	OHTANI, Yoshiki
	OKAMOTO, Kohei,	OTANI, Francis,	SAKURAI, Shunsuke,
	SHIN, Heungsu,	SONODA, Yutaro,	SONOMOTO, Eisuke,
	SUZUKI, Takumi,	TAKENAKA, Akira,	TANAKA, Kenta,
	TANG, Shenli,	XIA, Junjie,	YAMADA, Tomohiro,
	ZHANG, Haibin,		

Master	ABE, Hyuga,	ABE, Shotaro,	BAXTER, Joshua Ryo,
	FUJISUE, Kozo,	GOTO, Ryota,	HAN, Seungho,
	HASHIYAMA, Kazuaki,	IIDA, Kento,	IMAGAWA, Kaname,
	ISOBE, Yuki,	IWAYA, Masaki,	KANEMURA, Yuki,
	KARIYA, Yasuhiro,	KATO, Takashi,	LEE, Eunsub,
	MIKI, Shintaro,	MIYAZAKI, Kazuyoshi,	NAGAO, Yoshiki,
	NAKAYAMA, Yuhei,	NISHIMOTO, Takumi,	NISHIWAKI, Kosuke,
	NOMURA, Ryosuke,	OKIMOTO Naoya,	SAKAI, Nao,
	SATO, Yuta,	SHIBATA, Minato,	SHIMODATE, Karin,
	SUGIYAMA, Takumu,	SUN, Dongsheng,	SUZUKI, Ryota
	TAKAHASHI, Mari,	UEDA, Shusuke,	WANG, Xubin,
	WATANABE, Shuhei,	XU, Yi,	YAN, Haochen,
	YOKOE, Yoshichika,		

Administrative Division

Administrative Staff	AKAIDA, Yohei,	AKIYAMA, Makiko,	FUKUHARA, Nana,
	HIRAGA, Takuya,	KOBAYASHI, Toyoki,	MARUMORI, Yasuko,
	OHURA, Kiichi,	OKANO, Yuka,	ONO, Kazumi,
	SAITO, Akiko,	TAKAMICHI, Ryo,	WATANABE, Shinji,
	YAMADA, Takaharu,	YAMAGUCHI, Akiko,	YAMASUE, Akiko,
Research Administrator	ITO, Michiru,	SATO, Ritsuko,	SUGIMOTO, Kumiko,
Public Relations Staff	ITO, Yoriko,	NAKAMURA, Makio,	
Archive Room	NAKAMURA, Kenzo,		

INSTITUTE FOR COSMIC RAY RESEARCH
THE UNIVERSITY OF TOKYO

Address 5-1-5, Kashiwanoha, Kashiwa-shi, Chiba, 277-8582 Japan
TEL +81-4-7136-3102
FAX +81-4-7136-3115
URL www.icrr.u-tokyo.ac.jp

ICRR
Institute for Cosmic Ray Research
University of Tokyo